UNIVERSITÀ DEGLI STUDI DI MILANO

Department of Chemistry

PhD Course in Chemical Sciences, XXVIII Cycle

Pt-free Nano- and Micro-Structured Carbons for Electrochemical Oxygen Reduction Reaction

Stefania Marzorati

Matr. n. R10065

Tutor: Dr. Mariangela LONGHI

Co-tutor: Prof. Leonardo FORMARO

Coordinator: Prof. Emanuela LICANDRO

2015

"Can't you give me brains?" asked the Scarecrow.
"You don't need them. You are learning something every day.
A baby has brain, but it doesn't know much.
Experience is the only thing that brings knowledge,
and the longer you are on earth
the more experience you are sure to get"

(L. Frank Baum, The Wonderful Wizard of Oz)

Table of Contents

List of Acronyms

APM	Aerosol Pyrolysis Method
BE	Binding Energy
BET	Brunauer-Emmet-Teller
BJH	Barrett-Joyner-Halenda
CE	Counter Electrode
CTACl	CetylTrimethylAmmonium Chloride
CV	Cyclic Voltammetry
DOE	U.S. Department Of Energy
DSC	Differential Scanning Calorimetry
DFT	Density Functional Theory
EIS	Electrochemical Impedance Spectroscopy
FCs	Fuel Cells
FRU	Fructose
GBI	2-Guanidinobenzimidazole
GLU	Glucose
GUA	Guanidine acetate
HIS	Histidine
HR	High Resolution
K-L	Koutecky-Levich
LSV	Linear Sweep Voltammetry
LPM	Liters Per Minute
MBDOE	Million Barrels per Day of Oil Equivalent
MEA	Membrane Electrode Assembly
NHE	Normal Hydrogen Electrode
N-CMSs	N-doped Carbon MicroSpheres
N-CNCs	N-doped Carbon NanoCubes
N-CNTs	N-doped Carbon NanoTubes

ODC	Oxygen Depolarized Cathode
ORR	Oxygen Reduction Reaction
PEMFC	Polymer Electrolyte Membrane Fuel Cell
RE	Reference Electrode
RM	Reactant Mixture
RDE	Rotating Disk Electrode
RPM	Revolutions Per Minute
RRDE	Rotating Ring Disk Electrode
SEM	Scanning Electron Microscopy
TEM	Transmission Electron Microscopy
TGA	ThermoGravimetric Analysis
TM	Transition metal
TMG	1,1,3,3-Tetramethylguanidine
TPD-MS	Temperature Programmed Desorption-Mass Spectroscopy Analysis
UPS	Ultraviolet Photoelectron Spectroscopy
USP	UltraSpray Pyrolysis
XPS	X-Ray Photoelectron Spectroscopy
XRPD	X-Ray Powder Diffraction
XYL	Xylose
WE	Working Electrode

Abstract

Oxygen reduction reaction (ORR) catalysts are of crucial importance in developing low- and medium-temperature fuel cells, as PEMFCs (Polymer Electrolyte Membrane Fuel Cells), from which sizeable energy saving and reduction of greenhouse gas emission are expected in comparison with the use of coal and oil based fuels in thermal engines. The same electrochemical oxygen reduction reaction takes place in oxygen depolarized cathodes (ODC) in chlor-alkali electrolysis, replacing the conventional hydrogen evolving cathode, gaining about 30% energy consumption reduction in the overall process. At present carbon-supported Pt and Pt-rich alloys are best credited to the ORR purpose. However, Pt-based catalysts are not free from certain drawbacks, such as oxide formation and Pt particle coarsening through Ostwald ripening, that decrease the overall cell energy conversion efficiency. Furthermore, attendant problems concerning natural availability, geographic distribution and cost of platinum, render platinum supply strategic and fuel cells hardly scalable to mass production [1-5]. At present, projections on platinum usage for PEMFCs are estimated at ~15 ton y^{-1} in addition to the current ones, at a cost of ~40 \$ g^{-1}.

Therefore, non-precious metal catalysts are actively searched for, such as to meet already established operational benchmarks for conventional platinum PEMFC vehicular requirements (0.5 W cm^{-2}; 5500 h durability) [3] with the additional target of significant cost reduction.

Several papers on non-precious ORR catalysts have been published after a first report by Jasinski [6] in 1964 demonstrating the ORR activity of metal substitutes-phthalocyanines. Then, research on metal-nitrogen macrocycles significantly expanded, leading to the picture that ORR catalytic activity can be related to N_4-Me and N_2-Me moieties. However, for precursors cost and unsatisfactory lifetime performance, research was steered toward more simple nitrogen-containing reactants and preparation procedures. Significant steps in this direction were obtained by Dodelet *et al.* [7-11] who demonstrated that ORR overpotentials almost linearly decrease with increasing nitrogen content in carbon. Positive results were obtained on a series of samples prepared by high temperature treatment of carbon precursors in $NH_3/H_2/N_2$ mixtures; doping of these modified carbons with iron rather than cobalt salts was shown to be preferable for better efficiency in oxygen reduction, even though still lower than that of platinum. Further improvements both in terms of incipient ORR potentials and currents were obtained by Maruyama *et al*. using carbons from hemoglobin [12] and adenine-glucose [13] pyrolysis in the presence of added Fe(II) and Cu(II)/Fe(II) mixtures, respectively. The ORR promoting role of nitrogen in carbon was independently demonstrated both theoretically and experimentally. Indeed, it was found that substitutional nitrogen at a few, specific, peripheral positions of graphene layers in well-ordered carbon nanostructures is in itself able to promote ORR activity even in the absence of accompanying metal centers [14-16].

Besides the above examined composition-dependent factors, catalyst activity also depends on structural and morphological carbon support features. In fact, many electrocatalytic reactions show faster kinetics on carbon edge planes compared with basal ones. This is related to the ability of the edges to more readily chemisorb O_2 (this is the same reason why O_2 combusts faster from edges and defects) [15]. On the other hand, an optimized porosity of carbon supports is beneficial for an easy access of the oxygen to the catalyst layer in contact with the proton exchange electrolyte membrane [17]. Despite carbon materials of different textural morphology are widely used at an industrial level as supports for precious metal catalysts, in the PEMFC field, electrocatalysts are by far supported on the same VULCAN XC72 carbon. Given that improved catalytic activity of Pt-based catalysts has been achieved by the use of carbons with pore size centered in the mesoporous region, even developed with advanced synthesis, including template methods, such strategy should be pursued also for Pt-free catalytic systems.

In this project a number of Pt-free N-doped C-based catalysts have been synthesized on the basis of different synthetic and templating strategies aiming to understand how compositional, morphological and textural aspects of the end material can affect the electrochemical behaviour of ORR. Materials have been characterized using different physico-chemical methods including a study of the kinetics and mechanism of the electrochemical oxygen reduction reaction. Electrochemical results were obtained by rotating disk electrode (RDE) and rotating ring disk electrode (RRDE). Surface and bulk analyses have been performed by BET technique, XPS and XRPD (sometimes data were recorded at synchrotron facilities). (HR) TEM, SEM (combined with FIB milling) imaging was also performed to characterize samples morphology.

Many types of samples have been synthesized, starting with mesoporours N-, Fe- doped carbons obtained by heat treatment of a solution of precursors, using silica as a templating agent. Outstanding results in terms of ORR electroactivity in acidic and alkaline conditions have been recorded. Some samples, especially in alkaline media, catalyze ORR even better than commercial Pt-based catalysts. Then, attempting to prepare materials with a precise and defined order and trying to emphasize some of their properties such as surface area and conductivity, ordered carbonaceous nano- and microstructures were synthesized. By chemical vapor deposition N-, Fe- doped carbon nanotubes (N-CNTs) were prepared and some interesting aspects related to the aging of the Fe-doped MgO catalyst used to grow N-CNTs were evidenced. Then, a modified method, but very similar to that used in the synthesis of nanotubes, surprisingly allowed the synthesis of innovative N-doped hollow carbon nanocubes (N-CNCs). This is the great novelty of the work. Due to nanocubes endothermal transformation, happening at 37°C, as detected by DSC, and to the empty space available in the internal part of each cube, many applications can be thought for example involving cubes as nano-reactors that can be opened/close in correspondence of body's temperature changes. This feature could be taken into considerations for medical applications, after testing and verifying the biocompatibility of nanocubes. Finally, a completely different technique, an ultraspray pyrolysis method (USP) was used to obtain N-, Fe- doped carbon microspheres. The inherent scalability of continuous flow methods such as USP represents a significant advantage compared to alternative synthetic strategies requiring batch processing or surface catalyzed deposition of nanostructured carbon materials (e.g. CVD growth), this feature might be useful

in order to improve electrode packing and, consequently, mass transport electrocatalytic applications.
The last results section, apparently diverging from the main goals of the present work, was thought to better understand the electronic C-surface behavior in charge transfer reactions. This is actually strongly connected to the oxygen reduction reaction, for which all the catalysts, hereby synthesized, were designed. However, instead of starting from complicated systems involving porous and doped-carbons, the choice was addressed to the simplest but closest material: annealed and non-annealed amorphous carbon thin films prepared by DC-magnetron sputtering technique.

Part of the work described was carried out at Trinity College Dublin in the laboratory of Prof. Colavita as a part of an academic collaboration and 5 months exchange granted by the European LLP Erasmus Program.

References

1. H.A. Gasteiger, J. Garche, Fuel Cells, in Handbook of Heterogeneous Catalysis, G. Ertl, H. Knözinger, F. Schüth, J. Weitkamp (Eds.), Wiley-VCH (2008).

2. X. Yu, S. Ye, Recent advances in activity and durability enhancement of Pt/C catalytic cathode in PEMFC, Journal of Power Sources, 172 (2007), 133-144.

3. H.A. Gasteiger, S.S. Kocha, B. Sompalli, F.T. Wagner, Activity benchmarks and requirements for Pt, Pt-alloy, and non-Pt oxygen reduction catalysts for PEMFCs, Applied Catalysis B, 56 (2005), 9-35.

4. P.J. Ferreira, G.J. la O', Y. Shao-Horn, D. Morgan, R. Makharia, S. Kocha, H.A. Gasteiger, Instability of Pt/C electrocatalysts in proton exchange membrane fuel cells: A mechanistic investigation, Journal of the Electrochemical Society, 152 (2005), A2256-A2271.

5. U.A. Paulus, T.J. Schmidt, H.A. Gasteiger, R.J. Behm, Oxygen reduction on a high-surface area Pt/Vulcan carbon catalyst: a thin-film rotating ring-disk electrode study, Journal of Electroanalytical Chemistry, 495 (2001), 134-145.

6. R.J. Jasinski, New fuel cell cathode catalyst, Nature, 201 (1964), 1212-1213.

7. F. Jaouen, S. Marcotte, J.-P. Dodelet, G. Lindbergh, Oxygen Reduction Catalysts for Polymer Electrolyte Fuel Cells from the Pyrolysis of Iron Acetate Adsorbed on Various Carbon Supports, Journal of Physical Chemistry B, 107 (2003), 1376-1386.

8. S. Marcotte, D. Villers, N. Guillet, L. Roue, J.-P. Dodelet, Electroreduction of oxygen on Co-based catalysts: determination of the parameters affecting the two-electron transfer reaction in an acid medium, Electrochimica Acta, 50 (2004), 179-188.

9. C. Medard, M. Lefevre, J.-P. Dodelet, F. Jaouen, G. Lindbergh, Oxygen reduction by Fe-based catalysts in PEM fuel cell conditions: Activity and selectivity of the catalysts obtained with two Fe precursors and various carbon support, Electrochimica Acta, 51 (2006), 3202-3213.

10. M. Lefevre, E. Proietti, F. Jaouen, J.-P. Dodelet, Iron-Based Catalysts with Improved Oxygen Reduction Activity in Polymer Electrolyte Fuel Cells, Science, 324 (2009), 71-74.

11. J. Tian, L. Birry, F. Jaouen, J.-P. Dodelet, Fe-based catalysts for oxygen reduction in proton exchange membrane fuel cells with cyanamide as nitrogen precursor and/or pore-filler, Electrochimica Acta, 56 (2011), 3276-3285.

12. J. Maruyama, J. Okamura, K. Miyazaki, Y. Uchimoto, I. Abe, Hemoglobin Pyropolymer Used as a Precursor of a Noble-Metal-Free Fuel Cell Cathode Catalyst, Journal of Physical Chemistry C, 112 (2008), 2784-2790.

13. J. Maruyama, I. Abe, Structure control of a carbon-based noble-metal-free fuel cell cathode catalyst leading to high power output, Chemical Communication, 27 (2007), 2879-2781.

14. R.A. Sidik, A.B. Anderson, N.P. Subramanian, S.P. Kumaraguru, B.N. Popov, O_2 Reduction on Graphite and Nitrogen-Doped Graphite: Experiment and Theory, Journal of Physical Chemistry B, 110 (2006), 1787-1793.

15. P.H. Matter, L. Zhang, U.S. Ozkan, The role of nanostructure in nitrogen-containing carbon catalysts for the oxygen reduction reaction, Journal of Catalysis, 239 (2006), 83-96.

16. P.H. Matter, E. Wang, U.S. Ozkan, Preparation of nanostructured nitrogen-containing carbon catalysts for the oxygen reduction reaction from SiO_2- and MgO-supported metal particles, Journal of Catalysis, 243 (2006), 395-403.

17. H. Chan, S.H. Joo, C. Pak, Synthesis and characterization of mesoporous carbon for fuel cell applications, Journal of Materials Chemistry, 17 (2007), 3078-3088.

Chapter 1
Introduction

It is well-known that mankin'sd lifestyle is directly affected by energy and energy issues. Various indexes point out the relationships between energy consumption and average life expectancy, childhood mortality rate and, more in general, life quality. With respect to the past, animal work has been replaced by efficient engines and energy sources underwent deep changes, passing from the wood and water mills of last centuries, to hydroelectric energy, carbon, oil, gas, nuclear energy, solar energy and so on. Low cost energy availability has improved life quality of developed countries and for this reason, every country yearns for more and more energy to obtain optimal products and services. With time, products quantity yield, normalized by working hours, has increased, thus diminishing the daily working time and leaving more space for spare-time activities and culture. However, due to the economic and technological growth of countries, the increasing energy demand is making the whole world face the problem of the non-infinite availability of the mostly used energy sources, fossil fuels, stimulating the research in the field of renewables. In Italy, in the period between 1950 and 1970, it has been recorded a 10% increase of energy consumption per year per person. This data gives an idea of the importance of energy during the development history periods of a country. Unfortunately, all energy sources present, in lower or higher degree, their multiple drawbacks. It is enough to consider, for instance, of the wide green areas that have been deforested at the beginning of the last century to gain wood, to the oceans oil contamination due to oil-platforms disasters, to deaths in carbon mines, to the Chernobyl nuclear reactor accident. Every energy source utilization needs a very careful environmental and risk evaluation and a study of a plan to minimize it. However, safety concerns are just a slice of the overall energy issues, and far more consideration is given to energy availability and costs.

1.1. The Energy Problem

Even if a few decades ago it was thought that the energetic problem was just a developed countries concern, at present emerging countries such as India and China, are making the whole world realize how important energy is for the world's continuous development and that reliable and affordable energy is central to world economy and national security. United States of America and Europe, through their competent authorities, the General Directorate for Energy and Transportation and the Department of Energy, edited in the last years a number of documents which are considered to be the most reliable in the energy field. For this reason, documents from these agencies will be the main sources of data given in this introduction section, also considering the wide range of contradictory data and elaborations found in the literature [1].

According to the Energy Security and Solidarity Action Plan from the General Directorate for Energy and Transportation: "Europe has agreed a forward-looking political agenda to achieve its energy objectives of sustainability, competitiveness and security of supply, by reducing greenhouse gas emissions by 20%, increasing the share of renewables in the energy consumption to 20% and improving energy efficiency by 20%, all of it by 2020. This agenda means very substantial change in Europe's energy system over the coming years, with public authorities, energy regulators, infrastructure operators, the energy industry and citizens all actively involved. It means choices and investments during a time of much change in global energy markets and international relations. Europe's political leaders need to give clear messages on the energy strategy" [2]. Similar recommendations were given by the U.S. Department of Energy (DOE): increase the use of renewables, moderate energy consumption and minimize energy-related carbon dioxide emissions in the absence of new policies designed to mitigate greenhouse gas emissions.

As **Fig. 1.1** (from 2010 DOE Annual Energy Outlook) shows, at present and in the next 20 years projections, the majority of the energy sources comes and will come from fossil fuels, that are not renewable and whose reserves are often located in politically unstable areas. In the future it is expected that the annual production of fossil fuels will reach a peak followed by a decrease. DOE Annual Energy Outlook reported that for the U.S. the production curve is already in the decreasing zone while the world production is increasing. According to British Petroleum the decrease is not yet observed because technological developments allow new deposits to be discovered and greater depths to be reached. Thus, depending on the projection, the world production peak will manifest before 2020. The same 2010 DOE Annual Energy Outlook (**Fig. 1.1**) forecasted an increase in primary energy consumption of 14 percent from 2008 to 2035, with an average annual growth of 0.5 percent. It also projected that the major growth will concern the renewable fuels in electricity generation and liquid fuels production for transportation. Notwithstanding fossil fuels will continue providing most of the consumed energy over the next 20 years, their use will necessarily fall from 84% in 2008 to 78% in 2035, therefore bringing the fossil fuel issues to the forefront and increasingly putting pressure on the authorities. The role of renewables could grow further still if current policies that support renewable fuels are extended [3].

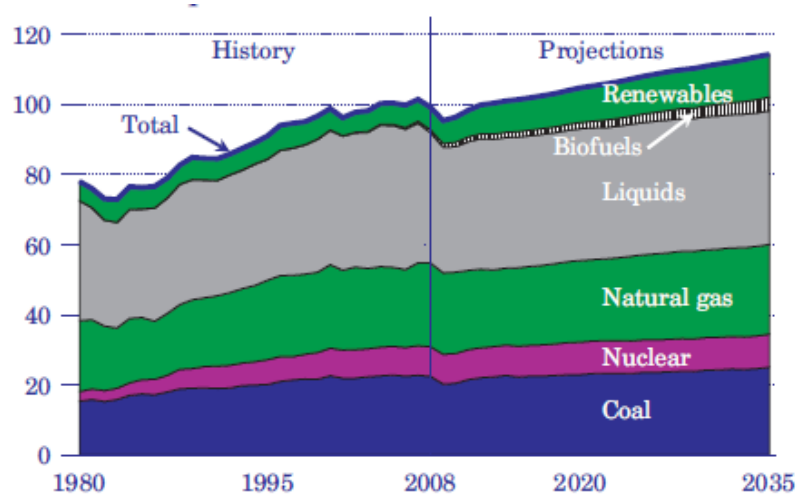

Fig. 1.1: U.S. primary energy consumption (2010), 1980-2035 (quadrillion Btu) [3].

The more recent 2015 DOE Annual Energy Outlook, provides updated data that, interestingly, have somewhat changed from the 2010 document. In fact, in the most recent report, coal, petroleum and nuclear resources usage is, in projection, kept equal from 2013 to 2040, as shown in **Fig. 1.2**; in the previous document these resources were forecasted to be increased in their usage for energy production. This points out, once again, the complexity of the energetic field, which strongly depends on scientific and technological discoveries and society development. Apart from forecasts, and focusing on recent data, it is evident in the **Fig. 1.2** that the largest part of energy is still provided by fossil fuels, mostly petroleum, which are not renewable and whose reserves are, in the future, draining.

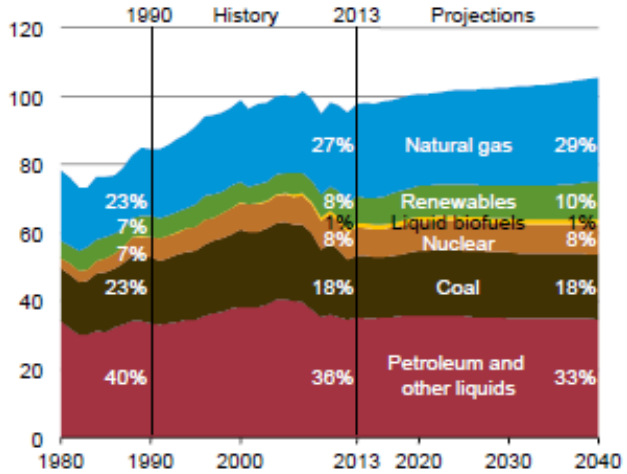

Fig. 1.2: U.S. primary energy consumption (2015), 1980-2040 (quadrillion Btu) [4].

Fig. 1.3 shows that the major economic sectors - industrial, transportation, commercial and residential, power generation - recorded and are recording a tremendous and continuous growth in the energy consumption.

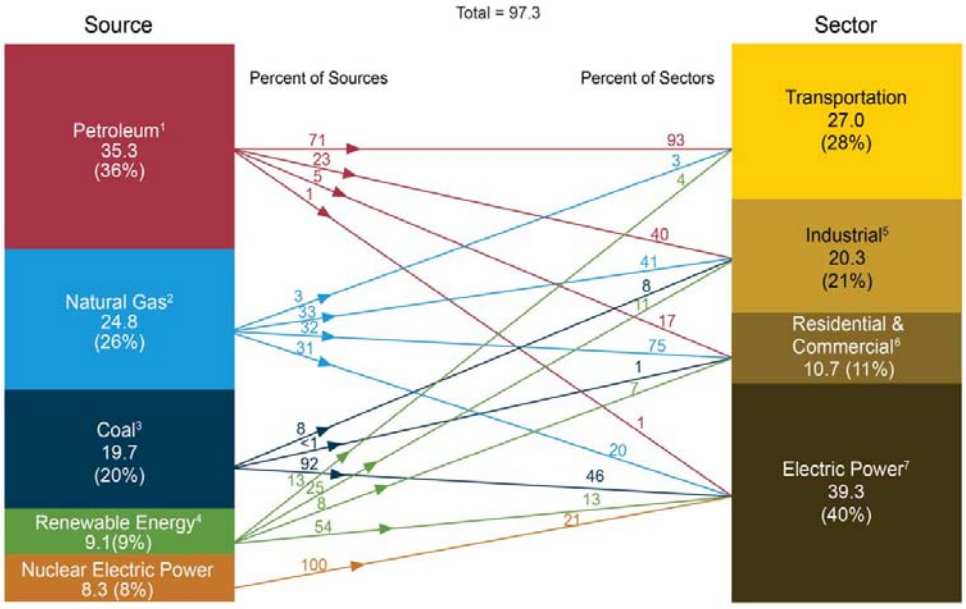

Fig. 1.3: Primary Energy Consumption by Source and Sector, 2011 (Quadrillion Btu) [5].

At present, the mostly energy demanding sector is relative to "power generation"; it is also worth pointing out that the "transportation sector" is important as well and it is known to show the highest growth rate. From these considerations, both transportation and power generation sectors are expected to be deeply affected by energy issues and by the innovative technologies that will be applied to the energetic field.

Each economic sector uses fossil energy sources like petroleum, natural gas, coal and biomass, in different ways. In the 1950s and 1960s coal was the main energy sources for all the economic sectors; then it was replaced by other forms of energy: in residential consumer it was replaced by natural gas and in the industrial sector by petroleum. Starting from early 1970s electricity use raised dramatically in all the energetic sectors while the natural gas and petroleum consumption, with mild fluctuations, held fairly steady constant in the following years.

So far the transportation sector is completely dependent from the use of petroleum as energy source. Petroleum use in this sector overall is still tremendously growing, recorded just a few registered noticeable pauses in the years 1974, 1979-1982, 1990 and 1991, 2001 and 2008, related to economical or international economical crisis. In fact in 2008, about 70% of all petroleum used per day was consumed for transportation purposes.

Fig. 1.4 presents the world distribution of petroleum, pointing out that major reserves are located in the Middle East. On the basis of actual petroleum consumption, optimists claim that this resource is expected to finish within 40 years. As already mentioned, future innovative technologies, allowing to reach deeper reserves and to better the refinement process, will extend the availability period of petroleum but its destiny is, surely, sooner or later, to drain. Other fossil fuels are projected to be longer lasting, with natural gas exhausting in 60 years and coal in 200 years. The need for alternative energy sources, renewable or, at least, more available, however has been causing concern and alarm for many years.

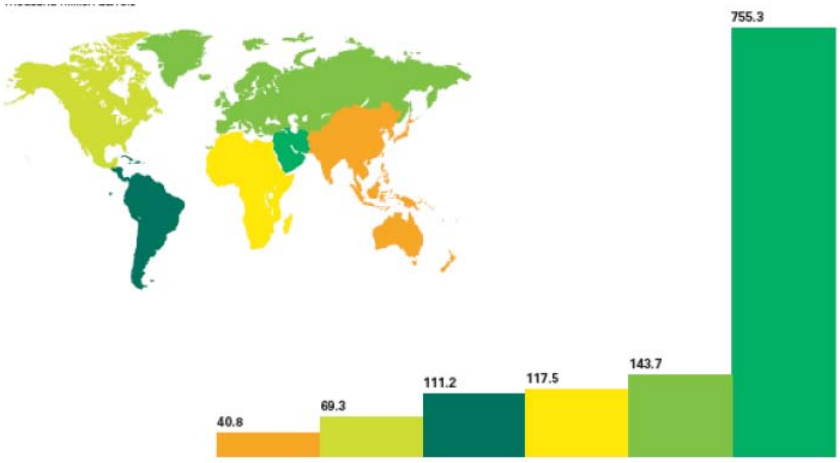

Fig. 1.4: Word wide petroleum reserves (quantity expressed in thousand million barrels) [6].

The complexity of the energetic worldwide problem is an issue under continuous debate, due to many interconnected aspects (economic growth, technology discoveries, population increase, etc.), all affecting and influencing light equilibria between countries, the society and their development. Governments and research efforts are therefore since decades focused on diversifying energy supply, improving energy efficiency and modernizing the energy infrastructure. Aggressive and coordinated research and development in revolutionary energy systems are necessary to sustain the quality of life associated with an energy-intensive lifestyle.

1.2. Renewable energy resources

The main conclusion of the last section is that the world is, at present, addicted to cheap, readily available fossil fuels. It is however a polluting energy source that exists in finite amounts, the bulk of which is concentrated in the politically unstable Persian Gulf.

The key topics of concern for the future are to diminish the world dependence on fossil fuels, to moderate energy consumption growth and greater use of renewables. There are many forms of renewable energy. Most of these renewable energies depend in one way or another on sunlight. Wind and hydroelectric power are the direct result of differential heating of the Earth's surface which leads to air moving (wind) and precipitation forming. Solar energy is the direct conversion of sunlight using panels or collectors. Other renewable energies that do not depend on sunlight are geothermal energy, which is a result of radioactive decay in the crust combined with the original heat of accreting the Earth, and tidal energy, which is a conversion of gravitational energy.

Overall, the so called renewable energy sources are: hydropower, biomass, wind, geothermal, solar power and tidal energy. **Fig. 1.5** shows 2011 renewable energy usages. Note that wood is part of renewable energy; wood is technically a renewable source of energy, since it is a form of biomass. Biomass is traditionally considered a renewable source of energy because it is part of the natural carbon cycle on Earth.

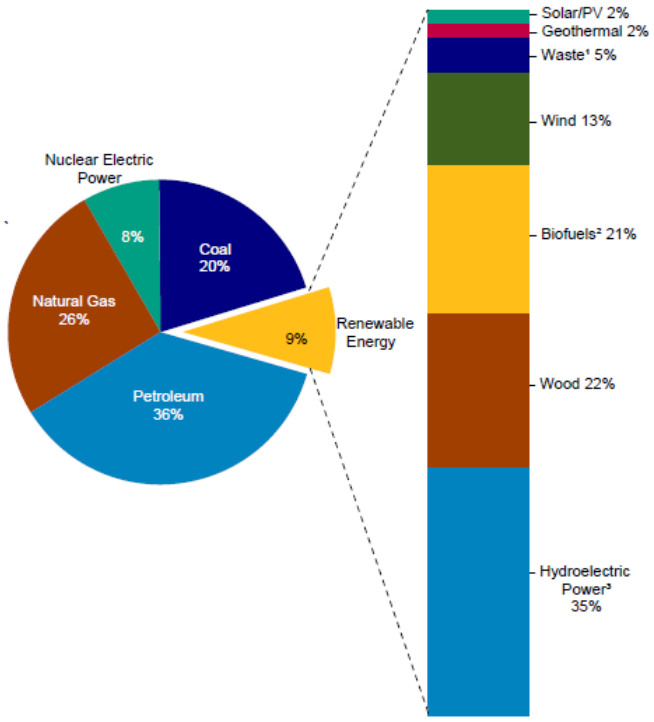

Fig. 1.5: Renewable energy as share of total primary energy consumption [7].

Hydropower is the most utilized renewable energy source. Its power derives from the energy

of falling or fast running water. It is a widespread resource in almost all geographic areas of the world and in developing countries it is the largest used renewable energy source. The cost of electricity generated by hydropower is competitive with coal and gas. Moreover there are no costs of transportation because, being water the fuel, it is naturally transported to the power generation. Dams are used as energy reservoir, pumping water in the dams when there is an extra energy production. However, dams alter the natural water flow and can modify the water cycle, diminishing precipitation. Thus, hydropower can be considered as cheap and mature technology with however non negligible environmental costs [8].

Biomass is biological material derived from living, or recently living organisms. In the context

of biomass as a resource for making energy, it most often refers to plants or plant-based materials which are not used for food or feed. The elementary composition depends on the source and it can be summarized in carbon (50wt.%), oxygen (40wt.%), hydrogen (5wt.%) and chlorine (0.01-2wt.%). Biomass can be considered as a stored source of solar energy in form of chemical energy which can be released and used, when the chemical bonds are broken. Thermo-

chemical conversion of biomass into bioenergy can be effected via: i) direct combustion to provide heat, for steam production and hence electricity generation; ii) gasification to provide a gaseous fuel for combustion; iii) pyrolysis to provide charcoal; iv) fast pyrolysis to provide a liquid fuel. The main problems are related to CO_2 emissions and to the fact that the energy market cannot compete with the food market so the amount of land useful for biomass cultivation decreases. The use of wastes and residues partially solves the problem [8,9].

Wind power generation is expanding. The movement of the atmosphere, generating winds, is

driven by differences of temperature at the Earth's surface due to varying temperatures of the Earth's surface when lit by sunlight. Actually wind, whose technology is mature and reliable, is already competitive with coal as energy production cost. The main advantage of wind is that it does not need fuel and the only cost is building and repairing the turbines and power lines. The only limitations to wind power are the intermittency and the location of the turbines, that is usually far from the energy utilization place. Wind power utilization also depends on public opinion that is also determining for building new centrals [8].

Geothermal power arises from geothermal gradient (increase in temperature with depth) in

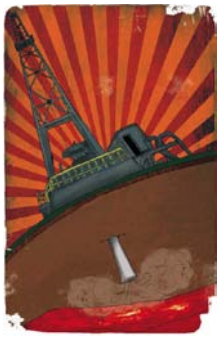

certain areas, that is high enough to exploit to generate electricity. This possibility is limited to a few locations on Earth (Costa Rica, El Salvador, Iceland, Philippines, Kenya) that use geothermal to produce more than 15% of their electricity; many technical problems exist that limit its utility [8].

Solar power can be turned into electricity using a solar photovoltaic cell, a device that uses a

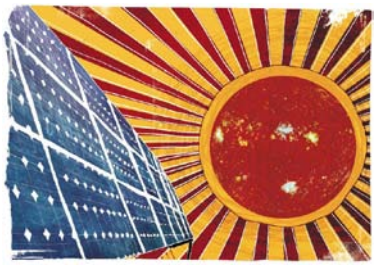

semiconductor-based material to convert sunlight directly into electricity; solar thermal systems are instead devices that use mirrors to focus the heat from the sun heating up a working fuel that work in a turbine. The sun is a fusion reactor that has been burning over 4 billion years. It provides enough energy in one minute to supply the world's energy requests for one year. In one day, it provides more energy than world's current population would consume in 27 years. It is incredible thinking that the amount of solar radiation striking the earth over a three-day period is equivalent to the energy stored in all fossil energy sources. Producing electricity from solar energy was an old unexplained discovery until Albert Einstein proposed an explanation for the "photoelectric effect" in the early 1900s, for which he won the Nobel Prize. Solar energy may have had great potential, but it was left over because fossil fuels were more affordable and available. In the last few decades, when growing energy demands, increasing environmental problems and declining fossil fuel resources, the attention has been focused on this powerful resource. There

are however some limitations to solar power development; first of all the day and night cycle because electricity cannot be generated during the night. Also clouds cause not predictable oscillations in the electricity production, that is the reason why new systems where heat/electricity can be stored when the sun is shining have been developed. Finally, last but not least advantage of solar power is related to the general acceptance by public opinion of solar technology more than nuclear, wind or hydro power; hence the technology can be used to install solar panels above private buildings [8].

Tidal energy works on the fundamental principle related to the difference in water elevation, caused by the difference between high and low tides. The technology involves building a dam, or barrage, across an estuary to block the incoming tide, the outgoing tide, or both. When the water level on one side of the dam is higher than the level on the other side due to a tidal change, the pressure of the higher water builds. The water is channeled through a turbine in the dam in order to get to the other side, which produces electricity by turning an electric generator. Since tidal power's estimated capacity is 50 times smaller than the world's hydroelectric power capacity, it cannot compare to other renewable [8].

Nuclear energy is not renewable but is actually available to satisfy a considerable amount of the energy demand and will be exposed hereby. Moreover, it can be included in the renewable sources of energy because the fuel represents only a small part of the value of energy and it is a CO_2-free emission technology. Apart from safety concerns which will not be discussed, nuclear energy contributes of 14% of the electricity generated worldwide. Nuclear plants use uranium as fuel which is not a rare element and it is available. In projections undiscovered reserves and the use of other fuels, like thorium, can provide enough energy to satisfy the world demand. Advantages of nuclear power are that the fuel used is relatively low cost and widespread so it is not afflicted by political factors. Disadvantages are nuclear wastes. A nuclear power plant produces plutonium as a waste that must be stored for thousands years in a stable environment to avoid radiation leakage and must also be military controlled to avoid terrorist attacks. At the moment there is not technical and a political solution to this problem. Nuclear power is not always publicly accepted and this is significant because nuclear plants are extremely capital intensive and must be built up by governments, that are usually influenced by public opinion. Another disadvantage is that is not possible to divide the energy generation in nuclear plants by nuclear weapons construction [8].

For the foreseeable future the energy demand relies on fossil fuels. Renewables usage for electricity generation will increase but the main problem is that renewables sources cannot guarantee the minimum load for the electrical grid. For that reason nuclear can satisfy the basic load and wind, geothermal and hydropower can also satisfy a considerable amount of energy request. Wind is, for the near future the renewable source that meets economical and

output power request. Solar must be developed to be considered a powerful energy source. To increase renewables use it is fundamental to develop an energy storage system because all the renewable are not continuous sources of energy. A good candidate material for energy storage is hydrogen. Burning hydrogen in air, water and heat are produced. In a futuristic "hydrogen economy", big energetic centrals, localized in uninhabited areas, will store energy by conversion into hydrogen, then directed into energy-requiring places by gaslines. Since hydrogen is an inflammable gas, safety concerns are of primary importance in the development of such an energy solution.

1.3. Automotive sector

The car is a primary mode of transportation for many developed economies. The global increase in vehicle population will increase the amount of greenhouse gas emissions and the amount of air pollutants. The burning of fossil fuels in an engine produces directly carbon monoxide and dioxide, volatile organic compounds and nitrogen oxides. The pressure of a reduction of pollutants in the urban area is pushing the research to develop zero emissions vehicles. For that a variety of alternative transportation technology and fuels have been proposed to solve the future environmental and energy security challenges. The new vehicle technologies include advanced internal combustion energy, technologies based on spark-ignition or compression ignition engines, hybrid electric vehicles, battery powdered and fuel cell vehicles. Recent studies have identified fuel cell vehicles working with hydrogen as the ones offering the lowest fuel cycle emissions and also the widest range of primary supply options. Fuel cells are hence one of the cleanest and most efficient technologies for generating electricity. Since there is no combustion, there are none of the pollutants commonly produced by other systems.

For decades scientific research has been studying a better way to store hydrogen and developing efficient systems to produce electrical energy by fuel cells; the current scientific and technological knowledge appears reliable allowing to plan the use of such devices on a large consumer scale. Apart from automotive sector, fuel cells are an important technology for a potentially wide variety of applications including on-site electric power for households and commercial buildings. These applications would be in a large number of industries worldwide. However, their relatively short lifetime, prohibitive costs of many involved processes and required materials make the engineering of fuel cells one of the greatest challenges of the present time [10].

1.4. Fuel cells

As early as in 1839, Sir William Grove discovered fuel cells by reversing water electrolysis to generate electricity from hydrogen and oxygen using an acid-electrolyte fuel cell. Since this time fuel cell technology has evolved substantially. Fuel cells are devices that convert the chemical energy contained in a fuel directly into electrical energy, without the intermediate formation of mechanical energy as in conventional devices based on the Carnot cycle. The basic physical structure of a fuel cell consists of an electrolyte layer in contact with a porous anode, on which fuel (hydrogen, methanol, etc.) oxidation takes place, and a porous cathode, on which oxygen is reduced on either side. Fuel and oxidant are continuously fed to the anode and to the cathode, respectively. Electric current is produced and flows through the

electrolyte, while a complementary electric current is driven to perform work on the load. A schematic representation of a fuel cell with the reactants, products and the ion conduction flow directions through the cell is shown in **Fig. 1.6**.

Typical batteries are in some ways similar to fuel cells, however there are some important differences to highlight. In fact batteries are energy storage device in which all the energy available is stored within themselves. Batteries cease to produce electrical energy when the chemical reactants are consumed. Fuel cells, on the contrary, are energy conversion devices to which fuel and oxidant are continuously fed. In principle, the fuel cell produces power as long as fuel and oxidant are supplied.

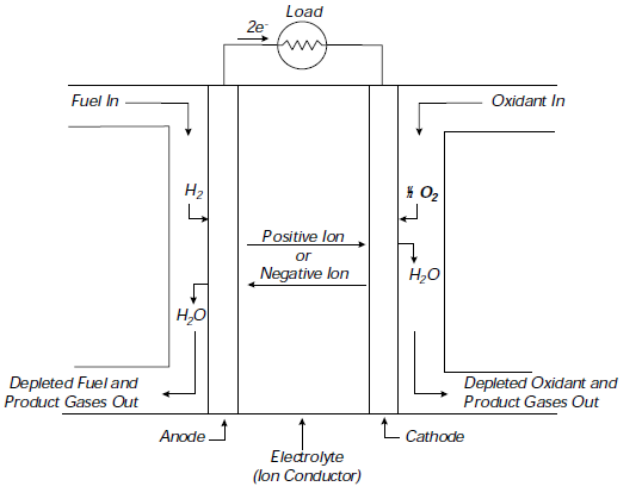

Fig. 1.6: Schematic of an individual fuel cell [11].

In **Tab. 1.1** are reported the different fuel cell types that so far have played the most important roles: the low-temperature proton exchange membrane fuel cell (PEMFC), the high-temperature molten carbonate fuel cell (MCFC) and the solid oxide fuel cell (SOFC); historically, the phosphoric acid fuel cell (PAFC) and alkaline fuel cell (AFC) had significant importance. For automotive application, PEMFCs are the most attractive fuel cells. The given classification of fuel cells in **Tab. 1.1** and **Tab. 1.2**, provides also an overview of the key characteristics and electrodes reactions, according to the choice of electrolyte and fuel, which determines the cathodic and anodic reactions and the type of ion that carries the current across the electrolyte. Appleby and Foulkes noted that, in theory, any substance capable to be oxidized, supplied continuously at the anode, can be used as fuel [12]. Similarly, the oxidant can be any substance capable to be reduced and fed at the cathode. However, most fuel cells under development today use gaseous hydrogen, or a synthesis gas rich in hydrogen, as a fuel. Hydrogen has a high reactivity for anode reactions, and can be produced chemically from renewables, as well as via electrolysis. For similar practical reasons, the most common oxidant is gaseous oxygen, which is readily available from air.

	PEFC	AFC	PAFC	MCFC	SOFC
Electrolyte	Hydrated Polymeric Ion Exchange Membranes	Mobilized or Immobilized Potassium Hydroxide in asbestos matrix	Immobilized Liquid Phosphoric Acid in SiC	Immobilized Liquid Molten Carbonate in $LiAlO_2$	Perovskites (Ceramics)
Electrodes	Carbon	Transition metals	Carbon	Nickel and Nickel Oxide	Perovskite and perovskite / metal cermet
Catalyst	Platinum	Platinum	Platinum	Electrode material	Electrode material
Interconnect	Carbon or metal	Metal	Graphite	Stainless steel or Nickel	Nickel, ceramic, or steel
Operating Temperature	40 – 80 °C	65°C – 220 °C	205 °C	650 °C	600-1000 °C
Charge Carrier	H^+	OH^-	H^+	$CO3^{=}$	$O^{=}$
External Reformer for hydrocarbon fuels	Yes	Yes	Yes	No, for some fuels	No, for some fuels and cell designs
External shift conversion of CO to hydrogen	Yes, plus purification to remove trace CO	Yes, plus purification to remove CO and CO_2	Yes	No	No
Prime Cell Components	Carbon-based	Carbon-based	Graphite-based	Stainless-based	Ceramic
Product Water Management	Evaporative	Evaporative	Evaporative	Gaseous Product	Gaseous Product
Product Heat Management	Process Gas + Liquid Cooling Medium	Process Gas + Electrolyte Circulation	Process Gas + Liquid cooling medium or steam generation	Internal Reforming + Process Gas	Internal Reforming + Process Gas

Tab. 1.1: Summary of major differences of the state-of-the-art fuel cell types [11].

Fuel Cell	Anode Reaction	Cathode Reaction
Proton Exchange Membrane	$H_2 \rightarrow 2H^+ + 2e^-$	$½\ O_2 + 2H^+ + 2e^- \rightarrow H_2O$
Alkaline	$H_2 + 2(OH)^- \rightarrow 2H_2O + 2e^-$	$½\ O_2 + H_2O + 2e^- \rightarrow 2(OH)^-$
Phosphoric Acid	$H_2 \rightarrow 2H^+ + 2e^-$	$½\ O_2 + 2H^+ + 2e^- \rightarrow H_2O$
Molten Carbonate	$H_2 + CO_3^{=} \rightarrow H_2O + CO_2 + 2e^-$ $CO + CO_3^{=} \rightarrow 2CO_2 + 2e^-$	$½\ O_2 + CO_2 + 2e^- \rightarrow CO_3^{=}$
Solid Oxide	$H_2 + O^{=} \rightarrow H_2O + 2e^-$ $CO + O^{=} \rightarrow CO_2 + 2e^-$ $CH_4 + 4O^{=} \rightarrow 2H_2O + CO_2 + 8e^-$	$½\ O_2 + 2e^- \rightarrow O^{=}$

CO - carbon monoxide
CO_2 - carbon dioxide
$CO_3^{=}$ - carbonate ion
e^- - electron
H^+ - hydrogen ion
H_2 - hydrogen
H_2O - water
O_2 - oxygen
OH^- - hydroxyl ion

Tab. 1.2: Electrochemical reactions in fuel cells [11].

The operating temperature of a fuel cell determines the physicochemical and mechanical properties of materials used in the devices main components. Aqueous electrolytes are limited to temperatures lower than 200°C because of the high vapor pressure.

Electrodes in fuel cells should be porous. The function of porosity, in addition to provide higher surface for electrochemical reactions taking place, is to conduct electrons away from or into the three-phase interface once they are formed (electrode must also be good electrical conductor). Moreover porosity ensures that reactants are equally distributed over the cell and that reaction products are efficiently led away. At low temperatures, only a few materials provide sufficient conductivity, while in high-temperature fuel cells, the bulk electrode conductivity is often sufficient. Though a wide range of fuel cell geometries has been considered, most fuel cells under development now are either planar or tubular.

A critical part of fuel cells is often referred to as the three-phase interface. In this microscopic region, the actual electrochemical reactions take place. Here electrode meets the electrolyte. For a site to be electroactive, it must be exposed to the reactant, be in electrical contact with the electrode and be in ionic contact with the electrolyte. The density and the nature of these regions and interfaces play a crucial role in the electrochemical performances of fuel cells.

Apart from this general overview on fuel cells type, constituent and main features, in the following the focus will be set onto PEMFCs, the most attractive fuel cells for automotive application.

1.5. Polymer Electrolyte Membrane Fuel Cells (PEMFCs)

Among the fuel cell technologies, PEMFCs are commercially most attractive owing to their quick start-up and ambient temperature operations. They exhibit high-operational efficiencies comparable to internal-combustion engines while emitting no pollutants.

1.5.1. Structure

The operating principle of a PEMFC is depicted in **Fig. 1.7**.

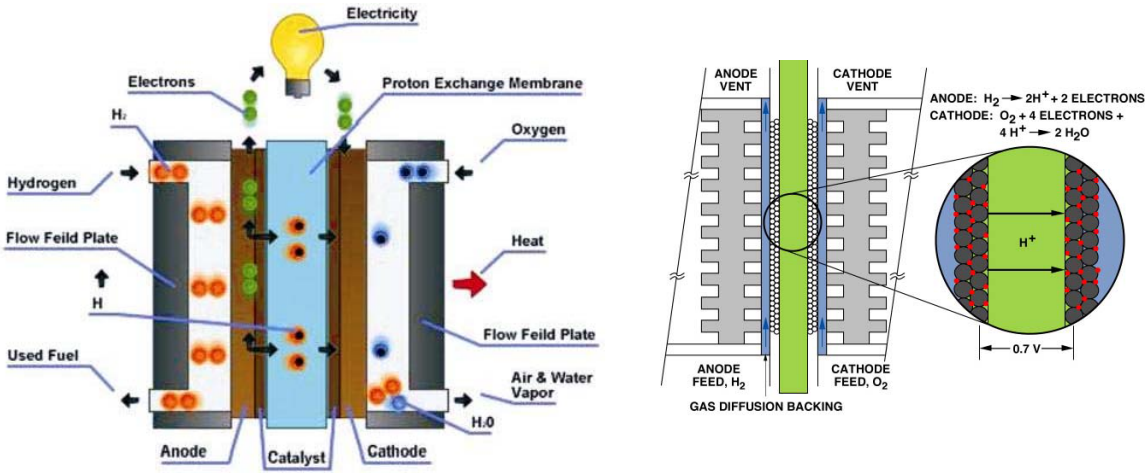

Fig. 1.7: Schematic diagrams of a PEMFC [13].

Typical cell components within devices include the ion exchange membrane, an electrically conductive porous backing layer, the electrodes at the interface between the

backing layer and the membrane, cell interconnects and flow plates that deliver the fuel and oxidant to reactive sites via flow channels and electrically connect the cells.

In PEMFCs the electrolyte is an ion exchange membrane (fluorinated sulfonic acid polymer) that is an excellent proton conductor. In the late 1960s, DuPont developed membranes from Nafion®, a copolymer of perfluoro-sulfonic acid with hydrophobic fluorocarbon backbone and hydrophilic sulfonic acid pendent side chains, as depicted in **Fig. 1.8**. The function of Nafion® is to provide a conductive path, while at the same time separating the reactant gases. The material is an electrical insulator. Hence, conduction takes place via ionic groups within the polymer structure.

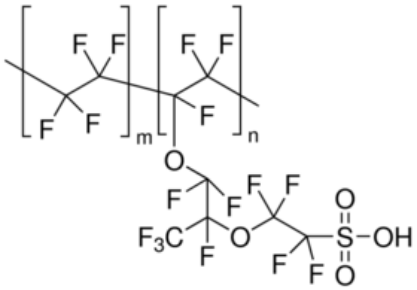

Fig. 1.8: Chemical structure of Nafion®.

The Nafion® membrane is sandwiched between two sheets of porous backing media (or gas diffusion layers) that act as current collectors. The functions of the backing layers, as said above, are to act as a gas diffuser, provide mechanical support and an electrical pathway for electrons, and channel product water away from the electrodes. The backing layer is typically carbon-based, and may be in cloth form or simply a felt-like material. To exploit their functions, the layer incorporates a hydrophobic material, such as polytetrafluoroethylene.

In intimate contact with the membrane and the backing layer is the catalyst layer. This catalyst layer, with its binder, forms the electrode. The degree of intimacy of the catalyst particles and the membrane is critical for optimal proton mobility.

1.5.2. Thermodynamics

The maximum electrical work (W) obtainable in a fuel cell operating at constant temperature and pressure is given by the change in the Gibbs free energy of the chemical reaction and it is related to the cell voltage via:

$$W=\Delta G^\circ = -nF\Delta E^\circ \qquad (1)$$

where n is the number of electrons involved in the reaction, F is the Faraday constant, and ΔE° is the voltage of the cell for thermodynamic equilibrium in the absence of a current flow.

For the case of a PEMFC, hence involving hydrogen oxidation and oxygen reduction reactions at the anode and cathode, respectively, these are the reactions:

Anodic reaction, hydrogen oxidation reaction (HOR): $H_2 \rightarrow 2H^+ + 2e^-$

Cathodic reaction, oxygen reduction reaction (ORR): $\frac{1}{2} O_2 + 2e^- \rightarrow O^{2-}$

Overall reaction: $H_2 + ½ O_2 \rightarrow H_2O$

with $\Delta G°=-237$ kJ mol^{-1}

By considering a cell $\Delta E°$ for standard conditions:

$\Delta E° = - \Delta G°/nF = 1.23$ V (2)

The equilibrium standard voltage for the cell is the difference of the equilibrium electrode potentials of cathode and anode which are determined by the electrochemical reaction taking place at the respective electrode, as the equation (3) shows:

$\Delta E^0 = E^0_{,c} - E^0_{,a}$ (3)

The overall reaction in a PEMFC can be used to produce both electrical energy and heat. The maximum work (W_{max}) available from a fuel source is related to the free energy of reaction, whereas the enthalpy (heat) of reaction is the quantity for a heat engine:

$W_{max}=\Delta G° = \Delta H° - T \Delta S°$ (4)

At room temperature, the thermodynamic values for H_2O formation from the elements ($S°_{f, H2O\ l}$=69.91 J K^{-1} mol^{-1}, $S°_{f, H2}$=130.684 J K^{-1}mol^{-1}, $S°_{f, O2}$=205.138 J K^{-1}mol^{-1}, $\Delta G°_{f, H2O\ l}$=-237.13 kJ mol^{-1} , $\Delta G°_{f, H2}$=0 J mol^{-1}, $\Delta G°_{f, O2}$=0 J mol^{-1}) are:

$\Delta S° = 69.91-130.684-205.138/2= -163.343$ J K^{-1}mol^{-1}
$\Delta G°= -237.13$ kJmol^{-1}

$\Delta G°$ values correspond to reversible potential in thermodynamically reversible conditions, from:

$\Delta G° = - n F \Delta E°$ (5)
$\Delta E° = - \Delta G°/nF = - \Delta G°/2F= 1.229$ V (NHE)

Under chemical conditions, variation of the free energy, $\Delta G°$ associated to combustion reaction, corresponds to the exchanged heat $\Delta H°$, from:

$\Delta G° = \Delta H° = -241.82$ kJ mol^{-1} (6)

In this case the reaction energy efficiency (η) expressed by (7) depends also from the associated Carnot cycle:

$$\eta = 1 - \frac{T_c}{T_h} \quad (7)$$

where T_h is the hot source temperature and T_c correspond to cold source one.

Assuming, for simplicity, T_c= 0.5 T_h ($\eta \cong 0.5$), the maximum energy from a chemical H_2 combustion would be: 0.5 $\Delta G° = 0.5 \Delta H°$= **-120.91 kJ mol^{-1}**

For comparison of this value with the electrochemical reaction associated one **$\Delta G°$=-237.13 kJ mol^{-1}** at 298.15 it is clear that the energy from a fuel cell is higher than energy gained from hydrogen chemical combustion.

Despite these conceptual advantages of fuel cells and their long history since Grove's discovery, no real fuel cell market exists as of today. At present there are a few prototypes of fuel cells devices for portable and non-portable systems; in 2013 Toyota launched to the Japanese market its fuel cell vehicle, Toyota Mirai, and last September the same FC car started to be sold in Europe.

The question is: why are fuel cell not widely commercialized yet?

1.5.3. Kinetics hindrances

The answer to the end-question of the last paragraph is given by the following **Fig. 1.9**.

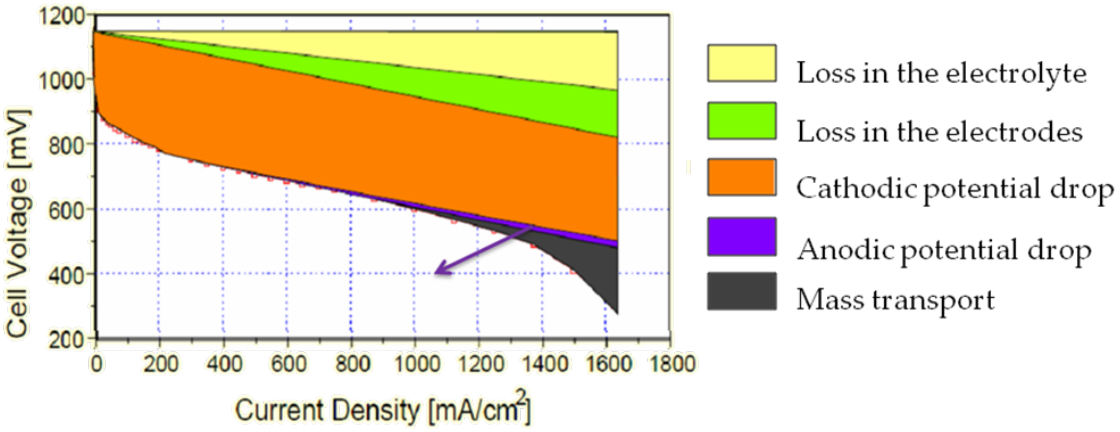

Fig. 1.9: Overpotential drops in a fuel cell device.

Being both cathodic and anodic reaction taking place in fuel cells kinetically hindered, they detract from the overall cell energy efficiency and must be catalyzed to proceed fast enough to cope with automotive variable and peak power requirements. As evidenced by **Fig. 1.9**, the greatest potential drop is due to the cathodic oxygen reduction reaction, being its occupied area even 10 times larger than the correspondent anodic part. Catalysts are in any case compulsory for both ORR and HOR.

The oxidation of hydrogen proceeds very fast on Pt-based catalysts: the first step is the adsorption of the gas onto the catalyst surface, with formation of adsorbed H-Pt radicals followed by their fast oxidation to H^+.
The oxygen reduction reaction (ORR) is kinetically much slower, requires a catalyst and can proceed by two different pathways:

- direct 4-electrons mechanism, the preferable one for thermodynamic reasons and because it does not involve the formation of hydrogen peroxide:

  $$O_2 + 4e^- + 4H^+ \rightarrow 2H_2O$$

- indirect 2-electrons mechanism, involving the formation of hydrogen peroxide, which, apart from safety concerns, decreases the energy reaction efficiency and, as an oxidant, adversely affects the fuel cell construction materials:

  $$O_2 \xrightarrow{+2e^- +2H^+} H_2O_2 \xrightarrow{+2e^- +2H^+} 2H_2O$$

1.6. Oxygen depolarized cathodes

Another process in which oxygen reduction reaction is involved, is related to the industrial chlor-alkali electrolysis. Chlorine is one of the most important product of the chemical industry mainly due to the increasing demand for polymers. Currently used electrolysis processes for chlorine production, oxidize chloride at the anode producing hydrogen at the cathode. The idea of substituting the H_2-evolving anode, operating the chlor-alkali electrolysis with an oxygen depolarized cathode, ODC, (where ORR takes place) is by no means new. By using ODC, hydrogen formation is prevented and, at the same time, cell voltage and energy demand are significantly decreased. Using such type of cathode, by considering the ORR overpotentials, the final gained voltage, compared to the classical process, is about 1 V. On ODC, electrochemical ORR is supposed to take place fast enough to be competitive with no excessive energy loss. Once again, being the involved cathodic reaction the ORR (as well as in fuel cells), at present carbon-supported Pt and Pt-alloys are best credited to the purpose.

1.7. The problem with Platinum

As already mentioned, the reaction of oxygen reduction is kinetically unfavorable and requires the use of very effective catalysts which, at present, are all based on Pt metal supported on conductive materials (mostly carbon). Hydrogen oxidation is much faster than oxygen reduction, so that the catalyst amount needed can be ca. 10 times lower. Though at present carbon-supported Pt and Pt-rich alloys (Pt_3Cr, Pt_3Fe) are best credited for both these reactions, using it on a large fuel cell production scale involves the problems of Pt natural availability and cost. Platinum reserves are localized in a few areas of the world, highlighted in **Fig. 1.10**, mainly in Russia, Canada and Southern Africa, and it is very improbable that new deposits of such metal may be found elsewhere in the future. As an example, South Africa claims 80% Pt production, with 90% of reserves concentrated in this small area; however, Pt grade, as soon as it is extracted, is less than 5 ppm and mines are located about 4-6 km depth. The severe working conditions of miners are easily imaginable.

Fig. 1.10: Platinum geographic distribution.

A study demonstrates that Pt resources could cope with the setting up of 500 million fuel cell vehicles in a time span of 15 years, without considering other, already established Pt uses, such as in industrial catalysis and jewellery, with a request of 16.6 tons y^{-1}. This means that platinum cost will be subject to, and increase with, the demand. On the other hand, being a time-ending resource, Pt be subject to the same issues as fossil fuels [14].

In the following **Tab. 1.3**, from US Department of Energy, is evidenced that, in 2011, 0.19 g of Pt were calculated to be necessary to make a 1 kW fuel cell engine work [15].

Table 3.4.13 Technical Targets: Electrocatalysts for Transportation Applications[h]			
Characteristic	Units	2011 Status	2020 Targets
Platinum group metal total content (both electrodes)[a]	g / kW (rated)	0.19[b]	0.125

Tab. 1.3: Extract from DOE report [15].

Imagining that all cars nowadays circulating in the world - this number is about 10^9 cars - were fuel cell cars, needing a power of 80 kW car^{-1}, the quantity of needed platinum would be:

$$10^9 cars \cdot 80kW \cdot 0.19g\ kW^{-1} \cdot 10^6 ton\ g^{-1} = 15200\ tons\ of\ Pt$$

Repeating the same calculation, but now just considering cars circulating in Italy, the quantity of needed platinum would be:

$$1.2 \cdot 10^7 cars \cdot 80kW \cdot 0.19g\ kW^{-1} \cdot 10^6 ton\ g^{-1} = 184.4\ tons\ of\ Pt$$

The following **Tab. 1.4**, from Johnson Matthey, gives an idea of platinum supply by considering all the producing countries. This value was estimated to be 178.5 tons in 2013. The total demand for the same year, considering all the applications apart from fuel cell one, is 261.9 tons, reduced down to 197.4 tons when including in calculations the Pt from recycling processes. By simply comparing these values it is clear that Pt supply is not able to cover the demand even without considering fuel cell application. In any case, Pt total supply would not even allow just to make each Italian car circulate by means of a fuel cell device.

Tonnes	2013
Supply	
South Africa	128.1
Russia	24.3
North America	9.8
Zimbabwe *	12.4
Others	3.9
Total Supply	**178.5**
Demand by Application	
Autocatalyst	97.2
Chemical	16.8
Electrical	6.4
Glass	7.3
Investment	23.8
Jewellery*	85.2
Medical & Biomedical**	7.3
Petroleum	4.8
Other	13.1
Total Gross Demand	**261.9**
Recycling	
Autocatalyst	-39.7
Electrical	-0.8
Jewellery	-24.1
Total Recycling	**-64.5**
Total Net Demand	**197.4**
Movements in Stocks	**-18.8**

Tab. 1.4: Data from 2013 Johnson Matthey calculations.

However, costs and availability are not the only problems related to platinum catalysts; indeed, under fuel cell working conditions, carbon-support is corroded over time and platinum efficiency is reduced, because it undergoes oxidation, dissolution and migration, loss of surface active area and it is also poisoned by carbon monoxide, a contaminant of hydrogen from steam reforming. A review of these processes is shown in **Fig. 1.11**.

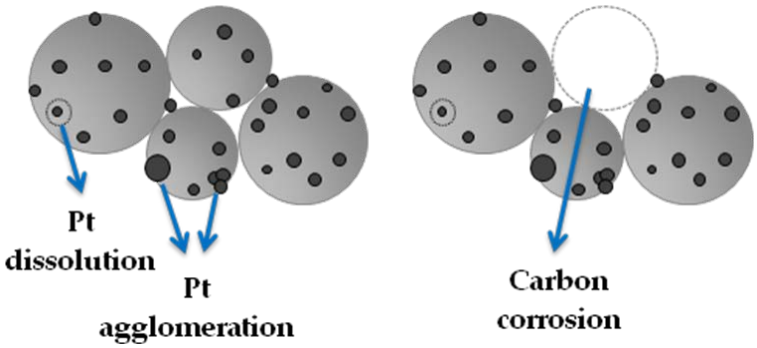

Fig. 1.11: Technological issues related to state-of-the-art Pt-based catalysts.

Therefore, a hypothetical massive fuel cell commercialization is only possible provided an effective substitute of this catalytic metal could be achieved [16].

1.7.1. Alternatives to Platinum

Today, efforts are addressed to develop and synthesize new catalysts for ORR, containing a low platinum percentage or even platinum-free materials. Several papers on non-precious ORR catalysts have been published after a first report by Jasinski [17] in 1964 demonstrating ORR activity of metal substitutes-phthalocyanines. Then, in the last 51 years (a scheme of research achievements is given in **Fig. 1.12**), research on metal-nitrogen macrocycles significantly expanded, leading to the picture that ORR catalytic activity can be related to N_4-Me and N_2-Me moieties. However, for precursor cost and unsatisfactory lifetime performance, research was steered towards more simple nitrogen-containing reactants and preparation procedures. Significant steps in this direction were obtained by Dodelet *et al.* who demonstrated that ORR overpotentials almost linearly decrease with increasing nitrogen content in carbon. Positive results were obtained on a series of samples prepared by high temperature treatment of carbon precursors in $NH_3/H_2/N_2$ mixtures; doping of these modified carbons with iron rather than cobalt salts was shown to be preferable for better efficiency in oxygen reduction, even though still lower than that of platinum [18-22].

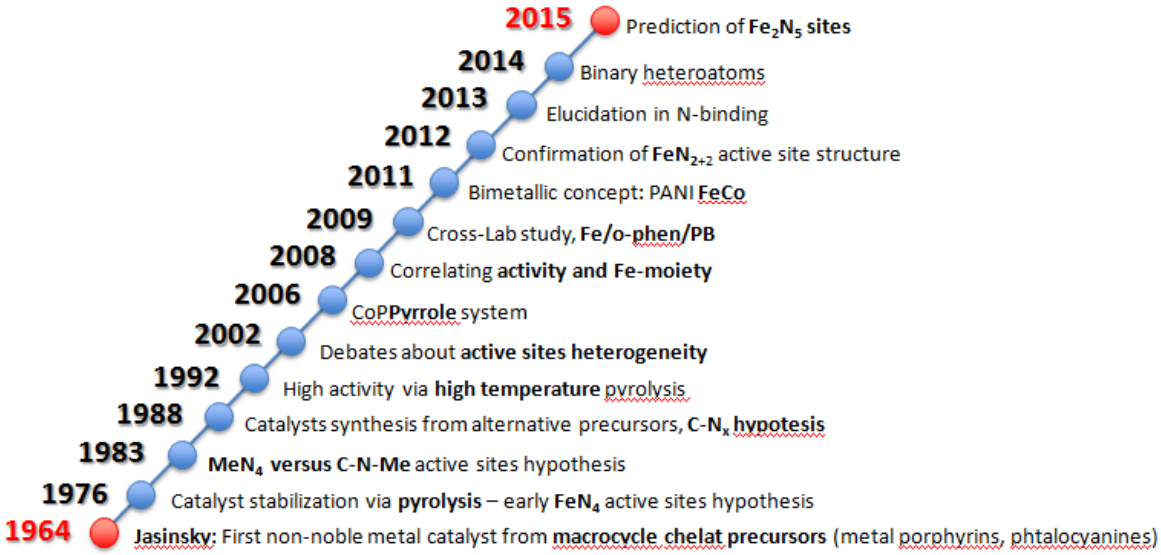

Fig. 1.12: Research on Pt-free catalysts for ORR in the last 51 years.

Further improvements both in terms of incipient ORR potentials and currents were recently obtained by Maruyama *et al.* using carbons from hemoglobin [23] and adenine-glucose [24] pyrolysis in the presence of added Fe(II) and Cu(II)/Fe(II) mixtures, respectively. The ORR promoting role of nitrogen in carbon was independently demonstrated both theoretically and experimentally. Indeed, it was found that substitutional nitrogen at a few, specific, peripheral positions of graphene layers in well-ordered carbon nanostructures is in itself able to promote ORR activity even in the absence of accompanying metal centers [25-27]. Besides the above examined composition-dependent factors, catalyst activity also depends on structural and morphological carbon support features. In fact, many electrocatalytic reactions show faster kinetics on carbon edge planes compared with basal ones. This is related to ability of the edges to more readily chemisorb O_2 (this is the same reason why O_2 combusts faster from edges and defects) [26]. On the other hand, an optimized porosity of carbon supports is beneficial for an

easy access of the oxygen to the catalyst layer in contact with the proton exchange electrolyte membrane [28]. Despite carbon materials of different textural morphology are widely used at an industrial level as supports for precious metal catalysts, in the PEMFC field, electrocatalysts are by far supported on the same VULCAN XC72 carbon. Given that improved catalytic activity of Pt-based catalysts has been achieved by the use of carbons with pore size centered in the mesoporous region, even developed with advanced synthesis, including template methods, such strategy should be pursued also for Pt-free catalytic systems.

1.8. References

1. U. S. Department of Energy web site, http://www.eia.doe.gov.
2. http://europa.eu/rapid/press-release_MEMO-08-703_en.htm.
3. "Annual Energy Outlook 2010, With Projections to 2035", Energy Information Administration Office of Energy Markets and End Use U.S. Department of Energy Washington DC, 2010.
4. "Annual Energy Outlook 2015, With Projections to 2040", Energy Information Administration Office of Energy Markets and End Use U.S. Department of Energy Washington DC, 2015.
5. U.S. Energy Information Administration / Annual Energy Review 2011.
6. British Petroleum, Statistical Review of Word Energy, 2007-2008.
7. U.S. Energy Information Administration / Annual Energy Review 2011.
8. Q. Schiermeier, J. Tollefson, T. Scully, A. Witze, O. Morton, Energy alternatives: Electricity without carbon, Nature, 454 (2004), 816-823.
9. L. Zhang, C.-X. Chunbao, P. Champagne, Overview of recent advances in thermo-chemical conversion of biomass, Energy Conversion and Management, 51 (2010), 969-982.
10. L. Carrette, K.A. Friederich, U. Stimming, Fuel cells - fundamentals and applications, Fuel Cells, 1 (2001), 5-39.
11. Fuel Cell Handbook (Seventh Edition), EG&G Technical Services, U.S. Department of Energy, Office of Fossil Energy, National Energy Technology Laboratory, Morgantown, West Virginia.
12. A.J. Appleby, F.R. Foulkes, Fuel Cell Handbook, Van Nostrand Reinhold, New York, NY, 1989.
13. A.K. Sahu, S. Pitchumani, P. Sridhar, A.K. Shukla, Nafion and modified-Nafion membranes for polymer electrolyte fuel cells: An overview, Bulletin of Materials Science, 32 (2009), 285-294.
14. M. Gerst, T.E. Graedel, In-use stocks of metals: status and implications, Environmental Science and Technology, 42 (2008), 7038-7045.
15. Multi-Year Research, Development and Demonstration Plan, DOE.
16. C. Sealy, The problem with Platinum, Materials Today, 11 (2008), 65-68.
17. R.J. Jasinski, New fuel cell cathode catalyst, Nature, 201 (1964), 1212-1213.

18. F. Jaouen, S. Marcotte, J.-P. Dodelet, G. Lindbergh, Oxygen Reduction Catalysts for Polymer Electrolyte Fuel Cells from the Pyrolysis of Iron Acetate Adsorbed on Various Carbon Supports, Journal of Physical Chemistry B, 107 (2003), 1376-1386.

19. S. Marcotte, D. Villers, N. Guillet, L. Roue, J.-P. Dodelet, Electroreduction of oxygen on Co-based catalysts: determination of the parameters affecting the two-electron transfer reaction in an acid medium, Electrochimica Acta, 50 (2004), 179-188.

20. C. Medard, M. Lefevre, J.-P. Dodelet, F. Jaouen, G. Lindbergh, Oxygen reduction by Fe-based catalysts in PEM fuel cell conditions: Activity and selectivity of the catalysts obtained with two Fe precursors and various carbon support, Electrochimica Acta, 51 (2006), 3202-3213.

21. M. Lefevre, E. Proietti, F. Jaouen, J.-P. Dodelet, Iron-Based Catalysts with Improved Oxygen Reduction Activity in Polymer Electrolyte Fuel Cells, Science, 324 (2009), 71-74.

22. J. Tian, L. Birry, F. Jaouen, J.-P. Dodelet, Fe-based catalysts for oxygen reduction in proton exchange membrane fuel cells with cyanamide as nitrogen precursor and/or pore-filler, Electrochimica Acta, 56 (2011), 3276-3285.

23. J. Maruyama, J. Okamura, K. Miyazaki, Y. Uchimoto, I. Abe, Hemoglobin Pyropolymer Used as a Precursor of a Noble-Metal-Free Fuel Cell Cathode Catalyst, Journal of Physical Chemistry C, 112 (2008), 2784-2790.

24. J. Maruyama, I. Abe, Structure control of a carbon-based noble-metal-free fuel cell cathode catalyst leading to high power output, Chemical Communication, 27 (2007), 2879-2781.

25. R.A. Sidik, A.B. Anderson, N.P. Subramanian, S.P. Kumaraguru, B.N. Popov, O_2 Reduction on Graphite and Nitrogen-Doped Graphite: Experiment and Theory, Journal of Physical Chemistry B, 110 (2006), 1787-1793.

26. P.H. Matter, L. Zhang, U.S. Ozkan, The role of nanostructure in nitrogen-containing carbon catalysts for the oxygen reduction reaction, Journal of Catalysis, 239 (2006), 83-96.

27. P.H. Matter, E. Wang, U.S. Ozkan, Preparation of nanostructured nitrogen-containing carbon catalysts for the oxygen reduction reaction from SiO_2- and MgO-supported metal particles, Journal of Catalysis, 243 (2006), 395-403.

28. H. Chan, S.H. Joo, C. Pak, Synthesis and characterization of mesoporous carbon for fuel cell applications, Journal of Materials Chemistry, 17 (2007), 3078-3088.

Chapter 2

Characterization Techniques

In the following, among the great number of characterization techniques used in this work, only two techniques will be exposed with their main theoretical derivations. The first one will be the BET technique, for surface area and pore structure evaluation; the second one is related to electrochemical measurements by Rotating Disk Electrode (RDE) and Rotating Ring Disk Electrode (RRDE). For the other techniques only specific technical details of used instrumentations and protocols will be reported.

Since there are many cases, especially those ones concerning the collaboration with Prof. Colavita from Trinity College Dublin, for which it is not clear if the analysis has been performed in the Department of Chemistry of Università degli Studi di Milano, or in CRANN (Centre for Research on Adaptive Nanostructures and Nanodevices) in Trinity College Dublin, in the Appendix is given detailed information about the place where each single analysis presented in the following chapters has been performed.

2.1. BET technique

Surface area and porosity are important parameters in powdered materials. The most widely used techniques for estimating surface area are based on physical adsorption of gas molecules on a solid surface. The BET (Braunauer-Emmet-Teller) technique is indeed based on the adsorption of a gas, usually nitrogen, at its condensation temperature, on the surface of a solid sample. Generally gas adsorption on solid surfaces is a complex phenomenon involving mass and energy interaction. Depending on the strength of the interaction, all adsorption processes can be divided into chemical or physical adsorption. The former, also called irreversible or chemisorption, is characterized mainly by large interaction potentials, which lead to high heats of adsorption, approaching the values of chemical bonds. Physical adsorption exhibits characteristics that make it most suitable for surface area determinations as indicated by the following. In fact physical adsorption is accompanied by low heats of adsorption with no disruptive structural changes occurring during measurements. Unlike chemisorption, physical adsorption may lead to surface coverage by more than one layer of adsorbate. Thus, pores can be filled by the adsorbate for pore volume measurements. Physical adsorption equilibrium is rapidly reached since no activation energy is required as in chemisorption. Finally, physical adsorption is fully reversible, enabling both the adsorption and desorption processes to be studied.

Braunauer, Emmet and Teller were able to build a model that explains how the quantity of adsorbed gas depends on Van der Waals gas-solid interactions through the gas partial pressure [1]. By BET technique, the molar quantity of a gas taken up, or released, at a constant temperature T, as a function of gas pressure P, is measured. Most frequently the test is conducted at a cryogenic temperature, usually that of liquid nitrogen at its boiling point (77.35 K at 1 atm pressure). Convention has established that the quantity of gas adsorbed is expressed as its volume at standard temperature and pressure conditions (0°C and 760 torr and denoted by STP), while the pressure is expressed as a relative pressure, which is the actual gas pressure p divided by the vapor pressure p^0 of the adsorbing gas.
In applying the BET technique, some hypotheses were adopted:

- Adsorption is localized
- Surface sites are energetically equivalent
- There are no lateral interactions between successively adsorbed gas molecules
- There are no interactions between adsorbed layers
- There are no limits to the number of adsorbed layers
- The nature of adsorbed molecules from the second layer onward is liquid

Under these hypotheses, the BET equation is obtained and relates the quantity of adsorbed gas to the experimental pressure:

$$\frac{V}{V_m} = \frac{C\frac{p}{p_o}}{\left(1-\frac{p}{p_o}\right)\times\left[1+(C-1)\frac{p}{p_o}\right]} \qquad (1)$$

where V is the gas volume at pressure p, V_m is the gas volume corresponding to the monolayer formation, p_0 is the gas saturation pressure and C is a gas-surface interaction constant.

The value of parameter C is given by the following:

$$C \propto e^{\left(\frac{q_1 - q_L}{RT}\right)} \qquad (2)$$

where q_1 = heat of adsorption of the first layer, q_L = heat of liquefaction of the adsorptive.

When using nitrogen at 77 K, C value is frequently between 50 and 300. Small values of the C parameter stand for a higher affinity between molecules than between the molecules and the adsorbing species. On the contrary, high C value is indicative of micropores and it is typical for monolayer adsorption and then by the multilayer one, layer by layer.

The adsorption isotherm is obtained by plotting $V\,Vm^{-1}$ versus $p\,p_0^{-1}$, while the linearization of the previous equation gives C and the V_m value which is necessary in the calculus of the surface area.

$$S = \frac{V_m N_{Av} A}{22.414} \times 10^{-19} \qquad (3)$$

where A = 16.2 Å^2 is the surface of a N_2 molecule.

To ensure absence of humidity and other contaminating species on material surfaces, before BET adsorption measurement, a degassing step is always experimentally adopted.

By measuring both the adsorption and desorption branches, it is possible to gain many information about pore size distribution and pores shape. A further detailed analysis is given in section (**4.1. Investigating pores shape**).

Used instrumentation and protocols: The Brunauer-Emmett-Teller (BET) technique was used to achieve surface area and porosity information from N_2 adsorption/desorption isotherms at 77 K using a Micromeritics Tristar II apparatus (Tristar II 3020). Measurements were performed many times to assess isotherms reproducibility and accuracy. Specific surface area was determined by the instrumental software. Porosity distribution was evaluated for each sample by using Barrett-Joyner-Halenda (BJH) or DFT theory methods applied to the N_2 adsorption data. Before measurements, sample powders were heat-treated at 150°C for 4 h under a N_2 flow to remove adsorbed foreign species.

2.2. Electrochemistry by RDE and RRDE

The aim of this work has been to develop catalysts for the electrochemical oxygen reduction reaction; therefore electrochemical measurements would require an environment simulating fuel cells working conditions (continuous flow of hydrogen and oxygen to the electrodes and temperatures around 60°C-80°C). The direct approach would be to get a MEA (Membrane Electrode Assembly) and measure the provided current density. However, it is

very difficult to work with such complicated systems with many interconnected parameters: mass transport processes, partial effective utilization of the catalytic sites, etc.

This is why it is preferable to reduce the number of variables and electrochemically characterize just a single catalyst, in this case for ORR by cyclic voltammetry, using Rotating Disk Electrode (RDE) and/or Rotating Ring Disk Electrode (RRDE). The main advantages of such working electrodes is their geometry. In fact, for these electrodes the hydrodynamics is controlled by reproducible laminar flux, and analytical equations are known.

Cyclic voltammetry allows the study of the electrochemical behavior of the synthesized materials for oxygen reduction reaction.

This technique requires three electrodes:

- A working electrode (WE), on which a catalyst powder is deposited on a solid electrode (Glassy carbon) in the form of a suspension (ink).
- A reference electrode (RE), with a constant potential, in respect of which the working electrode potential is measured and varied over the experimental time.
- A counter electrode (CE), necessary to allow the measure of electric current flowing between CE and WE at a given WE potential.

In cyclic voltammetry the potential is varied over time, at a (usually) constant rate between two limits. When one of this limit potential is reached, the potential ramp direction is inverted. This inversion can occur many times during a single experiment.

The measured current is then plotted against the applied potential to obtain a cyclic voltammogram.

If the working electrode is a Rotating Disk Electrode (RDE), a platinum, gold or glassy carbon disk is enclosed in a Teflon cylinder. During measurement, a controller rotates the electrode at a specified angular rate. The advantage of using such electrode is the ability of controlling the incoming reagent flux at the electrode surface, which allows the separation of kinetic mass transfer from electron charge transfer contributions such as to evidence the latter ones, which are most important to catalytic electrode behavior.

If the working electrode is a Rotating Ring Disk Electrode (RRDE), the disk electrode is surrounded by an electrically insulated ring (usually Pt). This electrode configuration makes possible to join the advantages of RDE with monitoring of soluble products formation at the central disk, given that these are convection-transported by experimentally known amounts to the outer ring of the assembly. This is for example the case of H_2O_2 produced at the disk during O_2 reduction: H_2O_2 is oxidized at the ring and the oxidation current becomes a quantitative measure of the local H_2O_2 concentration. The ring potential is normally kept constant and equal to the oxidation (or reduction) potential of the analyzed species.

As already mentioned, RDE and RRDE belong to the electrodes category for which rigorous solution to hydrodynamics and convective diffusion equations are known.

The disk of RDE/RRDE, due to the centrifuge force, pushes the solution in contact with its own surface towards the external part, generating a radial flux. The central part of the disk, in this way, is continuously supplied by new fluid, normal to its surface, as shown in **Fig. 2.1**.

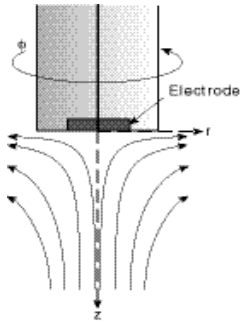

Fig. 2.1: RDE electrode scheme. Fluid flux profiles when the electrode is rotating.

The total current at the surface of the electrode is limited by the reactants mass transfer processes (whose current density is indicated as i_d), the charge transfer reaction (whose current density is indicated as i_k) and by protecting layers (here due to Nafion®) possibly present (whose current density is indicated as i_f). The total resistance is hence given by the following equation:

$$\frac{1}{i} = \frac{1}{i_d} + \frac{1}{i_k} + \frac{1}{i_f} \qquad (4)$$

where *i* is the measured current density.

The mass transfer current density, i_d, is defined by Levich equation:

$$i_d = 0.62 \cdot n \cdot F \cdot D^{2/3} \cdot \nu^{-1/6} \cdot c_0 \cdot \omega^{1/2} \quad (5)$$

where *n* is the transferred electrons, *F* is the Faraday constant (96485.31 C mol^{-1}), D is the diffusion coefficient of the reactant, ν the solution kinematic viscosity, c_0 the solution concentration of reactant, ω the angular electrode rotation rate.

Finally, the current density due to the Nafion® protecting layer, i_f, is given by:

$$i_f = (n \cdot F \cdot C_f \cdot D_f) \cdot L^{-1} \qquad (6)$$

where C_f is the solubility of the reactant in Nafion®, D_f is the diffusion coefficient of the reactant in Nafion® and *L* is the layer thickness. It has been demonstrated that, if these layers are less than 2 μm thick, the i_f contribute could be neglected [2].

By this approximation, equation (4) can be rewritten as the Koutechy-Levich equation for thin layers:

$$\frac{1}{i} = \frac{1}{i_k} + \frac{1}{0.62 \cdot n \cdot F \cdot D^{2/3} \cdot \nu^{-1/6} \cdot c_0 \cdot \omega^{1/2}} \qquad (7)$$

Hence, by plotting the reciprocal of the measured current density versus the reciprocal of the square root of the electrode angular electrode rotation rate, a line is obtained. From its intercept, i_k value is obtained and from its slope, the number of exchanged electrons is given.

i_k value is then useful to build a Tafel plot. In fact from the Butler- Volmer equation:

$$i = i_0\left[\exp\left(\frac{(1-\beta)F\eta}{RT}\right) - \exp\left(\frac{-\beta F\eta}{RT}\right)\right] \qquad (8)$$

where i_0 is the exchange current density, η is the overpotential, β is the charge transfer symmetry factor, *R* and *T* have their usual meanings. Under the high negative overpotential approximation (η < 0.050 V), (8) can be rewritten as:

$$\eta = \frac{RT}{\beta F}\ln|i_0| - \frac{RT}{\beta F}\ln|i_k| \qquad (9)$$

Hence, by plotting, η versus *ln* i_k, a Tafel plot is built and the Tafel slope, an important kinetic parameter, together with i_0, can be evaluated and discussed.

By RRDE, the hydrogen peroxide production efficiency and, again, the number of transferred electrons can be calculated. A detailed explanation of relative equations is given in the section (**3.4.1. Fructose as C- and O-source: experimental and results**) [3].

Used instrumentation and protocols: Electrochemical characterization was performed in 0.1 mol dm^{-3} $HClO_4$ or 0.1 mol dm^{-3} KOH by the Thin Film Rotating Disk Electrode (RDE)/ Thin Film Rotating Ring Disk Electrode (RRDE) methods using Cyclic Voltammetry (CV) and Linear Sweep Voltammetry (LSV). The preparation of the ink depends on the material to be tested:

- N-CNTs (tested only by RDE): catalyst aliquots (4 mg) were dispersed in water (1.02 mL), sonicated 5 min, then added with Nafion® (80 μL) and sonicated for 10 min; 14 μL of this mixture were pipetted onto the graphite tip (geometric surface area: A=0.07 cm^2) of a rotating disk electrode (EDI 101, Radiometer) and dried in a bottom-up position above a tungsten lamp (100 W). Electrode loading was 0.7 mg cm^{-2}.
- Other materials: 10 mg of the catalyst powder were suspended in 1 mL of water; 5 μL of commercial Nafion® were added to the suspension which underwent 20 minutes of sonication; finally, 7 μL/20 μL of this suspension were deposited onto the RDE (EDI 101, Radiometer)/RRDE (PINE) glassy carbon tip (geometric surface area of 0.07 cm^2 and 0.1963 cm^2 for RDE and RRDE, respectively) and dried in a bottom-up position under a tungsten lamp (100 W).

A two-compartment cell with a graphite counterelectrode (Amel 201/S-016 for both RDE and RRDE) and a AgCl/Ag external reference electrode (Amel and PINE for RDE and RRDE, respectively) in 3 mol dm^{-3} NaCl was used. The instrument was an Amel mod. 7050 potentiostat for RDE and an Amel bipotentiostat for RRDE. Before CV recording, the electrode was conditioned cycling 45 min in N_2 in the potential range E= -0.275 ÷ +0.800 V (vs Ag/AgCl) in acidic conditions and E= -0.900 ÷ 0.250 V (vs Ag/AgCl) in alkaline conditions, followed by 100 min cycling in O_2 saturated solution (v=5 mV s^{-1}, ω=1600 rpm). CVs in O_2 were recorded in the

same conditions at different rotation rates. To verify electrode stability and internal reproducibility several CVs at ω=1600 rpm were recorded in each run. After measurements in O_2, CVs were again recorded in N_2 to obtain background faradaic currents for O_2 reduction data correction.

2.3. Other techniques. Experimentals and protocols

For the sake of clarity, whenever more than a single instrumental choice was possible, in the appendix is specified for each set of data the used instrumentation.

X-Ray powder diffraction (XRPD) patterns were recorded in Università degli Studi di Milano on a Philips PW3020 powder diffractometer, by using the Cu-Kα radiation (λ = 1.54056 Å) in a 2θ range from 20 to 80° (0.02° steps, 1s counting).

High resolution (HR) quality X-Ray Powder Diffraction (HR-XRPD) measurements were performed at the ESRF (Grenoble) and Alba-CELLS (Barcellona) synchrotron facilities at the beamlines ID22 [10] and MSPD, respectively. Both are high resolution powder diffraction beamlines equipped with a multi-1D detector and a Mythen linear detector [11] respectively. This technique was used to analyse two MgO-based samples (Fe/MgO 3 and Fe/MgO 4) that will be presented in the section "5.2.3. The Fe/MgO catalyst ageing". Fe/MgO 3 and Fe/MgO 4 ground powders samples were packed into 1 mm diameter Kapton® capillaries and measured at room temperature. Kapton® was selected in spite of quartz in order to minimize the diffraction by the capillary that would overlap with MgO diffraction peaks. For HR measurements the capillaries containing samples were mounted on the axis of the diffractometer and spun during measurements in order to improve powder randomization. Fe/MgO 3 sample was analysed at beamline ID22 @ESRF using an energy of 31.0 keV (λ = 0.40002 Å); scans were collected up to a maximum wavevector Q_{max} [=$4\pi\sin\theta\lambda^{-1}$]~11 Å^{-1}. Fe/MgO 4 sample was analysed at beamline MSPD @ Alba-CELLS using an energy of 30.0 keV (λ = 0.4131 Å); scans were collected up to a maximum wavevector Q_{max} ~11 Å^{-1}. Rietveld refinements on the diffraction patterns were carried out using the program GSAS [12] through its graphical interface EXPGUI [13]. Phase weight fractions were determined from the relative scale factors returned by the refinement. Fitting accuracy was given by the program according to the parameter R(F^2).

X-ray photoelectron spectroscopy (XPS) measurements were performed in Università degli Studi di Milano with a M-Probe Instrument (SSI) equipped with a monochromatic Al Kα source (1486.6 eV). For all samples, the C1s peak level was taken as the internal reference at 284.6 eV. Precision of reported binding energies (BEs) is approximately $\pm$0.2 eV. Uncertainty in spectral decomposition is estimated at $\pm$1%. Peaks were fitted to Gaussian function after Shirley background correction [4], using XPSPEAK 4.1 software.

Other X-ray photoelectron spectroscopy (XPS) measurements were recorded in Trinity College Dublin (TCD) at room temperature at a 45° takeoff angle with an analyzer resolution of 0.5 eV using a monochromatized Al Kα source (1486.6 eV). Peaks were fitted to Voigt functions after Shirley background correction [4], using commercial software (Igor Pro 6.04). Atomic relative

percentages were obtained from peak area ratios corrected by empirical relative sensitivity factors derived by Wagner *et al.*[5]: F 1s=1, C 1s=0.25, O 1s=0.66, N 1s=0.42, Fe $2p_{3/2}$=2.

Ultraviolet Photoelectron Spectroscopy (UPS) was performed in Trinity College Dublin (TCD), using a He(I) line as an excitation source, a takeoff angle of 90°, and an analyzer resolution of 0.02 eV. Measurements were collected by applying a negative bias to the sample in order to measure the high binding energy edge of the photoelectron spectrum. Spectra were corrected for bias and referenced to the Fermi energy, as measured from the Fermi step of a metallic screw inside the chamber [6]. Relative spectral intensities near the Fermi energy were found to be similar when the normalization was carried out using the full energy range. The work function was calculated from the difference between the incident photon energy (21.2 eV) and the energy cutoff at high binding energy. The cutoff value was determined from the intercept of linear fits of the spectrum before and after the emission threshold [7,8].

Raman spectra were obtained in Trinity College Dublin on a Raman microscope (NTEGRA Spectra NT-MDT) equipped with a CCD camera using 514 nm excitation and 1 cm^{-1} spectral resolution. In order to obtain I_D/I_G ratios, peaks were fitted using a combination of a Breit-Wigner-Fano and a Lorentzian peak using a commercial software (Igor Pro 6.04) [9].

Other Raman spectra were collected in Università degli Studi di Milano by a Jasco RMP 100 microprobe equipped with a 50x objective and connected by fiber optics to a frequency-doubled Nd:YAG laser (λ_{exc} = 532 nm) and to a Lot Oriel MS25 spectrometer with a CCD detector. The laser power at the sample was in all cases of few milliwatts. An exposure time of 2 s was used and all spectra were obtained as sum of 100 accumulations. The estimated resolution was about 8 cm^{-1}.

Optical microscope images were recorded in Università degli Studi di Milano by a Nikon Eclypse Optical Microscope.

Scanning Electron Microscopy (SEM) was performed in Trinity College Dublin at an accelerating voltage of 10 keV using a Zeiss Ultra microscope equipped with an Energy Dispersive X-ray Spectroscopy (EDS) detector (Oxford Instruments). Sample cross-sections were obtained on a Zeiss Auriga dual-beam system with a Ga focused ion beam (FIB, probe at 30 kV and 240 pA) and a SEM for imaging.

Other SEM images were recorded in Università degli Studi di Milano with a Leo 1430 scanning electron microscopy (Zeiss, Oberkochen,Germany).

Transmission Electronic Microscopy (TEM) images were obtained in Università degli Studi di Milano by a Zeiss EFTEM LEO 912AB (120 kV) microscope. To obtain average characteristics many different sample areas were analyzed. The HRTEM images were recorded in Milano at CNR (Consiglio Nazionale delle Ricerche) using a Zeiss LIBRA 200FE TEM LIBRA 200FE-HR TEM, operating at 200 kV and equipped with an in-column omega filter for energy selective imaging and diffraction. The associated EDX analysis were performed using Oxford EDS/EDX system and Inca software. For both TEM and HRTEM analyses, samples were prepared by casting a drop of their suspension in ethanol (after 5 min sonication) on a carbon

coated copper grid, letting it dry for some hours before analysis. The dimension analysis was performed using iTEM Olympus Soft Imaging Solutions.

Magnetic Susceptibility measurements were performed in Università degli Studi di Pavia by means of a superconducting quantum interference device (SQUID) magnetometer, in the temperature range 2<T<300K at applied DC magnetic field H=1000 Oe, operating in the standard extraction technique mode. The magnetic susceptibility was obtained by the formula: $\chi \approx M/H$, valid for low fields, with M and H the magnetization of the material and magnetic field strength, respectively.

Electrochemical Impedance Spectroscopy (EIS) measurements on amorphous carbon surfaces was carried out in Trinity College Dublin (TCD) in a home-built Teflon cell in which the carbon surface was exposed from a circular hole in its bottom part. Prepared carbon films were utilized as working electrodes with a bottom contact. A Pt wire (5 cm, CH Instruments) and an Ag/AgCl (1M KCl internal solution, CH Instruments) were the counter and the reference electrodes, respectively. Measurements were performed at room temperature on an Autolab potentiostat (model PGSTAT302N). Nova (Version 1.8) was the used software for data collection and preliminary elaboration. Solutions were degassed before measurements with Ar and, during electrochemical measurements, the cell was covered and a weak flux of Ar was blown over the solution. 1 mM solutions of either hexaminеruthenium(III) chloride, potassium hexachloroiridate (IV) or potassium ferrocyanide were prepared in 0.1 M KCl supporting electrolyte solution. The formal potential (E_0') for each reversible redox couple was determined by cyclic voltammetry. The potential scan rate was varied in the range between 1 V s^{-1} and 0.005 Vs^{-1} in order to determine the working electrode area applying the Randles-Sevcik equation. Impedance spectra were performed at E_0' for each surface; an equilibration time of 5 min at the applied potential was employed before each impedance measurement. The frequency response was recorded between 100 kHz and 0.01 Hz using a sinusoidal voltage with an amplitude of 10 mV. Equivalent electrical circuit modeling was performed using Nova (Version 1.8).

Temperature Programmed Desorption-Mass Spectroscopy analysis (TPD-MS) was performed in Università CNR Milano using a system composed by a "U-shaped" quartz reactor (positioned inside a furnace) and connected to a gas line and an on-line mass spectrometer with a quadrupole mass analyser. TPD-MS ananysis was performed under Ar flow. After 30 min of equilibration, making sure gas tubes were clean (recording H_2O, CO_2 and Ar profiles), 20 mg of the sample, diluted in quartz powder, were heated (10°C min^{-1}) up to 600°C and then kept 10 min at this temperature.

Thermogravimetric analyses (TGA) were performed in Università degli Studi di Milano on a Perkin Elmer TGA4000 under nitrogen atmosphere on samples weighting 2 mg. After 25 min in N_2 flow at T=25°C, samples were heated up to 900°C (10°C min^{-1}).

Differential scanning calorimetry (DSC) were performed in Università degli Studi di Milano on a Mettler Toledo instrument, under nitrogen atmosphere. After 25 min in N_2 flow at T=25°C, samples were heated up to 450°C (3°C min^{-1}).

2.4. References

1. S. Brunauer, P.H. Emmet, E. Teller, Adsorption of Gases in Multimolecular Layers, Journal of the American Chemical Society, 60 (1938), 309-319.

2. Handbook of fuel cells, Wiley, 1st edition, Vol. 2, Cap. 22.

3. C. Song, J. Zhang, Electrocatalytic Oxygen Reduction Reaction, PEM Fuel Cell Electrocatalysts and Catalyst Layers, Springer, London, 89-134.

4. A. Proctor, P.M.A. Sherwood, Data analysis techniques in X-ray photoelectron spectroscopy. Analytical Chemistry, 54 (1982), 13-19.

5. C.D. Wagner, L.E. Davis, M.V. Zeller, J.A. Taylor, R.H. Raymond, L.H. Gale, Empirical atomic sensitivity factors for quantitative analysis by electron spectroscopy for chemical analysis, Surface and Interface Analysis, 3 (1981), 211-25.

6. P.E. Colavita, B. Sun, K.Y. Tse, R.J. Hamers, Photochemical Grafting of N-Alkenes onto Carbon Surfaces: The Role of Photo-electron Ejection, Journal of the American Chemical Society, 129 (2007), 13554-13565.

7. G. Ertl, J. Küppers, Low Energy Electrons and Surface Chemistry; Wiley-VCH: Weinheim, 1986.

8. R. Schlaf, P.G. Schroeder, M.W. Nelson, B.A. Parkinson, P.A. Lee, K.W. Nebesny, N.R. Armstrong, Observation of Strong Band Bending in Perylene Tetracarboxylic Dianhydride Thin Films Grown on Sns2. Journal of Applied Physics, 86 (1999), 1499-1509.

9. A.C. Ferrari, J. Robertson, Interpretation of Raman spectra of disordered and amorphous carbon, Physical Review B, 61 (2000), 14095-14107.

10. Y. Watier, T. Mairs, F. Fihman, A. Fitch, The upgraded and refurbished High Resolution Powder Diffraction beamline at ESRF - ID22, Acta Crystallographica, A70 (2014), C1759.

11. F. Fauth, I. Peral, C. Popescu, M. Knapp, The new Material Science Powder Diffraction beamline at ALBA Synchrotron, Powder Diffraction, 28 (2013), S360-S370.

12. A.C. Larson, R.B. Von Dreele, General Structure Analysis System (GSAS), Los Alamos National Laboratory Report LAUR (2000), 86-748.

13. B.H. Toby, EXPGUI, a graphical user interface for GSAS, Journal of Applied Crystallography, 34 (2001), 210-213.

Chapter 3
Mesoporous N-, Fe-doped Carbons

Facing the problem of high costs and scarcity of platinum means to explore and choose between two different approaches: improving catalysts performances per Pt mass unit, or replacing the noble metal by less expensive materials. However, the other side of the coin of the latter is that these materials have to show some peculiar behaviors:

- *Comparable kinetics for ORR to Pt-based commercial catalysts*
- *Direct reduction of oxygen to water, without formation of intermediates which might lower the process efficiency and damage the constituent materials of the device*
- *High surface area, to maximize the accessibility of reactants to active sites*
- *An optimized porosity in terms of shape and dimension*
- *Low cost of precursors and, more in general, of the overall synthetic process*
- *Long term stability(in automotive application about 5000 h)*

Focusing on this way, carbon represents a very attractive material because its wide range of unique properties: i) high fraction of sp^2 content, related to electron conductivity, fundamental to charge transfer processes; ii) high specific surface area, necessary to maximize the access of reactants to catalytic sites; iii) easy surface functionalization or doping with heteroatoms and/or metals; iv) costs, carbon is not expensive and can be obtained by pyrolysis of a countless variety of organic precursors ranging from sugars to biomass, organic wastes and polymers.

Several papers on non-precious C-based ORR catalysts have been published after a first report by Jasinski [1] in 1964 demonstrating the ORR activity of pyrolysis of metal phthalocyanines and porphyrins. Then, research on metal-heteroatoms macrocycles significantly expanded, leading to the picture that ORR catalytic activity can be related to metal-heteroatoms-containing moieties. However, for precursors cost and unsatisfactory lifetime performance, research was steered towards more simple reactants and preparation procedures. The number of possible combinations of precursor, synthetic strategy and templating procedures amplifies a lot the field of the study and the optimization of nature and number of active sites towards ORR. This can explain why debate about ORR mechanism on C-based catalysts is still alive in the literature. ***Fig. 3.1*** *gives an idea of the last 51 years of research efforts in this field.*

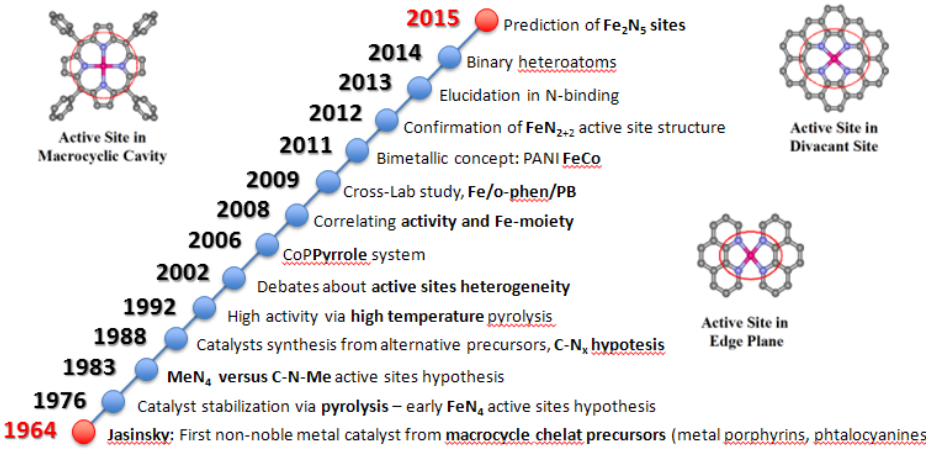

Fig. 3.1: *Timeline of progresses in non-precious metal catalysts for ORR.*

In the following, first of all results reported in the literature about precursors, synthetic strategies and templating procedures in the field of C-based Pt-free catalysts will be introduced and discussed; then a number of samples, synthesized in this work, will be described and characterized and their electroactivity, sometimes outstanding, will be discussed and compared to Pt-based commercial catalysts.

3.1. Choice of precursors: (not only) a matter of money

Provided that the aim of the work is to obtain a heteroatom- and transition metal (TM)-doped C-based samples, the choice of a precursor should be based on the pyrolysis of either a organic/polymeric compound containing all the requested chemical elements (C, O and a heteroatom) or a mixture of different organic/polymeric molecules. In both cases the TM source can be added in the mixture (unless already present in one of the precursors) before pyrolysis. In **Fig. 3.2** many synthetic processes have been summarized by Quiao *et al.*. From just a rapid glance it is easy to realize how wide is the range of possible choices [2].

C precursor	N precursor	TM precursor	T [°C][a]	Ref.
HEDA[b]	HEDA	$Co(NO_3)_2$	900	[33,65]
PANI[c]	melamine	$FeCl_3$	700–1000	[34]
PANI	PANI	Mn_3O_4	900	[35]
Polypyrrole	polypyrrole	$FeCl_3$	800–1100	[36]
GO, PANI	PANI	$FeCl_2$, $Co(NO_3)_2$	850	[37]
CNF,[d] PANI	PANI, EDA	$Co(NO_3)_2$	800	[38]
KetjenBlack, PANI	PANI	$FeCl_3$, $Co(NO_3)_2$	400–1000	[30,39]
VB12[e]	VB12	VB12	600–900	[40]
AFC[f]	AFC	AFC	500–800	[41]
PB[g]	PB	PB	550	[32]
P123	melamine	$Fe(NO_3)_3$	800	[42]
Co porphyrin based polymer	Co porphyrin based polymer	Co porphyrin based polymer	600–1000	[43]
PF resin[h]	melamine	$FeCl_2$, $FeCl_3$	750–1050	[29]
SBA-15	2,2-bipyridine	$FeCl_3$	600–1000	[44]
Mesoporous carbon	cyanamide	$Co(NO_3)_2$	900	[45]
PWAR[i]	ammonia	$FeCl_2$	1000	[46]
KetjenBlack	melamine	$FeCl_2$	800–1000	[47]
KetjenBlack	EDA[j]	$Co(NO_3)_2$, $FeSO_4$	900	[48]
KetjenBlack	FePc, CoPC	FePc, CoPC	600, 800	[31]
BP 2000[k]	melamine	$FeCl_3$	900	[49]
BP 2000	cyanamide	$Fe(OAc)_2$	950	[50]
BP 2000	TPPZ[l]	$Fe(OAc)_2$	600–900	[51]
BP 2000	DETA[m]	$CoCl_2$	600–900	[52]
Vulcan XC-72R	DCDA	Fe_2O_3	700–900	[53]
Vulcan XC-72R	pyridine	$Co(SO_4)_2$	200–900	[54]
Vulcan XC-72R, GO	urea	$FeCl_3$	1000	[55]
GO	C_3N_4	$FeCl_3$	800	[56]
GO	PEHA[n]	$FeCl_3$	900	[57]
GO	ammonia	CoO	500	[58]
GO	cyanamide	$FeCl_3$	900	[59]
GO	polypyrrole	$Fe(OAc)_2$	600	[60]
GO, CNT	ammonia	Fe	900	[61]
CNT	BTA[o]	$Co(NO_3)_2$	300–800	[62]
MWCNT[p]	C_3N_4	$FeCl_3$, FeTMPP-Cl[q]	800	[63]

[a] Annealing temperature. If multistep heating is adopted, the highest temperature is shown. [b] Hexamethylenediamine. [c] Polyaniline. [d] Carbon nanofiber. [e] Vitamin B12. [f] Ammonium ferric citrate. [g] Prussian blue. [h] Phenol formaldehyde resin. [i] Polyacrylic weak-acid cation-exchange resin. [j] Ethylenediamide. [k] Black Peals 2000. [l] Tripyridyltriazine. [m] Diethylenetriamine. [n] Pentaethylenehexamine. [o] Benzotriazole. [p] Multiwalled CNTs. [q] 5,10,15,20-Tetrakis(4-methoxyphenyl)-21 H,23H-porphine iron(III) chloride.

Fig. 3.2: Samples synthesized by furnace processes; for the references column, see the original paper [2].

3.1.1. C-, O- sources

In the context of looking for alternative sources in order to take into account the environmental and economic concerns, a number of solutions might be identified in renewable materials. About this, the hydrothermal carbonization of biomass derivatives could be consider a promising solutions in terms of “reusing” materials that otherwise should be stored or

processed. In fact biomass, because of its low economic value, huge amount and easy access, represents a very promising starting material for the synthesis of carbonaceous matrix [3].
Furthermore, the heat-treatment of biomasses can be considered a "green" synthetic pathway that, starting from sustainable natural sources, enables to obtain directly N-doped carbons [4]. By hydrothermal carbonization, biomass is first converted into polymers and then, through dehydration, polymerization and condensation steps, into carbon rich derivatives [5]. However, due to the impossibility of handle exactly the same biomass composition, which depends strongly on the environment and the source, this process still does not appear to be satisfactory and optimal because of its intrinsic long-term irreproducibility.

An alternative and abundant C- and O-source is represented by commonplace and inexpensive polysaccharides, e.g. cellulose and starch, composed of long chains of a monosaccharide, ranging in structures from linear to highly branched. If compared to biomass and organic wastes, polysaccharides offer the advantage of being often quite homogeneous, containing only slight modifications of the repeating unit.
Cellulose, considered the most common molecule on earth, and starch, consist of long (many hundreds of units, at least) chains of *D*-glucose, differently bonded to each other, as shown in **Fig. 3.3**.

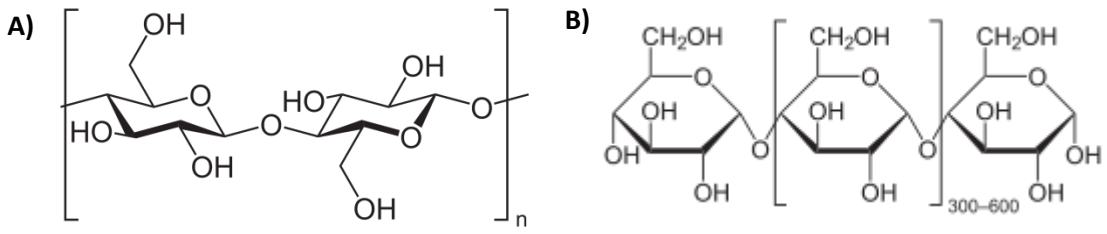

Fig. 3.3: Cellulose (A) and starch (B) structures.

Many works in the literature use these C- and O-sources to synthesize carbon-based matrix, especially in a fiber-shaped material [6]. The main disadvantage of using polysaccharides is related to cellulose and starch insolubility in water and in many organic solvents; this aspect limits the possibility of obtaining homogeneous solutions (it is preferred working with a solution when it is necessary to achieve a homogeneous mixture of all precursors, TM included) to be carbonized. Using suspensions is a possible alternative but some aspects should be taken into account to prevent the fast precipitation of suspended particles, such as the use of suspension stabilizers. As a consequence, the chemical complexity of the final carbonized system is increased and some poisoning and undesired elements (due to the use of surfactants as stabilizers), e.g. chlorides [7], might be present in the final carbonaceous matrix.

In the same carbohydrates family, the presence of monosaccharides, offers an alternative solution. Keeping the advantage of dealing with common, inexpensive and easily available molecules, e.g. glucose, fructose and xylose, many obstacles such as the polysaccharides insolubility, are indeed overcome [8,9].

Surely the wide field of C-containing molecules goes beyond this focus on the carbohydrates family. However, balancing availability, costs and easy-practical chemistry aspects, monosaccharides represent only one of the smartest alternative.

3.1.2. Heteroatom-sources

The goal of doping carbon with heteroatoms, in the presence of transition metals, has attracted increasing attention because it was demonstrated to improve the ORR electroactivity. Since the first report by Jasinski [1] in 1964 demonstrating the ORR activity of pyrolysized metal phthalocyanines and porphyrins, the research was addressed to other molecules, with lower complexity and costs. In a cross-laboratory study by Ustinov *et al.*, [10] many N-doped carbon materials have been synthesized in different ways and their ORR electroactivity has been confirmed. A first approach, similar to Jasinski one, was to carbonize metal-N_4 chelate as the exclusive or main precursor for metal, nitrogen and carbon; a second one used a metal salt as the unique metal precursor and a N-containing molecule as the exclusive N source. No pre-existing carbon support was used here; the last one used a metal salt as exclusive metal precursor and NH_3 under pyrolysis as exclusive N precursor. Carbon precursors were carbon blacks. All these catalysts were found to be more ORR performing than their correspondent blank test (without N). The ORR promoting role of nitrogen in carbon was hence independently demonstrated both theoretically and experimentally. Indeed, it was found that substitutional nitrogen at a few, specific, peripheral positions of graphene layers in well-ordered carbon nanostructures is in itself able to promote ORR activity even in the absence of accompanying metal centers [11].

Apart from nitrogen, boron doping was also confirmed to improve the ORR behavior; theoretical calculations demonstrated that this enhancement is related to electron accumulation in the boron vacant $2p_z$ orbital from the π^* electrons of the conjugated system. Electron transfer occurs readily to the chemisorbed O_2 molecule with a B-bridge, weakening the O-O bond.

Phosphorus, belonging to the same group of N, has the same number of valence electrons and was found indeed to be an effective dopant in order to improve the catalysts activity for the ORR. Many P-containing nanostructures have been prepared for this purpose [12].

After studying carbon materials doped with atoms having larger (nitrogen) or lower (phosphorous and boron) electronegativity than carbon and observing that the electrocatalytic activity was improved, the focus was set onto doping carbon with element having similar electronegativity, such as selenium and sulfur. An ORR enhancement that was found again [13].

It is believed that the ORR enhancement, when N or B are the dopant elements, is due to discontinuities in the electroneutrality of graphitic materials which form positively charged sites where oxygen is more favorably adsorbed. This explanation however is not valid for sulfur and selenium, having an electronegativity comparable to carbon one. The accepted hypothesis is that breaking the electroneutrality of graphitic planes might be important but not necessary to ORR enhancement and that, instead, other aspects, such as the conjugation between the sulfur lone pair and the graphene π system may play a fundamental role [13].

Similarly to what said before presenting C- and O-sources, heteroatoms doping can be obtained in so many different ways that is hard to rationalize and choose the best synthetic strategy with a particular heteroatom-containing molecule, considering that the carbonization at high temperature modifies the molecule structures, producing graphitic systems in which heteroatoms are still present but completely losing the chemical structure they had before the heat treatment.

It is worth mentioning that generally nitrogen is the preferred dopant because it was often found to be the most beneficial to ORR catalysis. For instance, it has been found that substitutional nitrogen at specific positions of graphene layers in well-ordered carbon nanostructures is more able to promote ORR activity than other heteroatoms [11,14].

3.1.3. Transition metals

Synthesis of catalytic sites based on nitrogen-coordinated transition metals (TM) on a carbon matrix led to many progresses in the ORR electrocatalysis. This improvement has been studied and investigated also from the theoretical point of view by DFT studies [15]. Other non-precious metals, belonging to the other groups in the periodic table, are not catalytically active, while Pt-group metals, a subcategory of TM, will be not discussed because beyond the scope of the work.

However, although the TM catalytic activity has been extensively confirmed, its role in the catalysts active sites is still a subject of controversy. In fact, there is a debate in the literature. On the one hand scientists state that, catalyzing the formation of N-containing (or, more in general, heteroatom-containing) active sites, the predominant role of iron is limited to the synthetic step. This theory seems to be supported by TEM images of active catalysts showing metal nanoparticles covered by graphitic planes. From this point of view, the presence of a metal center facilitates the incorporation of nitrogen into the carbon matrix during the pyrolysis, and, finally, the ORR activity is attributed to the nitrogen incorporated in the carbon matrix. This opinion is partially supported by the fact that the doped nitrogen can induce a charge delocalization in adjacent carbon atoms, thanks to its strong electron affinity, so that carbon atoms can show a slightly positive charge, which promotes a break of oxygen molecules by a formation of weak parallel bonds in a parallel diatomic adsorption process onto the carbon atoms [16].

On the other hand, metal itself plays an active role in the adsorption step of the oxygen molecules by a formation of specific interactions between heteroatoms and TM [17,18]. This theory has been taken into consideration in this work when studying the reaction mechanism of ORR on synthesized catalysts hereby.

Apart from the specific roles that TM plays during the ORR, many investigations in the literature aim at finding out the best TM in order to gain the best ORR electroactivity. Fe and Co have been often found to be the preferred and most active TM, hence they are the most commonly used precursor metal ions in catalyst synthesis, whereas other transition metals, adjacent to them in the chemical Periodic Table, such as Mn, Ni and Cu, are less investigated [19,20].

3.1.4. ORR most electroactive surface groups

As mentioned above, among the great number of potential available molecules and TM sources, the focus will be set on those ones giving N- and Fe-doped carbon matrix as end products.

On the basis of the coordination theory, the lone pair of nitrogen is able to coordinate TM with empty orbitals, as in the case of iron. In a nitrogen-doped graphene plane, this element (N) can be in the graphitic, pyrrolic, pyridinic form. Similarly to pyridine, pyridinic nitrogen has a lone

pair (**Fig. 3.4**). The pyrrolic nitrogen, losing a proton, has a lone pair as well. Hence, in principle, both pyridinic and pyrrolic nitrogen are able to coordinate iron.

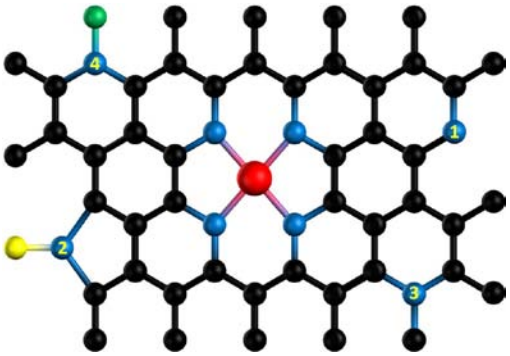

Fig. 3.4: Scheme of the atomic structure of a N- and Fe-doped graphene plane; atoms in black correspond to carbon, in blue to nitrogen, in red to iron and in green to oxygen. Nitrogen atoms are 1) pyridinic, 2) pyrrolic, 3) graphitic, 4) oxidized. In the center is shown the Fe-N_4 motif [6].

Iron or, more in general, TM incorporation in a graphene structure, can give raise to many different intra-molecular structures, comprising nitrogen-containing motifs. Recent works have proposed that active sites would consist of a Fe cation coordinated by four pyridinic N, which are incorporated to graphitic carbon, having the same geometry of Fe-porphyrin molecules, a well-known ORR catalysts. Among all the TM-N_x motifs, TM-N_4 has the lowest formation energy and, therefore, it is considered to be the most likely and stable structure. From DFT calculations, it is generally accepted that the origin of ORR electroactivity is the formation of an adsorbed intermediate onto the surface, such as O_2, HOO, H_2O_2, OH, etc.. The energy of this adsorption process determines the reaction rate, as already demonstrated for Pt-surfaces [21].

The possibility that the catalytic site does not comprise the metal center has to be taken into account. If the TM cluster is embedded and hidden by a few layers of graphitic planes, the metal inside might change the work function of outer graphene. It was demonstrated by Bao *et al.*, that the electroactivity might arise from a decrease in the work function due to electron transfer by the embedded TM in single-walled carbon nanotubes. This theory is however not widely accepted yet and will not be further discussed in the following [22].

3.2. Templating procedures. State of the art.

The goal of obtaining surface area and specific pores dimensions and shape implies the use of templating techniques. Ordered mesoporous carbon materials have been always surrounded by great research interest because of their widespread applications not only as catalysts but also in many areas such as adsorbents, supports for many important catalytic processes and gas storage hosts. The most common synthetic methods involve hard and soft templates, which have proven to be the most successful methods for the preparation of mesoporous carbons with well-defined pore structures and narrow pore-size distribution. Activated carbon has long been produced in large scale, and used for many applications mostly related to gas adsorption. However, the synthesis of mesoporous carbon by templating method was not accomplished until the 1980s, when Knox and co-workers reported the

synthesis of mesoporous carbon using a gel as the template [23]. Knox's approach includes many steps, which are often used today in the hard template synthesis of mesoporous carbons with well-defined mesoporous structure: 1) preparation of silica gel with controlled pore structure, 2) impregnation of the silica template with the precursors mixture, 3) carbonization of the composite, 4) dissolution of the silica template.
The space once occupied by the host silica materials is thus transferred into the pores in the resulting carbon materials, and the carbon in the pores of the host silica becomes the continuous carbon framework.

In other works, silica have been replaced by zeolites as the template materials. However, the fine crystalline structure of zeolites was not replicated in the templated porous materials after dissolution of the zeolite frameworks [24]. In principle, using ordered hard template can enable the synthesis of ordered carbon structures with a precise porosity; in the literature, the first ordered carbon material in organized silica pores was achieved by Wu and Bein, who were studying properties of carbon inside the hexagonally structured cylindrical mesopores of MCM-41 [25]. In addition to the development of ordered mesoporous carbon materials using ordered silica as templates, many other approaches have been developed for the synthesis of disordered mesoporous carbon materials with uniform pores. These approaches include templating with silica nanoparticles, alumina, silica gel, or alumina-silica and copolymerization of carbon precursors with alkoxide inorganic precursors such as tetraethylorthosilicate (TEOS).

On what concerns soft-templating, amphiphilic molecules, such as surfactants and block copolymers, have been extensively employed. There are some requirements for a successful synthesis of mesoporous carbon materials using soft templates: the ability of the precursors to self-assemble into nanostructures, the presence of at least one pore-forming component and at least one carbon-yielding component, the thermal stability of the pore-forming component. So far only a few materials meet these requirements. An alternative was found by using cetyltrimethylammonium bromide (CTAB) in combination with a phenolic resin [26].
Block copolymers are interesting soft-templating agents because of their tunable properties that result from the self-assembly nature of various macromolecular architectures. However, many block copolymers are not suitable for the direct synthesis of carbon nanostructures because of the structural instability under carbonization temperatures.

For these considerations, in the recent literature the preferred templating agent is still silica because it offers advantages of being easily available, low cost and easy to be removed by lixiviation in alkaline conditions.

3.3. Carbonization temperatures

Although a broad range of methodologies and materials have been employed to produce active ORR catalysts, there are still difficulties in discerning the controlling parameters involved in the preparation of active catalysts. The general procedure of N-, TM-doped carbon matrix, whatever the templating strategy is, comprises at least one heat-treatment step that is found to be beneficial on both the activity and the stability of these electrocatalysts. A crucial choice is hence related to adopted carbonization/pyrolysis temperature. Surely, it is impossible to identify a unique optimized value of temperature valid for any precursor/mixture of

precursors that undergoes the heat-treatment. Depending on the chosen temperature, different N- and TM-doped graphene-like planes are formed. At present there is general agreement that low temperature active site is based on the N_4-metal type. However, even better identifiable, these active sites are not as active as they further become after a second heating step. However, the nature of the high temperature active sites is still controversial, as previously discussed [18].

It was also studied that metal–N_4 moiety can be maintained at relatively low temperatures and gradually disappears going higher. Hence, generally, in order to activate the catalytic sites, achieving a good graphitization degree but avoiding to lose many metal–N_4 moieties, preferred final pyrolysis temperature is around 900°C [18].

3.4. Choices by the authors, syntheses

On the basis of what discussed so far, a very specific and precise choice to deal with materials containing only some specific elements has been done: these elements are carbon, oxygen, (hydrogen), nitrogen and iron.

3.4.1. Fructose as C- and O-source: experimental and results

All chemicals and reagents were used as received without further purification. *D*-fructose, Guanidine acetate, 2-Guanidinobenzimidazole, 1,1,3,3-Tetramethylguanidine, iron(II) acetate, glacial acetic acid, Nafion® (5 wt. % EtOH solution), 37% hydrochloric acid, concentrated sulfuric acid and ethanol were purchased from Sigma Aldrich. Silica (70-230 mesh) and 60% $HClO_4$ solution was from Merck. KOH from Fluka was used to prepare 0.1 mol dm^{-3} solution.

A fructose (FRU in the following) water solution (1.68 mol dm^{-3}) was added either with guanidine acetate (GUA) or 2-Guanidinobenzimidazole (GBI) or 1,1,3,3-Tetramethylguanidine (TMG). Molar ratios between the sugar and the N-molecules were kept 1:1 independently on the chosen N-compound. Adding glacial acetic (molar ratio CH_3COOH : N-compound = 3 : 1) was found necessary to dissolve all the reactants. Iron acetate was then added in a proper quantity to obtain 0.96 wt.% of Fe with respect to fructose plus N-compound mass. Ten milliliters of this solution were stirred with 4.3 g of silica for 5 min to form a gel, and stirred again 5 min after 15 min standing. The gel was loaded in a quartz reactor, degassed with N_2 (100 cm^3 min^{-1}) for at least 5 min and inserted in a preheated vertical oven at T = 600 °C in order to rapidly carbonize the precursors mixture. Heating was kept for 1 h under continuous N_2 flow. Then, the reactor was rapidly quenched to room temperature. Silica was removed by lixiviation in 3 mol dm^{-3} boiling NaOH followed by repeated carbon washing/filtering (MilliQ water, 0.45 μm Durapore filters) until water conductivity became lower than 4 μS. Products were dried in nitrogen (100 °C, 24 h). All materials were heat-activated in a second step at T = 900 °C under constant N_2 flow (100 cm^3 min^{-1}) in the following conditions: 30 min at room temperature, ramping at 6 °C min^{-1} and 3 h standing at T = 900 °C, fast quenching to room temperature.

Final samples have been labelled FAG, FGBI and FTMG depending if the N-compound precursor was Guanidine acetate, 2-Guanidinobenzimidazole or 1,1,3,3-Tetramethylguanidine,

respectively. The label is always followed by numbers "6" or "9" reminding the last heat-treatment at 600°C or 900°C that samples underwent.

The preparation of a silica gel with the precursors mixture, before carbonization, allows, after lixiviation, the formation of a sponge-like, highly porous structure, as evidenced in TEM image, in **Fig. 3.5**, relative to a sample synthesized in the lab by this method, using different precursors from those one above mentioned [9]. This feature can be also confirmed by BET surface analysis, before and after the final heat-treatment at 900°C. In **Tab. 3.1** are presented the data of specific surface area for the three samples.

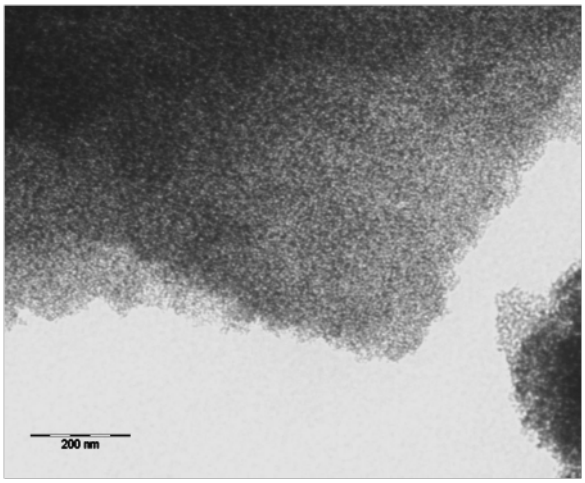

Fig. 3.5: TEM image of a mesoporous carbon, from a previous work [9].

Sample	Surface area / $m^2 g^{-1}$ (T = 600°C)	Surface area / $m^2 g^{-1}$ **(T = 900°C)**	Micropore % (T = 900°C)
FAG	684 ± 3	569 ± 3	11%
FGBI	617 ± 4	490 ± 4	11%
FTMG	820 ± 4	646 ± 3	15%

Tab. 3.1: Specific surface area values, before and after the final heat-treatment.

Fig. 3. 6 A-C show the experimental BET adsorption isotherms of the synthesized mesoporous carbons before (FAG6, FGBI6 and FTMG6) and after (FAG9, FGBI9 and FTMG9) the final 900°C heat-treatment.

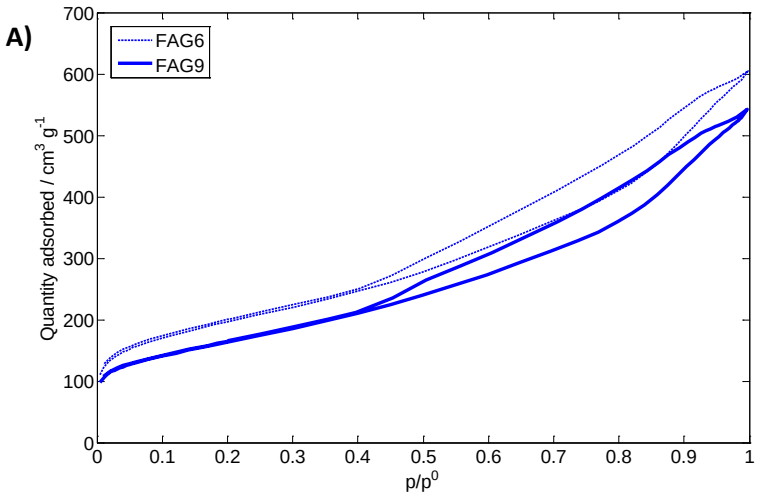

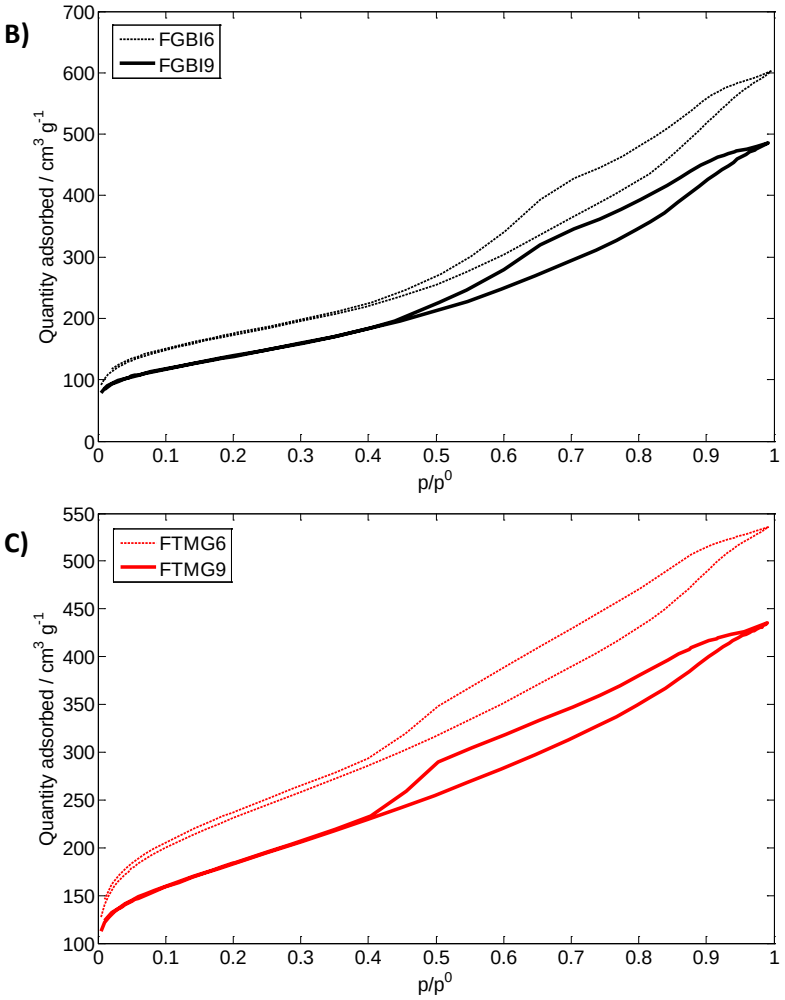

Fig. 3.6 A-C: Adsorption and desorption nitrogen isotherms at T= 77 K. A) FAG; B) FGBI; C) FTMG.

All samples are characterized by an high value of surface area, slightly decreasing after the final 900°C treatment, and exhibit a type IV isotherm, with a hysteresis loop which is characteristic of mesoporous materials [27]. The loop morphology of all the samples, independently from their heat-treatment, can be assigned to the H3-type hysteresis loop [27], which suggests specific pore morphologies. In the relevant literature [28] H3-type hysteresis is attributed to a non-fixed aggregation of plate-like particles giving rise to slit-shaped pores.

An evaluation of the pores distribution (**Fig. 3.7**) was done for final 900°C annealed samples, the only ones active for ORR, as shown in the following. This kind of analysis is fundamental because it is well-known in the literature that size and shape of pores are factors deeply affecting the mass transport processes and, as a consequence, the electroactivity of materials [29,30].

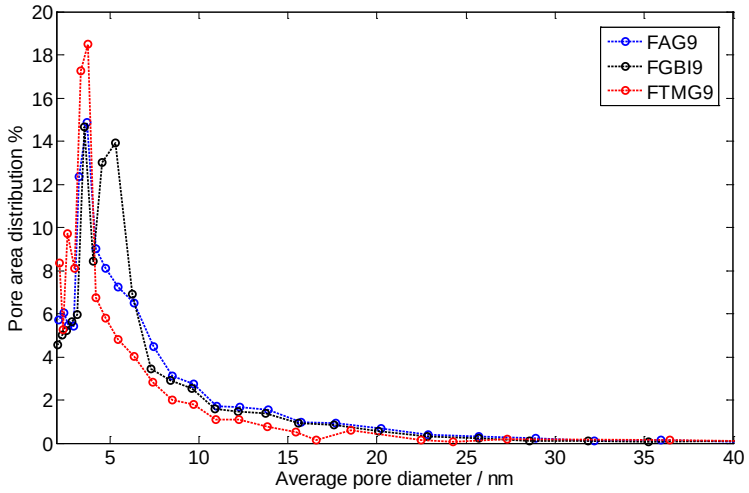

Fig. 3.7: Pore area distribution in mesopores for samples FAG9, FGBI9 and FTMG9.

The three samples that underwent the 900°C heat-treatment, as presented in **Tab. 3.1**, do not show evident differences in the percentage of micropores, which is low than 15 % for all the materials. By plotting pore area distribution in the range of mesopores (**Fig. 3.7**) it is notable that a peak between 2 and 7 nm is identifiable for all samples. This is a positive feature that, in many literature points of view, is relevant and requested when dealing with C-based catalysts for ORR. From this viewpoint in fact, mesoporosity is useful to improve the ORR performance, allowing efficient mass transport of reactants/products to/from the electrode, respectively, and ensuring a better metal dispersion in the catalytic material [31,32].

The ORR electroactivity of the 900°C heat-treated samples was first measured and compared by RDE technique in acidic media, 0.1 mol dm^{-3} $HClO_4$. In **Fig. 3.8** are reported ORR polarization curves for the three samples FAG9, FGBI9 and FTMG9. For comparison, a polarization curve for a commercial Pt-based catalyst, Pt EC20 (20% Pt/C), was recorded in the same conditions.

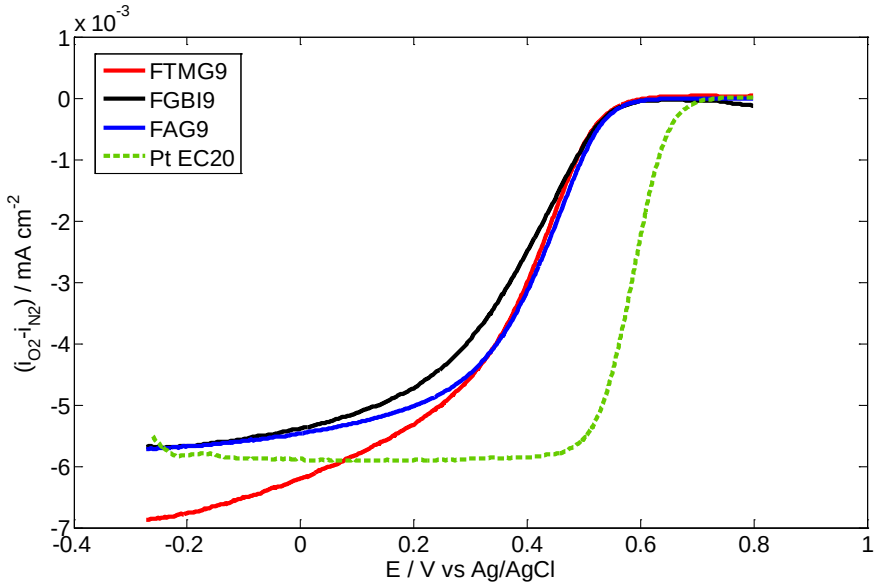

Fig. 3.8: RDE ORR polarization curves for mesoporous carbons recorded in oxygen-saturated 0.1 mol dm^{-3} $HClO_4$, ω=1600 rpm, v= 5 mV s^{-1}, T=25°C.

Except for the FTMG9 sample, a limiting current, even not completely defined, can be detected for FAG9 and FGBI9 carbons. FAG9 and FGBI9 polarization curves display a reduction profile more similar to that of the commercial catalyst Pt EC20 in **Fig. 3.8**. The ORR onset potential, equal for all the three synthesized materials, was calculated by the tangent method and it is about 0.550 V (vs Ag/AgCl). This value is displaced by 100 mV at more cathodic potentials than the reference commercial Pt EC20. Even though the onset value is worse if compared to Pt EC20 one, it can be stated that the synthesized mesoporous carbons are satisfying catalysts for ORR in acidic conditions [33].

Apart from the onset potential determination, a deeper kinetic analysis of ORR data has been done and the number of electrons was determined. The number of exchanged electrons, was obtained using the Koutecky-Levich (K-L) equation from cathodic CV data recorded at different electrode rotation rates on each catalytic material.

$$i^{-1} = i_k^{-1} + \left(0.62 \cdot n \cdot F \cdot D^{2/3} \cdot \nu^{-1/6} \cdot c_0 \cdot \omega^{1/2}\right)^{-1} \qquad (1)$$

where i is the experimental current density at a given potential E, F is the Faraday constant, D the O_2 diffusion coefficient, ν the solution kinematic viscosity, c_0 the solution concentration of reacting O_2, n the number of exchanged electrons, ω the angular electrode rotation rate and, finally, i_k is the kinetic current density extrapolated at infinite ω. (For calculations in acidic conditions the used parameters are: D= 1.67•10^{-5} cm^{2}s^{-1}, ν = 0.01 cm^{2}s^{-1}, c_0= 1.38•10^{-6} mol cm^{-3} in O_2-saturated (p=1 atm) 0.1 mol dm^{-3} $HClO_4$ [34]).

As shown in **Tab. 3.2**, n is in any case close to 4, thus permitting to conclude that all samples essentially obey the same ORR mechanism of direct H_2O formation. Focusing on the Tafel slopes columns in **Tab. 3.2**, calculated in the high overpotential region, all their values are quite high, if compared to Pt EC20 one. Tafel data, were obtained from extrapolated kinetic currents (I_k) values at many different potentials, and plotting them in Tafel $ln\ I_k$ vs E coordinates (not reported).

Sample	ORR onset potential / V (vs AgAgCl)	n. of electrons	|Tafel slopes|* / mV	|Tafel slopes|** / mV
FAG9	0.550	4.11 ± 0.07	30.1 ± 0.3	60.5 ± 0.3
FGBI9	0.550	4.3 ± 0.2	-	97.4 ± 0.3
FTMG9	0.550	3.7 ± 0.4	-	103.6 ± 0.4
Pt EC20	0.650	4.0 ± 0.1	26 ± 0.4	52.2 ± 0.4

Tab. 3.2: $HClO_4$ 0.1 mol dm^{-3}. ORR onset potentials and calculated kinetic ORR parameters for the synthesized catalysts and reference material, Pt EC20. * Tafel slopes at lower overpotentials, ** Tafel slopes at higher overpotentials.

Note that only in the case of FAG9 sample two linear Tafel regions, with different Tafel slopes, could be detected. Differences in Tafel slopes values can be due to an intrinsic property of the reaction mechanism [35] - different rate determining steps, with different charge transfer

coefficients, or different mechanisms- or, as stated by Dolelet *et al.* [36] invoking an incomplete catalyst utilization caused by transport and conductivity problems in the catalyst layer.

In order to better understand and highlight differences in the ORR electroactivity of the 900°C heat-treated samples, polarization curves have been recorded also in alkaline media, 0.1 mol dm^{-3} KOH. An RRDE working electrode has been employed, setting the ring potential at 0.33 V (vs AgAgCl), enough to oxidize peroxide species, possibly produced. In **Fig. 3.9** are reported ORR polarization curves for the three samples FAG9, FGBI9 and FTMG9. For comparison, a polarization curve for a commercial Pt-based catalyst, Pt EC20 (20% Pt/C), was recorded in the same conditions. In the figure, data from literature relative to a Pt-based catalyst by Antonietti *et al.*, has been also reported [37].

As evidenced in **Fig. 3.9**, a limiting current is not clearly detected for FTMG9 material; FGBI9 displays a better limiting current and, finally, FAG9 sample displays a well-defined limiting current, similarly to Pt EC20 and Pt literature. The ORR onset potential values, calculated by the tangent method, are displayed in **Tab. 3.3**. The outstanding result is relative to FAG9 sample, whose ORR onset potential (-0.01 V vs Ag/AgCl) is equal to the reference Pt literature and even higher than Pt EC20, the commercial Pt-based catalyst. It is followed by the ORR onset potential relative to FGBI9 sample and, as the worst catalyst among these three samples, the FTMG9 one. It is however worth to highlight that the ORR behavior is appreciable for all the catalysts synthesized by this method, being the worst one (FTMG9) just 100 mV more cathodic than reference commercial Pt EC20.

As shown in **Tab. 3.3**, similarly to what observed in acidic conditions, *n* is in any case close to 4, thus permitting to conclude that all samples essentially obey the same ORR mechanism of direct H_2O formation (for calculations in alkaline conditions the used parameters in (1) are: $D = 1.90 \bullet 10^{-5}$ $cm^2 s^{-1}$, $\nu = 0.01$ $cm^2 s^{-1}$, $c_0 = 1.20 \bullet 10^{-6}$ mol cm^{-3} in O_2-saturated (p=1 atm) 0.1 mol dm^{-3} KOH [34]).

Sample	ORR onset potential / V (vs AgAgCl)	n. of electrons	|Tafel slopes|* / mV	|Tafel slopes|** / mV
FAG9	-0.010	4.3 ± 0.3	20.2 ± 0.2	49.3 ± 0.4
FGBI9	-0.039	4.2 ± 0.1	-	58.7 ± 0.5
FTMG9	-0.102	3.8 ± 0.2	-	90.9 ± 0.9
Pt EC20	-0.047	4.0 ± 0.1	26.1 ± 0.4	50.1 ± 0.2

Tab. 3.3: KOH 0.1 mol dm^{-3}. ORR onset potentials and calculated kinetic ORR parameters for the synthesized catalysts and a reference material, Pt EC20. * Tafel slopes at lower overpotentials, ** Tafel slopes at higher overpotentials.

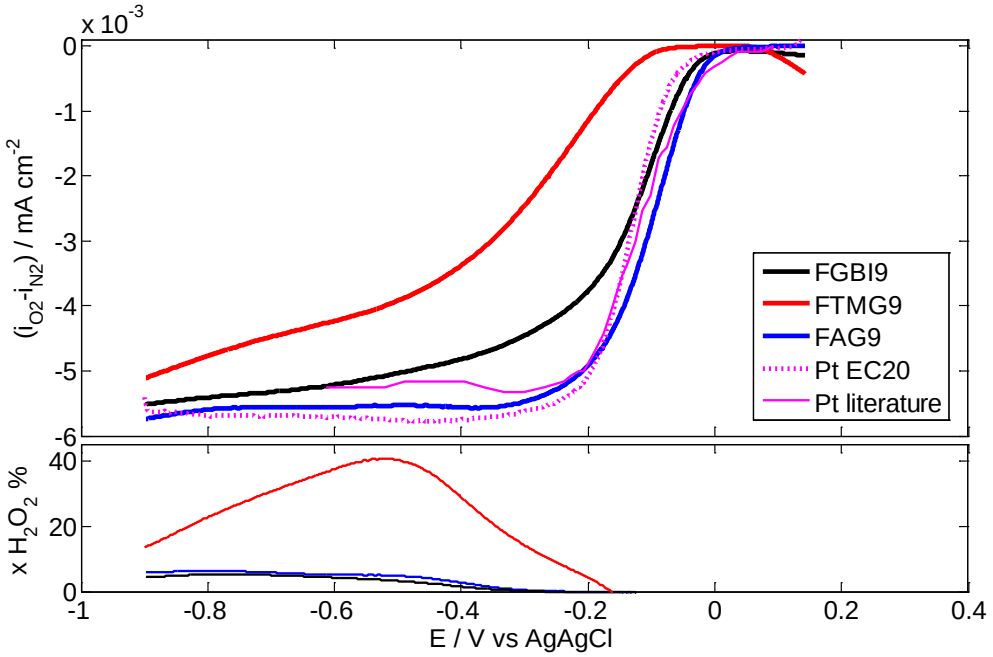

Fig. 3.9: Top: RRDE ORR polarization curves for mesoporous carbons recorded in oxygen-saturated 0.1 mol dm^{-3} KOH, ω=1600 rpm, v= 5 mV s^{-1}, T=25°C. Two reference samples from a commercial Pt-based catalyst and a literature Pt-based catalyst, are reported for comparison [37]. Bottom: Peroxide production efficiency.

Since in alkaline conditions an RRDE has been used, some more information can be derived from experimental data. First, the transferred electron number n, in addition to values calculated from Koutecky-Levich equations (1), as shown above, can be evaluated for each potential value on the basis of the following equation[38]:

$$n = \frac{4 \cdot I_D}{I_D + \frac{I_R}{N}} \qquad (2)$$

where n is total transferred electron number, I_D is the disk current, I_R is the ring current, N is the RRDE collection efficiency, which was determined to be 0.26 herein (it is common practice to empirically measure the collection efficiency using a well-behaved redox system rather than to rely upon a computed value. The ferrocyanide/ferricyanide half reaction was used here).

By applying (2), plotting the calculated n vs the potential values, as presented in **Fig. 3.10**, it can be realized that, as expected and in agreement on what found from K-L equation, the number of transferred electrons is equal to 4, confirming a direct reduction to water for all the synthesized catalysts in alkaline conditions.

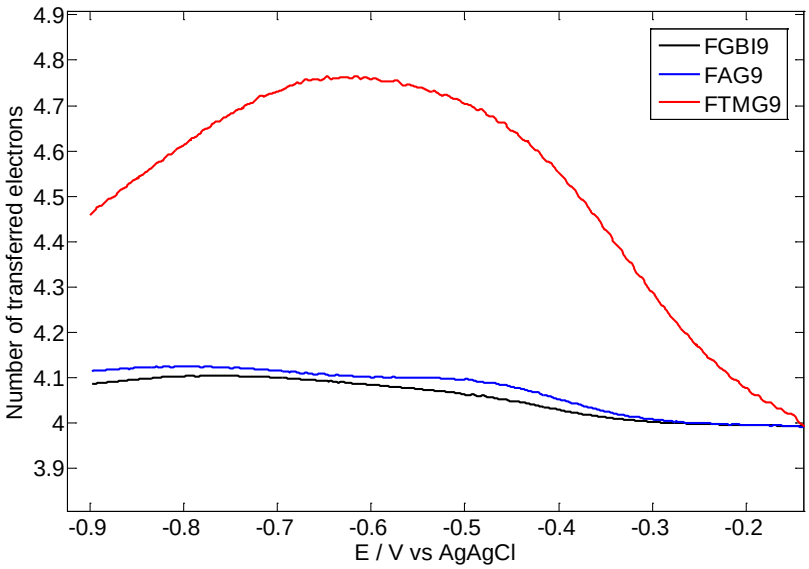

Fig. 3.10: Number of transferred electrons, calculated from (2).

Focusing on Tafel slopes in **Tab. 3.3**, it is worth noting that FAG9 sample, the best catalyst for ORR in terms of ORR onset potential, presents a Tafel slope even lower, and hence better, than the correspondent Pt EC20 one. This is a great result. A deeper discussion is hence needed. Tafel slopes were calculated in the high overpotential region; Tafel data were obtained from extrapolated kinetic currents (I_k) values at many different potentials, and plotting them in Tafel *ln* I_k *vs E* coordinates (not reported). Note that only in the case of FAG9 sample two linear Tafel region, with different Tafel slopes, could be detected. Some mechanistic studies are presented in one of the section "**3.4.3 Mechanistic considerations**".

An interesting parameter that has not been discussed yet, reported in **Fig. 3.9**, is the hydrogen peroxide production yield $\%H_2O_2$, whose value was calculated by [38]:

$$\%H_2O_2 = \frac{2 \cdot \frac{I_R}{N}}{I_D + \frac{I_R}{N}} \cdot 100 \qquad (3)$$

where *N* is the RRDE collection efficiency, which was determined to be 0.26 herein. As evidenced in **Fig. 3.9**, hydrogen peroxide production increases when the disk potential decreases. The onset potential value, for which the ring current signal of $\%H_2O_2$ can be distinguished from the baseline, is about -0.3 V (vs AgAgCl) for FAG9 and FGBI9 samples. It is noticeable that, focusing on ORR curves reported in the same **Fig. 3.9**, from this potential value, going more cathodic, FAG9 and FGBI9 samples show a well-defined limiting current. The maximum value of $\%H_2O_2$ production, equal to 5%, is reached at about -0.5 V and remains constant until the left extreme of potential range. It is quite common a production of peroxides species around 5-10% even for very promising Pt-free catalysts [39]. Therefore, FAG9 and FGBI9 catalysts are promising also in terms of the low production of peroxides species. The disadvantages of producing large quantities of H_2O_2, lowering the overall cell process efficiency and damaging the constituent material of devices, have been already mentioned.

FTMG9 sample, instead, which is the worst sample among this series in alkaline conditions, has another inconvenient peculiarity: as shown in **Fig. 3.9** it produces very large quantities of peroxides species. For this sample the onset potential value, for which the ring current signal of $\%H_2O_2$ can be distinguished from the baseline, is about -0.170 V (vs AgAgCl), ~ 130 mV more anodic than FAG9 and FGBI9 ones. A maximum in H_2O_2 production yield is reached at 0.520 V; in correspondence of this potential value, $\%H_2O_2$ is 40%, eight times higher than the $\%H_2O_2$ value, calculated at the same potential, for samples FAG9 and FGBI9. This implies that the ORR does not proceed entirely through the $4e^-$ reduction pathway and the formation of peroxides species is slow enough to let them be detected on the ring of the RRDE. These aspects, joined to a not very satisfying onset potential for ORR, render this sample a bad catalyst for ORR.

On the basis of previous results and the above discussion, some considerations could be done by evaluating the relations among the molecular structure of precursors and the electroactivity of final materials. In **Fig. 3.11** is reported the molecular structure of Guanidine acetate (GUA), 2-Guanidinobenzimidazole (GBI) and 1,1,3,3-Tetramethylguanidine (TMG).

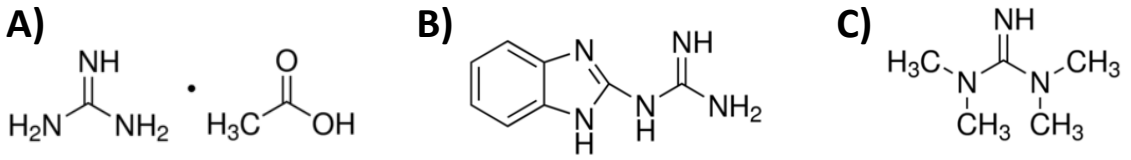

Fig. 3.11: Molecular structures of A) Guanidine acetate (GUA), B) 2-Guanidinobenzimidazole (GBI) and C) 1,1,3,3-Tetramethylguanidine (TMG).

It is quite interesting to highlight that a relation between the structure of the N-compound used in the synthesis and the final electrocatalytic activity indeed exists: the lower is the substitution degree of the N composing the guanidinium group, the better is the ORR behavior of the final material. The trend in the N-compound, on the basis of the final ORR electroactivity is indeed: GUA > GBI > TMG. These differences in the electroactivity are more evident in alkaline media, because it is well known that the kinetics is more favored than in acidic conditions and small differences might be better evidenced in KOH rather than $HClO_4$.

Focusing onto 1,1,3,3-Tetramethylguanidine, two of the three nitrogen of the guanidinium group are completely substituted by methyl functionalities, thus rendering the molecule less basic, due to the steric hindrance, and hence less prone to react with metallic centers. Being the formation of N-Fe catalytic sites prevented, this might be an explanation for the unsatisfying behavior of FTMG9 catalyst.

2-Guanidinobenzimidazole is a polyfunctional planar molecule with a delocalized π electronic system, five nitrogen atoms, that may act as basic centers, and five labile N–H bonds. The reactions of 2-guanidinobenzimidazole with metal ions such as Co, Ni, Cu and Zn under different conditions have been studied in many works [40]. The chelating ability of GBI, however, cannot work well with an iron metal center, thus likely explaining the unsuccessful formation of very active catalytic sites. Being the activity of FGBI9 sample however quite satisfying, the carbonization steps at 600°C and later at 900°C, might help the formation and inclusion of N moieties, together with Fe centers. Catalytic sites formation has been interpreted in this case to be due to the very high temperature used, rather than chemical reactions in solution before

pyrolysis. In addition, the delocalized π electronic system, with its "graphene-like" structure, might easily produce graphene planes during the pyrolysis.
The Guanidine acetate molecule displays a very high basicity, where the electronic lone pairs of nitrogen are more available than in other used molecules where the steric hindrance prevents an otherwise possible coordination. The molecule basicity, together with the high ratio of N/C (if compared to GBI and TMG) might help the formation of Fe- and N- containing catalytic sites and the inclusion of many N-functionalities, possibly bonded to Fe centers, in the graphene layers of the final C-matrix.

In conclusion of this paragraph:

- among the series of synthesized materials the best sample (FAG9) was prepared starting with fructose and guanidine acetate as precursors. The activity of this sample is rewarding in acidic conditions and excellent in alkaline media.
- It is still unknown whether the formation of ORR active sites is related to products of reactions happening in the starting solution or to reactions taking place at high temperature, during the heat-treatments.

3.4.2. Changing the sugar

On the basis of the above results, in particular related to FAG9 sample, found to be extremely active both in acidic and alkaline conditions, the next step was to move towards different C- and O-sources, since an active N-compound in the formation of catalytic sites was identified in Guanidine acetate. In the same carbohydrates family of fructose, that is the monosaccharides family, some other choices can be found out. Keeping the advantage of dealing with common, inexpensive and easily available molecules, glucose and xylose, were taken into consideration [8,9].

All chemicals and reagents were used as received without further purification. *D*-fructose, *D*-glucose, *D*-xylose, guanidine acetate, iron(II) acetate, glacial acetic acid, Nafion® (5 wt. % EtOH solution), 37% hydrochloric acid, concentrated sulfuric acid and ethanol were purchased from Sigma Aldrich. Silica (70-230 mesh) and 60% $HClO_4$ solution was from Merck. KOH concentrate from Fluka was used to prepare 0.1 mol dm^{-3} solution.

A glucose or xylose (GLU or XYL in the following, respectively) water solution (1.68 mol dm^{-3}) was added with guanidine acetate (GUA). Molar ratios between the sugar and the N-molecule were kept 1:1 independently on the chosen monosaccharide. Adding glacial acetic (molar ratio CH_3COOH : GUA = 3 : 1) was found necessary to dissolve all the reactants. Iron acetate was then added in a proper quantity to obtain 0.96 wt.% of Fe with respect to fructose plus N-compound mass. Ten milliliters of this solution were stirred with 4.3 g of silica for 5 min to form a gel, and stirred again 5 min after 15 min standing. The gel was loaded in a quartz reactor, degassed with N_2 (100 cm^3 min^{-1}) for at least 5 min and inserted in a preheated vertical oven at *T* = 600 °C in order to rapidly carbonize the precursors mixture. Heating was kept for 1 h under continuous N_2 flow. Then the reactor was rapidly quenched to room temperature. Silica was removed by lixiviation in 3 mol dm^{-3} boiling NaOH followed by repeated carbon washing/filtering (MilliQ water, 0.45 μm Durapore filters) until water conductivity became lower than 4 μS. Products were dried in nitrogen (100 °C, 24 h). All

materials were heat-activated in a second step at T = 900 °C under constant N_2 flow (100 cm^3 min^{-1}) in the following conditions: 30 min at room temperature, ramping at 6 °C min^{-1} and 3 h standing at T = 900 °C, fast quenching to room temperature.
Final samples have been labelled GAG and XAG depending if the sugar precursor was glucose or xylose, respectively. The label is always followed by numbers "6" or "9" reminding the last heat-treatment at 600°C or 900°C that samples underwent.

As in the previous section, the first analysis to be considered is relative to samples surface area, from BET technique. In **Tab. 3.4** are presented the data of specific surface area and micropores percentage.

Sample	Surface area / m^2 g^{-1} (T = 900°C)	Micropore % (T = 900°C)
FAG9	569 ± 3	11%
GAG9	671 ± 1	9%
XAG9	533 ± 2	13%

Tab. 3.4: Specific surface area values, after the final 900°C heat-treatment.

GAG9 and XAG9 samples have been prepared by exactly the same synthetic method of materials presented above (FAG9, FGBI9 and FTMG9); this is the reason why BET surface area values are high, as expected, and similar to what found before for all the fructose-based samples of the previous section.

Fig. 3.12 shows the experimental BET adsorption isotherms of the synthesized mesoporous after the final 900°C heat-treatment.

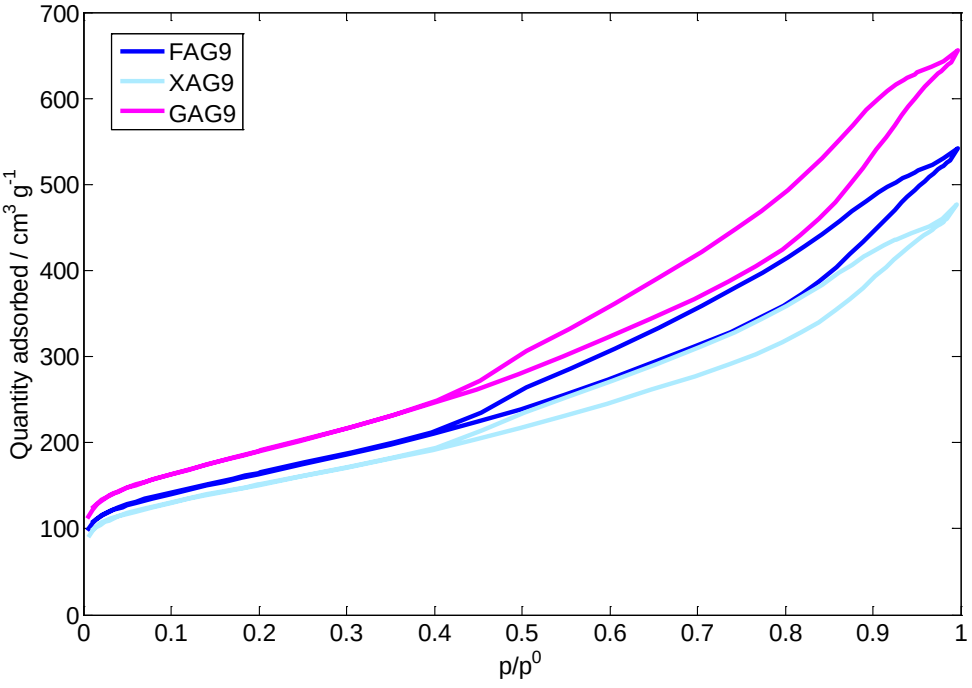

Fig. 3.12: Adsorption and desorption nitrogen isotherms at T= 77 K for FAG9, GAG9 and XAG9.

Samples before the final heat-treatment will not be further analyzed because not active for the ORR. All samples exhibit a type IV isotherm, with a hysteresis loop which is characteristic of mesoporous materials [27]. The loop morphology can be assigned to the H3-type hysteresis loop, [27], which suggests specific pore morphologies: H3-type hysteresis is attributed to a non-fixed aggregation of plate-like particles giving rise to slit-shaped pores [28].

An evaluation of the pores distribution (**Fig. 3.13**) was done for final 900°C annealed samples, the only ones active for ORR. This kind of analysis is fundamental because it is well-known in literature that dimension and shape of pores are factors deeply affecting the mass transport processes and, as a consequence, the electroactivity of materials [29].

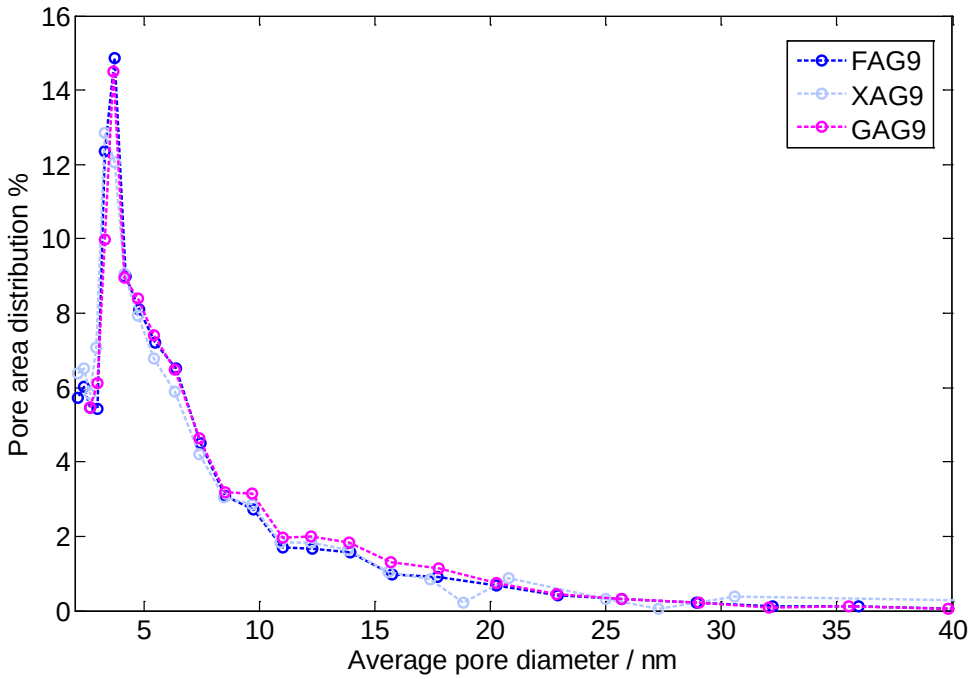

Fig. 3.13: Pore area distribution in mesopores for samples FAG9, GAG9 and XAG9.

The three samples that underwent the 900°C heat-treatment, as presented in **Tab. 3.4**, do not show evident differences in the percentage of micropores, which is around 10 % for all the materials. By plotting pore area distribution in mesopores range (**Fig. 3.13**) it is notable that curves are almost overlapping and a peak between 2 and 10 nm is identifiable for all samples. In the literature, this porosity, in a carbon-based material, is considered very beneficial to ORR. In fact, mesoporosity is useful to improve the ORR performance, allowing efficient mass transport of reactants/products to/from the electrode, respectively, and ensuring a better metal dispersion in the catalytic material [31,32].

The ORR electroactivity of the samples was first measured and compared by RDE technique in acidic media, 0.1 mol dm^{-3} $HClO_4$. In **Fig. 3.14** are reported ORR polarization curves for the three samples FAG9, GAG9 and XAG9. For comparison, a polarization curve for a commercial Pt-based catalyst, Pt EC20 (20% Pt/C), was recorded in the same conditions.

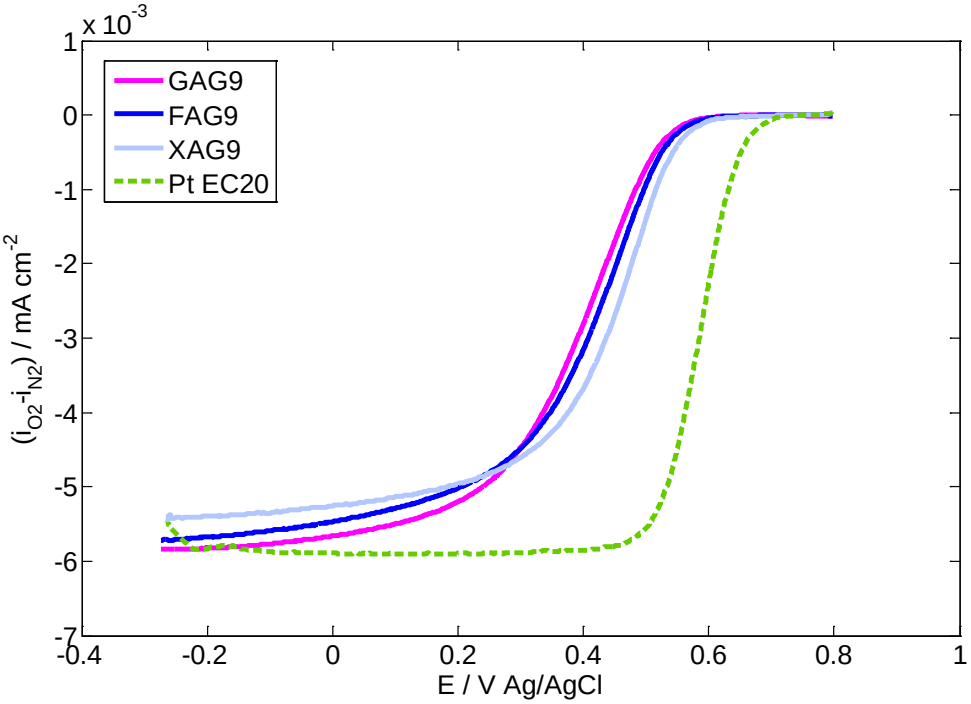

Fig. 3.14: RDE ORR polarization curves for mesoporous carbons recorded in oxygen-saturated 0.1 mol dm^{-3} $HClO_4$, ω=1600 rpm, v= 5 mV s^{-1}, T=25°C.

Differently from the above results, where almost all materials (apart from FAG9) do not show any completely satisfying limiting current in acidic media, here all samples, FAG9, GAG9 and XAG9, are characterized by a well-defined limiting current, displaying, even at higher overpotentials, an ORR reduction profile similar to Pt EC20 in **Fig. 3.14**. The ORR onset potentials, calculated by the tangent method, are reported in **Tab. 3.5**. The best material in terms of onset potential is XAG9, whose value is 80 mV more cathodic than the reference commercial Pt EC20, gaining 20 mV if compared to FAG9 sample. Even though the onset values are worse if compared to Pt EC20 one, it can be stated that all the material are satisfying catalysts for ORR in acidic conditions.

Sample	ORR onset potential / V (vs AgAgCl)	n. of electrons	|Tafel slopes|* / mV	|Tafel slopes|** / mV
FAG9	0.550	4.11 ± 0.07	30.1 ± 0.3	60.5 ± 0.3
GAG9	0.550	4.3 ± 0.2	30.9 ± 0.9	67.4 ± 0.9
XAG9	0.570	3.8 ± 0.1	30.3 ± 0.4	73.0 ± 0.4
Pt EC20	0.650	4.0 ± 0.1	26 ± 0.4	52.2 ± 0.4

Tab. 3.5: $HClO_4$ 0.1 mol dm^{-3}. ORR onset potentials and calculated kinetic ORR parameters for the synthesized catalysts and reference material, Pt EC20. * Tafel slopes at lower overpotentials, ** Tafel slopes at higher overpotentials.

A deeper kinetic analysis of ORR data has been done by determining the number of transferred electrons. The number of exchanged electrons, was obtained using the Koutecky-Levich (K-L) equation from cathodic CV data recorded at different electrode rotation rates on each catalytic material, as extendedly reported before.

As shown in **Tab. 3.5**, *n* is in any case close to 4, thus permitting to conclude that all samples essentially obey the same ORR mechanism of direct H_2O formation. Focusing on the Tafel slopes column in **Tab. 3.5**, calculated in the high overpotential region, all their values are higher if compared to Pt EC20 one. Tafel data were obtained from extrapolated kinetic currents (I_k) values at many different potentials, and plotting them in Tafel *ln* I_k *vs* η (overpotential) coordinates (not reported). The same considerations on what suggested by Chlistunoff [35,36], and previously discussed, can be done. Briefly, the variability of Tafel plots for oxygen reduction reaction might be explained by an intrinsic property of the reaction mechanism or result from an incomplete catalyst utilization caused by transport and conductivity problems in the catalyst layer [35,36].

In order to better understand and evidence differences in the ORR electroactivity of the samples, polarization curves have been recorded also in alkaline media, 0.1 mol dm^{-3} KOH. Since XAG9 sample looks very promising, the curiosity was address in particular to the production of peroxides and quantify the production efficiency. An RRDE working electrode has been employed, setting the ring potential at 0.33 V (vs AgAgCl), enough to oxidize peroxide species, possibly produced. In **Fig. 3.15** are reported ORR polarization curves for the three samples FAG9, GAG9 and XAG9. For comparison, a polarization curve for a commercial Pt-based catalyst, Pt EC20 (20% Pt/C), was recorded in the same conditions. In the same figure, data from literature relative to a Pt-based catalyst by Antonietti *et al.*, has been also reported [37].

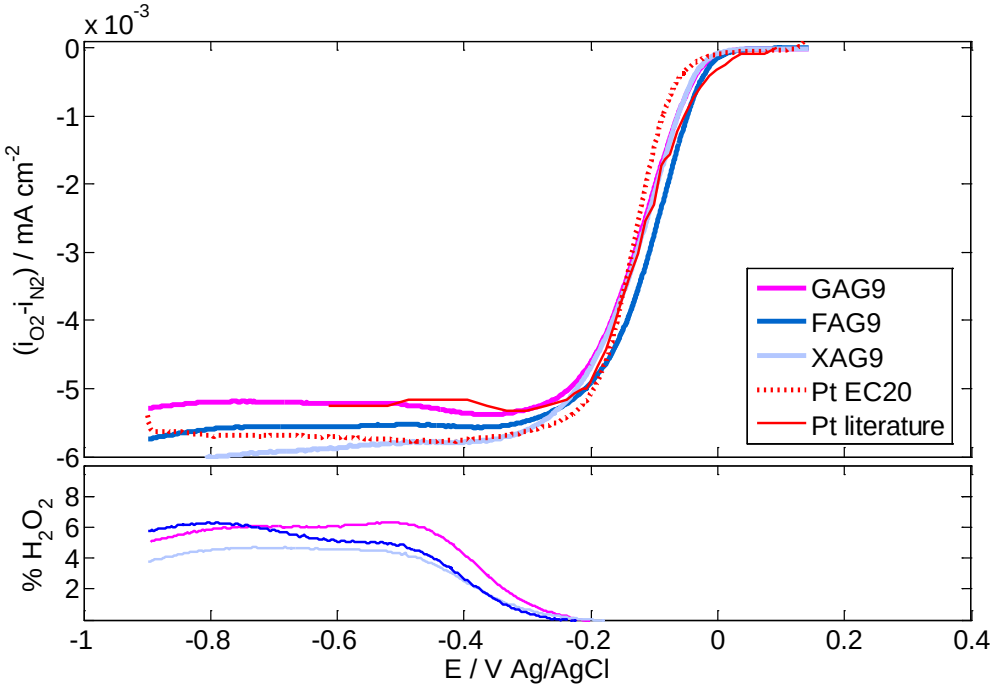

Fig. 3.15: Top: RRDE ORR polarization curves for mesoporous carbons recorded in oxygen-saturated 0.1 mol dm^{-3} KOH, ω=1600 rpm, v= 5 mV s^{-1}, T=25°C. Two reference samples from a commercial Pt-based catalyst and a literature Pt-based catalyst, are reported for comparison [37]. Bottom: Peroxide production efficiency.

As evidenced in **Fig. 3.15**, a well-defined limiting current is clearly detected for all the synthesized carbons similarly to Pt EC20 and Pt literature. The ORR electroactivity of the three samples is surprisingly higher than the reference commercial Pt EC20 material. This is the first great result. Then, even if the best sample was expected to be XAG9, due to its rewarding performances in acidic conditions, FAG9 in alkaline media was found to be the most catalytically active. Hence, the outstanding result is again relative to FAG9 sample, whose ORR onset potential (-0.01 V vs Ag/AgCl) is equal to the reference Pt literature one and even higher than Pt EC20, the commercial Pt-based catalyst. The kinetic analysis of this sample has already been discussed in the last section. As presented in **Fig. 3.15**, the ORR polarization curves of GAG9 and XAG9 materials are almost overlapping with an onset potential just 12 mV more cathodic than FAG9 value, thus demonstrating that all catalysts ORR activities towards ORR are rewarding.
As shown in **Tab. 3.6**, similarly to what observed in acidic conditions, *n* is in any case close to 4, thus permitting to conclude that all samples essentially obey the same ORR mechanism of direct H_2O formation.

Sample	ORR onset potential / V (vs AgAgCl)	n. of electrons	|Tafel slopes|* / mV	|Tafel slopes|** / mV
FAG9	-0.010	4.3 ± 0.3	20.2 ± 0.2	49.3 ± 0.4
GAG9	-0.022	3.7 ± 0.2	22 ± 0.9	36.5 ± 0.4
XAG9	-0.022	4.1 ± 0.2	25.2 ± 1	41.1 ± 0.1
Pt EC20	-0.047	4.0 ± 0.1	26.1 ± 0.4	50.1 ± 0.2

Tab. 3.6: KOH 0.1 mol dm^{-3}. ORR onset potentials and calculated kinetic ORR parameters for the synthesized catalysts and a reference material, Pt EC20. [1] Tafel slopes at lower overpotentials, [2] Tafel slopes at higher overpotentials.

Since in alkaline conditions an RRDE has been used, some more information can be derived from experimental data. First, the transferred electron number *n*, in addition to values calculated from Koutecky-Levich equation, can be evaluated for each potential values on the basis of (2), as presented above and shown now in **Fig. 3.16**.

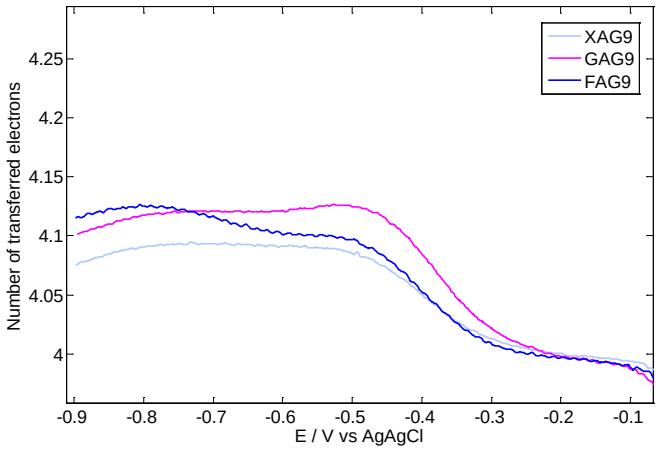

Fig. 3.16: Number of transferred electrons, calculated from (2).

Plotting the calculated *n* vs potential values, as presented in **Fig. 3.16**, it can be realized that, as expected and in agreement on what found from K-L equation, the number of transferred electrons is equal to 4, confirming a direct reduction to water for all the synthesized catalysts in alkaline conditions. From all the above results, electrocatalytical behavior towards ORR of FAG9 samples seems to be similar to the activity of commercial Pt- based catalysts. In fact, onset potential values are similar, number of transferred electrons is equal to 4 and Tafel slopes are closely similar and even better for FAG9. A further analysis of Tafel slopes and some mechanistic considerations will be discussed in the following (**3.4.3. Mechanistic considerations**).

An interesting parameter that has not been discussed yet, reported in **Fig. 3.15**, is the hydrogen peroxide production yield $\%H_2O_2$, whose value was calculated by (3) [38]. As evidenced in **Fig. 3.15**, hydrogen peroxide production increases when the disc potential decreases. The onset potential value, for which the ring current signal of $\%H_2O_2$ can be distinguished from the baseline, is about -0.25 V (vs AgAgCl) for all samples. The maximum value of $\%H_2O_2$ production, equal to 5%, is reached at about -0.4 V and remains constant until the left extreme of potential range. It is quite common a production of peroxides species around 5-10% even for very promising Pt-free catalysts [39]. FAG9, GAG9 and XAG9 are hence promising also from the point of view of yielding low quantity of peroxides species.

On the basis of previous results and the above discussion, some considerations could be done by evaluating the relations among the molecular structure of the monosaccharide used precursors and the electroactivity of the final material. Being all three monosaccharides, the simplest form of carbohydrate, as the name implies, they all contain only one sugar group; thus, they can't be broken down any further.
The first point to be clarified is related to the question: why do fructose and glucose derivates catalysts products, FAG9 and GAG9, show different electrocatalytic behavior, being the chemical composition of sugars the same?

In **Fig. 3.17** is reported the molecular structure of Glucose (GLU) and Fructose (FRU).

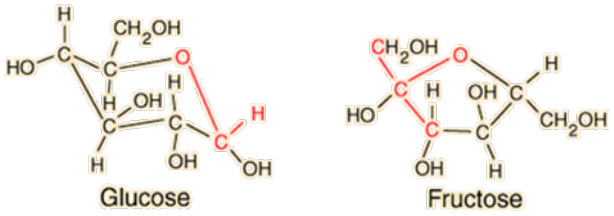

Fig. 3.17: Molecular structures of Glucose (GLU) and Fructose (FRU).

GLU and FRU have indeed the same molecular formula, $C_6H_{12}O_6$, but different structures. They are classified differently as hydrocarbon derivatives, glucose being classified as an aldehyde and fructose as a ketone. The sugars differ in the bond environment of the oxygen atom in the sugar. The differences in the functional groups can be seen more clearly in the linear forms below in **Fig. 3.18**.

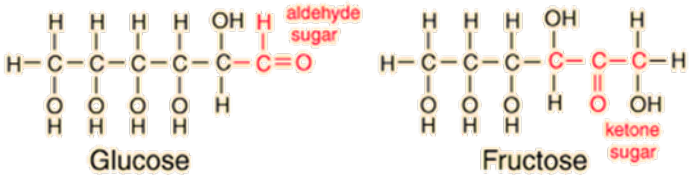

Fig. 3.18: Fisher projections of Glucose (GLU) and Fructose (FRU).

When they form a hemiacetal (ring), a 6-membered ring is formed in glucose (pyranose) with one CH_2OH group while for fructose a 5-membered ring (furanose) with two CH_2OH groups is obtained. They are constitutional isomers. This structure features imply some differences in the physico-chemical properties of FRU and GLU: for example, FRU melting point is 103°C, GLU melting point is 146 °C.

Provided that the reactions happening between precursors at the high temperatures used (600°C and then 900°C) are difficult to be rationalized and unequivocally identified, the structure differences between GLU and FRU, even if very slight, are the only one that can be responsible of the final differences in the end materials. However, a clarification whether the reactions in the starting precursors solution, prepared at room temperature, or those ones happening during heat treatments are responsible of final changes in FAG9 and GAG9, is still missing.

An XRPD analysis was recorded on FAG9 and GAG9 sample, with the aim of possibly identify any difference in the crystalline structure of materials. In **Fig. 3.19** XRPD patterns are reported.

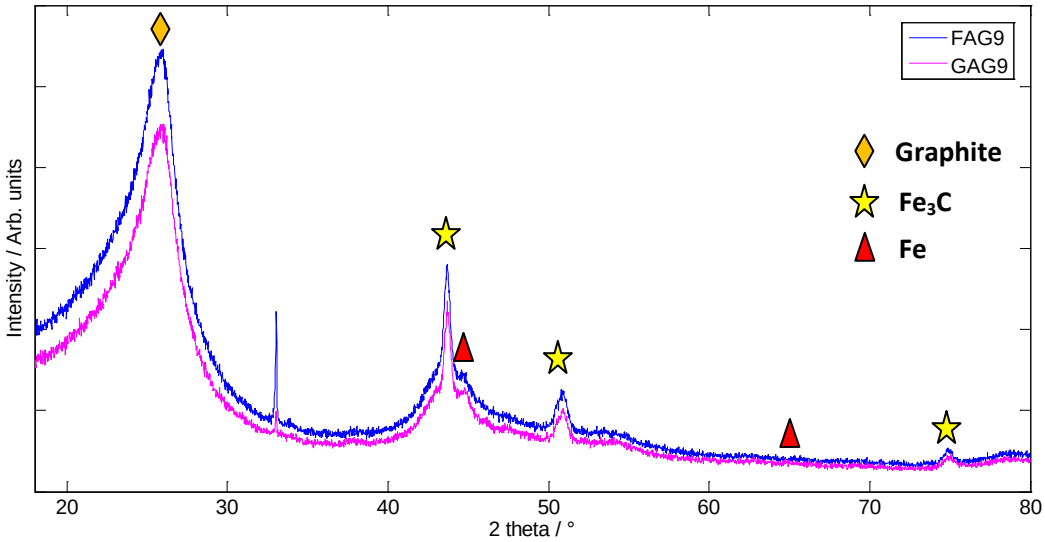

Fig. 3.19: XRPD pattern of GAG9 (pink) and FAG9 (blue).

The peaks at 2θ = 44.7° and 65.0° (not clearly identifiable) are assigned to the (110) and (200) reflections of α-Fe, respectively (PDF#00-006-0696); the peak at 26.4° is assigned to the (002) reflection of graphite (PDF#00-041-1487); the remaining peaks compare well to those of the iron carbide (Fe_3C) pattern (PDF#00-035-0772). The formation of Fe^0 and Fe_3C is often observed after pyrolysis of organic compounds in the presence of iron salts and are the result

of carbothermal reduction and thermal decomposition of iron oxides [41-43]. The carbon phase undergoes graphitization, as indicated by the appearance of a strong reflection characteristic of graphite.
However, all the above considerations are not useful when trying to discern between two samples GAG9 and FAG9, whose XRPD actually overlap. From the structural point of view, samples are identical.

Some more information, more specific on what concerns the surface, were obtained by XPS analysis. In **Tab. 3.7** are presented XPS atomic percentages relative to FAG9 and GAG9 materials.

	XPS		
	C %	**O %**	**N %**
FAG9	93.2	2.8	4.0
GAG9	92.5	2.9	4.6

Tab. 3.7: Sample composition: atomic percent from XPS.

From a comparison between GAG9 and FAG9 surface atomic composition, no evident differences can be detected. Iron was not detected in both analyzed samples.
In **Fig. 3.20** and **Fig. 3.21** are reported results by recording XPS spectra in the high resolution regions of C1s, O1s and N1s of samples FAG9 and GAG9, respectively. The surveys are also presented.

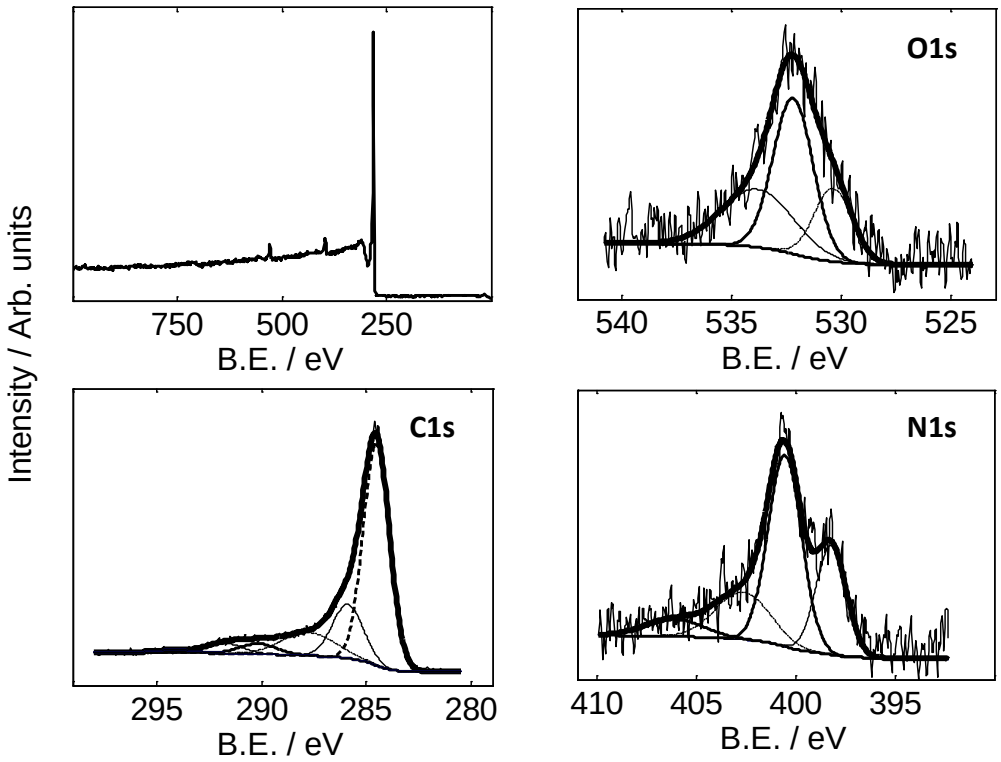

Fig. 3.20: Survey (top left) and High Resolution XP spectra of sample GAG9 in the C1s, N1s and O1s regions.

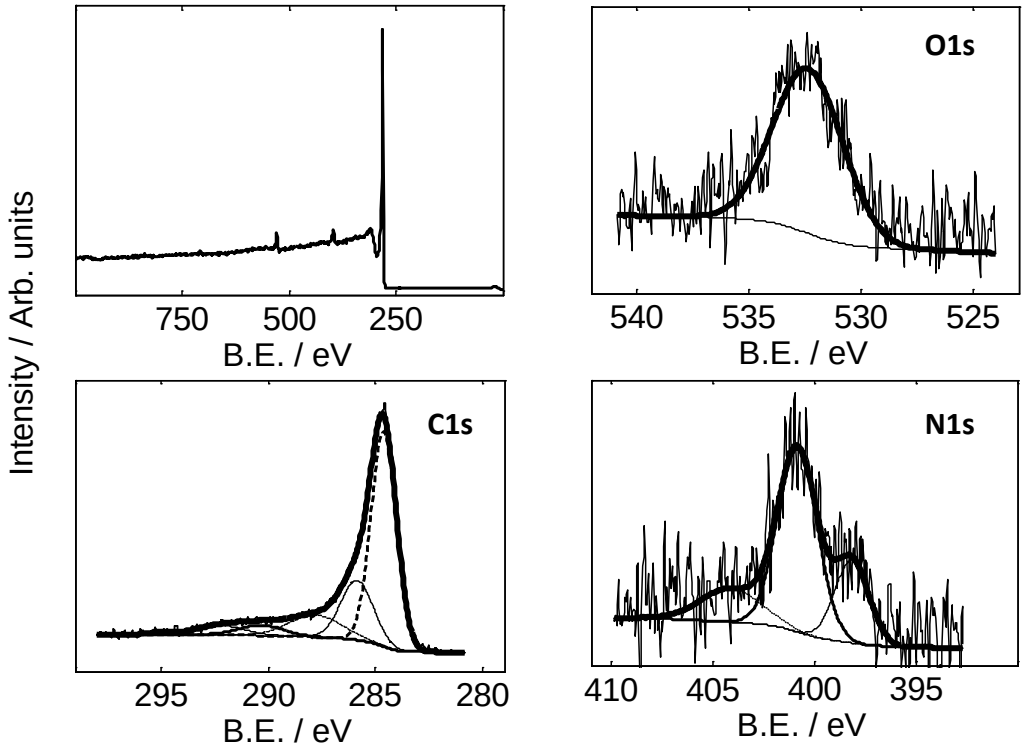

Fig. 3.21: Survey (top left) and High Resolution XP spectra of sample FAG9 in the C1s, N1s and O1s regions.

The C1s region of both FAF9 and GAG9 materials is, as expected, the richest in contributions from sp^2 carbon (~284.6 eV), sp^3 carbon (~286 eV) and the other peaks at higher binding energies are attributable to oxygenated species on the surface. By calculating the relative ratio between sp^3 and sp^2 peak areas, a parameter related to the graphitization degree can be achieved [44-48].

The graphitization degree is equal to 30% for both sample, meaning that the final annealing treatment at 900°C, satisfyingly graphitized the materials, likely improving their conductivity.

The high resolution N1s region has been deconvoluted as shown in **Fig. 3.20** and **Fig. 3.21**; the two main peaks are attributable to pyridinic nitrogen (~398 eV) and pyrrolic/pyridonic nitrogen (~400.4 eV), peaks at higher binding energies are assigned to N-O contributions (~403 eV) and shake up satellites (~406 eV) [45]. Just slight differences between samples might be found by calculating pyridinic and pyrrolic peak areas ratio; this value is equal to 50% for GAG9 and 40% for FAG9, meaning an increased percentage of pyridinic nitrogen in the first material, that is also the worst in ORR. However, both pyridinic and pyrrolic nitrogen, depending on their coordination with the metal center, are found in the literature to be part of active catalytic sites in ORR.

GAG9 O1s region was deconvoluted in three peaks (**Fig. 3.20**), with a main component maximum being attributable to oxygen-carbon single bonds (532.5 eV), a secondary one instead to double-bonded oxygen-carbon (B.E. 530.5 eV) and a third one attributable to adsorbed water (B.E. 534 eV) [46].

It was found impossible, due to the very high noise, to deconvolute the FAG9 O1s region (**Fig. 3.21**) into more than one only peak, with the maximum at 532.5 eV, corresponding to the main contribution in the spectrum of the latter sample GAG9.

Again, the above considerations are not useful when trying to discern between two samples GAG9 and FAG9, due to almost similar compositional surface features. More information, specifically focused onto the metal center and its coordination with N-moieties are needed to clarify differences in ORR performances of samples GAG9 and FAG9. Mössbauer spectroscopy, for instance, could help for the purpose. It is an analytical technique that have proven to be extremely useful for the characterization of Fe-based ORR-catalysts [49].
This spectroscopy is indeed very sensitive to the immediate structural and chemical neighborhood of the probed Fe atom in the materials. Moreover, it can distinguish between various Fe-sites of similar structure but in different oxidation and/or spin states. In perspective, performing this technique, is the following and fundamental step.

On what concerns xylose-derived sample XAG9, its differences from GAG9 and FAG9 are easier to be (at least) guessed because, differently from GLU and FRU, it contains five carbon atoms and includes a formyl functional group. As shown in **Fig. 3.22 A-D**, the cyclic hemiacetal isomers are more prevalent in solution and are of two types: the pyranoses, which feature six-membered C_5O rings, and the furanoses, which feature five-membered C_4O rings (with a pendant CH_2OH group). Each of these rings undergoes further isomerism, depending on the relative orientation of the anomeric hydroxyl group.

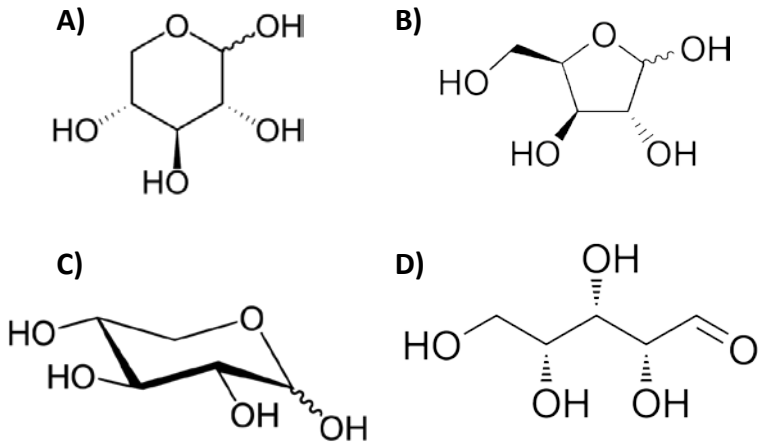

Fig. 3.22 A-D: A) D-Xylopyranose, B) Xylofuranose, C) Xylose chair, D) Xylose linear.

Having 5 carbon atoms, instead of 6, like GLU and FRU, the ratio N/C increses in XAG sample rather than FAG and GAG ones. It is known from the literature that an increased nitrogen content in the final sample is able to enhance the ORR electroactivity. Hence, it is not surprising that XAG9 has rewarding performances in ORR.

Some analyses on XAG sample are still missing, e.g. XPS and XRPD, which could help to better understand the structural and surface feature of sample and compared them to samples of the same series (FAG and GAG) with the aim of discovering possibly any relation between the precursors composition/structure and the final ORR electroactivity.

In conclusion, in the last section it was found out that FAG9 sample, prepared starting from fructose and guanidine acetate, has an outstanding electroactivity. Here, even by

substituting fructose with glucose or xylose, FAG9 sample was confirmed to be the most active in alkaline media. Instead, in acidic media XAG9 catalyst, prepared replacing fructose with xylose, surprisingly shows a better ORR electroactivity than FAG9 sample.

3.4.3. Mechanistic considerations

Even if some authors state that metal center is not necessary to promote and initiate the oxygen reduction reaction [50] many reports point out unequivocally the importance of metal-nitrogen coordinated sites [51].

The oxygen reduction reaction mechanism has been the subject of many studies over the past century. The very strong irreversibility of the cathodic process in aqueous solutions has limited the information which can be obtained from electrochemical kinetic studies about the pathway, the reaction orders etc.
To discriminate between proposed mechanism and to identify the real path for investigated catalysts it is important to have available diagnostic criteria for each mechanism. The most often determined kinetic parameters in mechanism studies are:

- Tafel slope: $\left(\frac{\partial \Delta\eta}{\partial \ln i}\right)$
- Symmetry factors: $\alpha, \beta, \gamma, \ldots$
- Reaction order: $\left(\frac{\partial \ln i}{\partial \ln p_{O_2}}\right)\left(\frac{\partial \ln i}{\partial 2.3pH}\right)$

These parameters are obtained from mechanistic considerations applied on each single step of a specific mechanism. Since in these pathways adsorbed species are involved, it is necessary to consider different types of adsorption isotherms in the derivation of diagnostic parameters. Usually, Langmuir, for low or very high coverage, and Temkin-type isotherm, for intermediates, are taken in account.

In the following it is reported an example of the determination of kinetic parameters applied to reaction mechanism proposed by Mukerjee *et al.* for Pt-free catalysts. The reaction mechanism is displayed in **Fig. 3.23**. By employing a combination of in situ X-ray spectroscopy and electrochemical methods, Mukerjee identified the various structural and functional forms of the active centers in Fe/N/C catalysts. Both methods confirm the single site $2e^- \times 2e^-$ mechanism in alkaline media on the primary Fe^{2+}-N_4 centers and the dual-site $2e^- \times 2e^-$ mechanism in acid media with the significant role of the surface bound coexisting Fe/Fe_xO_y nanoparticles as secondary active sites [52].

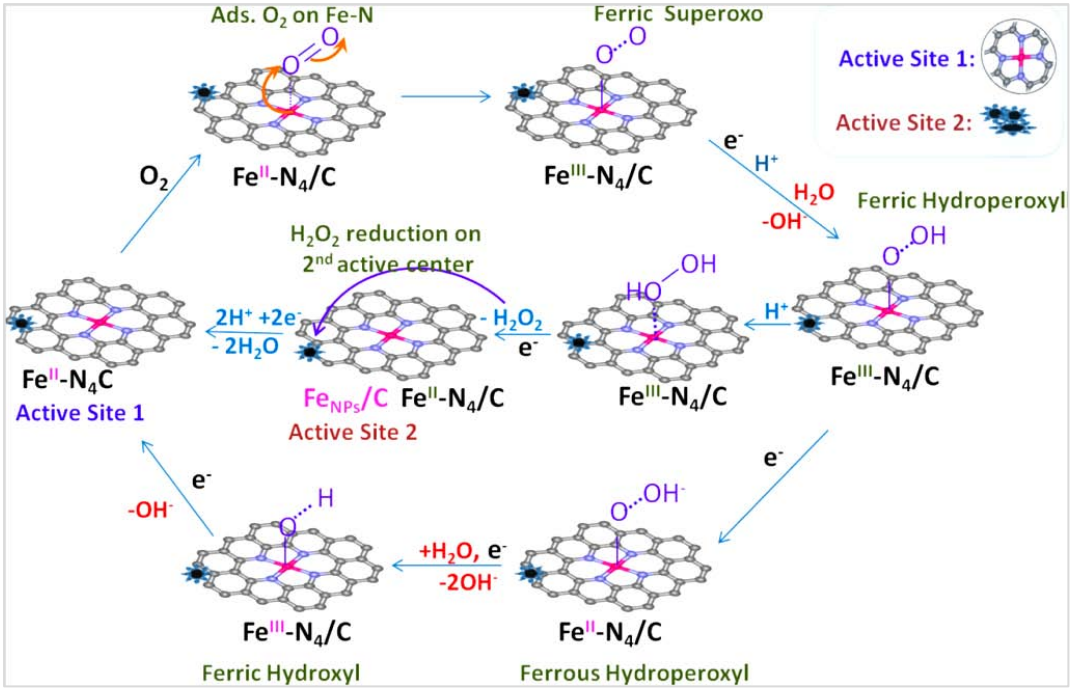

Fig. 3.23: Proposed ORR mechanistic pathways on Fe-N_4/C and adjacent Fe_{NPs}/C in acidic and alkaline electrolyte [52].

The authors verified that independently from the variety of precursors and their synthetic methods used, the final activation step by high temperature annealing, leads to similar ORR active metal centers on carbonaceous surfaces: iron cations coordinated by pyridinic nitrogen atoms (in agreement on Fe-N_4/C sites, earlier proposed) and very stable forms of metal nanoparticles (Fe_{NPs}/C).

The Fe-N_4 centers (sometimes defined as Fe-N_{2+2}) show redox features at potentials close to thermodynamic potential of ORR. This is the main reason for the rewarding ORR activity of this type of sites where the Fe center should be in oxidation state "+2" to ensure optimal active sites for ORR processes.

In both alkaline and acidic media, the Fe-N site is involved in the ORR initiation process of O_2 adsorption on the Fe^{2+}–N_4 site. In alkaline solution the electroreduction of HO_2^- intermediate proceeds on the same initial Fe^{2+}–N_4 active center to yield the overall $4e^-$ ORR mechanism. On the contrary, in acid media the H_2O_2 intermediate needs a secondary active sites, in this case Fe_{NPs}/C, which is situated at close proximity to the primary Fe–N_4 centers to ensure the subsequent reduction to the $4e^-$ product or else the peroxide intermediate desorbs into electrolyte resulting in only an overall $2e^-$ ORR mechanism. The detailed form of these active iron nanoparticles is not yet well understood and their detailed function however is still under question. It is possible that the metal particles act as dopants, which change electronic structure of the neighboring atoms, perhaps carbon or nitrogen, activating the last toward oxygen reduction.

A deep mechanistic study is presented in the following sections by considering the ORR reaction mechanism proposed by Mukerjee and co-workers for Pt-free catalysts [52].

3.4.3.1 Alkaline media

For sake of clarity, in the following, when considering a generic reaction *i*:

$$Ox + ne^- \rightarrow Red$$

the current density for the reduction reaction is: $\vec{i_i} = F \cdot \vec{k_i} \cdot e^{(-(1-\beta)\frac{F\eta}{nRT})}$; the direct reaction is considered the oxidation reaction.

By writing schematically the reaction mechanism proposed by Mukerjee in alkaline conditions, here are the reaction steps:

1) $Fe(II) - OH^- + O_2 \rightleftarrows Fe(II) - O_{2\,ads} + OH^-$

2) $Fe(II) - O_{2\,ads} \rightleftarrows Fe(III) - O - O$

3) $Fe(III) - O - O + H_2O + e^- \rightleftarrows Fe(III) - O - O - H + OH^-$

4) $Fe(III) - O - O - H + e^- \rightleftarrows Fe(II) - O - OH^-$

5) $Fe(II) - O - OH^- + H_2O + e^- \rightleftarrows Fe(III) - OH + 2OH^-$

6) $Fe(III) - OH + e^- \rightleftarrows Fe(II) - OH^-$

<u>Diagnostic parameters for Langmuir adsorption conditions:</u>

In the presence of an "ideal" oxygen adsorption, either low or high coverage, a Langmuir type isotherm is used. Kinetic equations for Mukerjee's mechanism [52] become:

(For simplification: $\theta_1 = \theta_{Fe(II)-OH}$, $\theta_2 = \theta_{Fe(II)-O_2}$, $\theta_3 = \theta_{Fe(III)-O-O}$, $\theta_4 = \theta_{Fe(III)-O-OH}$, $\theta_5 = \theta_{Fe(II)-OOH^-}$, $\theta_6 = \theta_{Fe(III)-OH}$)

$$\vec{i_1} = F \cdot \vec{k_1} \cdot \theta_1 \cdot p_{O_2}$$
$$\overleftarrow{i_1} = F \cdot \overleftarrow{k_1} \cdot \theta_2 \cdot c_{OH^-}$$

$$\vec{i_2} = F \cdot \vec{k_2} \cdot \theta_2$$
$$\overleftarrow{i_2} = F \cdot \overleftarrow{k_2} \cdot \theta_3$$

$$\vec{i_3} = F \cdot \vec{k_3} \cdot \theta_3 \cdot e^{(-(1-\beta)\frac{F\eta}{RT})}$$
$$\overleftarrow{i_3} = F \cdot \overleftarrow{k_3} \cdot \theta_4 \cdot c_{OH^-} \cdot e^{(\frac{\beta F\eta}{RT})}$$

$$\vec{i_4} = F \cdot \vec{k_4} \cdot \theta_4 \cdot e^{(-(1-\gamma)\frac{F\eta}{RT})}$$

$$\overleftarrow{i_4} = F \cdot \overleftarrow{k_4} \cdot \theta_5 \cdot e^{(\frac{\gamma F\eta}{RT})}$$

$$\vec{i_5} = F \cdot \vec{k_5} \cdot \theta_5 \cdot e^{(-(1-\delta)\frac{F\eta}{RT})}$$

$$\overleftarrow{i_5} = F \cdot \overleftarrow{k_5} \cdot \theta_6 \cdot c_{OH^-}{}^2 \cdot e^{(\frac{\delta F\eta}{RT})}$$

$$\vec{i_6} = F \cdot \vec{k_6} \cdot \theta_6 \cdot e^{(-(1-\omega)\frac{F\eta}{RT})}$$

where: $\vec{i_i}$ and $\overleftarrow{i_i}$ are the current densities for the forward and backward reaction, respectively; $\vec{k_i}$ and $\overleftarrow{k_i}$ are the constant rates for the forward and backward reaction, respectively; β, γ, δ, ω are the charge transfer symmetry factors; θ is the surface coverage; η is the overpotential; *F, R* and *T* have the usual meaning.
In the following are calculated the diagnostic parameters by assuming that each step corresponds to the rate determining step (RDS) of the overall reaction.

• THE RDS IS THE FIRST STEP:

For low coverage, $\theta \to 0$

$$\vec{i_1} = F \cdot \vec{k_1} \cdot \theta_1 \cdot p_{O_2}$$

$$\ln \vec{i_1} = \cos t + \ln p_{O_2} + \ln \theta_1$$

$$\left(\frac{\partial \Delta\eta}{\partial \ln i}\right)_{p_{O_2}} = \infty \qquad \left(\frac{\partial \ln i}{\partial \ln p_{O_2}}\right) = 1 \qquad \left(\frac{\partial \ln i}{\partial (2.3pH)}\right) = 0$$

For high coverage, $\theta \to 1$

$$\vec{i_1} = F \cdot \vec{k_1} \cdot p_{O_2}$$

$$\ln \vec{i_1} = \cos t + \ln p_{O_2}$$

$$\left(\frac{\partial \Delta\eta}{\partial \ln i}\right)_{p_{O_2}} = \infty \qquad \left(\frac{\partial \ln i}{\partial \ln p_{O_2}}\right) = 1 \qquad \left(\frac{\partial \ln i}{\partial (2.3pH)}\right) = 0$$

• THE RDS IS THE SECOND STEP:

For low coverage, $\theta \to 0$ and on the quasi-equilibrium hypothesis:

$$\vec{i_2} = F \cdot \vec{k_2} \cdot \theta_2$$
$$F \cdot \vec{k_1} \cdot \theta_1 \cdot p_{O_2} = F \cdot \overleftarrow{k_1} \cdot \theta_2 \cdot c_{OH^-}$$
$$\theta_2 = \frac{\vec{k_1}}{\overleftarrow{k_1}} \cdot \theta_1 \cdot \frac{p_{O_2}}{c_{OH^-}}$$

$$\vec{i_2} = F \cdot \vec{k_2} \cdot \frac{\vec{k_1}}{\overleftarrow{k_1}} \cdot \theta_1 \cdot \frac{p_{O_2}}{c_{OH^-}}$$

$$\ln \vec{i_2} = \cos t + \ln p_{O_2} + \cos t + \ln \theta_1 - \ln c_{OH^-}$$

$$c_{OH^-} \cdot c_{H^+} = k_w$$
$$\ln c_{OH^-} = -\ln c_{H^+} + \ln k_w$$
$$\ln c_{H^+} = 2.3 \cdot \log c_{H^+} = -2.3 \cdot pH$$

$$\left(\frac{\partial \Delta\eta}{\partial \ln i}\right)_{p_{O_2}} = \infty \qquad \left(\frac{\partial \ln i}{\partial \ln p_{O_2}}\right) = 1 \qquad \left(\frac{\partial \ln i}{\partial (2.3pH)}\right) = -1$$

For high coverage, $\theta \to 1$

$$\vec{i_2} = F \cdot \vec{k_2}$$

$$\left(\frac{\partial \Delta\eta}{\partial \ln i}\right)_{p_{O_2}} = \infty \qquad \left(\frac{\partial \ln i}{\partial \ln p_{O_2}}\right) = 0 \qquad \left(\frac{\partial \ln i}{\partial (2.3pH)}\right) = 0$$

• THE RDS IS THE THIRD STEP:

For low coverage, $\theta \to 0$ and on the quasi-equilibrium hypothesis:

$$\vec{i_3} = F \cdot \vec{k_3} \cdot \theta_3 \cdot e^{(-(1-\beta)\frac{F\eta}{RT})}$$
$$F \cdot \vec{k_2} \cdot \theta_2 = F \cdot \overleftarrow{k_2} \cdot \theta_3$$
$$\theta_3 = \frac{\vec{k_2}}{\overleftarrow{k_2}} \cdot \theta_2 = \frac{\vec{k_1}}{\overleftarrow{k_1}} \cdot \theta_1 \cdot pO_2 \cdot c_{OH^-}^{-1}$$

$$\vec{i_3} = F \cdot \vec{k_3} \cdot \frac{\vec{k_2}}{\overleftarrow{k_2}} \cdot \frac{\vec{k_1}}{\overleftarrow{k_1}} \cdot \theta_1 \cdot pO_2 \cdot c_{OH^-}{}^{-1} \cdot e^{(-(1-\beta)\frac{F\eta}{RT})}$$

$$\ln \vec{i_3} = \cos t + \ln \theta_1 + \ln pO_2 - \ln c_{OH^-} - (1-\beta)\frac{F\eta}{RT}$$

$$\ln \vec{i_3} = \cos t + \ln \theta_1 + \ln pO_2 - 2.3 \cdot pH - (1-\beta)\frac{F\eta}{RT}$$

$$\left(\frac{\partial \Delta\eta}{\partial \ln i}\right)_{p_{O_2}} = -\frac{RT}{(1-\beta)F} \qquad \left(\frac{\partial \ln i}{\partial \ln p_{O_2}}\right) = 1 \qquad \left(\frac{\partial \ln i}{\partial (2.3pH)}\right) = -1$$

For high coverage, $\theta \to 1$

$$\vec{i_3} = F \cdot \vec{k_3} \cdot e^{(-(1-\beta)\frac{F\eta}{RT})}$$

$$\ln \vec{i_3} = \cos t - (1-\beta)\frac{F\eta}{RT}$$

$$\left(\frac{\partial \Delta\eta}{\partial \ln i}\right)_{p_{O_2}} = -\frac{RT}{(1-\beta)F} \qquad \left(\frac{\partial \ln i}{\partial \ln p_{O_2}}\right) = 0 \qquad \left(\frac{\partial \ln i}{\partial (2.3pH)}\right) = 0$$

- **THE RDS IS THE FOURTH STEP:**

For low coverage, $\theta \to 0$ and on the quasi-equilibrium hypothesis:

$$\vec{i_4} = F \cdot \vec{k_4} \cdot \theta_4 \cdot e^{(-(1-\gamma)\frac{F\eta}{RT})}$$

$$F \cdot \vec{k_3} \cdot \theta_3 \cdot e^{(-(1-\beta)\frac{F\eta}{RT})} = F \cdot \overleftarrow{k_3} \cdot \theta_4 \cdot c_{OH^-} \cdot e^{(\frac{\beta F\eta}{RT})}$$

$$\theta_4 = \frac{\vec{k_3}}{\overleftarrow{k_3}} \cdot \theta_3 \cdot c_{OH^-}{}^{-1} \cdot e^{([-(1-\beta)-\beta]\frac{F\eta}{RT})}$$

$$\theta_4 = \frac{\vec{k_3}}{\overleftarrow{k_3}} \cdot \frac{\vec{k_2}}{\overleftarrow{k_2}} \cdot \frac{\vec{k_1}}{\overleftarrow{k_1}} \cdot \theta_1 \cdot p_{O_2} \cdot c_{OH^-}{}^{-2} \cdot e^{(-\frac{F\eta}{RT})}$$

$$\vec{i_4} = F \cdot \vec{k_4} \frac{\vec{k_3}}{\overleftarrow{k_3}} \cdot \frac{\vec{k_2}}{\overleftarrow{k_2}} \cdot \frac{\vec{k_1}}{\overleftarrow{k_1}} \cdot \theta_1 \cdot p_{O_2} \cdot c_{OH^-}{}^{-2} \cdot e^{(-\frac{F\eta}{RT} - (1-\gamma)\frac{F\eta}{RT})}$$

$$\ln \vec{i_4} = \cos t + \ln \theta_1 + \ln p_{O_2} - 2\ln c_{OH^-} - (2-\gamma)\,\frac{F\eta}{RT}$$

$$\left(\frac{\partial \Delta\eta}{\partial \ln i}\right)_{p_{O_2}} = -\frac{RT}{(2-\gamma)F} \qquad \left(\frac{\partial \ln i}{\partial \ln p_{O_2}}\right) = 1 \qquad \left(\frac{\partial \ln i}{\partial (2.3pH)}\right) = -2$$

For high coverage, $\theta \to 1$

$$\vec{i_4} = F \cdot \vec{k_4} \cdot e^{(-(1-\gamma)\frac{F\eta}{RT})}$$

$$\ln \vec{i_4} = \cos t - (1-\gamma)\frac{F\eta}{RT}$$

$$\left(\frac{\partial \Delta\eta}{\partial \ln i}\right)_{p_{O_2}} = -\frac{RT}{(1-\gamma)F} \qquad \left(\frac{\partial \ln i}{\partial \ln p_{O_2}}\right) = 0 \qquad \left(\frac{\partial \ln i}{\partial (2.3pH)}\right) = 0$$

- **THE RDS IS THE FIFTH STEP:**

For low coverage, $\theta \to 0$ and on the quasi-equilibrium hypothesis:

$$\vec{i_5} = F \cdot \vec{k_5} \cdot \theta_5 \cdot e^{(-(1-\delta)\frac{F\eta}{RT})}$$

$$F \cdot \vec{k_4} \cdot \theta_4 \cdot e^{(-(1-\gamma)\frac{F\eta}{RT})} = F \cdot \overleftarrow{k_4} \cdot \theta_5 \cdot e^{(\frac{\gamma F\eta}{RT})}$$

$$\theta_5 = \frac{\vec{k_4}}{\overleftarrow{k_4}} \cdot \theta_4 \cdot e^{(-\frac{F\eta}{RT})}$$

$$\theta_5 = \frac{\vec{k_4}}{\overleftarrow{k_4}} \cdot \frac{\vec{k_3}}{\overleftarrow{k_3}} \cdot \frac{\vec{k_2}}{\overleftarrow{k_2}} \cdot \frac{\vec{k_1}}{\overleftarrow{k_1}} \cdot \theta_1 \cdot p_{O_2} \cdot c_{OH^-}{}^{-2} \cdot e^{(-\frac{F\eta}{RT})} \cdot e^{(-\frac{F\eta}{RT})}$$

$$\vec{i_5} = F \cdot \vec{k_5} \frac{\vec{k_4}}{\overleftarrow{k_4}} \cdot \frac{\vec{k_3}}{\overleftarrow{k_3}} \cdot \frac{\vec{k_2}}{\overleftarrow{k_2}} \cdot \frac{\vec{k_1}}{\overleftarrow{k_1}} \cdot \theta_1 \cdot p_{O_2} \cdot c_{OH^-}{}^{-2} \cdot e^{(-\frac{F\eta}{RT})} \cdot e^{(-\frac{F\eta}{RT})} \cdot e^{(-(1-\delta)\frac{F\eta}{RT})}$$

$$\ln \vec{i_5} = \cos t + \ln \theta_1 + \ln p_{O_2} - 2\ln c_{OH^-} + [-(1-\delta)-2] \cdot \frac{F\eta}{RT}$$

$$\left(\frac{\partial \Delta\eta}{\partial \ln i}\right)_{p_{O_2}} = -\frac{RT}{(3-\delta)F} \qquad \left(\frac{\partial \ln i}{\partial \ln p_{O_2}}\right) = 1 \qquad \left(\frac{\partial \ln i}{\partial (2.3pH)}\right) = -2$$

For high coverage, $\theta \to 1$

$$\vec{i_5} = F \cdot \vec{k_5} \cdot e^{(-(1-\delta)\frac{F\eta}{RT})}$$

$$\ln \vec{i_5} = \cos t - (1-\delta)\frac{F\eta}{RT}$$

$$\left(\frac{\partial \Delta\eta}{\partial \ln i}\right)_{p_{O_2}} = -\frac{RT}{(1-\delta)F} \qquad \left(\frac{\partial \ln i}{\partial \ln p_{O_2}}\right) = 0 \qquad \left(\frac{\partial \ln i}{\partial (2.3pH)}\right) = 0$$

• **THE RDS IS THE SIXTH STEP:**

For low coverage, $\theta \to 0$ and on the quasi-equilibrium hypothesis:

$$\vec{i}_6 = F \cdot \vec{k}_6 \cdot \theta_6 \cdot e^{(-(1-\omega)\frac{F\eta}{RT})}$$

$$F \cdot \vec{k}_5 \cdot \theta_5 \cdot e^{(-(1-\delta)\frac{F\eta}{RT})} = F \cdot \overleftarrow{k}_5 \cdot \theta_6 \cdot {c_{OH^-}}^2 \cdot e^{(\frac{\delta F\eta}{RT})}$$

$$\theta_6 = \frac{\vec{k}_5}{\overleftarrow{k}_5} \cdot \theta_5 \cdot {c_{OH^-}}^{-2} \cdot e^{(-\frac{F\eta}{RT})}$$

$$\theta_6 = \frac{\vec{k}_5}{\overleftarrow{k}_5} \cdot \frac{\vec{k}_4}{\overleftarrow{k}_4} \cdot \frac{\vec{k}_3}{\overleftarrow{k}_3} \cdot \frac{\vec{k}_2}{\overleftarrow{k}_2} \cdot \frac{\vec{k}_1}{\overleftarrow{k}_1} \cdot \theta_1 \cdot p_{O_2} \cdot {c_{OH^-}}^{-4} \cdot e^{(-3\frac{F\eta}{RT})}$$

$$\vec{i}_6 = F \cdot \vec{k}_6 \cdot \frac{\vec{k}_5}{\overleftarrow{k}_5} \cdot \frac{\vec{k}_4}{\overleftarrow{k}_4} \cdot \frac{\vec{k}_3}{\overleftarrow{k}_3} \cdot \frac{\vec{k}_2}{\overleftarrow{k}_2} \cdot \frac{\vec{k}_1}{\overleftarrow{k}_1} \cdot \theta_1 \cdot p_{O_2} \cdot {c_{OH^-}}^{-4} \cdot e^{(-3\frac{F\eta}{RT})} \cdot e^{(-(1-\omega)\frac{F\eta}{RT})}$$

$$\ln \vec{i}_6 = \cos t + \ln \theta_1 + \ln p_{O_2} - 4 \ln c_{OH^-} + [-(4-\omega)] \cdot \frac{F\eta}{RT}$$

$$\left(\frac{\partial \Delta\eta}{\partial \ln i}\right)_{p_{O_2}} = -\frac{RT}{(4-\omega)F} \qquad \left(\frac{\partial \ln i}{\partial \ln p_{O_2}}\right) = 1 \qquad \left(\frac{\partial \ln i}{\partial (2.3pH)}\right) = -4$$

For high coverage, $\theta \to 1$

$$\vec{i}_6 = F \cdot \vec{k}_6 \cdot e^{(-(1-\omega)\frac{F\eta}{RT})}$$

$$\ln \vec{i}_6 = \cos t - (1-\omega)\frac{F\eta}{RT}$$

$$\left(\frac{\partial \Delta\eta}{\partial \ln i}\right)_{p_{O_2}} = -\frac{RT}{(1-\omega)F} \qquad \left(\frac{\partial \ln i}{\partial \ln p_{O_2}}\right) = 0 \qquad \left(\frac{\partial \ln i}{\partial (2.3pH)}\right) = 0$$

Diagnostic parameters for Temkin adsorption conditions:

For intermediate coverage, 0.2<θ<0.8, it is more realistic to consider a dependence of the adsorption free energy from the coverage using a Temkin-like isotherm. In this case the adsorption standard free energy, $\Delta G^0{}_\theta$, proportional to the standard free energy of activation for adsorption, is equal to:

$\Delta G^0{}_\theta = \Delta G^0{}_\theta + g\theta$

where $\Delta G^0{}_\theta$ and $\Delta G^0{}_\theta$ are the standard free energy of the adsorption corresponding to $\theta \neq 0$ and Langmuir conditions, respectively. *g* is an interaction lateral parameter. It has a negative sign when interactions between adsorbed species are attractive and positive in the opposite repulsive case. This term is strictly a free-energy parameter. Kinetic equations for Mukerjee's mechanism become:

(For simplification: $\theta_1 = \theta_{Fe(II)-OH}$, $\theta_2 = \theta_{Fe(II)-O_2}$, $\theta_3 = \theta_{Fe(III)-O-O}$, $\theta_4 = \theta_{Fe(III)-O-OH}$, $\theta_5 = \theta_{Fe(II)-OOH^-}$, $\theta_6 = \theta_{Fe(III)-OH}$)

$$\vec{i}_1 = F \cdot \vec{k}_1 \cdot \theta_1 \cdot p_{O_2} \cdot e^{(-a\frac{g\theta_1}{RT})}$$

$$\overleftarrow{i}_1 = F \cdot \overleftarrow{k}_1 \cdot \theta_2 \cdot c_{OH^-} \cdot e^{(1-a)\frac{g\theta_1}{RT} - a\frac{g\theta_2}{RT}}$$

$$\vec{i}_2 = F \cdot \overrightarrow{k_2} \cdot \theta_2 \cdot e^{(1-b)\frac{g\theta_3}{RT} - b\frac{g\theta_2}{RT}}$$

$$\overleftarrow{i}_2 = F \cdot \overleftarrow{k_2} \cdot \theta_3 \cdot e^{(1-b)\frac{g\theta_2}{RT} - b\frac{g\theta_3}{RT}}$$

$$\vec{i}_3 = F \cdot \overrightarrow{k_3} \cdot \theta_3 \cdot e^{(-(1-\beta)\frac{F\eta}{RT})} \cdot e^{(1-c)\frac{g\theta_4}{RT} - c\frac{g\theta_3}{RT}}$$

$$\overleftarrow{i}_3 = F \cdot \overleftarrow{k_3} \cdot \theta_4 \cdot c_{OH^-} \cdot e^{(\frac{\beta F\eta}{RT})} \cdot e^{(1-c)\frac{g\theta_3}{RT} - c\frac{g\theta_4}{RT}}$$

$$\vec{i}_4 = F \cdot \overrightarrow{k_4} \cdot \theta_4 \cdot e^{(-(1-\gamma)\frac{F\eta}{RT})} \cdot e^{(1-d)\frac{g\theta_5}{RT} - d\frac{g\theta_4}{RT}}$$

$$\overleftarrow{i}_4 = F \cdot \overleftarrow{k_4} \cdot \theta_5 \cdot e^{(\gamma\frac{F\eta}{RT})} \cdot e^{(1-d)\frac{g\theta_4}{RT} - d\frac{g\theta_5}{RT}}$$

$$\vec{i}_5 = F \cdot \overrightarrow{k_5} \cdot \theta_5 \cdot e^{(-(1-\delta)\frac{F\eta}{RT})} \cdot e^{(1-h)\frac{g\theta_6}{RT} - h\frac{g\theta_5}{RT}}$$

$$\overleftarrow{i}_5 = F \cdot \overleftarrow{k_5} \cdot \theta_6 \cdot c_{OH^-}{}^2 \cdot e^{(\frac{\delta F\eta}{RT})} \cdot e^{(1-h)\frac{g\theta_5}{RT} - d\frac{g\theta_6}{RT}}$$

$$\vec{i}_6 = F \cdot \overrightarrow{k_6} \cdot \theta_6 \cdot e^{(-(1-\omega)\frac{F\eta}{RT})} \cdot e^{(1-m)\frac{g\theta_7}{RT} - m\frac{g\theta_6}{RT}}$$

where: $\vec{i}_i$ and $\overleftarrow{i}_i$ are the current densities for the forward and backward reaction, respectively; $\overrightarrow{k_i}$ and $\overleftarrow{k_i}$ are the constant rates for the forward and backward reaction, respectively; $\beta, \gamma, \delta, \omega$ are the charge transfer symmetry factors; *a, b, c, d, h, m* are the adsorption symmetry factors; θ is the surface coverage; η is the overpotential; *g* is an interaction lateral parameter; *F, R* and *T* have the usual meaning.

In the following are calculated the diagnostic parameters by assuming that each step corresponds to the rate determining step (RDS) of the overall reaction.

• THE RDS IS THE FIRST STEP:

$$\vec{i}_1 = F \cdot \vec{k}_1 \cdot \theta_1 \cdot p_{O_2} \cdot e^{(-a\frac{g\theta_1}{RT})}$$

$$\ln \vec{i}_1 = \cos t + \ln p_{O_2} + \ln \theta_1 - a\frac{g\theta_1}{RT}$$

$$\left(\frac{\partial \Delta\eta}{\partial \ln i}\right)_{p_{O_2}} = \infty \qquad \left(\frac{\partial \ln i}{\partial \ln p_{O_2}}\right) = 1 \qquad \left(\frac{\partial \ln i}{\partial (2.3pH)}\right) = 0$$

• THE RDS IS THE SECOND STEP:

$$\vec{i_2} = F \cdot \vec{k_2} \cdot \theta_2 \cdot e^{(1-b)\frac{g\theta_3}{RT} - b\frac{g\theta_2}{RT}}$$

$$\ln \vec{i_2} = \cos t + \ln \theta_2 - b\frac{g\theta_2}{RT} + (1-b)\frac{g\,\theta_3}{RT}$$

$$\left(\frac{\partial \Delta\eta}{\partial \ln i}\right)_{p_{O_2}} = \infty \qquad \left(\frac{\partial \ln i}{\partial \ln p_{O_2}}\right) = 0 \qquad \left(\frac{\partial \ln i}{\partial (2.3pH)}\right) = 0$$

• THE RDS IS THE THIRD STEP:

$$\vec{i_3} = F \cdot \vec{k_3} \cdot \theta_3 \cdot e^{(-(1-\beta)\frac{F\eta}{RT})} \cdot e^{(1-c)\frac{g\theta_4}{RT} - c\frac{g\theta_3}{RT}}$$

$$\ln \vec{i_3} = \cos t + \ln \theta_3 - (1-\beta)\frac{F\eta}{RT} + (1-c)g\,\theta_4 - c\frac{g\theta_3}{RT}$$

$$\left(\frac{\partial \Delta\eta}{\partial \ln i}\right)_{p_{O_2}} = -\frac{RT}{(1-\beta)F} \qquad \left(\frac{\partial \ln i}{\partial \ln p_{O_2}}\right) = 0 \qquad \left(\frac{\partial \ln i}{\partial (2.3pH)}\right) = 0$$

• THE RDS IS THE FOURTH STEP:

$$\vec{i_4} = F \cdot \vec{k_4} \cdot \theta_4 \cdot e^{(-(1-\gamma)\frac{F\eta}{RT})} \cdot e^{(1-d)\frac{g\theta_5}{RT} - d\frac{g\theta_4}{RT}}$$

$$\ln \vec{i_4} = \cos t + \ln \theta_4 - (1-\gamma)\frac{F\eta}{RT} + (1-d)g\,\theta_5 - d\frac{g\theta_4}{RT}$$

$$\left(\frac{\partial \Delta\eta}{\partial \ln i}\right)_{p_{O_2}} = -\frac{RT}{(1-\gamma)F} \qquad \left(\frac{\partial \ln i}{\partial \ln p_{O_2}}\right) = 0 \qquad \left(\frac{\partial \ln i}{\partial (2.3pH)}\right) = 0$$

• THE RDS IS THE FIFTH STEP:

$$\vec{i_5} = F \cdot \vec{k_5} \cdot \theta_5 \cdot e^{(-(1-\delta)\frac{F\eta}{RT})} \cdot e^{(1-h)\frac{g\theta_6}{RT} - h\frac{g\theta_5}{RT}}$$

$$\ln \vec{i_5} = \cos t + \ln \theta_5 - (1-\delta)\frac{F\eta}{RT} + (1-h)g\,\theta_6 - h\frac{g\theta_5}{RT}$$

$$\left(\frac{\partial \Delta\eta}{\partial \ln i}\right)_{p_{O_2}} = -\frac{RT}{(1-\delta)F} \qquad \left(\frac{\partial \ln i}{\partial \ln p_{O_2}}\right) = 0 \qquad \left(\frac{\partial \ln i}{\partial (2.3pH)}\right) = 0$$

- **THE RDS IS THE SIXTH STEP:**

$$\vec{i_6} = F \cdot \vec{k_6} \cdot \theta_6 \cdot e^{(-(1-\omega)\frac{F\eta}{RT})} \cdot e^{(1-m)\frac{g\theta_7}{RT} - m\frac{g\theta_6}{RT}}$$

$$\ln \vec{i_6} = \cos t + \ln \theta_6 - (1-\omega)\frac{F\eta}{RT} + (1-m)g\,\theta_7 - m\frac{g\theta_6}{RT}$$

$$\left(\frac{\partial \Delta\eta}{\partial \ln i}\right)_{p_{O_2}} = -\frac{RT}{(1-\omega)F} \qquad \left(\frac{\partial \ln i}{\partial \ln p_{O_2}}\right) = 0 \qquad \left(\frac{\partial \ln i}{\partial (2.3pH)}\right) = 0$$

Assuming that all the charge transfer symmetry factors (α, β, γ, δ, ω) are equivalent, and that α=(1-β) is the charge transfer coefficient, in the following **Tab. 3.8** are summarized theoretical Tafel slopes, on the basis of Langmuir and Temkin models.

Reaction steps	Langmuir		Temkin
	$\frac{\partial \eta}{\partial \ln i}/mV$		$\frac{\partial \eta}{\partial \ln i}/mV$
	$\theta \to 0$	$\theta \to 1$	$0.2 < \theta < 0.8$
$Fe(II)-OH^- + O_2 \rightleftarrows Fe(II)-O_{2ads} + OH^-$	∞	∞	∞
$Fe(II)-O_{2ads} \rightleftarrows Fe(III)-O-O$	∞	∞	∞
$Fe(III)-O-O+H_2O+e^- \rightleftarrows Fe(III)-O-O-H+OH^-$	$-\frac{RT}{\alpha F}$	$-\frac{RT}{\alpha F}$	$-\frac{RT}{\alpha F}$
$Fe(III)-O-O-H+e^- \rightleftarrows Fe(II)-O-OH^-$	$-\frac{RT}{(1+\alpha)F}$	$-\frac{RT}{\alpha F}$	$-\frac{RT}{\alpha F}$
$Fe(II)-O-OH^- + H_2O+e^- \rightleftarrows Fe(III)-OH+2OH^-$	$-\frac{RT}{(2+\alpha)F}$	$-\frac{RT}{\alpha F}$	$-\frac{RT}{\alpha F}$
$Fe(III)-OH+e^- \rightleftarrows Fe(II)-OH^-$	$-\frac{RT}{(3+\alpha)F}$	$-\frac{RT}{\alpha F}$	$-\frac{RT}{\alpha F}$

Tab. 3.8: Theoretical Tafel slopes, on the basis of Langmuir or Temkin models, in alkaline conditions.

In alkaline conditions, for the most active samples FAG9, GAG9 and XAG9, two experimental Tafel slopes were found, depending on the overpotential region in which they were calculated. More in details, a first and a second Tafel slope are, from **Tab. 3.6** for catalysts GAG9, FAG9 and XAG9, in the range:

$$\left(\frac{\partial\eta}{\partial \ln i}/mV\right)_{low\ \eta}$$ = 20-25 mV $$\left(\frac{\partial\eta}{\partial \ln i}/mV\right)_{high\ \eta}$$ = 41-49 mV

Considering that the yellow-highlighted step in **Tab. 3.8** is the rate determining step of the reaction, the two values agree with theoretical Tafel slopes. In fact, assuming a value of α within the range 0.5-0.7 a theoretical Tafel slope for $\theta \rightarrow 0$ (low overpotential region) ≅20 mV is obtained and at higher overpotentials, where $\theta \rightarrow 1$ can be considered, theoretical Tafel slope is ≅40-50 mV.
Hence, the rate determining step in alkaline condition is the formation of the $Fe(II)-O-OH^-$ species (a ferrous hydroperoxyl species), stable in these conditions.

3.4.3.2 Acidic media

For sake of clarity, in the following, when considering a generic reaction *i*:

$$Ox + ne^- \rightarrow Red$$

the current density for the reduction reaction is: $\vec{i_i} = F \cdot \vec{k_i} \cdot e^{(-(1-\beta)\frac{F\eta}{nRT})}$; the direct reaction is considered the oxidation reaction.

By writing schematically the reaction mechanism proposed by Mukerjee[52] in acidic conditions, here are the reaction steps:

1) $Fe(II) + O_2 \rightleftarrows Fe(II) - O_{2\,ads}$

2) $Fe(II) - O_{2\,ads} \rightleftarrows Fe(III) - O - O$

3) $Fe(III) - O - O + H^+ + e^- \rightleftarrows Fe(III) - O - OH$

4) $Fe(III) - O - O - H + H^+ \rightleftarrows Fe(III) - OH - OH$

5) $Fe(III) - OH - OH + e^- \rightleftarrows Fe(II) + H_2O_2$

6) $H_2O_2 + 2H^+ + 2e^- \rightleftarrows H_2O$

Diagnostic parameters for Langmuir adsorption conditions:

In the presence of an "ideal" oxygen adsorption, either low or high coverage, a Langmuir type isotherm is used. Kinetic equations for Mukerjee's mechanism[52] become:

(For simplification: $\theta_0 = \theta_{Fe(II)}$, $\theta_1 = \theta_{Fe(II)-O_2}$, $\theta_2 = \theta_{Fe(III)-O-O}$, $\theta_3 = \theta_{Fe(III)-O-OH}$, $\theta_4 = \theta_{Fe(III)-OH-OH^-}$)

$$\vec{i_1} = F \cdot \vec{k_1} \cdot c_{Fe(II)} \cdot \theta_0 \cdot p_{O_2}$$
$$\overleftarrow{i_1} = F \cdot \overleftarrow{k_1} \cdot \theta_1$$

$$\vec{i_2} = F \cdot \vec{k_2} \cdot \theta_1$$
$$\overleftarrow{i_2} = F \cdot \overleftarrow{k_2} \cdot \theta_2$$

$$\vec{i_3} = F \cdot \vec{k_3} \cdot \theta_2 \cdot c_{H^+} \cdot e^{(-(1-\beta)\frac{F\eta}{RT})}$$
$$\overleftarrow{i_3} = F \cdot \overleftarrow{k_3} \cdot \theta_3 \cdot e^{(\frac{\beta F\eta}{RT})}$$

$$\vec{i_4} = F \cdot \vec{k_4} \cdot \theta_3 \cdot c_{H^+}$$
$$\overleftarrow{i_4} = F \cdot \overleftarrow{k_4} \cdot \theta_4$$

$$\vec{i_5} = F \cdot \vec{k_5} \cdot \theta_4 \cdot e^{(-(1-\gamma)\frac{F\eta}{RT})}$$
$$\overleftarrow{i_5} = F \cdot \overleftarrow{k_5} \cdot c_{Fe(II)^-} \cdot c_{H_2O_2} \cdot e^{(\gamma\frac{F\eta}{RT})}$$

$$\vec{i_6} = F \cdot \vec{k_6} \cdot c_{H_2O_2} \cdot c_{H^+} \cdot e^{(-2(1-\delta)\frac{F\eta}{RT})}$$

Where: $\vec{i_i}$ and $\overleftarrow{i_i}$ are the current densities for the forward and backward reaction, respectively; $\vec{k_i}$ and $\overleftarrow{k_i}$ are the constant rates for the forward and backward reaction, respectively; β, γ, δ are the charge transfer symmetry factors; θ is the surface coverage; η is the overpotential; *F, R* and *T* have the usual meaning.
In the following are calculated the diagnostic parameters by assuming that each step corresponds to the rate determining step (RDS) of the overall reaction.

- **THE RDS IS THE FIRST STEP:**

$$\vec{i_1} = F \cdot \vec{k_1} \cdot c_{Fe(II)} \cdot \theta_0 \cdot p_{O_2}$$

$$\ln \vec{i_1} = \cos t + \ln p_{O_2} + \ln \theta_0 + \ln c_{Fe(II)}$$

$$\left(\frac{\partial \Delta\eta}{\partial \ln i}\right)_{p_{O_2}} = \infty \qquad \left(\frac{\partial \ln i}{\partial \ln p_{O_2}}\right) = 1 \qquad \left(\frac{\partial \ln i}{\partial (2.3pH)}\right) = 0$$

• THE RDS IS THE SECOND STEP:

For low coverage, $\theta \to 0$ and on the quasi-equilibrium hypothesis of step 1):

$$\vec{i_2} = F \cdot \vec{k_2} \cdot \theta_1$$
$$F \cdot \vec{k_1} \cdot c_{Fe(II)} \cdot p_{O_2} = F \cdot \overleftarrow{k_1} \cdot \theta_1$$
$$\theta_1 = \frac{\vec{k_1}}{\overleftarrow{k_1}} \cdot c_{Fe(II)} \cdot p_{O_2}$$

$$\vec{i_2} = F \cdot \vec{k_2} \cdot \frac{\vec{k_1}}{\overleftarrow{k_1}} \cdot c_{Fe(II)} \cdot p_{O_2}$$

$$\ln \vec{i_2} = \cos t + \ln p_{O_2} + \ln c_{Fe(II)}$$

$$\left(\frac{\partial \Delta\eta}{\partial \ln i}\right)_{p_{O_2}} = \infty \qquad \left(\frac{\partial \ln i}{\partial \ln p_{O_2}}\right) = 1 \qquad \left(\frac{\partial \ln i}{\partial (2.3pH)}\right) = 0$$

For high coverage, $\theta \to 1$

$$\vec{i_2} = F \cdot \vec{k_2}$$

$$\left(\frac{\partial \Delta\eta}{\partial \ln i}\right)_{p_{O_2}} = \infty \qquad \left(\frac{\partial \ln i}{\partial \ln p_{O_2}}\right) = 0 \qquad \left(\frac{\partial \ln i}{\partial (2.3pH)}\right) = 0$$

• THE RDS IS THE THIRD STEP:

For low coverage, $\theta \to 0$ and on the quasi-equilibrium hypothesis:

$$\vec{i_3} = F \cdot \vec{k_3} \cdot \theta_2 \cdot c_{H^+} \cdot e^{(-(1-\beta)\frac{F\eta}{RT})}$$
$$F \cdot \vec{k_2} \cdot \theta_1 = F \cdot \overleftarrow{k_2} \cdot \theta_2$$

$$\theta_2 = \frac{\overrightarrow{k_2}}{\overleftarrow{k_2}} \cdot \theta_1 = \frac{\overrightarrow{k_1}}{\overleftarrow{k_1}} \cdot \frac{\overrightarrow{k_2}}{\overleftarrow{k_2}} \cdot c_{Fe(II)} \cdot pO_2$$

$$\vec{i_3} = F \cdot \overrightarrow{k_3} \cdot \frac{\overrightarrow{k_1}}{\overleftarrow{k_1}} \cdot \frac{\overrightarrow{k_2}}{\overleftarrow{k_2}} \cdot c_{Fe(II)} \cdot pO_2 \cdot c_{H^+} \cdot e^{(-(1-\beta)\frac{F\eta}{RT})}$$

$$\ln \vec{i_3} = \cos t + \ln c_{Fe(II)} + \ln pO_2 + \ln c_{H^+} - (1-\beta)\frac{F\eta}{RT}$$

$$\left(\frac{\partial \Delta\eta}{\partial \ln i}\right)_{p_{O_2}} = -\frac{RT}{(1-\beta)F} \qquad \left(\frac{\partial \ln i}{\partial \ln p_{O_2}}\right) = 1 \qquad \left(\frac{\partial \ln i}{\partial (2.3pH)}\right) = -1$$

For high coverage, $\theta \to 1$

$$\vec{i_3} = F \cdot \overrightarrow{k_3} \cdot c_{H^+} \cdot e^{(-(1-\beta)\frac{F\eta}{RT})}$$

$$\left(\frac{\partial \Delta\eta}{\partial \ln i}\right)_{p_{O_2}} = -\frac{RT}{(1-\beta)F} \qquad \left(\frac{\partial \ln i}{\partial \ln p_{O_2}}\right) = 0 \qquad \left(\frac{\partial \ln i}{\partial (2.3pH)}\right) = -1$$

• THE RDS IS THE FOURTH STEP:

For low coverage, $\theta \to 0$ and on the quasi-equilibrium hypothesis:

$$\vec{i_4} = F \cdot \overrightarrow{k_4} \cdot \theta_3 \cdot c_{H^+}$$

$$F \cdot \overrightarrow{k_3} \cdot \theta_2 \cdot c_{H^+} \cdot e^{(-(1-\beta)\frac{F\eta}{RT})} = F \cdot \overleftarrow{k_3} \cdot \theta_3 \cdot c_{OH^-} \cdot e^{(\frac{\beta F\eta}{RT})}$$

$$\theta_3 = \frac{\overrightarrow{k_3}}{\overleftarrow{k_3}} \cdot \theta_2 \cdot c_{H^+} \cdot e^{(-\frac{F\eta}{RT})}$$

$$\theta_3 = \frac{\overrightarrow{k_3}}{\overleftarrow{k_3}} \cdot \frac{\overrightarrow{k_2}}{\overleftarrow{k_2}} \cdot \frac{\overrightarrow{k_1}}{\overleftarrow{k_1}} \cdot c_{Fe(II)} \cdot pO_2 \cdot c_{H^+} \cdot e^{(-\frac{F\eta}{RT})}$$

$$\vec{i_4} = F \cdot \overrightarrow{k_4} \frac{\overrightarrow{k_3}}{\overleftarrow{k_3}} \cdot \frac{\overrightarrow{k_2}}{\overleftarrow{k_2}} \cdot \frac{\overrightarrow{k_1}}{\overleftarrow{k_1}} \cdot c_{Fe(II)} \cdot pO_2 \cdot {c_{H^+}}^2 \cdot e^{(-\frac{F\eta}{RT})}$$

$$\ln \vec{i_4} = \cos t + \ln c_{Fe(II)} + \ln p_{O_2} + 2\ln c_{H^+} - \frac{F\eta}{RT}$$

$$\left(\frac{\partial \Delta\eta}{\partial \ln i}\right)_{p_{O_2}} = -\frac{RT}{F} \qquad \left(\frac{\partial \ln i}{\partial \ln p_{O_2}}\right) = 1 \qquad \left(\frac{\partial \ln i}{\partial (2.3pH)}\right) = -2$$

For high coverage, $\theta \to 1$

$$\vec{i_4} = F \cdot \vec{k_4} \cdot c_{H^+}$$

$$\ln \vec{i_4} = \cos t + \ln c_{H^+}$$

$$\left(\frac{\partial \Delta\eta}{\partial \ln i}\right)_{p_{O_2}} = \infty \qquad \left(\frac{\partial \ln i}{\partial \ln p_{O_2}}\right) = 0 \qquad \left(\frac{\partial \ln i}{\partial (2.3pH)}\right) = -1$$

- **THE RDS IS THE FIFTH STEP:**

For low coverage, $\theta \to 0$ and on the quasi-equilibrium hypothesis:

$$\vec{i_5} = F \cdot \vec{k_5} \cdot \theta_4 \cdot e^{(-(1-\gamma)\frac{F\eta}{RT})}$$

$$F \cdot \vec{k_4} \cdot \theta_3 \cdot c_{H^+} = F \cdot \overleftarrow{k_4} \cdot \theta_4$$

$$\theta_4 = \frac{\vec{k_4}}{\overleftarrow{k_4}} \cdot \theta_3 \cdot c_{H^+}$$

$$\theta_4 = \frac{\vec{k_4}}{\overleftarrow{k_4}} \cdot c_{Fe(II)} \cdot p_{O_2} \cdot {c_{H^+}}^3 \cdot e^{(-\frac{F\eta}{RT})}$$

$$\vec{i_5} = F \cdot \vec{k_5} \cdot \frac{\vec{k_4}}{\overleftarrow{k_4}} \cdot c_{Fe(II)} \cdot p_{O_2} \cdot {c_{H^+}}^3 \cdot e^{(-\frac{F\eta}{RT})} \cdot e^{(-(1-\gamma)\frac{F\eta}{RT})}$$

$$\ln \vec{i_5} = \cos t + \ln c_{Fe(II)} + \ln p_{O_2} + 3\ln c_{H^+} - (2-\gamma) \cdot \frac{F\eta}{RT}$$

$$\left(\frac{\partial \Delta\eta}{\partial \ln i}\right)_{p_{O_2}} = -\frac{RT}{(2-\gamma)F} \qquad \left(\frac{\partial \ln i}{\partial \ln p_{O_2}}\right) = 1 \qquad \left(\frac{\partial \ln i}{\partial (2.3pH)}\right) = 3$$

For high coverage, $\theta \to 1$

$$\vec{i_5} = F \cdot \vec{k_5} \cdot e^{(-(1-\gamma)\frac{F\eta}{RT})}$$

$$\ln \vec{i_5} = \cos t - (1-\gamma)\frac{F\eta}{RT}$$

$$\left(\frac{\partial \Delta\eta}{\partial \ln i}\right)_{p_{O_2}} = -\frac{RT}{(1-\gamma)F} \qquad \left(\frac{\partial \ln i}{\partial \ln p_{O_2}}\right) = 0 \qquad \left(\frac{\partial \ln i}{\partial (2.3pH)}\right) = 0$$

- **THE RDS IS THE SIXTH STEP:**

$$\vec{i_6} = F \cdot \vec{k_6} \cdot c_{H_2O_2} \cdot c_{H^+} \cdot e^{(-2(1-\delta)\frac{F\eta}{RT})}$$

$$\ln \vec{i_6} = \cos t + \ln c_{H_2O_2} + 2\ln c_{H^+} - 2(1-\delta) \cdot \frac{F\eta}{RT}$$

$$\left(\frac{\partial \Delta\eta}{\partial \ln i}\right)_{p_{O_2}} = -\frac{RT}{2(1-\delta)F} \qquad \left(\frac{\partial \ln i}{\partial \ln p_{O_2}}\right) = 0 \qquad \left(\frac{\partial \ln i}{\partial (2.3pH)}\right) = -2$$

Diagnostic parameters for Temkin adsorption conditions:

For intermediate coverage, 0.2<θ<0.8, it is more realistic to consider a dependence of the adsorption free energy from the coverage using a Temkin-like isotherm. In this case the adsorption standard free energy, ΔG^0_θ, proportional to the standard free energy of activation for adsorption, is equal to:

$\Delta G^0_\theta = \Delta G^0_\theta + g\theta$

where ΔG^0_θ and ΔG^0_θ are the standard free energy of the adsorption corresponding to $\theta \neq 0$ and Langmuir conditions, respectively. *g* is an interaction lateral parameter. It has a negative sign when interactions between adsorbed species are attractive and positive in the opposite, repulsive, case. This term is strictly a free-energy parameter. Kinetic equations for Mukerjee's mechanism become:

(For simplification: $\theta_0 = \theta_{Fe(II)}$, $\theta_1 = \theta_{Fe(II)-O_2}$, $\theta_2 = \theta_{Fe(III)-O-O}$, $\theta_3 = \theta_{Fe(III)-O-OH}$, $\theta_4 = \theta_{Fe(III)-OH-OH^-}$)

$$\vec{i_1} = F \cdot \vec{k_1} \cdot p_{O_2} \cdot c_{Fe(II)} \cdot \theta_0 \cdot e^{-a\frac{g\theta_0}{RT}}$$

$$\overleftarrow{i_1} = F \cdot \overleftarrow{k_1} \cdot \theta_1 \cdot e^{(1-a)\frac{g\theta_0}{RT}} \cdot e^{-a\frac{g\theta_1}{RT}}$$

$$\vec{i_2} = F \cdot \vec{k_2} \cdot \theta_1 \cdot e^{-b\frac{g\theta_1}{RT}} \cdot e^{(1-b)\frac{g\theta_2}{RT}}$$

$$\overleftarrow{i_2} = F \cdot \overleftarrow{k_2} \cdot \theta_2 \cdot e^{-b\frac{g\theta_2}{RT}} \cdot e^{(1-b)\frac{g\theta_1}{RT}}$$

$$\vec{i_3} = F \cdot \vec{k_3} \cdot \theta_2 \cdot c_{H^+} \cdot e^{(-(1-\beta)\frac{F\eta}{RT})} \cdot e^{-c\frac{g\theta_2}{RT}} \cdot e^{(1-c)\frac{g\theta_3}{RT}}$$

$$\overleftarrow{i_3} = F \cdot \overleftarrow{k_3} \cdot \theta_3 \cdot e^{(\frac{\beta F\eta}{RT})} \cdot e^{-c\frac{g\theta_3}{RT}} \cdot e^{(1-c)\frac{g\theta_2}{RT}}$$

$$\vec{i_4} = F \cdot \vec{k_4} \cdot \theta_3 \cdot c_{H^+} \cdot e^{-d\frac{g\theta_3}{RT}} \cdot e^{(1-d)\frac{g\theta_4}{RT}}$$

$$\overleftarrow{i_4} = F \cdot \overleftarrow{k_4} \cdot \theta_4 \cdot e^{-d\frac{g\theta_4}{RT}} \cdot e^{(1-d)\frac{g\theta_3}{RT}}$$

$$\vec{i_5} = F \cdot \vec{k_5} \cdot \theta_4 \cdot e^{(-(1-\gamma)\frac{F\eta}{RT})} \cdot e^{-h\frac{g\theta_4}{RT}} \cdot e^{(1-h)\frac{g\theta_3}{RT}}$$

$$\overleftarrow{i_5} = F \cdot \overleftarrow{k_5} \cdot c_{Fe(II)^-} \cdot c_{H_2O_2} \cdot e^{(\gamma\frac{F\eta}{RT})} \cdot e^{-h\frac{g\theta_0}{RT}} \cdot e^{(1-b)\frac{g\theta_4}{RT}}$$

$$\vec{i}_6 = F \cdot \overrightarrow{k_6} \cdot c_{H_2O_2} \cdot c_{H^+} \cdot e^{(-2(1-\delta)\frac{F\eta}{RT})}$$

Where: $\vec{i}_i$ and $\overleftarrow{i}_i$ are the current densities for the forward and backward reaction, respectively; $\overrightarrow{k_i}$ and $\overleftarrow{k_i}$ are the constant rates for the forward and backward reaction, respectively; β, γ, δ are the charge transfer symmetry factors; *a, b, c, d, h, m* are the adsorption symmetry factors; θ is the surface coverage; η is the overpotential; *g* is an interaction lateral parameter; *F, R* and *T* have the usual meaning.
In the following are calculated the diagnostic parameters by assuming that each step corresponds to the rate determining step (RDS) of the overall reaction.

• THE RDS IS THE FIRST STEP:

$$\vec{i}_1 = F \cdot \vec{k}_1 \cdot p_{O_2} \cdot \theta_0 \cdot e^{-a\frac{g\theta_0}{RT}}$$

$$\ln \vec{i}_1 = \cos t + \ln p_{O_2} + \ln \theta_0 - a\frac{g\theta_0}{RT}$$

$$\left(\frac{\partial \Delta\eta}{\partial \ln i}\right)_{p_{O_2}} = \infty \qquad \left(\frac{\partial \ln i}{\partial \ln p_{O_2}}\right) = 1 \qquad \left(\frac{\partial \ln i}{\partial (2.3pH)}\right) = 0$$

• THE RDS IS THE SECOND STEP:

$$\vec{i}_2 = F \cdot \overrightarrow{k_2} \cdot \theta_1 \cdot e^{-b\frac{g\theta_1}{RT}} \cdot e^{(1-b)\frac{g\theta_2}{RT}}$$

$$\ln \vec{i}_2 = \cos t + \ln \theta_1 - b\frac{g\theta_1}{RT} + (1-b)\frac{g\theta_2}{RT}$$

$$\left(\frac{\partial \Delta\eta}{\partial \ln i}\right)_{p_{O_2}} = \infty \qquad \left(\frac{\partial \ln i}{\partial \ln p_{O_2}}\right) = 0 \qquad \left(\frac{\partial \ln i}{\partial (2.3pH)}\right) = 0$$

• THE RDS IS THE THIRD STEP:

$$\vec{i}_3 = F \cdot \overrightarrow{k_3} \cdot \theta_2 \cdot c_{H^+} \cdot e^{(-(1-\beta)\frac{F\eta}{RT})} \cdot e^{-c\frac{g\theta_2}{RT}} \cdot e^{(1-c)\frac{g\theta_3}{RT}}$$

$$\ln \vec{i}_3 = \cos t + \ln \theta_2 - (1-\beta)\frac{F\eta}{RT} + (1-c)g\,\theta_3 - c\frac{g\theta_2}{RT} + \ln c_{H^+}$$

$$\left(\frac{\partial \Delta\eta}{\partial \ln i}\right)_{p_{O_2}} = -\frac{RT}{(1-\beta)F} \qquad \left(\frac{\partial \ln i}{\partial \ln p_{O_2}}\right) = 0 \qquad \left(\frac{\partial \ln i}{\partial (2.3pH)}\right) = 1$$

- **THE RDS IS THE FOURTH STEP:**

$$\vec{i_4} = F \cdot \vec{k_4} \cdot \theta_3 \cdot c_{H^+} \cdot e^{-d\frac{g\theta_3}{RT}} \cdot e^{(1-d)\frac{g\theta_4}{RT}}$$

$$\ln \vec{i_4} = \cos t + \ln \theta_3 + (1-d) g\, \theta_4 - d\,\frac{g\theta_3}{RT} + \ln c_{H^+}$$

$$\left(\frac{\partial \Delta\eta}{\partial \ln i}\right)_{p_{O_2}} = \infty \qquad \left(\frac{\partial \ln i}{\partial \ln p_{O_2}}\right) = 0 \qquad \left(\frac{\partial \ln i}{\partial (2.3pH)}\right) = 1$$

- **THE RDS IS THE FIFTH STEP:**

$$\vec{i_5} = F \cdot \vec{k_5} \cdot \theta_4 \cdot e^{(-(1-\gamma)\frac{F\eta}{RT})} \cdot e^{-h\frac{g\theta_4}{RT}} \cdot e^{(1-h)\frac{g\theta_3}{RT}}$$

$$\ln \vec{i_5} = \cos t + \ln \theta_4 - (1-\gamma)\frac{F\eta}{RT} + (1-h) g\, \theta_3 - h\frac{g\theta_4}{RT}$$

$$\left(\frac{\partial \Delta\eta}{\partial \ln i}\right)_{p_{O_2}} = -\frac{RT}{(1-\gamma)F} \qquad \left(\frac{\partial \ln i}{\partial \ln p_{O_2}}\right) = 0 \qquad \left(\frac{\partial \ln i}{\partial (2.3pH)}\right) = 0$$

- **THE RDS IS THE SIXTH STEP:**

$$\vec{i_6} = F \cdot \vec{k_6} \cdot c_{H_2O_2} \cdot c_{H^+} \cdot e^{(-2(1-\delta)\frac{F\eta}{RT})}$$

$$\ln \vec{i_6} = \cos t + \ln c_{H_2O_2} + \ln c_{H^+} - 2(1-\delta)\frac{F\eta}{RT}$$

$$\left(\frac{\partial \Delta\eta}{\partial \ln i}\right)_{p_{O_2}} = -\frac{RT}{2(1-\delta)F} \qquad \left(\frac{\partial \ln i}{\partial \ln p_{O_2}}\right) = 0 \qquad \left(\frac{\partial \ln i}{\partial (2.3pH)}\right) = 1$$

Assuming that all the charge transfer symmetry factors (α, β, γ, δ) are equivalent, and that α=(1-β) is the transfer charge coefficient, in the following **Tab. 3.9** are summarized theoretical Tafel slopes, on the basis of Langmuir and Temkin models.

Reaction steps	Langmuir		Temkin
	$\frac{\partial\eta}{\partial \ln i} / mVdec^{-1}$		$\frac{\partial\eta}{\partial \ln i} / mVdec^{-1}$
	$\theta \to 0$	$\theta \to 1$	$0.2 < \theta < 0.8$
$Fe(II) + O_2 \rightleftarrows Fe(II) - O_{2ads}$	∞		∞
$Fe(II) - O_{2ads} \rightleftarrows Fe(III) - O - O$	∞		∞
$Fe(III) - O - O + H^+ + e^- \rightleftarrows Fe(III) - O - OH$	$-\frac{RT}{\alpha F}$	$-\frac{RT}{\alpha F}$	$-\frac{RT}{\alpha F}$
$Fe(III) - O - O - H + H^+ \rightleftarrows Fe(III) - OH - OH$	$-\frac{RT}{F}$	∞	∞
$Fe(III) - OH - OH + e^- \rightleftarrows Fe(II) + H_2O_2$	$-\frac{RT}{(1+\alpha)F}$	$-\frac{RT}{\alpha F}$	$-\frac{RT}{\alpha F}$
$H_2O_2 + 2H^+ + 2e^- \rightleftarrows H_2O$	$-\frac{RT}{2\alpha F}$		$-\frac{RT}{2\alpha F}$

Tab. 3.9: Theoretical Tafel slopes, on the basis of Langmuir or Temkin models, in acidic conditions.

In acidic conditions, for the most active samples FAG9, GAG9 and XAG9, two experimental Tafel slopes were found, depending on the overpotential region in which they were calculated. More in details, a first and a second Tafel slope are, from **Tab. 3.6** for catalysts GAG9, FAG9 and XAG9, in the range:

$$\left(\frac{\partial\eta}{\partial \ln i} / mV\right)_{low\ \eta} \cong 30\ mV \qquad \left(\frac{\partial\eta}{\partial \ln i} / mV\right)_{high\ \eta} = 60\text{-}73\ mV$$

Assuming that the yellow-highlighted steps in **Tab. 3.9** are the rate determining steps of the reaction at low and high overpotentials, the experimental values of Tafel slopes agree with theoretical ones. In fact, assuming a value of α equal to 0.35-0.42 a theoretical Tafel slope for the last step, the reduction of hydrogen peroxide onto the second catalytic site, at low coverage, is about 30 mV. At higher overpotentials, the rate determing steps becomes the fifth, the production of H_2O_2, and theoretical Tafel slope for high coverage is ≅60-73 mV. This variation of rate determining step can be justified considering that to perform the last step is necessary to have a second active center near the first one and, when the coverage is low, the distance between these sites can be high. At higher coverage this distance might be reduced and in this way the reaction becomes faster and the formation of hydrogen peroxide becomes the rate determining step.
Hence, the rate determining step in acidic condition varies with the coverage of the surface.

By summarizing results obtained comparing theoretical value of Tafel slopes and experimental ones, some important considerations can be done. Reaction mechanism in acidic and alkaline media is equivalent until the third step, in which $Fe(III)-O-OH$ is formed. Then, the reaction follows different paths because of different stability in acidic and alkaline solutions of involved species. In fact, $Fe(II)-O-OH^{-}$ is stable in alkali, but very instable in acids, therefore the "alkaline" path is not favoured in acids anymore.

3.4.4. Shifting to polysaccharides

An alternative and abundant C- and O-source is represented by polysaccharides, e.g. cellulose and starch, composed of long chains of monosaccharide, ranging in structures from linear to highly branched. A few works in the literature studied an activated carbon synthesis starting from a specific type of polysaccharide: sugarcane [53,54]. It is an interesting material, with jointed fibrous stalks that are rich in the sugar sucrose, which accumulates in the stalk internodes.
This section in focused on sugarcane as the C- and O-source in the catalysts production, without making use of the silica templating method, presented in the previous section, under the hypothesis that the fibrous structure of sugarcane might act, by itself, as a template, without the need to be, at the end, removed.

All chemicals and reagents were used as received without further purification. Guanidine acetate, iron(II) acetate, glacial acetic acid, Nafion® (5 wt. % EtOH solution), 37% hydrochloric acid, concentrated sulfuric acid and ethanol were purchased from Sigma Aldrich. KOH concentrate from Fluka was used to prepare 0.1 mol dm^{-3} solution. Sugarcane was collected in a wild forest near Rio Caura, Venezuela by myself.

During a travel in the South of America, in Venezuela, I had the feeling of nearly being pushed to bring home a piece of greenery surrounding us, while having fun with the children of our guide near Rio Caura (**Fig. 3.24**), without clearly realizing the reasons why I was doing it. That's what I actually did, letting that sticky yellow-greenish cylinder dry under the warm Venezuelan sun, protecting it from hungry bugs attack. A few weeks later, back to the lab, I cut that piece of dried sugarcane into small slices, each one half centimeter thick.

In the following are reported a few images (**Fig. 3.24**) using an optical microscope, of the Venezuelan sugarcane slices before any further treatment.

Fig. 3.24: Left: Venezuelan children, harvesting and cutting into small pieces sugarcanes. Right: Optical microscope picture of sugarcane fibers before treatments. Magnification: 50X.

One selected piece of sugarcane, was put into the oven for 2 hours at 60°C under a nitrogen flow, in order to complete the drying process. After cooling down, it was weighted and the sample mass was found to be 0.4545 g, with a weight loss of 2%, thus confirming that the drying process was almost complete even before this treatment. As shown in **Fig. 3.24**, the fibrous structure of the sample is clearly visible, in which fibers are nearly parallel and grouped into large sticks, visible even by naked eyes.

The dried sugarcane slice was impregnated with 0.5 mL of an aqueous solution containing 1.68 mol dm^{-3} guanidine acetate and 0.2 mol dm^{-3} iron acetate (note that the guanidine acetate and iron acetate concentrations were kept equal to those ones used for the syntheses in the previous section). After 30 min waiting, letting the solution completely fill the dried solid sugarcane, the impregnated piece was placed in a quartz reactor, degassed with N_2 (100 cm^3 min^{-1}) for at least 5 min and inserted in a preheated vertical oven at T = 600 °C in order to rapidly carbonize the materials. Heating was kept for 1 h under continuous N_2 flow. Then the reactor was rapidly quenched to room temperature. Heat-activation was performed at T = 900 °C under constant N_2 flow (100 cm^3 min^{-1}) in the following conditions: 30 min at room temperature, ramping at 6 °C min^{-1} and 3 h standing at T = 900 °C, fast quenching to room temperature. Final sample have been labelled SC9, whose mass was 124.9 mg. In **Fig. 3.25** is shown a picture of the final sample SC9, before being ball-milled at 10 Hz for 5 min.

Fig. 3.25: Picture of sample SC9.

In order to immediately understand whether SC9 sample was promising in terms of ORR electroactivity, RDE polarization curves were recorded in KOH. In **Fig. 3.26** are reported the results and, as a reference material, FAG9 sample.

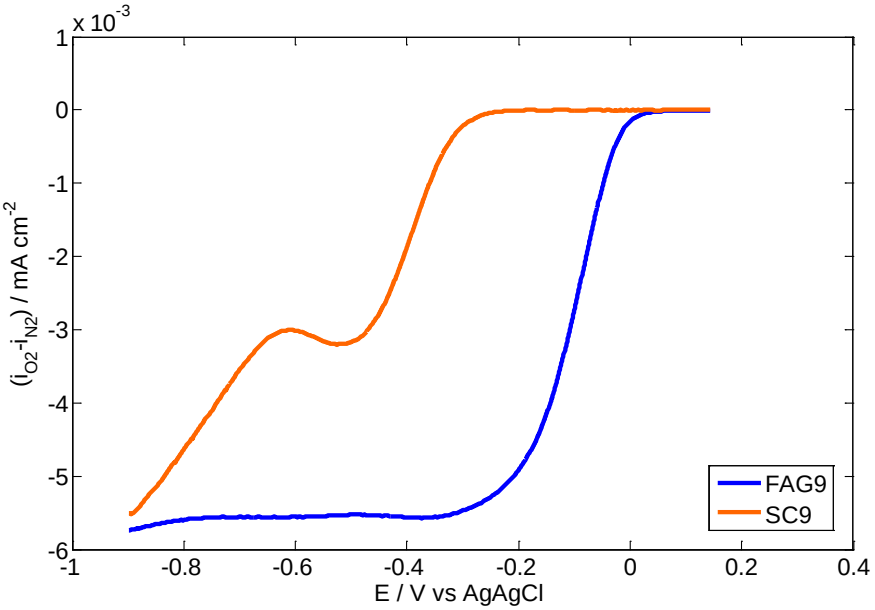

Fig. 3.26: RDE ORR polarization in oxygen-saturated 0.1 mol dm^{-3} KOH, ω=1600 rpm, v= 5 mV s^{-1}, T=25°C.

The ORR onset potential of SC9 sample is about 300 mV more cathodic, and hence worse, than FAG9 sample; moreover, instead of a well-defined limiting current, a further reduction process is happening at potentials lower than -0.5 V, probably involving peroxides species generation. In fact, by calculating the number of transferred electrons by K-L equation, the value is equal to two. This means that the rate determining step in the reduction mechanism of oxygen is the hydrogen peroxide formation.

An analysis of the surface of SC9 sample has been done by BET technique. **Fig. 3.27** shows the experimental BET adsorption/desorption isotherm of the synthesized material after the final 900°C heat-treatment. The surface area was found to be 470 ± 2 m^2 g^{-1}. It exhibits a type IV isotherm [27]. The loop morphology can be assigned to the H3/H4-type hysteresis loop [27],

which suggests specific pore morphologies: H3-type hysteresis is attributed to a non-fixed aggregation of plate-like particles giving rise to slit-shaped pores [28]. Moreover, the micropores percentage is 86%, a very high percentage. Even if in the literature the debate about the best porosity in order to optimize mass transport processes is still alive, this work is mostly supporting the viewpoint believing that mesoporosity only is useful to improve the ORR performance, this porosity allowing efficient mass transport of reactants/products to/from the electrode, respectively, and ensuring a better metal dispersion in the catalytic material [31,32]. The present results related to SC9 sample are likely supporting this viewpoint: a too high presence of microporosity might be deleterious and hinders the reactant and products diffusion to/from active sites. This could be the main reason why the material is not showing a rewarding electroactivity for ORR. Other reasons could be related to a too low N-content or to the presence of contaminants in the complex sugar starting matrix.

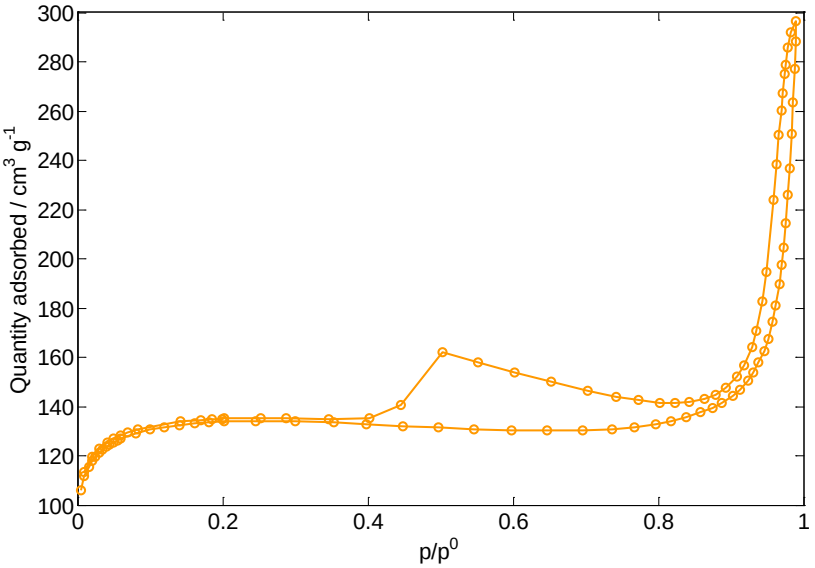

Fig. 3.27: Adsorption and desorption nitrogen isotherms at T= 77 K for SC9.

In conclusion, SC9 sample, prepared starting from sugarcane as C- and O-source and then impregnated with a guanidine acetate and iron containing solution, catalyzes the reduction of oxygen. Its activity however, is not satisfying if compared to other mesoporous materials prepared in this work. The reasons of the worse behavior might be related to the insufficient presence of mesopores; the surface area, that is actually quite high, is almost entirely comprised into micropores, with consequent issues related to mass transport processes of reactants and products from/to active sites.

3.5. References

1. R.J. Jasinski, New fuel cell cathode catalyst, Nature, 201 (1964), 1212-1213.

2. R. Zhou, M. Jaroniec, S.-Z. Qiao, Nitrogen-Doped Carbon Electrocatalysts Decorated with Transition Metals for the Oxygen Reduction Reaction, ChemCatChem, (2015), Ahead of Print.

3. G. Hegde, M. Abdul, A. Shoriya, A. Kumar, G. Ali, K.F. Chong, Z. Ngaini, K.V. Sharma, Biowaste Sago Bark Based Catalyst Free Carbon Nanospheres: Waste to Wealth Approach, ACS Sustainable Chemistry & Engineering, 3 (2015), 2247-2253.

4. N. Brun, S.A. Wohlgemuth, P. Osiceanu, M.M. Titirici, Original design of nitrogen-doped carbon aerogels from sustainable precursors: application as metal-free oxygen reduction catalysts, Green Chemistry, 15 (2013), 2514-2524.

5. M. Antonietti, M.M. Titirici, Coal from carbohydrates: The ‘‘chimie douce’’ of carbon, Comptes Rendus Chimie, 13 (2010), 167-173.

6. G. Chieffi, M. Braun, D. Esposito, Continuous Reductive Amination of Biomass-Derived Molecules over Carbonized Filter Paper-Supported FeNi Alloy, ChemSusChem (2015), Ahead of Print.

7. T.J. Schmidt, U.A. Paulus, H.A. Gasteiger, R.J. Behm, The oxygen reduction reaction on a Pt/carbon fuel cell catalyst in the presence of chloride anions, Journal of Electroanalytical Chemistry, 508 (2001), 41-47.

8. J. Maruyama, I. Abe, Structure control of a carbon-based noble-metal-free fuel cell cathode catalyst leading to high power output, Chemical Communication, 27 (2007), 2879-2881.

9. I. Galbiati, C.L. Bianchi, M. Longhi, L. Formaro, A. Carrà, Iron and copper containing oxygen reduction catalysts from templated glucose-histidine, Fuel Cells, 10 (2010), 251-258.

10. F. Jaouen, J. Herranz, M. Lefevre, J.-P. Dodelet, U.I. Kramm, I. Herrmann, P. Bogdanoff, J. Maruyama, T. Nagaoka, A. Garsuch, J.R. Dahn, T. Olson, S. Pylypenko, P. Atanassov, E.A. Ustinov, ACS Applied Materials and Interfaces, 1 (2009),1623-1639.

11. P.H. Matter, E. Wang, U.S. Ozkan, Preparation of nanostructured nitrogen-containing carbon catalysts for the oxygen reduction reaction from SiO_2- and MgO-supported metal particles, Journal of Catalysis, 243 (2006), 395-403.

12. V.V. Strelko, V.S. Kuts, P.A. Thrower, On the mechanism of possible influence of heteroatoms of nitrogen, boron and phosphorus in a carbon matrix on the catalytic activity of carbons in electron transfer reactions, Carbon, 38 (2000), 1499-1503.

13. Z. Yang, H. Nie, X. Chen, X. Chen, S. Huang Recent progress in doped carbon nanomaterials as effective cathode catalysts for fuel cell oxygen reduction reaction, Journal of Power Sources, 236 (2013), 238-249.

14. G. Wu, P. Zelenay, Nanostructured Nonprecious Metal Catalysts for Oxygen Reduction Reaction. Accounts of Chemical Research, 46 (2013), 1878-1889.

15. W. Orellana, Catalytic Properties of Transition Metal-N_4 Moieties in Graphene for the Oxygen Reduction Reaction: Evidence of Spin-Dependent Mechanisms, Journal of Physical Chemistry C, 117 (2013), 9812-9818.

16. P.H. Matter, U.S. Ozkan, Non-metal catalysts for dioxygen reduction in an acidic electrolyte, Catalysis Letters, 109 (2006), 115-123.

17. A. Serov, M.H. Robson, K. Artyushkova, P. Atanassov, Templated non-PGM cathode catalysts derived from iron and poly(ethyleneimine) precursors, Applied Catalysis B, 127 (2012), 300-306.

18. G. Faubert, R. Cote, J.P. Dodelet, M. Lefevre and P. Bertrand, Oxygen reduction catalysts for polymer electrolyte cells from the pyrolysis of Fe^{II} acetate adsorbed 3,4,9,10-perylenetetracarboxylic dianhydride, Electrochimica Acta, 44 (1999), 2589-2603.

19. I. Roche, E. Chaınet, M. Chatenet, J. Vondrak, Carbon-Supported Manganese Oxide Nanoparticles as Electrocatalysts for the Oxygen Reduction Reaction (ORR) in Alkaline Medium: Physical Characterizations and ORR Mechanism, Journal of Physical Chemistry C, 111 (2007), 1434-1443.

20. J. Ozaki, S. Tanifuji, A. Furuichi, K. Yabutsuka, Enhancement of oxygen reduction activity of nanoshell carbons by introducing nitrogen atoms from metal phthalocyanines, Electrochimica Acta, 55 (2010), 1864-1871.

21. J.K. Nørskov, J. Rossmeisl, A. Logadottir, L. Lindqvist, J. R. Kitchin, T. Bligaard, H. Jonsson, Origin of the Overpotential for Oxygen Reduction at a Fuel-Cell Cathode, Journal of Physical Chemistry B, 108 (2004), 17886-17892

22. D.H. Deng, L. Yu, X.Q. Chen, G.X. Wang, L. Jin, X.L. Pan, J. Deng, G.Q. Sun, X.H. Bao, Iron Encapsulated within Pod-like Carbon Nanotubes for Oxygen Reduction Reaction, Angewandte Chemie, 52 (2013), 371-375.

23. J.H. Knox, B. Kaur, G.R. Millward, Structure and performance of porous graphitic carbon in liquid chromatography, Journal of Chromatography, 352 (1986), 3-25.

24. T. Kyotani, T. Nagai, S. Inoue, A. Tomita, Formation of New Type of Porous Carbon by Carbonization in Nanochannels in Zeolite, Chemistry of Materials, 9 (1997), 609-615.

25. C.G. Wu, T. Bein, Conducting carbon wires in ordered, nanometer-sized channels, Science, 266 (1994), 1013-15.

26. I. Moriguchi, A. Ozono, K. Mikuriya, Y. Teraoka, S. Kagawa, M. Kodama, Micelle-templated mesophases of phenol-formaldehyde polymer, Chemical Letters, 11 (1999), 1171-1172.

27. K.S.W. Sing, D.H. Everett, R.A.W. Haul, L. Moscou, R.A. Pierotti, J. Rouquerol, T. Siemieniewska, Reporting physisorption data for gas/solid systems with special reference

to the determination of surface area and porosity, Pure Applied Chemistry, 57 (1985), 603-619.

28. M. Thommes, Physical adsorption characterization of nanoporous materials, Chemical Engineering & Technology, 82 (2010), 1059-1073.

29. H. Chang, S.H. Joo, C. Pak, Synthesis and characterization of mesoporous carbon for fuel cell applications, Journal of Materials Chemistry, 17 (2007), 3078-3088.

30. M.H. Robson, M. Smolnik, P. Atanassov, Tri-metallic transition metal-nitrogen-carbon catalysts derived by sacrificial support method synthesis, Electrochimica Acta, 109 (2013), 433-439.

31. N.D. Leonard, V. Nallathambi, S. Calabrese Burton, Carbon supports for non-precious metal proton exchange membrane fuel cells, ECS Transactions. 41 (2011), 1175-1181.

32. J.B. Xy, T.S. Zhao, Mesoporous carbon with uniquely combined electrochemical and mass transport characteristics for polymer electrolyte membrane fuel cells, RSC Advances, 3 (2013), 16-24.

33. J. Liu, L. Erling, R. Mingbo, P. Song, W. Xu, Recent Progress on Fe/N/C Electrocatalysts for the Oxygen Reduction Reaction in Fuel Cells, Catalysts, 5 (2015), 1167-1192.

34. C. Song, J. Zhang, PEM fuel cell electrocatalysts and catalyst layers. Fundamentals and applications. J. Zhang (Ed.), Springer, 2008.

35. J. Chlistunoff, RRDE and Voltammetric Study of ORR on Pyrolyzed Fe/Polyaniline Catalyst. On the Origins of Variable Tafel Slopes, Journal of Physical Chemistry C, 115 (2011), 6496-6507.

36. M. Lefevre, E. Proietti, F. Jaouen, J.-P. Dodelet, Iron-Based Catalysts with Improved Oxygen Reduction Activity in Polymer Electrolyte Fuel Cells, Science 324 (2009) 71-74.

37. W. Yang, T.P. Fellinger, M. Antonietti, Efficient metal-free oxygen reduction in alkaline medium on high-surface-area mesoporous nitrogen-doped carbons made from ionic liquids and nucleobases, JACS, 133 (2010), 206-209.

38. U.A. Paulus, T.J. Schmidt, H.A. Gasteiger, R.J. Behm, Oxygen reduction on a high-surface area Pt: Vulcan carbon catalyst: a thin-film rotating ring-disk electrode study, Journal of Electroanalytical Chemistry, 495 (2001), 134-145.

39. A.H.A. Monteverde Videla, , L. Osmieri, M. Armandi, S. Specchia, Varying the morphology of Fe-N-C electrocatalysts by templating Iron Phthalocyanine precursor with different porous SiO_2 to promote the Oxygen Reduction Reaction, Electrochimica Acta, 177 (2015), 43-50.

40. F. Téllez, H. López-Sandoval, S.E. Castillo-Blum, N. Barba-Behrens, Coordination behavior of benzimidazole, 2-substituted benzimidazoles and benzothiazoles, towards transition metal ions, ARKIVOC, (2008), 245-275.

41. J. Zhan J, B. Sunkara, J. Tang, Y. Wang, J. He, G.L. McPherson, *et al.* , Carbothermal Synthesis of Aerosol-Based Adsorptive-Reactive Iron-Carbon Particles for the Remediation of Chlorinated Hydrocarbons, 50 (2011), 13021-13029.

42. M. Hermanek, R. Zboril, M. Mashlan, L. Machala, O. Schneeweiss, Thermal behaviour of iron(ii) oxalate dihydrate in the atmosphere of its conversion gases, Journal of Materials Chemistry, 16 (2006), 1273-1280.

43. J.N. Wang, L. Zhang, F. Yu, Z.M. Sheng, Synthesis of Carbon Encapsulated Magnetic Nanoparticles with Giant Coercivity by a Spray Pyrolysis Approach, Journal of Physical Chemistry B, 111 (2007), 2119-2124.

44. A.S. Ingason, A.K. Eriksson, E. Lewin, J. Jensen, S. Olafsson, Growth and structural properties of Mg:C thin films prepared by magnetron sputtering, Thin Solid Films, 518 (2010), 4225-4230.

45. D. Hulicova-Jurcakova, M. Seredych, G.Q. Lu, T.J. Bandosz, Combined effect of nitrogen and oxygen-containing functional groups of microporous activated carbon on its electrochemical performance in supercapacitors, Advanced Functional Materials, 19 (2009), 438-447.

46. S. Biniak, G. Szymański, J. Siedlewski, A. Świątowski, The characterization of activated carbons with oxygen and nitrogen surface groups, Carbon, 35 (1997) 1799-1810.

47. D. Long, J. Zhang, J. Yang, Z. Hu, G. Cheng, X. Liu, R. Zhang, L. Zhan, W. Qiao, L. Ling, Chemical state of nitrogen in carbon aerogels issued from phenol-melamine-formaldehyde gels, Carbon, 46 (2008) 1259-1262.

48. J.R. Pels, F. Kapteijn, J.A. Moulijn, Q. Zhu, K. M. Thomas, Evolution of nitrogen functionalities in carbonaceous materials during pyrolysis, Carbon, 33 (1995) 1641-1653.

49. A.L. Bouwkamp-Wijnoltz, W. Visscher, J.A.R. van Veen, E. Boellaard, A.M. Van der Kraan, S.C. Tang, On Active-Site Heterogeneity in Pyrolyzed Carbon-Supported Iron Porphyrin Catalysts for the Electrochemical Reduction of Oxygen: An In Situ Moessbauer Study, Journal of Physical Chemistry B, 106 (2002), 12993-13001.

50. S. Maldonado, K.J. Stevenson, Influence of Nitrogen Doping on Oxygen Reduction Electrocatalysis at Carbon Nanofiber Electrodes, Journal of Physical Chemistry B, 109 (2005), 4707-4716.

51. F. Jaouen, S. Marcotte, J.-P. Dodelet, G. Lindbergh, Oxygen reduction Catalysts for Polymer Electrolyte Fuel Cells from the Pyrolysis of Iron Acetate Adsorbed on Various Carbon Supports, Journal of Physical Chemistry B, 107 (2003), 1376-1386.

52. U. Tylus, Q. Jia, K. Strickland, N. Ramaswamy, A. Serov, P. Atanassov, S. Mukerjee, Elucidating Oxygen Reduction Active Sites in Pyrolyzed Metal-Nitrogen Coordinated Non-Precious-Metal Electrocatalyst Systems, Journal of Physical Chemistry C, 118 (2014), 8999-9008.

53. E.F. Jaguaribe, L.L. Medeiros, M.C.S. Barreto, L.P. Araujo, The performance of activated carbons from sugarcane bagasse, babassu, and coconut shells in removing residual chlorine, Brazilian Journal of Chemical Engineering, 22 (2005), 41-47.

54. K. Qureshi, I. Bhatti, R. Kazi, A.K. Ansari, Physical and Chemical Analysis of Activated Carbon Prepared from Sugarcane Bagasse and Use for Sugar Decolorisation, International Journal of Chemical and Biomolecular Engineering, 1 (2008), 145-149.

Chapter 4
Templating Strategies

Besides the composition-dependent factors, catalyst activity also depends on structural and morphological carbon features. It is easy to guess that an optimized porosity of carbon is beneficial for an easy access of reacting oxygen to the catalyst layer in contact with the proton exchange electrolyte membrane [1,2]. Many works have been published about the best and most useful porosity range for ORR application, even though with controversial results.

The aim of this section is to investigate any effect that pore shape and morphology may introduce in the behavior of some platinum free catalysts for the oxygen reduction reaction. Samples of the catalyst were obtained heat-treating a reactant mixture with constant composition and using a variety of templating procedures, i.e. shape-imprinting materials (like high surface area silica and Black Pearls 2000), and some self-templating processes (freeze-drying and in-situ generation of gas bubbles) [3].

4.1. Investigating pores shape

Industrial products, catalysts, building materials, etc. are all solids whose values of surface area and porosity are fundamental parameters to be known for their different applications. Even if the characterization by BET theory is well-established and defined by accepted equations, there is still a lack in the general interpretation and evaluation of adsorption/desorption data due to the complexity of most solid surfaces. Attempts in the direction of standardizing the procedure for surface area and porosity evaluation have been formulated in the last decades [4-7]. However they have been not always widely accepted.

On the basis of IUPAC classification [8], pores are classified in three main families:

- *Macropores*, the largest ones, with diameter larger than 50 nm.
- *Mesopores*, whose diameter is comprised between 2 and 50 nm.
- *Micropores*, the smallest ones, with diameter below 2 nm.

In the same IUPAC document [8], physisorption isotherms are grouped into six types, shown in **Fig. 4.1**:

- *Type I isotherm*, given by microporous solids with small external surfaces.
- *Type II isotherm,* typical for non-porous or macroporous materials. The point B in the **Fig. 4.1**, is usually interpreted as the stage at which the monolayer coverage is complete and multilayer adsorption is beginning.
- *Type III isotherm,* uncommonly experimentally found, with important interactions between adsorbent and adsorbate.
- *Type IV isotherm,* whose feature is the hysteresis loop, associated to capillary condensation in mesopores.
- *Type V isotherm,* uncommon.
- *Type VI isotherm,* interpreted as stepwise multilayer adsorption on a non-porous surface.

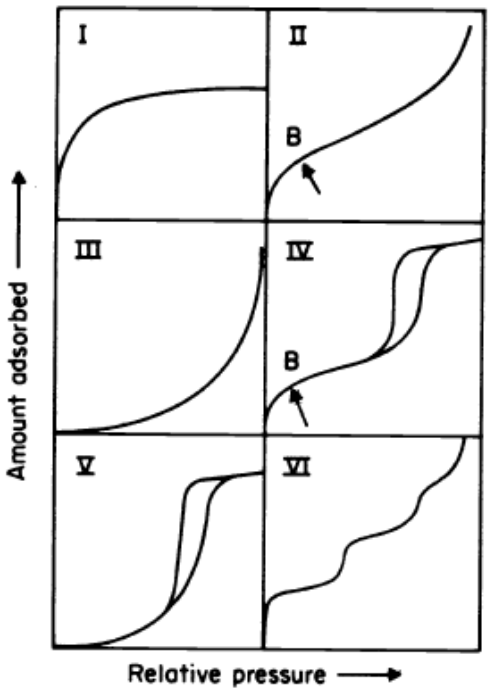

Fig. 4.1: Types of physisorption isotherms [8].

Concerning the hysteresis loop, usually associated to capillary condensation, it can exhibit a variety of possible shapes, as shown in the **Fig. 4.2** [8]:

- *H1 loop,* with the adsorption and desorption branches almost vertical and parallel one to each other, associated to porous agglomerates with narrow distribution of pore size.
- *H2 loop,* sometimes difficult to be interpret. It is often attributed to differences in the adsorption and desorption mechanism happening in the presence of pores with a particular shape. They show narrow necks and wide bodies, and hence they are called "ink-bottle pores" or "bottle-neck pores".
- *H3 loop,* without any limiting adsorption at high values of p/p^0. It is associated to aggregates of plate-like particles, forming slit-shaped pores.
- *H4 loop,* often attributed to slit-like pores, but the "type I" isotherm indicates the presence of microporosity.

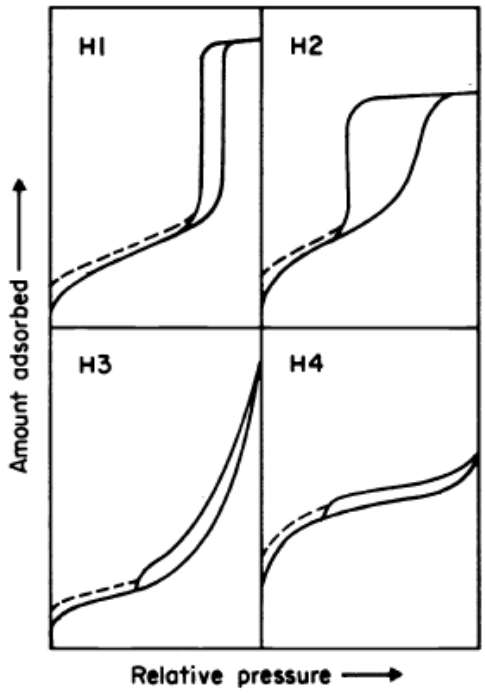

Fig. 4.2: Types of hysteresis loop [8].

The argumentation and discussion of results in the following are extensively focused on pore size distribution and pores shape.

The method chosen here in the evaluation of porosity is the Density Functional Theory (DFT), which has found many applications when calculating pore size distributions in traditional and newly discovered nanoporous solids. It has been more than 20 years since the DFT method has been first suggested for calculating the pore size distribution of carbons from nitrogen adsorption data, which are known to be the most reliable ones. This choice is also explained by considering that the traditional BJH interpretation sometimes lacks in distinguishing between different pore structure morphologies, which is actually an important part in the discussion of results that will be presented. However even after two decades of DFT methods development for porous materials characterization, still remain a number of issues, which are not currently

resolved, concerning, for instance, how to consider the adsorption-induced modification of porous networks [9]. The lacks of the DFT theory were however considered of minor importance for the scope of this section, if compared to those ones belonging to the BJH theory.

4.2. Achieving the optimized porosity: debates in the literature

As previously mentioned, many works have been published about the best and most useful porosity range for ORR application, even though with controversial results.

Dodelet and co-authors highlighted the importance of micropores to improve ORR activity proposing that an increase in micropores area promotes ORR activity because of formation of a catalytic molecular assembly at a specific distance corresponding to the micropore diameter, as shown if **Fig. 4.3** [10].

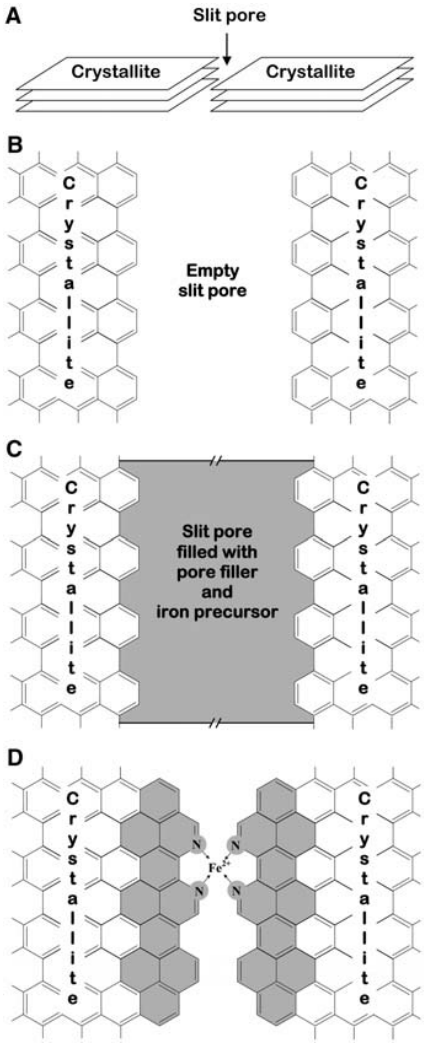

Fig. 4.3: Schematic representation of catalytic site formation in the micropores of the carbon support. A) Simplified 3D view of a slit pore between two adjacent graphitic crystallites in the carbon support. B) Plan view of an empty slit pore between two crystallites. C) Plan view of a pore filled with pore filler and iron precursor. D) Plan view of the catalytic site after pyrolysis [10].

This requirement means that the distance between two pore walls must have an exact value for a site to be formed, which in turn suggests that the catalytic site is a molecular assembly bridging two pore walls.
Dodelet assesses that probably not all micropores of width <22 Å are capable of hosting the active sites, but only those satisfying a more stringent, yet unknown, condition on their pore-width value. Overall, their results strongly support the case that micropores are required to obtain good catalysts with the synthesis method they performed [11,12].

However, this is contrasted by a picture in which mesoporosity is useful only to improve the ORR performance, this porosity allowing efficient mass transport of reactants/products to/from the electrode, respectively, and ensuring a better active site dispersion in the catalytic material [13,14].

4.3. Experimental

All chemicals and reagents were used as received without further purification. *D*-glucose, *L*-histidine, iron(II) acetate, glacial acetic acid, Nafion® (5 wt. % EtOH solution), 37% hydrochloric acid, concentrated sulfuric acid and ethanol were purchased from Sigma Aldrich. Silica (70-230 mesh) and 60% $HClO_4$ solution was from Merck. A Pt-based commercial catalyst (EC20, 20% Pt onto carbon) was tested and used as a reference material.

A constant composition reactant mixture (RM), comprising *D*-glucose, *L*-histidine (molar ratio glucose:histidine=10:1) and iron acetate (0.96 wt % Fe calculated on the total mass of glucose and histidine) was heat-treated adopting many templating procedures. Glacial acetic acid, equimolar to histidine, was always added to dissolve the N-containing compound. A constant final surface composition was obtained for all samples (C~95-96%; N~1-1.5%, O~1.5-3%, Fe<1%).

4.3.1. Silica wet templating

This method was previously reported in the literature [15] and follows the procedure adopted for the great part of catalysts whose synthesis and characterization has been already reported in Chapter 3.

Briefly, 10 mL of an aqueous RM solution was added to silica powder to obtain a silica gel (2.3 RM mL / SiO_2 g). The gel was treated by a first heating step (H1) of 1 hour at 600°C under a N_2 flow (100 cm^3 min^{-1}). After ball-milling (5 minutes, 10 Hz) the product was lixiviated in boiling NaOH (3 mol dm^{-3}) and washed to remove silica. The resulting carbon was dried in nitrogen (100 °C, 24 h) and finally ball-milled (5 minutes, 10 Hz). A second heating step (H2) was performed (900°C, 3h, under a N_2 flow), to activate catalytic sites. The resulting material will be labelled C/Si in the following.

4.3.2. Incipient Wetting of Black Pearls 2000

An active carbon (0.5 g, Black Pearls 2000, Cabot) was impregnated by "Incipient Wetting" with RM solution volumes such as to completely fill the carbon pore volume. Small quantities of RM solution were added dropwise under stirring to carbon to let the solution enter into the pores by capillarity, until the liquid volume was enough (ca. 4.7 mL g^{-1} of carbon)

to fully wet the catalyst with no liquid excess. The mixture underwent the same two heating steps H1 and H2 of the previous templating technique (see section **4.3.1. Silica wet templating**). The resulting material will be labelled C/BP in the following.

4.3.3. Freeze-drying

Freeze-drying was set up by freezing an RM solution under reduced pressure for 24 h. The freeze dried mixture was heat-treated using the above two heating steps H1 and H2 (see section **4.3.1. Silica wet templating**). The resulting material will be labelled C/Lio in the following.

4.3.4. Thermal Decomposition of a gas-evolving reactant

Promotion of pore formation was achieved by in-situ generation of gas bubbles, arising from thermal decomposition of a fragile molecule like oxalic acid. A semi-solid mixture of glucose (2 g), histidine (0.173 g), iron acetate (0.069 g) and glacial acetic acid was mechanically blended with oxalic acid (0.5 g) and ball-milled (15 minutes, 10 Hz). This mixture was put in a closed tube and heat treated at 140°C for 1 hour. The resulting brown-yellowish mass, with a strongly expanded overall volume, underwent the same two heating steps H1 and H2 (see section **4.3.1. Silica wet templating**). The end material will be labelled C/Gas in the following.

4.4. Results and discussion

Fig. 4.4 shows CV cathodic ORR polarization curves of all prepared catalysts recorded at ω =1600 rpm in 0.1 mol dm^{-3} $HClO_4$. For comparison a similar CV curve is also reported for a commercial Pt-based catalyst, EC20 (labelled as Pt EC20). Except for the Pt sample, a limiting current is not clearly detected for the synthesized carbons. The best onset potential, is observed for C/BP and C/Si, displaced by 200 mV at more cathodic potentials than the reference Pt EC20 (**Tab. 4.1**).

Sample	$E_{ORRonset}$ / V (NHE)	n. of electrons	i_k / mA cm^{-2}	|Tafel slopes| / mV
Pt EC20	0.880	4.0 ± 0.1	23 ± 10	52.2 ± 0.4
C/Si	0.692	4.0 ± 0.1	1.6 ± 0.2	97.8 ± 0.9
C/BP	0.682	3.7 ± 0.4	2.1 ± 0.2	82.6 ± 0.9
C/Gas	0.613	4.0 ± 0.1	0.46 ± 0.04	126.9 ± 0.9
C/Lio	0.612	3.8 ± 0.1	0.60 ± 0.03	132.6 ± 0.4

Tab. 4.1: Onset potentials and calculated kinetic ORR parameters for the synthesized catalysts and reference material, Pt EC20.

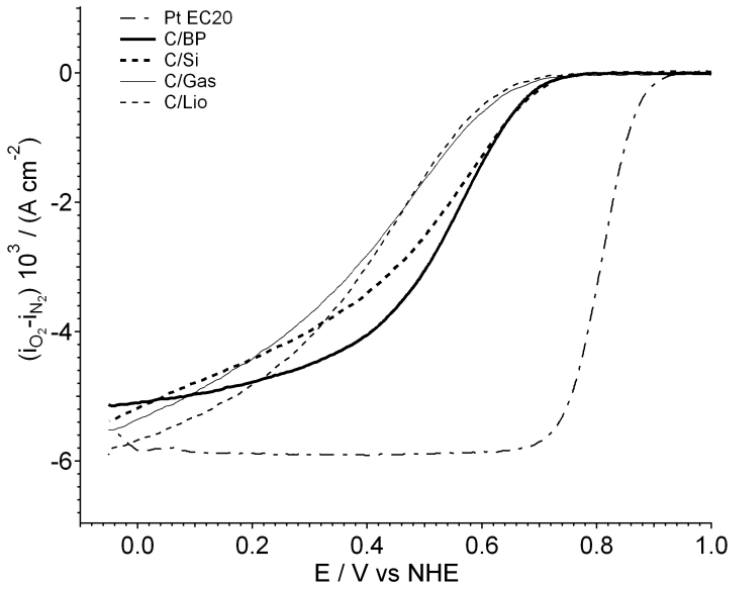

Fig. 4.4: ORR polarization curves recorded in oxygen saturated 0.1 mol dm^{-3} $HClO_4$, v= 5 mV s^{-1}, ω= 1600 rpm, T= 25°C.

The number of exchanged electrons, *n*, and kinetic current density in absence of mass-transfer effects, i_k, were obtained using the Koutecky-Levich equation (1) from cathodic CV data recorded at different electrode rotation rates on each catalytic material (as an example see **Fig. 4.5** for C/BP, a Koutecky-Levich plot is in the inset to **Fig. 4.5**)

$$i^{-1} = i_k^{-1} + \left(0.62 \cdot n \cdot F \cdot D^{2/3} \cdot \nu^{-1/6} \cdot c_0 \cdot \omega^{1/2}\right)^{-1} \qquad (1)$$

Where *i* is the experimental current density at a given potential *E*, *F* is the Faraday constant, *D* the O_2 diffusion coefficient, *v* the solution kinematic viscosity, c_0 the solution concentration of reacting O_2, *n* the number of exchanged electrons, *ω* the angular electrode rotation rate and, finally, i_k is the kinetic current density extrapolated at infinite *ω*.

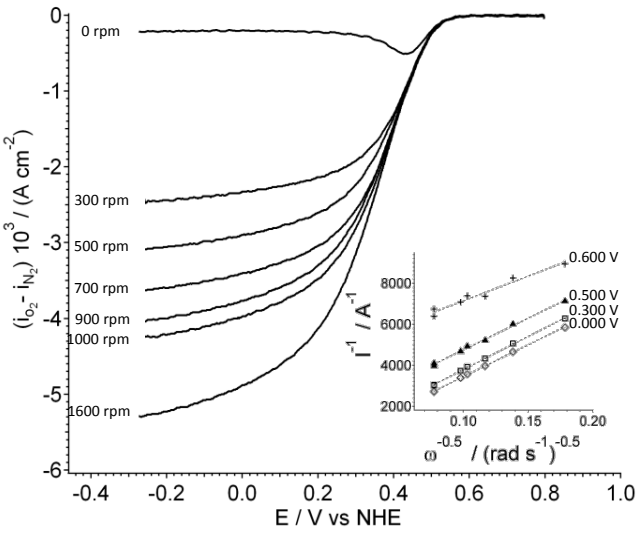

Fig. 4.5: ORR polarization curves for C/BP recorded in oxygen-saturated 0.1 mol dm^{-3} $HClO_4$, v= 5 mV s^{-1}, T=25°C. Inset: Koutecky-Levich plots at different potentials.

All the lines in the inset to **Fig. 4.5** have nearly the same slope value, thus suggesting that, the other equation parameters being constant, the number of exchanged electrons, *n*, is also nearly the same for all the samples. This qualitative assessment is in accordance with calculated *n* values in **Tab. 4.1** where *n* is in any case close to 4, thus permitting to conclude that all samples essentially obey the same ORR mechanism of direct H_2O formation.

Fig. 4.6 reports a representative Koutecky-Levich plot of all samples. The black solid line is a plot of the parent Levich equation in inverse coordinates calculated for a direct-to-water 4-e^- ORR in the absence of any kinetic O_2 reduction hindrance (the used parameters are: D= $1.67 \bullet 10^{-5}$ cm^2 s^{-1}, ν= 0.01 $cm^2 s^{-1}$, c_0= $1.38 \bullet 10^{-6}$ mol cm^{-3} for O_2-saturated 0.1 mol dm^{-3} $HClO_4$ [16]). On these assumptions and regardless of the assumed parameters the Levich line represents the maximum achievable ORR reaction rate, only limited by O_2 mass transport across the diffusion layer thickness and, in the used coordinates, is characterized by a zero intercept at infinite rotation rate ω, or by an exceedingly fast (actually infinite) kinetic reaction constant i_k.

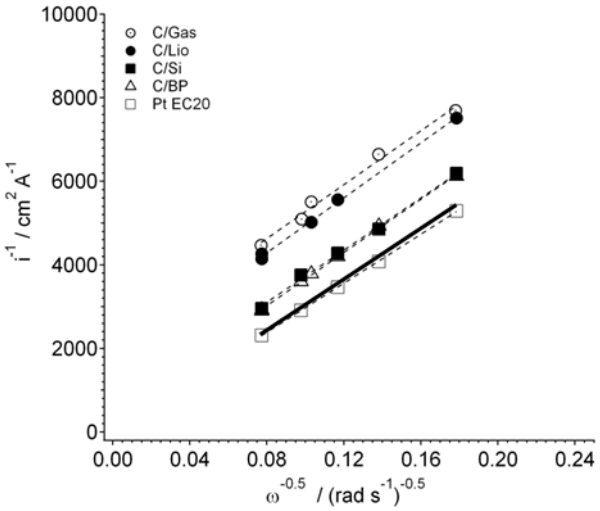

Fig. 4.6: Koutecky-Levich plots of synthesized materials at E= 0 V. The black solid line corresponds to Levich line calculated using D= $1.67 \bullet 10^{-5}$ cm^2 s^{-1}, ν= 0.01 $cm^2 s^{-1}$, c_0= $1.38 \bullet 10^{-6}$ mol cm^{-3} for O_2-saturated 0.1 mol dm^{-3} $HClO_4$.

The experimental line of Pt EC20 has intercept and slope that closely superimpose to the Levich ones thus showing that this material supports a 4-e^- O_2 reduction mechanism with an exceedingly high (nominally infinite) kinetic reaction constant (the experimental i_k is in **Tab. 4.1**). As to synthesized project catalysts, it is noted that, as outlined above, the relevant lines are close to parallel with each other and with the Levich line so that, also in accordance with the experimental n values in **Tab. 4.1**, O_2 reduction occurs by nearly the same 4-e^- mechanism on all these synthetic materials. However, the relevant **Fig. 4.6** lines are seen to shift to various, increasing extents along the Y axis with respect to the Levich (and Pt EC20) line thus showing a general worsening of their O_2 reduction rate and efficiency (i_k values from the extrapolated line intercepts are reported in **Tab. 4.1**). Nevertheless some ranking order emerges in the figure where C/Si and C/BP lines are at lower positions than C/Gas and C/Lio. By also keeping into account the trend of onset of O_2 reduction potentials C/Si and C/BP are therefore somewhat better catalysts than C/Gas and C/Lio. This is also supported by the Tafel slope values in **Tab. 4.1**. Tafel slope data (plots not reported) are obtained from log i_k vs E Tafel

plots, where i_k values were extrapolated at many different potentials. Tafel slope values of all synthesized materials are higher than observed in the work and reported in the literature for Pt-based catalysts (ca. 48 mV) [17]. It is however worth noting that C/BP and C/Si have lower Tafel slopes and therefore better catalytic activity than other synthesized materials of this work.

Unless unexplored effects may intervene by reactant interactions with the used surrounding templating media, the constant reactant composition adopted in sample preparation suggests that the observed variation in electrocatalytic properties may depend on the surface morphology, porosity and porosity distribution as determined by N_2 adsorption/desorption measurements.

Fig. 4.7 a-d show the experimental BET adsorption isotherms of the four synthesized catalysts. All samples exhibit a type IV isotherm, with a hysteresis loop which is characteristic of mesoporous materials [8].

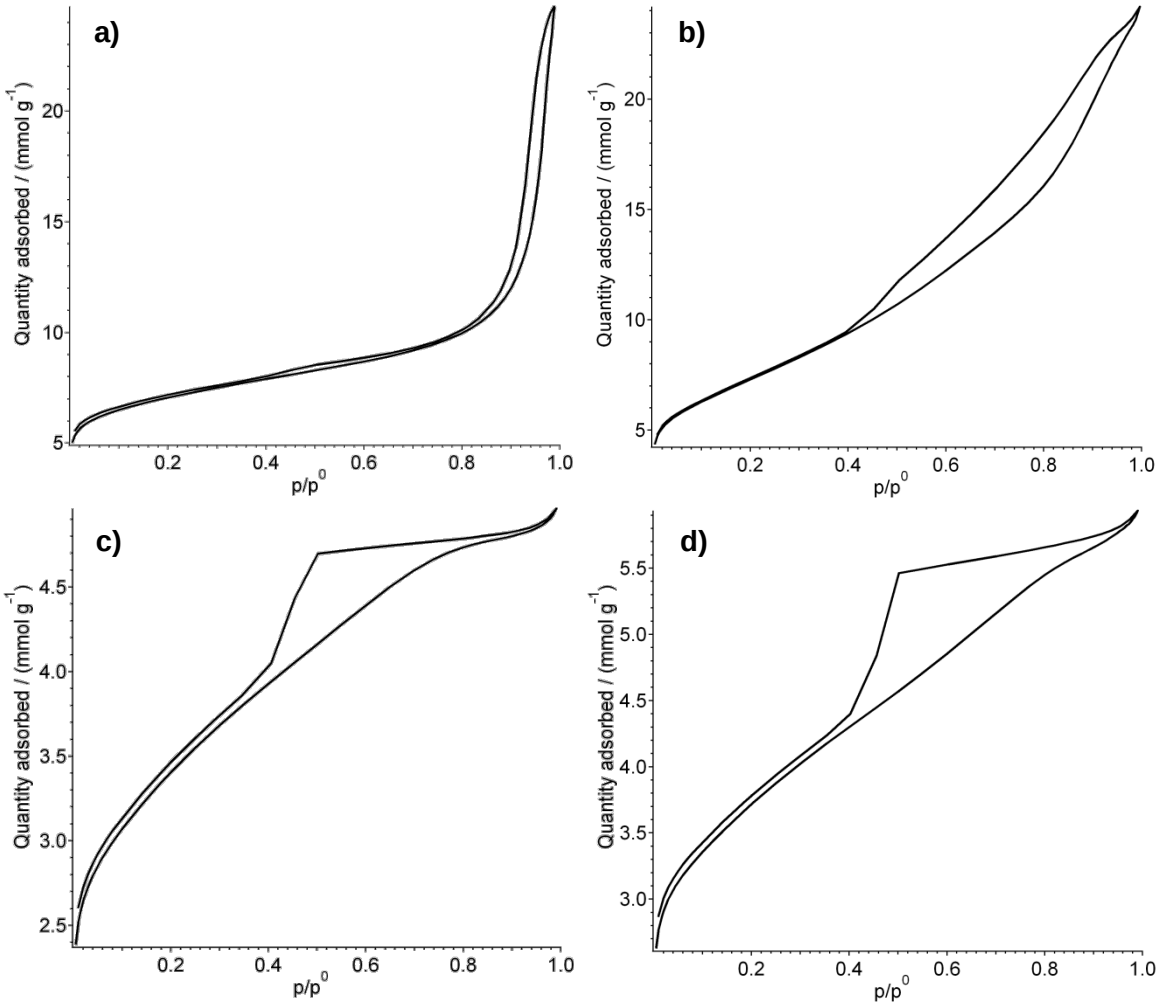

Fig. 4.7 a-d: Adsorption and desorption nitrogen isotherms at T= 77K. a) C/BP; b) C/Si. c) C/Lio and d) C/Gas.

By the loop morphology, the samples can be ordered in two main groups: a first one (C/BP, C/Si) characterized by a H3-type hysteresis loop and the second one (C/Lio and C/Gas) by a H2-

type [8], which suggests diverse pore morphologies. In the relevant literature [18], H3-type hysteresis is attributed to a non-fixed aggregation of plate-like particles giving rise to slit-shaped pores; the H2 hysteresis type can instead be due to pore blocking/percolation effects, typically observed in a complex pore network where the pore neck size distribution is narrower than the size distribution of the main cavities, namely like in cage-like or ink-bottle pores. Moreover, C/Lio and C/Gas also show a well defined low pressure hysteresis, which is absent in C/Si and only slightly outlined in C/BP. The presence of this low pressure hysteresis highlights the presence of pores with about the same width as that of nitrogen molecules, i.e. ultra-micropores (d<0.7 nm) [19]. Relevant to the reported ORR behavior it may be noted that ultra-micropores are not accessible to Nafion® [20], so that the fraction of surface area confined in these pores does not likely participate to the total ORR active area in operative ORR conditions.

Tab. 4.2 shows the specific surface area (A_{BET}) and the corresponding percentage of micropores of the samples.

Sample	A_{BET} / $m^2 g^{-1}$	% micropores
C/Si	578 ± 1	51
C/BP	614 ± 5	13
C/Gas	292 ± 2	38
C/Lio	268 ± 2	39

Tab. 4.2: BET analysis results.

In a first consideration, and because of some (though difficult to specify) relation between total surface area and number of available reacting centres, it may be expected that C/BP and C/Si, with a maximum surface area (ca. 600 $m^2 g^{-1}$) are also most active in ORR, which is indeed observed.

All samples except C/Si are characterized by a relevant micropore percent fraction of the overall area, with a maximum for C/BP. Also interesting to the following, the most active samples, C/BP and C/Si, are characterized, respectively, by the maximum and minimum micropore percent value. Dodelet *et al.* proposed that an enhancement in electrocatalytic activity may be attributed to better developed microporosity [11,12]. This is consistent with the comparatively better ORR activity of C/BP sample, but in disagreement with both the observed behaviour of C/Si, this having a low micropore content and similar ORR features, and with the performances of C/Lio and C/Gas, showing a large micropore fraction even if accompanied by unfavourable ORR behaviour. For C/Lio and C/Gas an explanation can be found considering that, as mentioned previously, this material porosity comprises unknown amounts of ultramicropores, not useful for ORR.

In order to better understand these aspects, a pore size distribution in the mesoporous range was evaluated using the adsorption nitrogen isotherm branch that, when hysteresis occurs, corresponds to a more stable thermodynamic condition [21]. Results are reported in **Fig. 4.8**. On the X axis samples are ordered from left to right with increasing catalytic activity (for

graphical clarity C/Si and C/BP are displaced to different positions even if with similar ORR features).

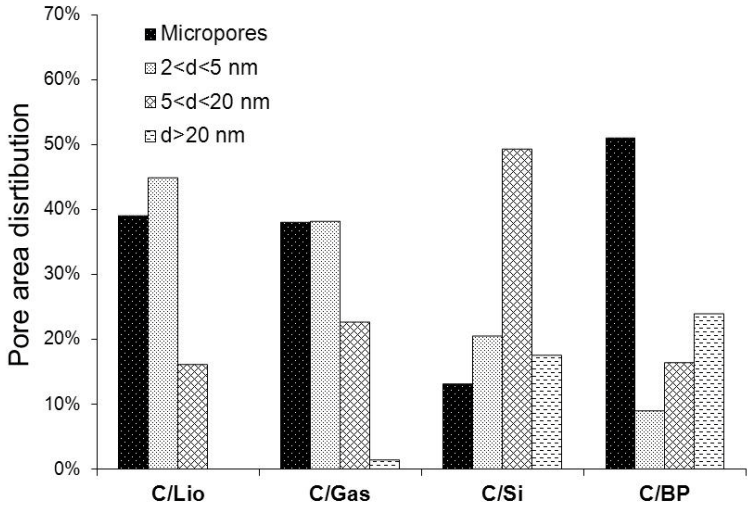

Fig. 4.8: Pore area distribution of synthesized catalysts.

Pores in the mesoporosity range (2-50 nm) are subdivided into three groups depending on their width (d): small mesopores (2<d<5 nm), mesopores (5<d<20 nm), large mesopores (d>20 nm). Though without further subdivision in size, for completeness the total micropore percentage that also comprises smaller pores (ultramicropores, d<0.7 nm) is also reported. C/Lio and C/Gas show the greatest pore amount with d<5 nm (84% and 76%, respectively), but also the minimum amount of large pores at d>20nm (0.2% and 1.3%, respectively). This lack of large mesopores together with the particular ink-bottle morphology of another pore fraction and the large ultramicropore abundance may be proposed to explain the scarce electrocatalytic properties of the samples. Such geometrical features would behave as constraints for reagent access and diffusion within a main fraction of the overall surface area thus excluding inner catalytic sites from reaction. The neck of ink-bottle pores might further act as a barrier for Nafion® permeation to inner sites thus again making ORR difficult for the lack of this essential reaction promoter. This condition of C/Lio and C/Gas compares with that of C/Si and C/BP that on the contrary have relevant mesopores amounts with d>5 nm (C/Si 67% and C/BP 40%), thus making easier mass transport processes to and from catalytic sites.
This point of view is in accordance with the position held by of many authors by which only pores in the true mesoporosity range are useful to support/improve catalytic ORR performances [13, 14]. As an additional feature, C/BP also has a large pore fraction (about 60%) that though smaller than d<5 nm has a slit instead ink-bottle shape, as it is for C/Lio and C/Gas, and this morphology should not hinder ORR. Comparison of these experimental evidences shows that electrocatalytic properties of carbons towards ORR are not only affected by pore size but also by their morphology and shape.
Overall, ORR is improved not only if mesopores and micropores with d>0.7 nm are generated, but also if their shape is other from the ink-bottle one.

4.5. Conclusions

In conclusion relations that presumably exist between ORR behaviour and textural features of catalytic carbons were investigated. Carbons were prepared by keeping constant the reactant composition and high-T treatments in a variety of templating methods. Different catalytic ORR activities resulted depending on templating conditions. As shown by comparison of electrochemical CV data and BET determinations mesopores are necessary and of the utmost importance to improve ORR behaviour. This is proposed to be due to the ease by which comparatively large cross section channels favour the diffusion access of reagents/products to the internal surface area. Micropores can also be beneficial provided they have greater width than 0.7 nm, otherwise they may be ineffective, or even harmful, because polymeric electrolytes like Nafion® cannot enter them, thus excluding a main surface area fraction from the reaction. Therefore, some combination of meso and micropores seems useful to ORR. Moreover, because of their shape ink-bottle pores are especially detrimental. Besides pore size, pore shape also affects ORR efficiency.

In conclusion, improving the performance of non-noble ORR electrodes involves the search of some optimized reactant composition, which is still under way, and, as shown by the present templating results, a suitable combination of pore size, pore shape and pore size distribution.

4.6. References

1. H. Chang, S.H. Joo, C. Pak, Synthesis and characterization of mesoporous carbon for fuel cell applications, Journal of Materials Chemistry, 17 (2007), 3078-3088.

2. M.H. Robson, M. Smolnik, P. Atanassov, Tri-metallic transition metal-nitrogen-carbon catalysts derived by sacrificial support method synthesis, Electrochimica Acta, 109 (2013), 433-439.

3. S. Marzorati, M. Longhi, Templating Induced Behavior of Pt-free Carbons for Oxygen Reduction Reaction, submitted to Journal of Catalysis B.

4. British Standard 4359: Part 1: 1969. Nitrogen adsorption (BET method).

5. Deutsche Normen DIN 66131, 1973. Bestimmung der spezifischen Oberfläche von Feststoffen durch Gasadsorption nach Brunauer, Emmett und Teller (BET).

6. Norme Française 11-621, 1975. Determination de l'aire massique (surface specifique) des poudres par adsorption de gaz.

7. American National Standard, ASTM D 3663-78. Standard test method for surface area of catalysts.

8. K.S.W. Sing, D.H. Everett, R.A.W. Haul, L. Moscou, R.A. Pierotti, J. Rouquerol, T. Siemieniewska, Reporting physisorption data for gas/solid systems with special reference to the determination of surface area and porosity, Pure Applied Chemistry, 57 (1985), 603-619.

9. J. Landers, G.Y. Gor, A.V. Neimark, Density functional theory methods for characterization of porous materials, Colloids and Surfaces A: Physicochemical and Engineering Aspects, 437 (2013), 3-32.

10. M. Lefèvre, E. Proietti, F. Jaouen, J.-P. Dodelet, Iron-Based Catalysts with Improved Oxygen Reduction Activity in Polymer Electrolyte Fuel Cells, Science, 324 (2009), 71-74.

11. J. Tian, L. Birry, F. Jaouen, J.-P. Dodelet, Fe-based catalysts for oxygen reduction in proton exchange membrane fuel cells with cyanamide as nitrogen precursor and/or pore-filler, Electrochimica Acta, 56 (2011), 3276-3285.

12. F. Jaouen, M. Lefevre, J.-P. Dodelet, M. Cai, Heat-Treated Fe/N/C Catalysts for O_2 electroreduction: Are active sites hosted in micropores?, Journal of Physical Chemistry B, 110 (2006), 5553-5558.

13. N.D. Leonard, V. Nallathambi, S. Calabrese Burton, Carbon supports for non-precious metal proton exchange membrane fuel cells, ECS Transactions. 41 (2011), 1175-1181.

14. J.B. Xy, T.S. Zhao, Mesoporous carbon with uniquely combined electrochemical and mass transport characteristics for polymer electrolyte membrane fuel cells, RSC Advances, 3 (2013), 16-24.

15. I. Galbiati, C.L. Bianchi, M. Longhi, A. Carrà, L. Formaro, Iron and copper containing oxygen reduction catalysts from templated glucose-histidine, Fuel Cells, 10 (2010), 251-258.

16 C. Song, J. Zhang, PEM fuel cell electrocatalysts and catalyst layers. Fundamentals and applications. J. Zhang (Ed.), Springer, 2008.

17. U.A. Paulus, A. Wokaun, G.G. Scherer, T.J. Schmidt, V. Stamenkovic, V. Radmilovic, N.M. Markovic, P.N. Ross, Oxygen reduction on carbon-supported Pt-Ni and Pt-Co alloy catalysts, Journal of Physical Chemistry B, 106 (2002), 4181-4191.

18. M. Thommes, Physical adsorption characterization of nanoporous materials, Chemical Engineering & Technology, 82 (2010), 1059-1073.

19. T.J. Bandosz, M.J. Biggs, Mark, K.E. Gubbins, Y. Hattori, T. Iiyama, K. Kaneko, J. Pikunic, K.T. Thomson, Molecular models of porous carbons in: L.R. Radovic, (Ed.), Chemistry and Physics of carbon, Vol. 28, Marcel Dekker Inc., Basel, 2003, pp.118.

20. R. Hiesgen, D. Eberhardt, E. Aleksandrova, K.A. Friedrich, Structure and local reactivity of supported catalyst/Nafion layers studied by in-situ STM, Fuel Cells, 6 (2006), 425-431.

21. S. Lowell, J.E. Shields, Powder surface Area and Porosity, Third ed., Chapman & Hall Ltd, London, 1991, p. 61.

Chapter 5
Ordered Structures for ORR

Aiming to go a step further ahead, setting the sights on attempting to prepare materials with a precise and defined order and trying consequently to emphasize some of their properties such as, for instance, surface area and conductivity, nanotechnological design and synthetic principles were found to be necessary. Keeping in mind the satisfying results in terms of electrocatalytic activity towards ORR previously obtained on mesoporous N- and Fe-doped carbon-based materials, in this section a number of attempts to synthesize ordered carbonaceous nano and microstructures are presented.

First of all a synthesis by chemical vapor deposition (CVD) and characterization of N-doped carbon nanotubes (N-CNTs) is shown and some discoveries in terms of the influence of the age of the catalyst used to grow N-CNTs are reported. Moreover, a modified method, but very similar to that used in the synthesis of nanotubes, is reported because it surprisingly allowed a synthesis of N-doped hollow carbon nanocubes (N-CNCs). Finally, in order to obtain microstructures, completely different techniques, an ultraspray pyrolysis method (USP) and an aerosol pyrolysis method (APM), were performed and the characterization of the so-obtained microspheres is hereby presented.

5.1. "There's plenty of room at the bottom"

In the last decades nanotechnology is attracting great interest because it spans a very wide range of scientific and engineering fields and, due to its applicability in many disciplines, it is undergoing revolutionary developments. The first scientist talking about nanotechnology, lacking however in calling it with the specific word "nanotechnology", was Richard Feynman in 1959, in his famous lecture (at an American Physical Society meeting at Caltech) known as "There's plenty of room at the bottom". He was talking about the possibility of "arranging atoms the way we want", doing chemical synthesis by mechanical manipulation at an atomic level. Actually this is, more typically, the definition of "nanochemistry", underlining the possibility of arranging, by synthetic chemistry, building blocks of specific shape, size, composition and surface structure, showing, at the end, at least one spatial dimension in the range 1-1000 nm.

In regards to the surface of nanostructures, it plays an absolutely priority role, much more important than in macrostructures because, in the former the ratio surface/volume is much higher than in the latter. This is the reason why nanotechnologies account for all the physico-chemical methods aiming to characterize chemical composition and width of the surface, such as X-Ray Photoelectron Spectroscopy (XPS) and Brunauer-Emmett-Teller (BET) method, respectively. Since nanoscaled materials exhibit physical and chemical properties different from the bulk, they reasonably show enhanced properties such as higher strength, lighter weight, increased control of light spectrum, and greater chemical reactivity than their larger-scale counterparts. This means they can behave in different ways and do not follow the same laws of physics that larger objects do. It is finally worth specifying that, even if nanotechnology generally refers to separate nanounits which might be useful as they singularly are, it is more common in many applications to deal with assemblies of them. These architectures, representing on a larger scale the nanostructure of the single building blocks, may be achieved through a spontaneous self-assembly, or through an "externally-forced" reaction [1].

5.2 N-doped carbon nanotubes (N-CNTs)

Since the discovery of the perfectly symmetric Buckyball (C_{60}), the possibility of finding out other alternative and interesting chemical contortions of carbon nanostructures arouse the enthusiasm of many scientists in this field [2-4].

One of the most exciting scientific events of the last decades happened in 1991, when Iijima observed carbon tubes depositing at the anode of an arc discharge system used during fullerenes synthesis [5]. These nanometric structures, named carbon nanotubes, have been already observed in other groups but Iijima was rewarded to be the first scientist studying them systematically and extensively. This innovative form of carbon had immediately great impact on nanosciences because it shows unparalleled strength, and a high thermal and electrical conductivity surpassing standard conductors and semiconductors [6], and has been studied for a wide range of applications. Moreover, depending on the angle the graphite sheet chooses to be rolled up forming nanotubular structures, the electrical transports changes dramatically. For instance, carbon nanotubes showing chirality, due to helical twist in their structure, have seminconducting properties, while achiral tubes were found to be metallic.

Many methods for carbon nanotubes synthesis are available but the most commonly used is chemical vapor deposition (CVD) [7]. Carbon nanotubes, both in their single walled and multi walled forms, are nowadays commercially available and even their price has definitely decreased, improving the synthetic methods and the yields.

Due to nanotubes outstanding properties, many studies aim to possibly change their physical and chemical features, by introducing heteroatoms such as nitrogen. Nanotubes doping can be achieved post-synthesis, by functionalization, or, more interestingly, during the synthetic process: within the graphene network carbon atoms are substituted by heteroatoms and, as expected consequence, not only the morphology, but also the final electronic properties, becomes deeply affected. It was observed that nitrogen doping, for instance, could induce nanotubes bending because nitrogen stabilizes a pentagonal network in spite of the hexagonal one, discouraging the formation of straight structures.

The last one is not the only consequence of nitrogen introduction: it was observed that N-doped nanotubes often show the so-called "bamboo-like structure" [8]. The reason explaining why such structures could originate during a CVD process, using metallic catalytic structures or Me-doped substrates to grow N-CNTs on them (that is a process close to the CVD system used in this work) has to be found in the synthetic formation mechanism. An organic N-containing molecule is first decomposed at high temperature near the catalytic substrate in an inert atmosphere. The catalyst stabilizes the intermediates allowing the formation of C-C bonds. When nitrogen is present, due to N-Me interaction that is higher than C-Me interaction, some "pin points" are generated, deforming and stretching the catalyst particles during the growth of the nanotube on it. When the surface energy of the particle overcomes the stabilization given by the bond with the nanotube, it contracts and it gets spherical again. The final morphological effect, due to this mechanism, is the formation of consecutive and joined "graphitic domes", typical for "bamboo-like" N-CNTs [9].

As a consequence of the nitrogen inclusion in the graphene plane of carbon nanotubes, a π-system perturbation, otherwise homogeneous for undoped carbon nanotubes, is obtained. The reactivity of N-CNTs is, in this way, increased, as well as their metallic character [2,10]. The resulting increase of the density of states near the Fermi level, together with a marked presence of defects, enhances also the catalytic properties towards reactions involving electronic transfer happening on N-CNTs surface.

This makes N-CNTs interesting materials as electrocatalysts for oxygen reduction reaction. Many papers show that the ORR activity of N-CNTs can be modified by varying preparation method, precursor nature and composition of the catalyst used in the nanotube synthesis. It is demonstrated that many parameters chosen during the CVD growth affect the morphology of the final sample: the material supporting the catalyst (Si, SiO_2, MgO, …) and the metallic catalyst itself (nature, oxidation state, …), the decomposing N-CNTs precursor and other physical parameters such as the decomposition temperature [11].

In this work 1,1,3,3-tetramethylguanidine was selected as precursor because it is liquid and can be used pure, does not show any particular safety concern, it is quite cheap and finally, more importantly, it contains the guanidinium-group, previously demonstrated to enhance the catalytic activity towards ORR. Magnesium oxide, impregnated with an iron (III) solution, was chosen as the catalyst for N-CNTs growth; the former is in fact easy to be removed and the presence of iron, possibly retained on the surface or inside N-CNTs, could help the formation of N-Fe moieties as catalytic sites for ORR.

In the following not only the synthesis of N-CNTs is reported, but also some intriguing results about surprising effects that aging time of the used catalyst (Fe/MgO) has on the produced N-CNTs. The starting point of this part of work is related to some incomprehensible results obtained repeating the synthesis in different days. In fact, varying the synthesis day, synthesized nanotubes were found to be morphologically different. At a first glance the synthesis looked irreproducible. Being all parameters and conditions equal in the different syntheses except the "age" of the catalyst, in order to highlight the origin of these incongruences, a deep study on a possible effect of the catalyst aging on the morphology and properties of N-CNTs was performed. A unique Fe-doped magnesium oxide batch was prepared, and fixing as time "zero" the day in which this catalyst was prepared, the syntheses of nanotubes were repeated in different days (from 1 to 70 days from the synthesis of Fe/MgO). Correspondingly, at the same days, a characterization of the FeMgO was done.
The catalyst age was found to affect the synthesized nanomaterials with respect to morphology, surface composition and electrocatalytic behavior towards the electrochemical oxygen reduction [12].

5.2.1. Experimental

All chemicals and solvents were purchased from Sigma Aldrich and used as received without further purification.

Synthesis of N-CNTs was performed by a catalytic reaction of 1,1,3,3-tetramethylguanidine over a MgO catalyst modified with an iron salt solution (Fe/MgO). MgO was synthesized by thermal decomposition (T=400°C, N_2 100 cm^3 min^{-1}, 4 h) of $MgCO_3 \bullet Mg(OH)_2 \bullet 5H_2O$. Modification with iron was obtained by suspending MgO in a $Fe(NO_3)_3 \bullet 9H_2O$ solution (w/w%=11) and sonicating it for 1 h. After filtration and drying (T=115°C, N_2 flow, 5 h), the powder was pyrolysed (T=300°C, N_2 100 cm^3 min^{-1}, 7.5 h). The final product was placed in a closed vial without other precautions.
Synthesis of N-CNTs was carried out in a vertical quartz tube reactor (N_2, 95 cm^3 min^{-1}); at the bottom of the tube a quartz beaker, containing the catalyst, was positioned. The design of the head of the reactor comprises a small diameter quartz tubular gas entrance proceeding straight into the reactor and reaching the edge of the beaker inside. In this way the drops of the precursors were carried directly onto the catalyst with the help of a nitrogen flow. For each preparation 300 mg of Fe/MgO were used and positioned inside the beaker. After 25 min in N_2 flow at T=25°C, the catalyst was heated slowly (6°C min^{-1}) up to T=800°C. At this temperature an aliquot of 1,1,3,3-tetramethylguanidine was added drop wise (2.6 mL h^{-1}, 70 min). At the end, the reaction was interrupted by quenching the reactor to T=25°C. The day after the reactor was placed into the same furnace and heated up to T=400°C (N_2, 100 cm^3 min^{-1}, 6°C min^{-1}). Then, the nitrogen flow was stopped, the reactor was opened and the sample left 2 h under static air to burn amorphous carbon. After quenching to T=25°C the black powder was lixiviated under sonication in 0.5 mol dm^{-3} H_2SO_4 (t=90 min) to eliminate Fe/MgO. Finally, after filtration and washing, the sample was dried (T=100°C, N_2 flow, 16 h).
To study Fe/MgO aging effects onto nanotube morphology and electrocatalytic properties, a single Fe/MgO batch was prepared. Aliquots were withdrawn at 1, 6, 10, 70 days from preparation (labeled Fe/MgO 1, Fe/MgO 2, Fe/MgO 3 and Fe/MgO 4, respectively) and were

employed to synthesize a relevant N-CNT sample, labeled CNT1, CNT2, CNT3 and CNT4 in the following.

5.2.2. Physico-chemical and electrochemical characterization

Fig. 5.1 a-d show TEM images of all samples prepared using Fe/MgO at different aging times. It is observed that product morphology changes with increasing catalyst aging. The CNT1 sample (**Fig. 5.1 a**) is characterized by the presence of bundles and multiwalled flexible nanostructures where a series of single, apparently independent, units form a nanochain with a diameter of ~30 nm and a wall thickness of ~5 nm. Bundles are also present in CNT2 (**Fig. 5.1 b**) with a nanostructure morphology that varies from nanochains to bamboo-like; diameters are greater (50 nm) than in CNT1. In CNT3 (**Fig. 5.1 c**) a well-developed nanotube morphology appears with a continuous external wall and an internal structure clearly composed by nanocups. The average diameter is ~50 nm and the wall is thicker (10 nm) than in CNT2 (5 nm) and CNT1. Finally, in CNT4 (**Fig. 5.1 d**) the well-defined CNT3 morphology is mostly lost even though some ordering still appears. Therefore, the nanostructure morphology becomes better organized with increasing catalyst aging time, until a threshold age is reached at which the catalyst is no longer suitable to sustain formation of well-structured nanotubes.

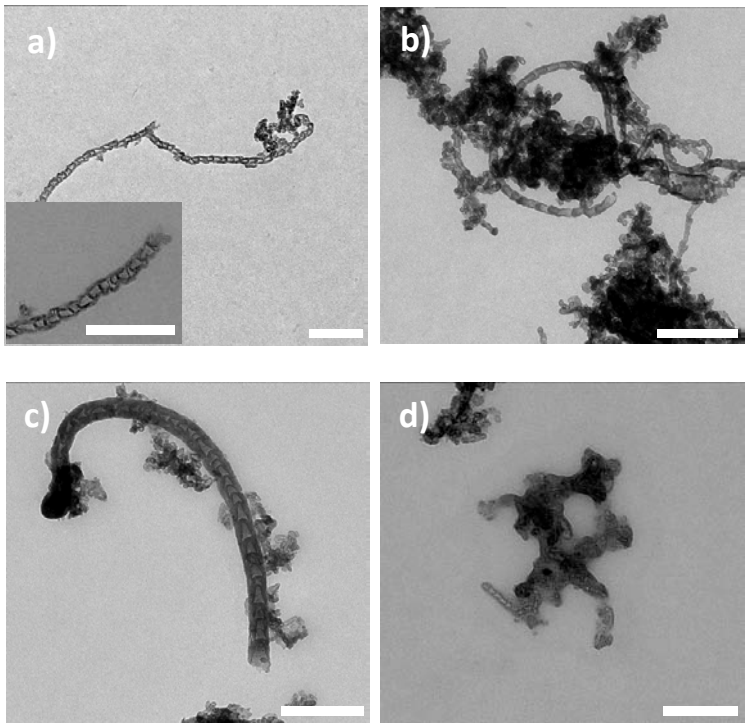

Fig. 5.1 a-d: TEM images: a) CNT1, b) CNT2, c) CNT3, d) CNT4. Inset in a): Magnification of CNT1 TEM image [12].

Fig. 5.2 shows the Raman sample spectra. Two bands are observed at ~1350 cm^{-1} (D band) and ~1595 cm^{-1} (G band), the first one being attributed to disordered amorphous carbon and edge defects, the second one to the tangential vibrations of the graphitic carbon atoms [13]. The ratio of the two bands intensities (I_D/I_G) is an estimate of the disorder level within N-CNTs [14]: the higher the value, the higher the extent of disorder and defects. For our samples I_D/I_G values are 1.28 (CNT1), 1.27 (CNT2), 1.22 (CNT3) and 1.31 (CNT4). This is an indication that N-

CNTs are reasonably graphitized but also contain some disordered carbon and defects [8]. The smallest I_D/I_G value of CNT3 shows that the average size of domains attributable to in-plane crystalline wall structure [15] reaches a maximum with respect to other sample results. This is consistent with the above TEM observations.

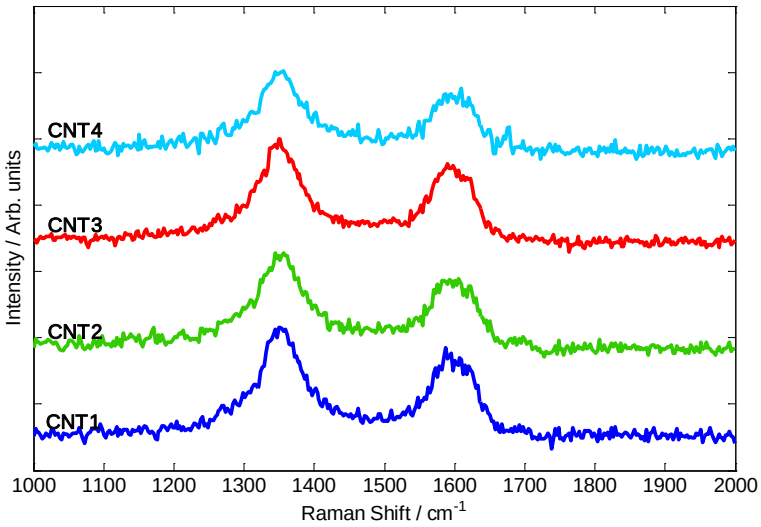

Fig. 5.2: Raman Spectra of N-CNTs. Scalebar: 200 nm [12].

Results of XPS atomic percent composition are reported in **Tab. 5.1**. As seen, C is the main component (95-97%), followed by O (2-4%), which is in general accordance with XPS literature data of most carbons. In a further aspect, C and O amounts oppositely vary by 2-3 atomic percent in going from CNT1 to CNT4. Such variations are above the experimental uncertainty and apparently unrelated to the otherwise constant experimental conditions adopted (the constant end sample heating in air at T=400°C is felt most relevant to show that the observed O/C variations are intrinsic sample features). Therefore, these elemental variations are surprisingly only attributable to increasing catalyst aging effects. Similar composition variations are observed for N1s that is only detected on CNT3 and CNT4 with a slight percentage increase in the latter instance. Finally, Fe signal, attributable to iron oxide, is only found in CNT4, possibly deriving from the catalyst Fe/MgO [16,17].

Since for low metal concentrations in CNTs XPS can give false-negative information [18], further results of metal impurities were obtained by DC magnetic susceptibility (DC-MS) measurements [18] and EDX. Results are reported in **Tab. 5.1**. In DC-MS results low amounts of paramagnetic centres are present in all samples and increase from CNT2 (6.2 ppm) to CNT4 (8.2 ppm) (the CNT1 sample amount was not enough for measurements). These results are confirmed by EDX analyses, showing that metal impurities are only attributable to iron species. Hence, even though in low quantities, iron is present in all N-CNTs, these being again related to the catalyst age. In a further aspect, the presence of variable iron amount could be related to different sample nitrogen amounts. In fact, nitrogen groups are thermally unstable at T=800°C, but can be stabilized by iron by formation of a sort of N-Fe complex [19] so that it may be inferred that the higher is iron, the higher becomes the stability and quantity of carbon bound nitrogen.

Sample	XPS				DC Magnetic Susceptibility	EDX
	C %	O %	N %	Fe %	Paramagnetic metal impurities / ppm	Fe %
CNT1	97.0	2.8	-	-	-	0.2
CNT2	97.2	2.7	-	-	6.2	0.2
CNT3	95.2	3.4	1.4	-	6.2	0.5
CNT4	93.4	4.6	1.7	0.3	8.2	0.9

Tab. 5.1: Sample composition: atomic percent from XPS and EDX and ppm from DC magnetic susceptibility [12].

Fig. 5.3 a-j show C1s, O1s, N1s XPS high resolution spectra for the samples.

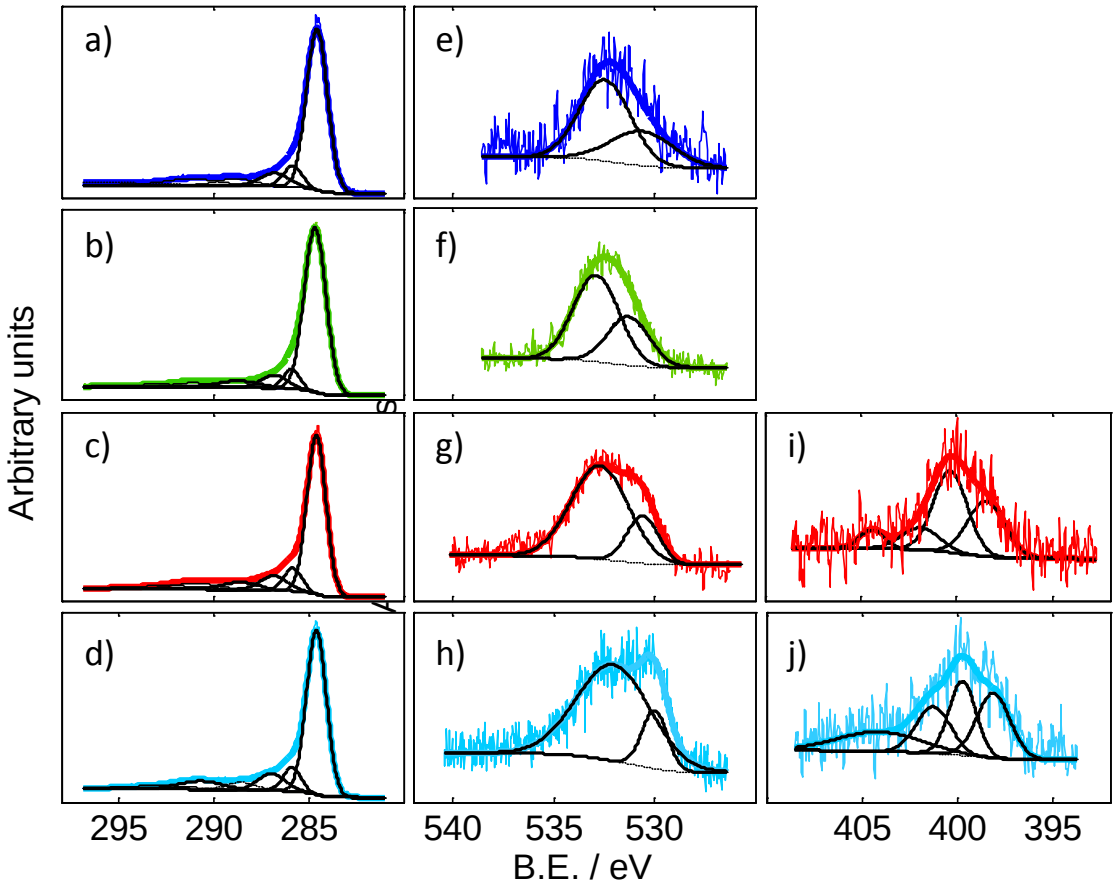

Fig. 5.3 a-j: XPS High Resolution Spectra: C1s, a) CNT1, b) CNT2, c) CNT3, d) CNT4; O1s, e) CNT1, f) CNT2, g) CNT3, h) CNT4; N1s, i) CNT3, j) CNT4 [12].

As outlined by peak deconvolution (**Fig. 5.3 a-d**), many carbon species may contribute to the C1s region (sp^2/sp^3 carbon, single C-O/C-N bonds, carbonyls/quinones, carboxyl/ester groups [20-23]). These data are not considered further because no evidence was detected of catalyst aging effects on C1s signals. The O1s region can be deconvoluted in two peaks (**Fig. 5.3 e-h** and **Tab. 5.2**), with a main component maximum (532.0-533.0 eV) and a secondary one (B.E. 530.0-531.0 eV), the former one being attributable to oxygen-carbon single bonds [21], the latter one instead to double-bonded oxygen-carbon [21]. The signal at B.E.= 530-531 eV remains constant in CNT1 and CNT2 and decreases with catalyst aging in CNT3 and CNT4. O=C significantly decreases when surface nitrogen is present, and becomes smallest in CNT4 where nitrogen is at a maximum. This behavior shows that carbonyl/carboxyl oxygen functional groups are less favorably introduced onto nitrogen containing surfaces. **Fig. 5.3 i,j** show the deconvolution of high resolution N1s. Four maxima can be identified at B.E.= ~ 398 eV (pyridinic nitrogen), B.E.= ~ 400 eV (pyrrolic nitrogen), B.E.= ~ 401.5 eV (quaternary nitrogen), and B.E. ~ 404 eV ($\pi-\pi^*$ shake-up satellite or oxidized nitrogen) [20]. The relative percentage of nitrogen contributions changes from CNT3 to CNT4. In particular, it is noticeable that with increasing catalyst aging, the contributions from pyridinic/pyrrolic or –C=N- nitrogen, known as active sites for ORR on N-CNTs [24,25], decrease while quaternary nitrogen and $\pi-\pi^*$shake-up satellites or oxidized nitrogen increase.

Peak Number	Peak Type	B.E. eV	Description	CNT1	CNT2	CNT3	CNT4
1	O1s	530.0-531.0	C=O	34.0	33.8	22.0	17.0
2	O1s	532.0-533.0	C-O; C-O-C	66.0	66.2	78.0	83.0
3	N1s	398.4-398.8	Pyridinic N	-	-	33.8	29.1
4	N1s	399.5-400.5	Pyrrolic-N or -C=N-	-	-	45.1	26.9
5	N1s	401.0-402.0	Quaternary-N	-	-	13.7	21.7
6	N1s	403.0-405.0	Oxidized Nitrogen or π-π^* Shake-up Satellite	-	-	7.4	22.3

Tab. 5.2: Relative Peak Areas of O1s and N1s XPS peaks [12].

Fig. 5.4 shows electrochemical performances of N-CNTs. It displays cathodic polarization curves for ORR recorded at ω=1600 rpm in 0.1M $HClO_4$. A limiting current is not detected for all samples; the best onset potential (CNT3, E_{on} ~ 0.390 V vs Ag/AgCl) is about 0.2 V more cathodic than a similar value for a commercial Pt catalyst (E_{on} ~ 0.6 V vs Ag/AgCl) [19].This is apparently rewarding for N-CNTs ORR data [24,26,27]. The onset potentials depend on catalyst aging (E_{on}=0.207, 0.311, 0.391 and 0.244 V for CNT1, CNT2, CNT3 and CNT4, respectively) favorably increasing on the first three samples, and decreasing instead on CNT4 where it becomes close to the CNT1 value.

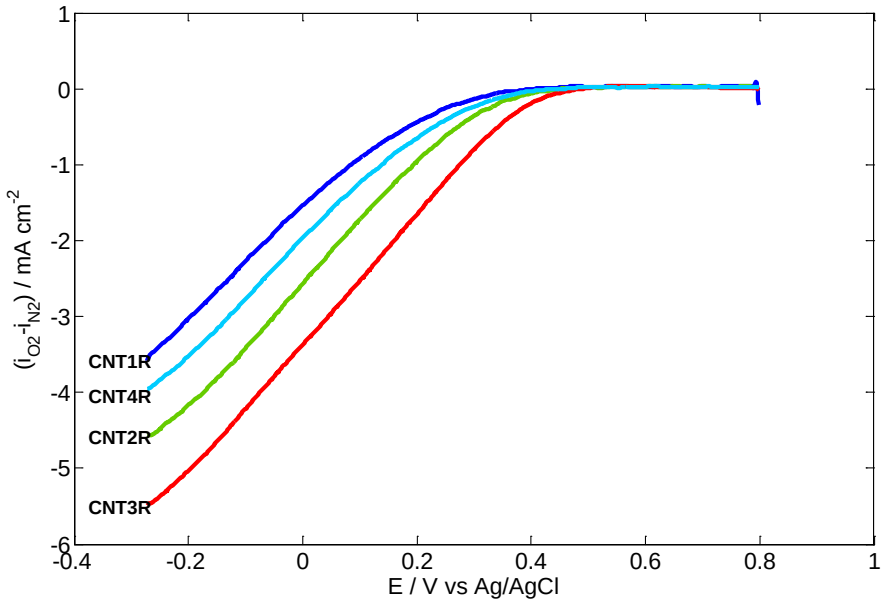

Fig. 5.4: Electrochemical behaviour recorded in oxygen-saturated 0.1 mol dm^{-3} $HClO_4$. T= 25 °C; cyclic voltammograms (v= 5mV s^{-1}; ω=1600 rpm) [12].

To confirm these data LSV measurements were done at v=50 mV s^{-1} (**Fig. 5.5**) [28,29]. In all cases, except for CNT1, a cathodic peak is rather clearly identified, implying that these materials have an acceptable ORR activity with a relative shift of the maximum peak potential that agrees with the similar shift of onset potentials in **Fig. 5.4**. CNT3 is the most active catalyst. In this case, as shown in **Fig. 5.6**, peak currents measured at different scan rates (v) are proportional to the square root of v. Hence, a mass transfer step is rate determining.

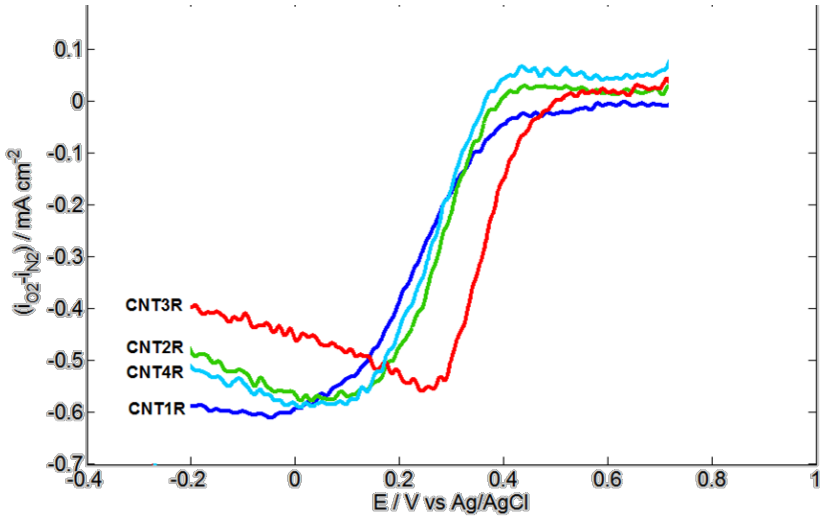

Fig. 5.5: Linear sweep voltammetry (v=50 mV s^{-1}; ω=0 rpm) [12].

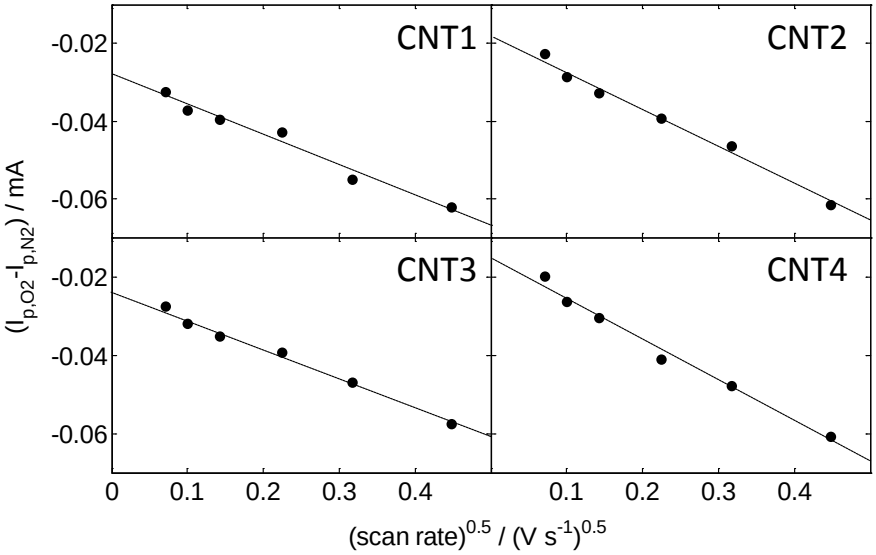

Fig. 5.6: Peak currents measured at different scan rates (v) for CNT1, CNT2, CNT3 and CNT4 [12].

Fig. 5.7 shows cathodic ORR polarization curves recorded on CNT3 at different electrode rotation rates. The inset shows the corresponding Koutecky-Levich plots at different potentials. From the average plot slopes, a number of exchanged electrons of CNT3 n=4.5±0.2 is obtained. It can be concluded that the preferred ORR mechanism is direct formation of H_2O.

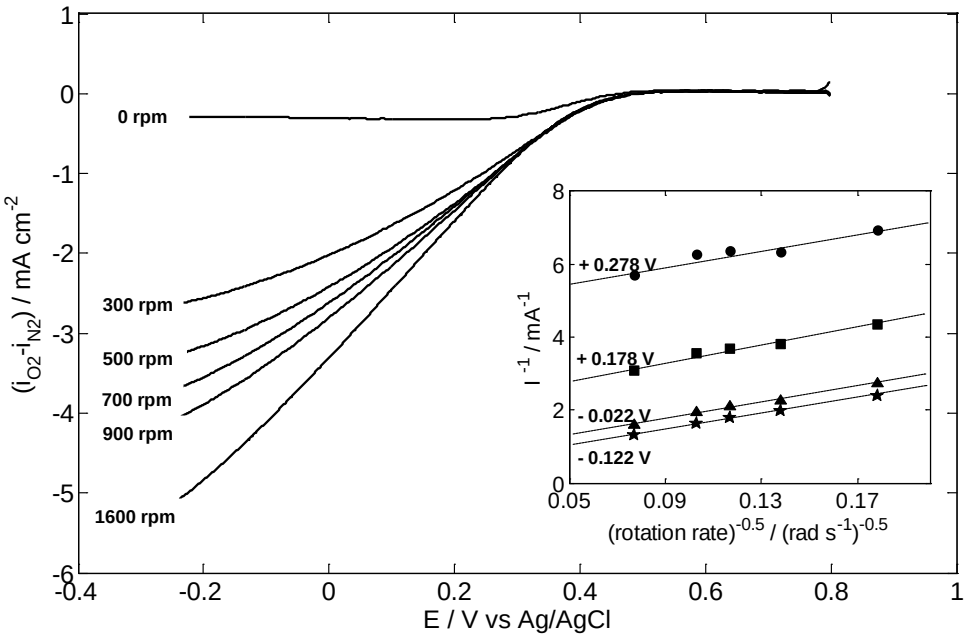

Fig. 5.7: Cyclic voltammograms of CNT3 (v=5 mV s^{-1}). Inset: Koutecky-Levich plot of CNT3 [12].

It is worth to highlight that the sample containing the highest iron and nitrogen amounts (CNT4) is not the most active for ORR. This is surprising, because the presence of metal impurities and synergistic effect between N and iron are known to improve ORR electrocatalytic properties of both CNTs [30] and N-CNTs [31]. It can be assumed that in our N-CNTs iron and nitrogen can interact in various ways of which only a fraction is useful to the formation of catalytic sites. As a fact, the best ORR results are obtained on the sample that

contains the highest amount of pyridinic/pyrrolic nitrogen, that are considered most active for ORR on N-CNTs [24,25]. CNT3 is also the material with the best developed morphology. The observed trend in onset potentials suggests a relation with surface composition: in a first instance, a sample that contains small iron amounts and no nitrogen is not electroactive, other samples containing both nitrogen and iron, are instead catalytically active to various extent. From this point of view, when pyridinic/pyrrolic nitrogen amount decreases the onset potential worsens (see CNT4). Hence, the presence and nature of nitrogen surface groups appear more important to improve N-CNTs ORR activity than the presence of metal impurities only.

Since in the literature the surface composition of the many catalysts adopted to synthesize N-CNTs is of extreme importance to impart specific end product properties [8,10], the above reported aging time effects point to variations in the surface composition of the present Fe/MgO vary during its shelf life: element diffusion in the lattice or changes in oxidation state could take place causing variations of nature and density of the active centres, and of the produced N-CNTs. Further studies, presented in the next section, on the structure and composition of the Fe/MgO catalyst as a function of aging may help to better understand the above results.

5.2.3. The Fe/MgO catalyst ageing

This section is focused on studying the differently aged Fe/MgO catalyst, aiming to understand the influence of its structure and composition on the nanotubes grown on it. As previously reported, a single Fe/MgO batch was prepared. Aliquots were withdrawn at 1, 6, 10, 70 days from the preparation and are labeled Fe/MgO 1, Fe/MgO 2, Fe/MgO 3 and Fe/MgO 4, respectively. These were employed to synthesize a relevant N-CNT sample, labeled CNT1, CNT2, CNT3 and CNT4, respectively.

It is worth to go deep into the surface physico-chemistry by BET characterization techniques. N-CNTs growth is in fact a reaction involving the surface of Fe/MgO and not its bulk fraction. Going through these data is indeed quite interesting, as shown in the following.

By comparing the N_2 adsorption-desorption isotherms, displayed in **Fig. 5.8**, it is noticeable that their shape is similar. On the basis of IUPAC classification they belong to the reversible type IV isotherm, with a hysteresis loop which is characteristic of mesoporous materials [32]. The desorption branches are characterized by a H3-type hysteresis loop which is, in the relevant literature [33], attributed to a non-fixed aggregation of plate-like particles giving rise to slit-shaped pores.

Apart from isotherms shape, samples show remarkable differences in their surface area, that surprisingly decreases with ageing, as shown in **Tab. 5.3**, from 149 ± 1 m^2g^{-1} for Fe/MgO 1 down to 30.4 ± 0.3 m^2g^{-1} for Fe/MgO 4, the oldest sample. In **Fig. 5.9** some considerations can be done in order to understand the relations between such evident modifications in surface area and distributions in pores. Just a rapid glance is useful in showing that pores with a diameter between 5 and 20 nm are the most abundant in all samples. Focusing on this pore range and on larger pores, no evident differences are noticeable among samples. Some interesting aspects, on the other hand, are coming out from the analysis of the same histogram, but focusing now onto smaller pores. Moving from sample Fe/MgO 1 to Fe/MgO 4, surface area decrease is indeed accompanied by an evident micropores percentage increase,

as presented in **Fig. 5.9** and **Tab. 5.3**. The micropores increase is also followed by a decrease in the abundance of pores between 2 and 5 nm. This might mean that the structure of the Fe/MgO catalysts is at least changing, and small mesopores are closing (or filling) in favor of micropores formation.

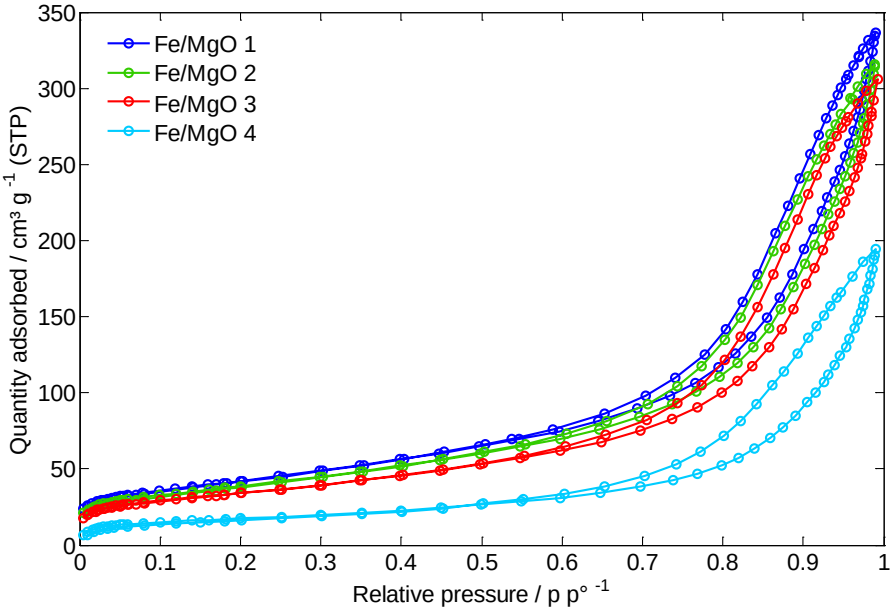

Fig. 5.8: N_2 adsorption/desorption isotherms at 77 K for Fe/MgO 1, Fe/MgO 2, Fe/MgO 3, Fe/MgO 4.

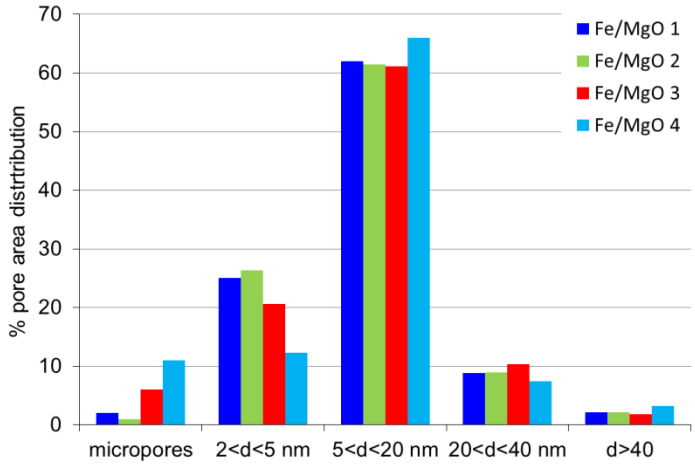

Fig. 5.9: Pore area distribution.

Sample	BET surface area / m^2g^{-1}	% Micropores
Fe/MgO 1	149 ± 1	2
Fe/MgO 2	137 ± 1	1
Fe/MgO 3	121 ± 1	6
Fe/MgO 4	30.4 ± 0.3	11

Tab. 5.3: BET surface area values and micropores percentages.

Results of XPS atomic percent composition are reported in **Tab. 5.4.**

Sample	Mg %	O %	C %	Fe %	O/Mg %	Fe/Mg %
Fe/MgO 1	38.7	51.2	7.6	0.5	1.32	0.013
Fe/MgO 2	34.5	48.7	16.0	0.4	1.41	0.012
Fe/MgO 3	42.9	49.0	11.6	0.6	1.14	0.014
Fe/MgO 4	41.9	53.1	4.3	0.1	1.27	0.002

Tab. 5.4: Sample composition: atomic percent from XPS.

Fig. 5.10 reports all XPS results. Considering O/Mg % value, it is not undergoing specific changes when moving from Fe/MgO 1 to Fe/MgO 4. Important considerations are instead related to the presence of iron on the surface, because in the last sample, Fe/MgO 4, the oldest one, Fe is almost absent after being unchanged in the first three samples (with a maximum Fe percentage in the Fe/MgO 3 sample, which gave best results in N-CNTs structure and activity). By considering that iron is the real catalyst for N-CNTs growth, its very low concentration on the surface of Fe/MgO 4 might explain the reason why N-CNTs are not well formed on it. A change in the structure of Fe/MgO samples, also detected by BET analysis, followed by elements moving/digging/being covered within the sample, could explain why iron is no more detectable on the surface of a too aged sample.

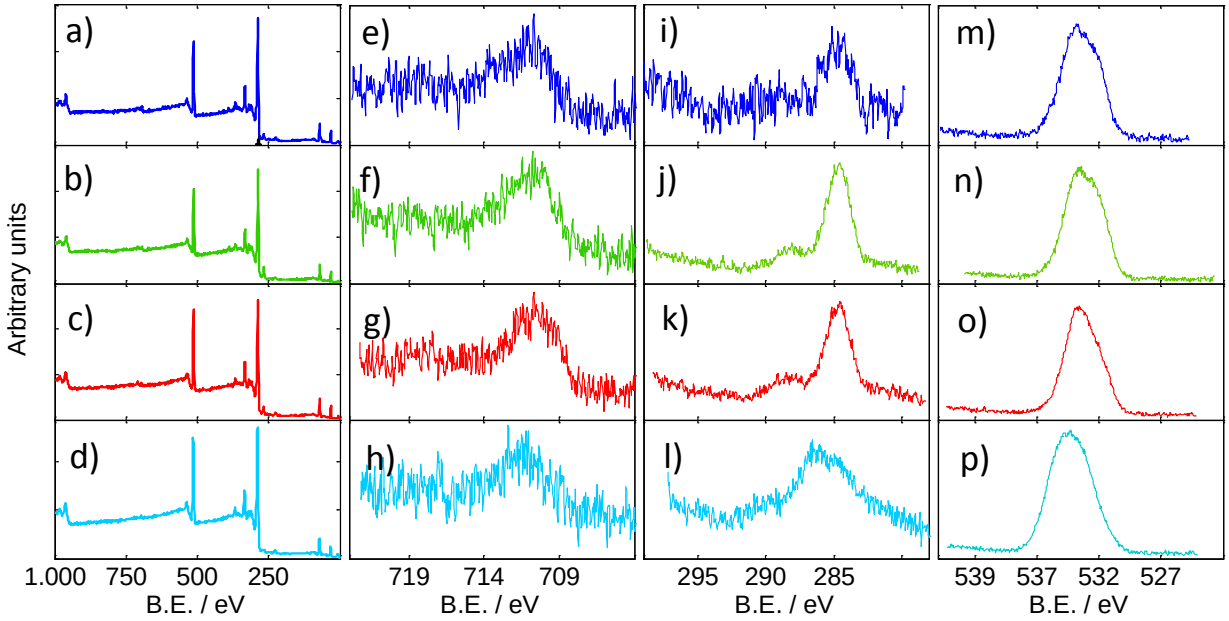

Fig. 5.10 a-p: Surveys (a-d) and XPS High Resolution Spectra: Fe2p$_{3/2}$, e) Fe/MgO 1, f) Fe/MgO 2, g) CNT Fe/MgO 3, h) Fe/MgO 4; C1s, i) Fe/MgO 1, j) Fe/MgO 2, k) Fe/MgO 3, l) Fe/MgO 4; O1s, m) Fe/MgO 1, n) Fe/MgO 2, o) Fe/MgO 3, p) Fe/MgO 4.

The HR-Fe 2p$_{3/2}$ XPS spectra were recorded only in the region at relative low binding energies, as shown in **Fig. 5.10 e-h**. It is not easy to achieve a straight peak deconvolution in the iron region in the XPS spectra, due to the low percentages of iron present on the surface and, as a consequence, the high noise. Instead of fitting this region with a lot of peaks, whose attribution might be openable, a simpler solution was found in order to compare the four samples and possibly identify the main differences. The region was deconvoluted by fitting

with one only peak, normalizing for the maximum and subtracting the base line of each spectrum. The resulting peaks were then superimposed, as shown in **Fig. 5.11**.

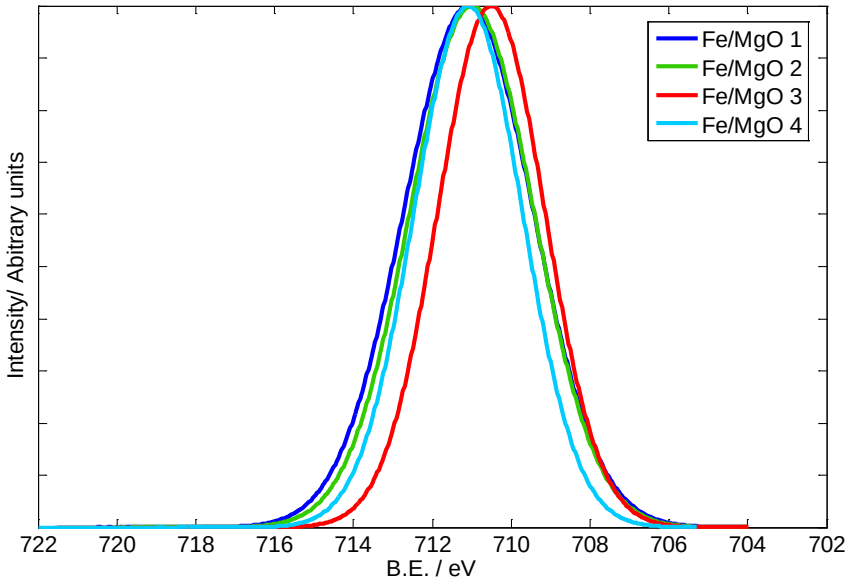

Fig. 5.11: Fe $2p_{3/2}$ HR-XPS region. Peak fitting.

It is clear that deconvoluted peaks relative to samples Fe/MgO 1, Fe/MgO 2 and Fe/MgO 4 overlap, and, surprisingly, the only non-overlapping peak corresponds to Fe/MgO 3 sample. Fe/MgO 3 peak shifting to lower binding energies is explained by considering that this samples has an higher surface content of Fe^{2+} species, compared to Fe^{3+} ones. It is worth mentioning that Fe/MgO 3 sample is the catalyst giving the most structured carbon nanotubes, as shown previously in TEM imaging. The hypothesis that, for a proper nanostructures growth, it is necessary to achieve a specific surface composition of the catalyst used in the synthesis can be here first mentioned. By considering that Fe/MgO sample is also the only one having the highest percentage of iron on the surface (as detected by XPS), it is however difficult to state without doubts if it is better having an high surface iron content, whatever its relative composition and oxidation states are, or if it is more important that the surface contains, unless in lower amounts, specific iron species [34-37].

The high resolution C1s region has been deconvoluted as shown in **Fig. 5.10 i-l**; a small peak at 281-282 eV is detectable in Fe/MgO 2, 3 and 4 samples, and it is attributable to the presence of C bond to another less electronegative element, probably Mg [38]. This carbide species, as shown in **Tab. 5.5**, increases by ageing in samples. The peak at 284.6 eV is instead assignable to adventitious carbon that is decreasing with time from Fe/MgO 1 to 4, and the peak, detectable only for Fe/MgO 4, at higher energies (286- 287 eV), is due to C-O species [20-23]. The last peak, at higher binding energies, detectable for all samples, at 289 eV might be due to the presence of carbonates [39]. It is interesting to notice that carbonates percentage on the surface of samples is increasing with time.

C1s % peaks				
Sample	**MgC 281-282 eV [38]**	**Adventitious carbon 284.6-284.8 eV [39]**	**C-O species 286-287 eV [20]**	**Carbonates 288-289.6 eV [20-23]**
Fe/MgO 1	-	86.4	-	13.6
Fe/MgO 2	5.8	78.0	-	16.2
Fe/MgO 3	12.7	69.0	-	18.3
Fe/MgO 4	15.3	40.0	25.6	19.1

Tab. 5.5: HR XPS C1s region: peaks attributions and relative percentages.

Deconvolution of the main peak in the high resolution region of O1s reveals the presence of a contribution of Fe-O at 528-529.5 eV which decreases with time [40] and another contribution due to MgO lies between 530.5 and 531 eV [41]. In the region between 531.5 and 532.6 eV, peaks are attributable to magnesium hydroxide and adsorbed water and their relative percentages, as shown in **Tab. 5.6** , increase with time [42,43].

O1s % peaks			
Sample	**Fe-O 528-529.5 eV [40]**	**MgO 530.5-531 eV [41]**	**$Mg(OH)_2$ 531.5-532.6 eV [42,43]**
Fe/MgO 1	**41.5**	**43.3**	**15.2**
Fe/MgO 2	**36.6**	**47.9**	**15.6**
Fe/MgO 3	**31.6**	**52.4**	**16.1**
Fe/MgO 4	**19.1**	**52.5**	**28.4**

Tab. 5.6: HR XPS O1s region: peaks attributions and relative percentages.

Aiming to deeply understand the chemistry beyond these modifications, a thermogravimetric analysis (TGA) was first performed on the $MgCO_3 \bullet Mg(OH)_2 \bullet 5H_2O$ precursor, as shown in **Fig. 5.12**. In this way bulk changes are taken into consideration as well as the surface ones. After the first slight loss of weight attributable to physisorbed water in the range between 25°C and 150°C, an appreciable decaying step between 210°C and 300°C can be attributed to crystallization water loss [44]. Finally, the main steep weight loss, between 380°C and 500°C, is due to CO_2 release and hydroxyl groups decomposition. Keeping in mind that the decomposition of $MgCO_3 \bullet Mg(OH)_2 \bullet 5H_2O$ precursor, in order to obtain MgO, was performed at 400°C, it can be therefore inferred that the chosen temperature was not high enough to achieve the complete carbonates and hydroxyl groups decomposition [44,45]. A TGA analysis of the final Fe/MgO samples was then performed in the same conditions. TGA of Fe/MgO 1, 2 and 4 samples is displayed in **Fig. 5.12**. In **Tab. 5.7** weight loss percentages are summarized and assigned to decomposing species.

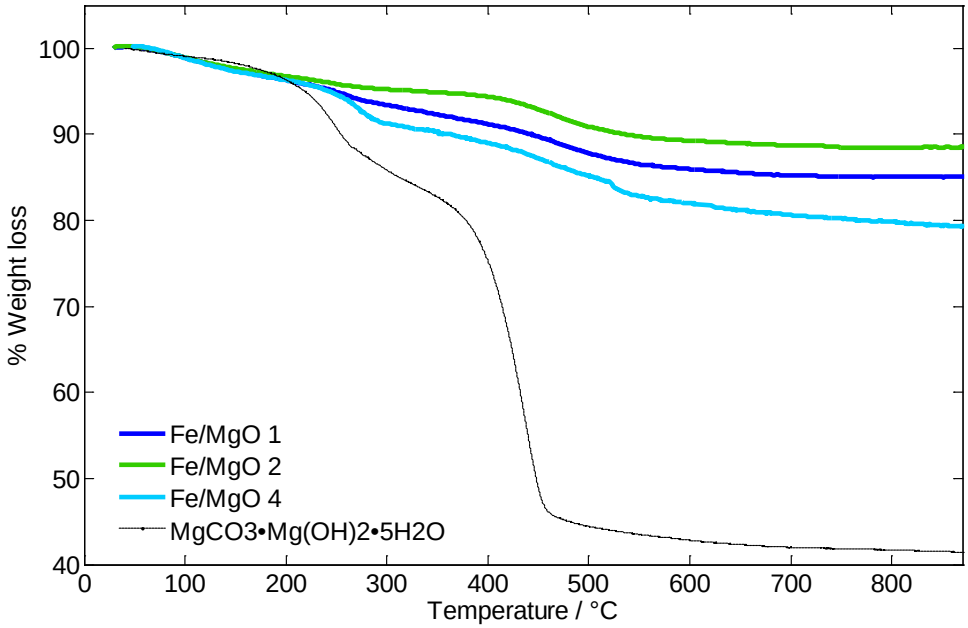

Fig. 5.12: Weight loss percentages measured by TGA.

Sample	% Physisorbed water loss	% Crystallization water and nitrates loss	% Carbonates and hydroxyles loss
Fe/MgO 1	2.5	1.5	8.5
Fe/MgO 2	2.5	0.5	7.5
Fe/MgO 3	Data not available	Data not available	Data not available
Fe/MgO 4	2.5	4	12.5

Tab. 5.7: Weight loss attributions and percentages.

The loss of physisorbed water is evident between 25°C and 150°C and, after the weight loss due to crystallization water, nitrates and hydroxyl groups (from 200°C to 280°C), it is noticeable that from 300°C there is an almost continuous and uniform loss of weight until the end of the analysis. Focusing on this last weight decrease, its starting point almost corresponds, in **Fig. 5.12**, to the temperature at which CO_2 and hydroxyl groups begins to be released as discussed above for $MgCO_3 \bullet Mg(OH)_2 \bullet 5H_2O$ TGA interpretation. This confirms the previous hypothesis that in the Fe/MgO samples, a fraction of carbonates and hydroxyl groups is still present. Being thermal labile groups, their presence in the sample might account for the fragility of the structure that changes with time.

In addition, MgO is known to be a CO_2 adsorber [46,47]. Hence, the presence of carbonates in the samples might be due both to an uncompleted decomposition of the $MgCO_3 \bullet Mg(OH)_2 \bullet 5H_2O$ precursor and to a further adsorbing process during the Fe/MgO shelf life, kept on the shelf without any kind of precautions. Undecomposed carbonates in the bulk fraction, might come to the surface as CO_2, causing a change in the structure (explaining the surface area and pore area distribution modifications), while the very external surface adsorbs CO_2 and water from the atmosphere, thus explaining the reason why micropores are forming with time. In fact, the adsorbing process might partially close pores by filling them, making their dimensions smaller.

These data were confirmed in part by Temperature Programmed Desorption-Mass Spectroscopy analysis (TPD-MS). CO and CO_2 release were mostly detected in $MgCO_3 \bullet Mg(OH)_2 \bullet 5H_2O$ sample at 600°C and above 550°C, respectively, as shown in **Fig. 5.13 A.** In **Fig. 5.13 B** the same analysis was performed on Fe/MgO 4 sample. From the last figure it can be inferred that both carbon monoxide and, more importantly, carbon dioxide were still present in the sample and released at lower temperature, a further confirmation that the decomposition of the $MgCO_3 \bullet Mg(OH)_2 \bullet 5H_2O$ precursor was not completely achieved and there were some undecomposed/adsorbed carbonates left in the final Fe/MgO 4 sample. As clearly depicted in **Fig. 5.13 C**, nitrates were detected only, as expected, in the Fe/MgO 4 sample, due to the doping process that the sample underwent before calcination.

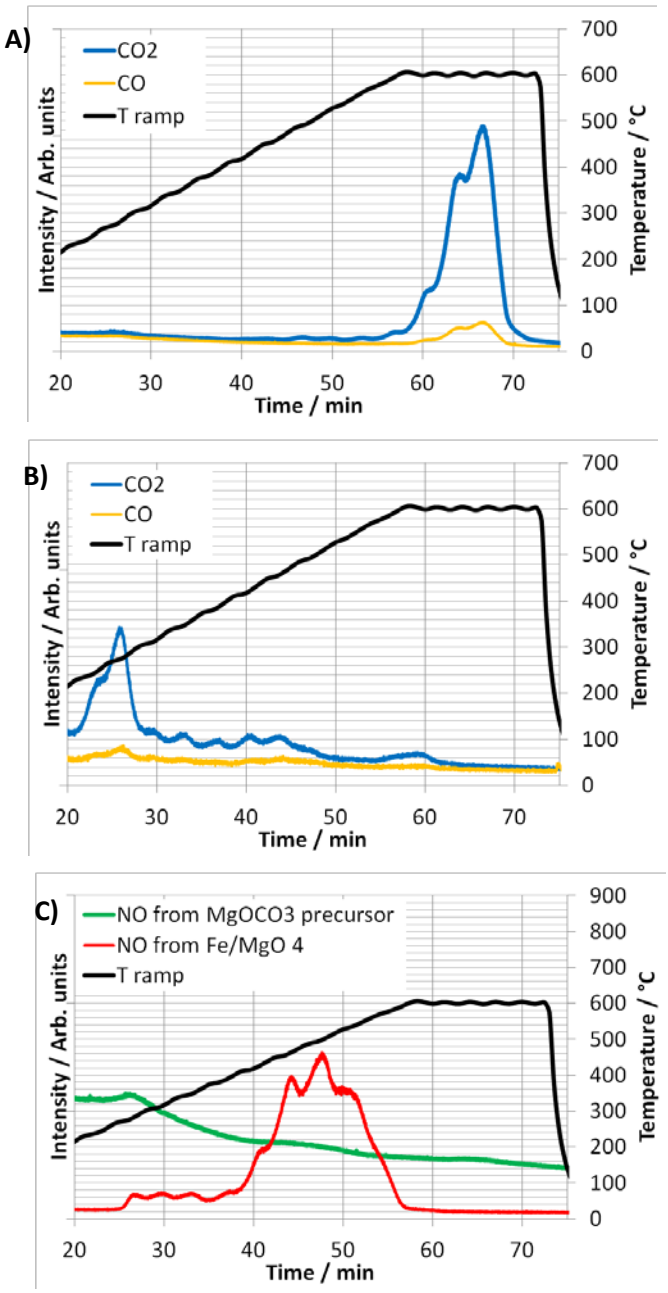

Fig. 5.13 A-C: TPD-MS analyses curves. A) $MgCO_3 \bullet Mg(OH)_2 \bullet 5H_2O$ sample. B) Fe/MgO 4 sample. C) Nitrates release comparison in samples $MgCO_3 \bullet Mg(OH)_2 \bullet 5H_2O$ and Fe/MgO 4.

In order to understand these surface and bulk modifications, XRPD measurements were first performed in-house on Fe/MgO 1, Fe/MgO 2, Fe/MgO 3 and Fe/MgO 4. All the diffraction patterns are almost perfectly overlapping with the curve reported in **Fig. 5.14** for FeMgO 1, meaning that apparently there is no evidence of long range symmetry phase changes during catalyst ageing.

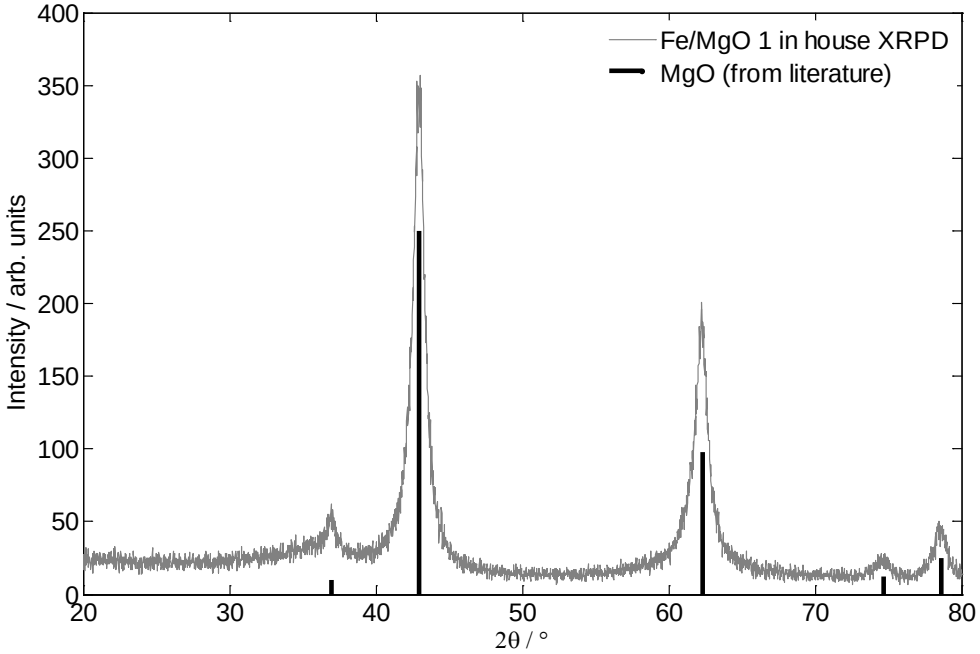

Fig. 5.14: XRPD diffraction pattern of sample Fe/MgO 1 and comparison with MgO data from literature.

Diffraction patterns interpretation is quite straightforward. Peaks at 2θ = 36.9°, 42.9°, 62.3°, 74.7° and 78.6° are rather broad, typical for not completely crystalline materials, and are assigned to the (111), (200), (220), (311) and (222) reflections of MgO syn periclase, respectively (PDF#00-045-0646). In these XRPD patterns there is no evidence of peaks assignable to carbonates and iron species; this could be explained by the presence of non-crystalline phases or too low quantities to be detected by this technique.

Synchrotron HR-XRPD was then performed (**Fig. 5.15**) on Fe/MgO 3 and Fe/MgO 4 samples in order to reveal impurity phases and subtle deviations from the previously obtained structure that could not be detected by in-house XRPD. In agreement with in-house XRPD measurements, the main Bragg peaks belong to the MgO cubic periclase phase (see peak assignment before). Qualitative comparison of the Fe/MgO 3 and Fe/MgO 4 synchrotron patterns highlight some interesting differences.

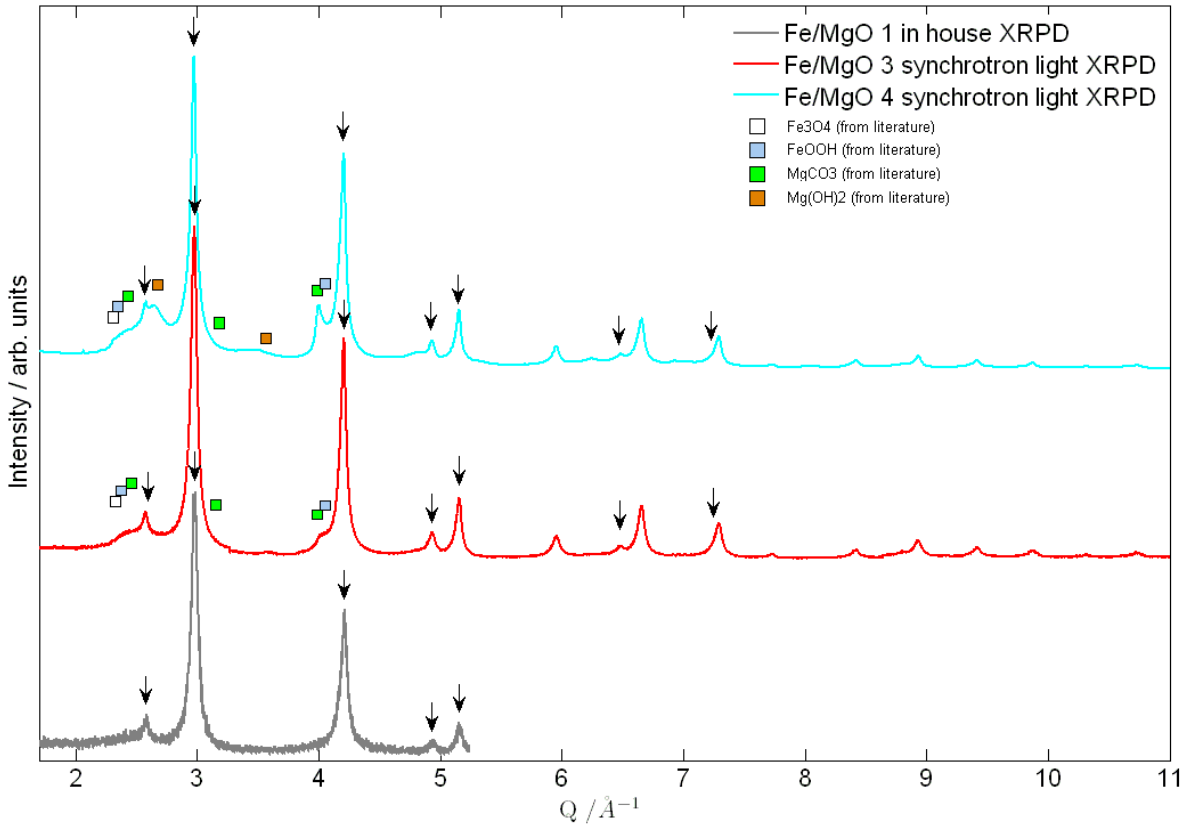

Fig. 5.15: Diffraction patterns measured by in-house XRPD and synchrotron light. Black arrows indicate MgO main peaks from literature.

As reported in **Tab. 5.8**, structure of MgO was modeled using the periclase phase with space group $F\ m\ \bar{3}\ m$. The refined cell parameters (a) did not evidence any cell expansion/contraction with time. This rules out formation of solvate crystals following encapsulation of water and/or CO_2 in MgO, which would result in a larger cell parameter.

Parameters	Fe/MgO 3 measured@esrf	Fe/MgO 4 measured@alba
a / Å	4.2250 ± 0.0002	4.2260 ± 0.0005
$100xU_{mean}$ / °Å^2	0.38 ± 0.01	0.12 ± 0.05
MgO phase wt. fraction	0.854 ± 0.004	0.693 ± 0.003
χ^2	6.499	392.1
$R(F^2)$	0.0215	0.0337
wR_p	0.0536	0.0676
Space group (n.)	*F m* $\bar{3}$ *m* (227)	
Mg	*4a* (0,0,0)	
O	*4b* (0.5,0.5,0.5)	

Tab. 5.8: Parameters derived by synchrotron light XRPD patterns interpretation.

A single Debye-Waller factor, U_{mean}, was used for Mg and O, as both are low-Z atoms and lie in sites with the same symmetry (4a e 4b in Wyckoff notation).

The accuracy of the structure assessment is expressed by two parameters: goodness of fit, χ^2, and fit residual, R(F^2), which ideally should be closest to 1 and 0, respectively.
Results evidence a poor fit of the Fe/MgO 4 pattern with the MgO phase only, owing to the presence of a number of phases besides MgO not taken into account.
The interesting aspect of these measurements is the detection of phases other than MgO, as evidenced by shoulders and secondary peaks in the patterns. Contributions of spurious phases evolved with time passing from Fe/MgO 3 to Fe/MgO 4. Rietveld refinement including additional phases allowed for the quantitative phase analysis of the two samples.
In the Fe/MgO 3 pattern, crystalline phases of FeOOH and FeO were detected and assigned as shown in **Fig. 5.15**. The relative ratio of the crystalline phases in Fe/MgO 3 was found to be MgO : FeO : FeOOH = 82 : 16 : 2 % wt.
In Fe/MgO 4 sample, crystalline phases of $Mg(OH)_2$, FeOOH and FeO were detected and assigned as shown in **Fig. 5.15**. The relative ratio of the crystalline phases in Fe/MgO 3 was found to be MgO : $Mg(OH)_2$: FeO : FeOOH = 53 : 24 : 11 : 12 % wt (these results are in accordance with XPS results).
The quantitative analysis shows that: i) the main product of iron nitrate calcination is FeO; ii) magnesium oxide takes up water during aging, forming magnesium hydroxide in considerable amount; iii) Mg and Fe carbonate and nitrate crystalline phases are inconsistent with the XRPD data of Fe/MgO 4.
However, amorphous iron nitrate might be left in the sample after calcination at 300 °C. Also, aging of Fe/MgO 3 in air is expected to yield $MgCO_3$, owing to the high affinity for CO_2 of alkaline-earth metals. Amorphous Fe nitrate and Mg carbonate, and their hydrated forms ($FeNO_3 \cdot nH_2O$ and $MgCO_3 \cdot nH_2O$), probably constitute the large amorphous scattering found in Fe/MgO 4 (see the irregular background at low Q in Fig) after 40 days aging in air.

In order to summarize the above results, in this section the shelf life of Fe/MgO samples was studied on what concerns both the material bulk and surface chemical composition and structure. In particular, by ageing:

- CO_2 was found in all samples (by TGA, TPD-MS, XPS), even in the youngest Fe/MgO 1, because it derives from an incomplete decomposition of the magnesium basic carbonate precursor [44,45]. The presence of instable carbon dioxide, migrating from the bulk to the surface to be released, might account for the fragility of the structure that, collapsing, changes with time the materials surface area and porosity features.

- CO_2 is, in the meanwhile, accumulating together with adsorbed water. MgO materials are indeed known to be good CO_2 adsorbers [46,47]. On the surface CO_2 was in fact found to increase (by XPS) its amount with time. This is a combined result of the migration and accumulation processes.

- Ageing modifies iron species relative percentages, as detected by XPS. In particular, Fe^{2+} was found to relevantly increase its percentage on the surface after 10 days from Fe/MgO catalyst preparation. Reasons of this surface changes are not known, yet, and need to be investigated in the future.

Therefore, when the N-CNTs synthesis was performed, the precursor was pyrolysed in the presence of a Fe/MgO material that has been modified both in its structure and in its surface composition during the time it waited to be used as the catalyst for nanotubes growth, thus being responsible of the differences found in the nanostructures morphologies.

This is actually an important result to be taken into account when working on carbon nanotubes and their synthesis. A confirmation of the stability and unchanged properties, by physico-chemical methods, of the catalyst used for CNTs growth, should always be done in order to make sure of the reproducibility of the overall synthetic process.

5.3. N-doped carbon nanocubes (N-CNCs)

Elemental carbon exists in a series of aesthetically pleasing architecture, arising from its sp, sp^2, sp^3 bonding models, fostering graphite, diamond, fullerenes, nanotubes, graphene and so on. Carbon is therefore an attracting element and it is considered a structural builder because of its different hybridization types. Lots of experiments has been performed up to now in order to find unconventional phases of carbon different from the recent trend in the field of graphene and nanotubes, showing consequently different morphologies and electrical properties.

To date just a few reports have been published about synthetic carbon nanocubes; while it is worth mentioning that in nature that large scale cuboid graphite has been found in many places [48].

Classes of synthetic cubic carbon exhibits properties like good thermostability, blue luminescence and super-hardness. Some works in literature make use of sophisticated techniques like laser ablation on a carbon substrate or arch discharge techniques [49]. Yang et *al.* [50] synthesized micro and nanocubes with a new bcc structure by pulsed laser ablation in salts solutions. At the liquid-solid interface, amorphous carbon was ablated. The inorganic salts contained in the solution belong to the cubic structure. Hence these salts act as templates for the cubes growth. Authors observed blue-purple luminescence in the cathodoluminescence spectrum at room temperature, indicating this novel carbon materials as candidates for new band gap semiconductors.

Sarkar *et al.*, [51] trying to avoid the difficulties of the laser ablation technique, started from powdered rice and subjected it to thermal treatments. The final product in these previous works was in all cases full cubes.

A few other reports are instead focusing on obtaining empty carbon nanocubes (sometimes also called nanocapsules). To achieve this goal, an MgO substrate was found to be necessary. In particular, Gedanken *et al.* [52] prepared MgO-carbon coated cubes with edges between 500 and 600 nm, by reaction of MgO substrate with $Mo(CO)_6$. Another work by Su *et al.* [53] reports on the synthesis of MgO-filled nanocapsules by reacting acetonitrile on a Fe-doped MgO catalyst.

The facility of the last approach, by using an MgO substrate, is surely to be preferred at least in terms of the quantity of produced material.

To date there is no evidence in the literature of simple methods for the synthesis of empty N-doped carbon nanocubes, as that one that is expose in the following.

The results are relative to a synthesis that was performed by using similar experimental conditions that have been followed in the previous synthesis of N-doped carbon

nanotubes but now using a different liquid precursor, diethylenetriamine, in which a certain quantity of ferrocene was dissolved. Since in this case Fe is already contained in the dropping solution, the MgO substrate, now prepared in a different way, was not impregnated, as in the N-CNTs synthesis, with iron nitrate.
The final product, surprisingly, was found to be composed by hollow N-doped carbon nanocubes (N-CNCs). Due to the available room in its inside part, in addition to the application as catalysts for ORR, this material is an interesting candidate for trapping molecules or nanoparticles. The synthesis and characterization of N-CNCs is presented in the following.

5.3.1. Experimental

All chemicals and solvents, unless differently specified, were purchased from Sigma Aldrich and used as received without further purification. Synthesis of N-CNCs was performed by a catalytic reaction of diethylenetriamine over two different MgO catalysts, labeled as MgOa and MgOb in the following, both of them leading to the same results.

MgOa was synthesized as follows: an aliquot of MgO (puriss.) was placed in a quartz tube and after 20 min in N_2 flow at T=25°C, it was heated slowly (5.5°C min^{-1}) up to T=300°C. The powder was kept at this temperature for 7 h and 30 min and then rapidly quenched to room temperature.

MgOb was synthesized by decomposition of a magnesium hydroxide carbonate precursor: an aliquot of $MgCO_3 \bullet Mg(OH)_2 \bullet 5H_2O$ was placed in a quartz tube and after 25 min in N_2 flow at T=25°C, it was heated (11.5°C min^{-1}) up to T=800°C. The powder was kept at this temperature for 4 h and then rapidly quenched to room temperature.

A fresh solution of ferrocene in diethylenetriamine (1:69 molar ratio) was prepared by 2 min sonication. Synthesis of N-CNCs was carried out in a vertical quartz tube reactor (N_2, 95 cm^3 min^{-1}); at the bottom of the tube a quartz beaker, containing the catalyst, was positioned. The design of the head of the reactor comprised a small quartz tubular gas entrance proceeding straight into the reactor and reaching the edge of the beaker inside. In this way the drops of the precursors were carried directly onto the catalyst with the help of the nitrogen flow.

For each preparation 300 mg of either MgOa or MgOb catalyst were used. After 25 min in N_2 flow at T=25°C, the catalyst was heated slowly (6°C min^{-1}) up to T=800°C. At this temperature an aliquot of the ferrocene/diethylenetriamine solution was added dropwise (2.6 mL h^{-1}, 70 min). At the end, the reaction was interrupted by quenching the reactor to T=25°C. The day after the reactor was placed into the same furnace and heated up to T=400°C (N_2, 100 cm^3 min^{-1}, 6°C min^{-1}). Then, the nitrogen flow was stopped, the reactor was opened and the sample left 2 h under static air to burn amorphous carbon. After quenching to T=25°C the black powder was lixiviated under sonication in 0.5 mol dm^{-3} H_2SO_4 (t=90 min) to eliminate MgO (a or b) catalyst. Finally, after filtration and washing, the sample was dried (T=100°C, N_2 flow, 16 h) [54].

5.3.2. Physico-chemical and electrochemical characterization

In **Fig. 5.16** TEM images are shown. Products (indifferently coming from synthesis on either MgOa or MgOb) have clearly a cubic shape, with average edge dimensions ranging from

100 to 200 nm. In some areas of the analyzed sample, groups of smaller cubic particles, with diameters < 50 nm, are also present (see **Fig. 5.16**). Moreover, under the electronic beam of the instrument, cubes were observed to collapse, burning at the end if the beam was too energetic. The great part of the sample is composed by cubic particles that look empty inside, or at least not electron dense, because the electronic beam let the observer look throughout them. The first hypothesis, confirmed in the following, is that nanocubes are mainly composed of carbon. In addition, as detectable in **Fig. 5.19**, some filled and denser particles are present, even in very scarce quantity in the sample. Their chemical identification will be reported afterwards. With the aim of improving the resolution of the image, and therefore achieving higher magnifications, HRTEM analysis was performed and the resulting images are shown in **Fig. 5.17**. The thickness of the walls, as calculated in **Fig. 5.17**, is estimated to be 5.9 nm; in **Fig. 5.17** many graphene planes are found to compose each wall of nanocubes, and their number is 4-5.

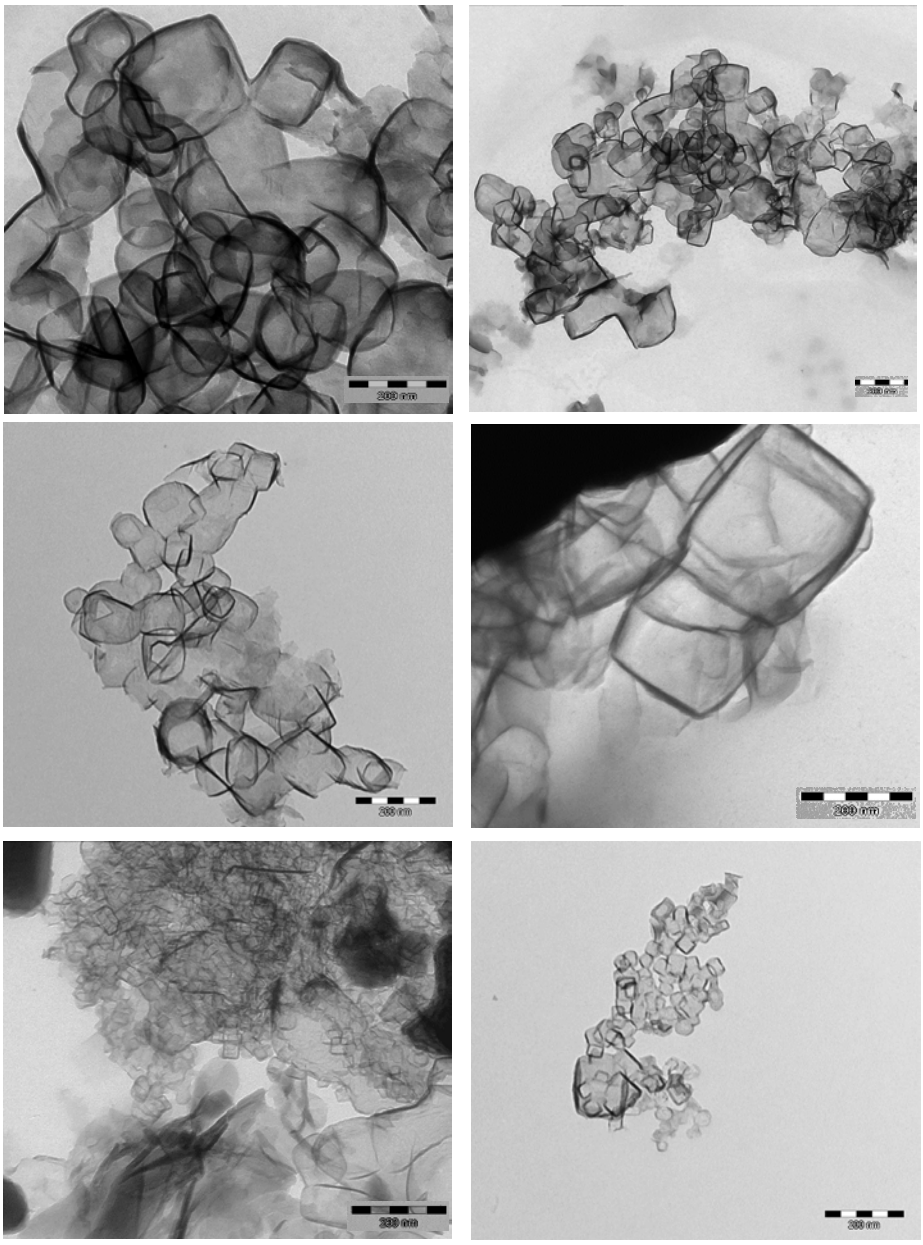

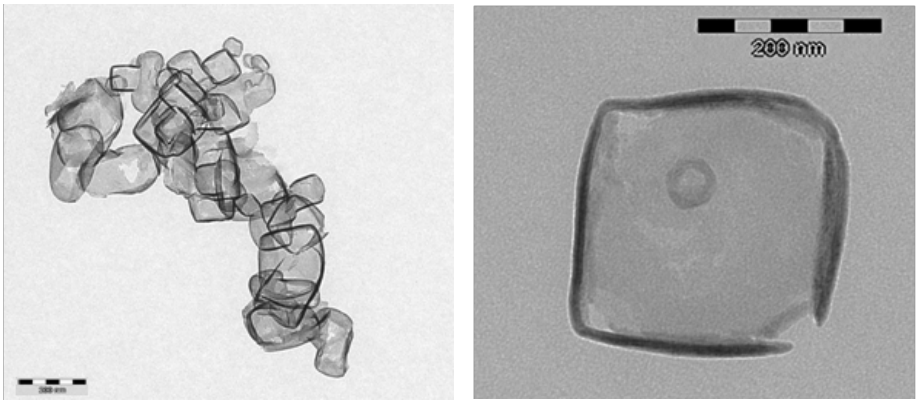

Fig. 5.16: TEM images.

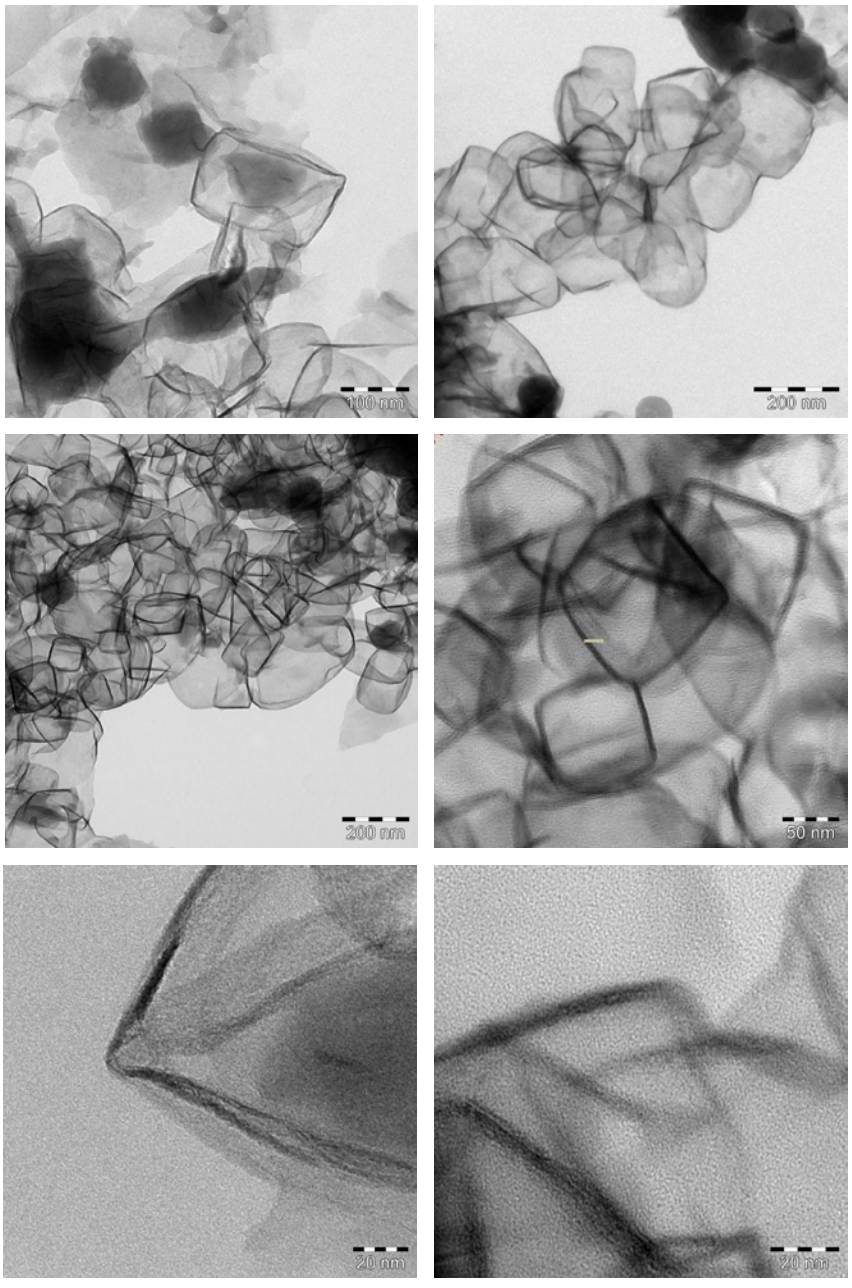

Fig. 5.17: HRTEM images.

By means of the EELS technique, some cubes have been analyzed in order to detect the Fe signal and understand its distribution in the sample. However, probably due to iron very low amount, under the limit of detection of the instrument, Fe peak was not distinguishable from the noise. In the **Fig. 5.18** is shown the energy decay in the energy range where Fe signal should be detected and, clearly, iron peak is not observed.

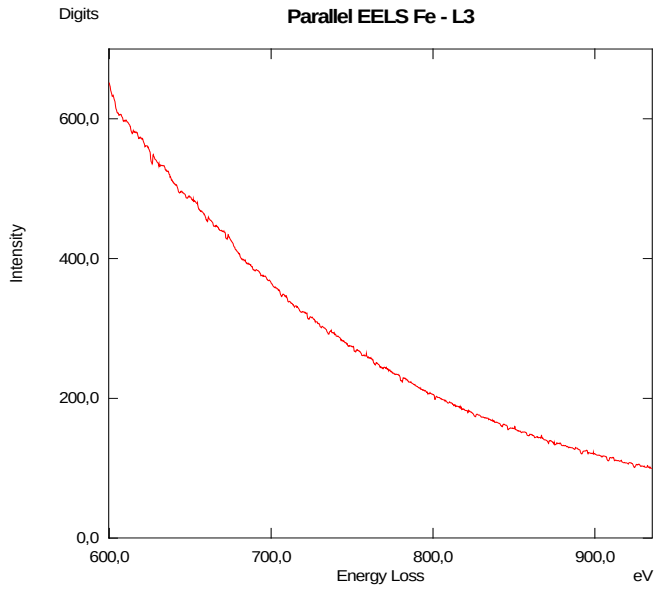

Fig. 5.18: Fe signal detected by HR TEM, EELS technique.

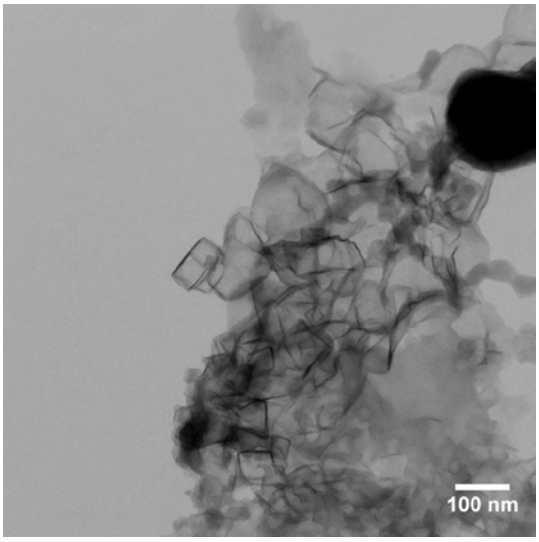

Fig. 5.19: TEM image showing the presence of solid particles.

In **Fig. 5.20** is shown the picture acquired with the STEM mode.

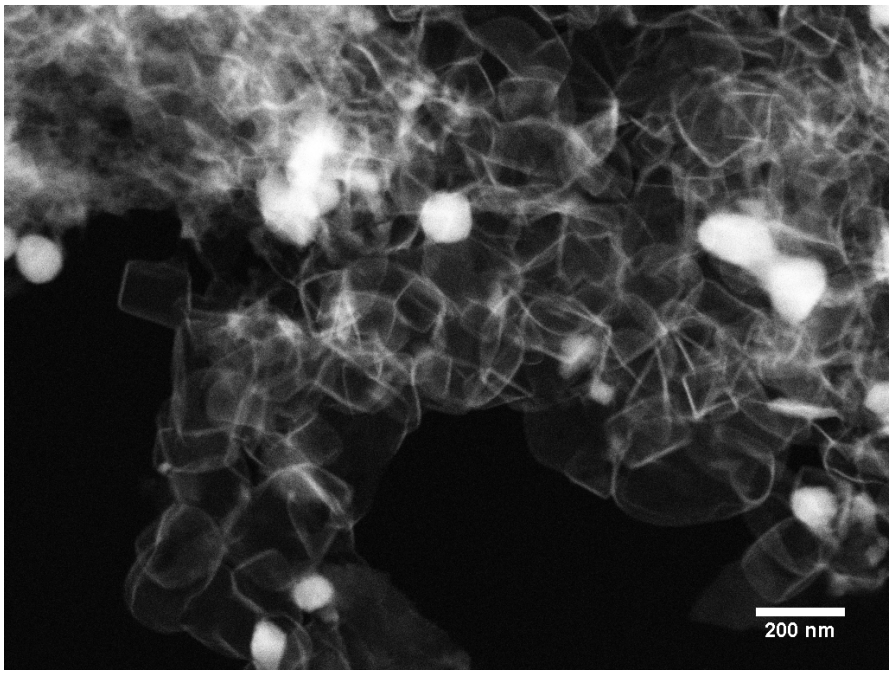

Fig. 5.20: STEM image.

By means of the EDX technique, a compositional analysis was performed in the areas shown in the STEM image in **Fig. 5.21**. Iron is not detectable, but, surprisingly, a strong peak of magnesium was found, together with Cu (due to the sample grid), C and O peaks. By focusing only in an area rich in filled and dark particles (**Fig. 5.21**), it was observed that these nanoparticles are composed of MgO, probably not completely washed away during the acidic washing step.

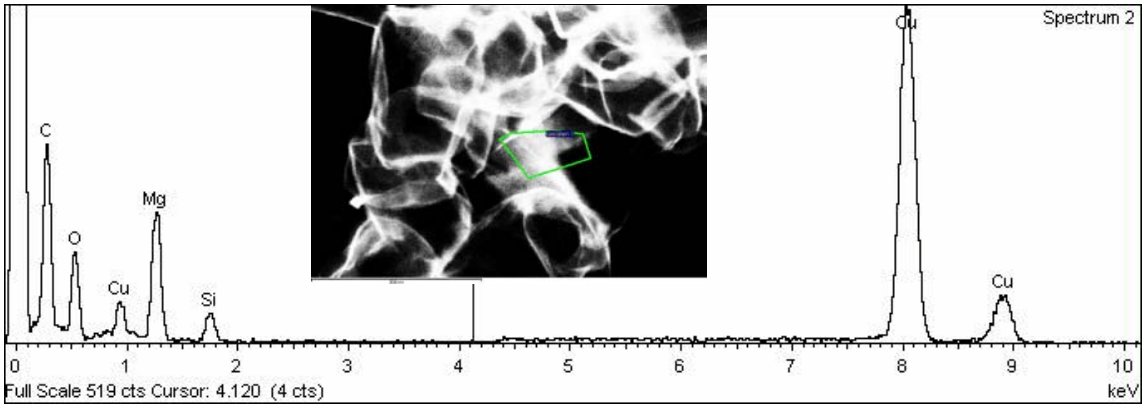

Fig. 5.21: HR TEM, EDX analysis. Inset: selected region.

A few attempts to completely wash away the MgO support have been performed by increasing the sonication time in one case and stirring for 24 hours (instead of sonicating) in the other. However all these experiments failed, because the collected product, as confirmed by TEM analysis (not shown), even if showing a shape similar to the previously obtained nanocubes, lacks however of the well-defined and closed polygonal morphology. The great part of nanocubes were damaged, probably due to the too intense acidic treatment. No further characterization of these damaged samples was performed.

The structure of synthesized nanocubes was then analyzed using SEM and FIB milling. **Fig. 5.22** is a SEM image confirming the cubic shape of the obtained material. Typical cross sections of nanocubes was obtained after exposure of the sample to a Ga-ion beam, as presented in **Fig. 5.22**. It is quite clear that the previous guess about the empty cavity inside each cube was right, even if, as already observed during TEM analysis, the structure is fragile and tends to collapse and dissolve under the electron beam.

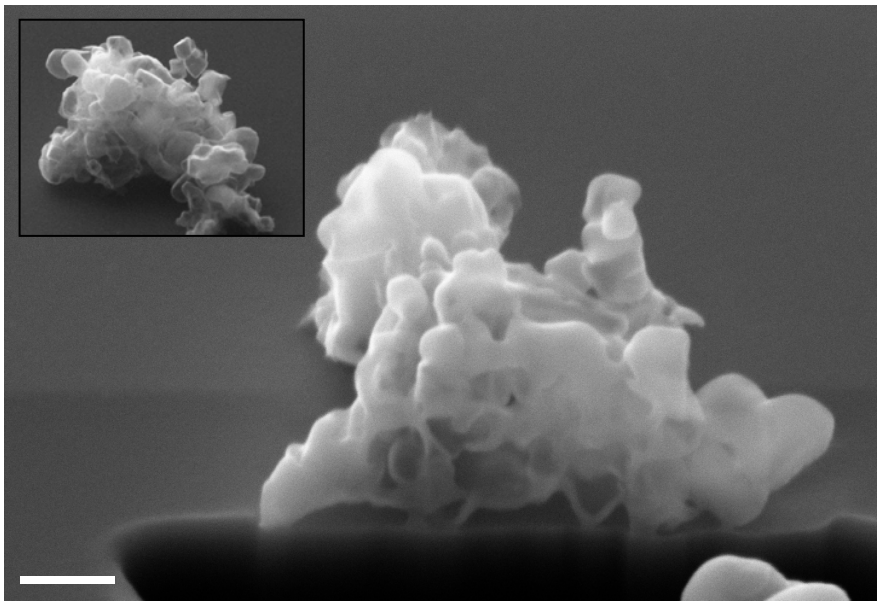

Fig. 5.22: FIB milling image. Inset: corresponding aggregate to be milled.

A deeper investigation of the thermal stability of the material was performed, because, as mentioned above, during SEM-FIB and TEM imaging, nanocubes were observed to "melt" under the electronic beam. By Differential Scanning Calorimetry (DSC) (**Fig. 5.23**) surprisingly an endothermic peak was found to start before room temperature, with a maximum at about 37.5°C and end at about 100°C, followed by peaks due at higher temperature due to change in the structures. Unfortunately, it was not possible to investigate the thermal behaviour at temperatures below 25°C in order to achieve a better baseline. However, as evidenced by **Fig. 5.23**, a modification involving heat flow, is clearly happening. By integrating the peak area, and normalizing for the sample mass, the heat involved in the reaction was calculated to be equal to 185 J g^{-1}. It is quite surprising that the temperature at which a transformation is happening is not high, even if the sample has been already heat treated at 800°C. A first guess is related to the instability of the carbonaceous matrix alone, without the presence of solid particles of magnesium oxide in between, which might act as "physical and mechanical stabilizers" during the treatments at high temperatures. When magnesium oxide is then removed, leaving a few graphene planes forming polyhedral empty structures, the stability of the system might not be ensured and, by giving the system energy, it collapses. Further investigation are absolutely needed to understand the type of transition/reaction taking place when nanocubes are manipulated at temperature just above room temperature.

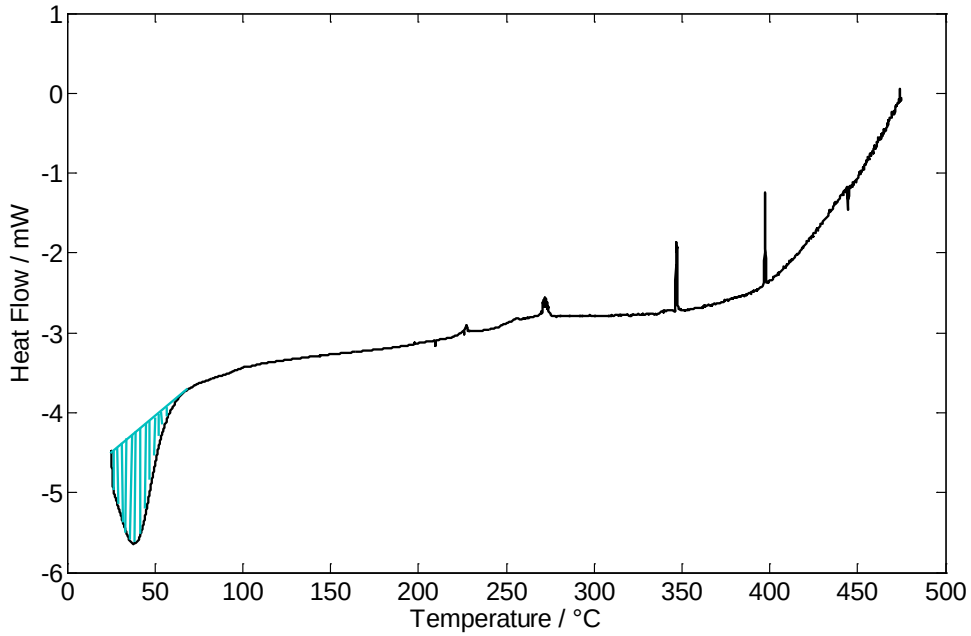

Fig. 5.23: DSC analysis of N-CNCs sample. (performed under N_2 flow, 3°C min^{-1}).

As a last aspect, the surface chemical composition of samples have been investigated by XPS analysis. Results of XPS atomic percent composition are reported in **Tab. 5.8.** Carbon, as expected, is the most abundant element on the surface, surprisingly followed by an high content of nitrogen, if compared to other N-doped samples synthesized in this work (e.g. N-CNTs).

In a similar way of bending edges of nanotubes, nitrogen here might play an important role in letting graphene plane bend and form dihedrals and this could partially explain the formation mechanism of nanocubes.

Moreover, as shown in **Tab. 5.9**, a very small percentage of Mg is present on the surface (1.63%), a lower quantity compared to what detected by EDX mapping, in which the Mg content was almost comparable to the oxygen one. This is another indication about the formation mechanism of N-CNCs. Being the penetration depth of the EDX beam in the order of micrometers, and the penetration depth of the XPS beam in the order of nanometers, it can be assumed that magnesium oxide particles are, during the synthesis, covered by a few layers of graphene, with almost no magnesium oxide left on the external part of nanocubes. After the washing treatment, the great part of MgO is lixiviated, and the remaining one is covered by carbon layers. XPS is not able to overtake the inner carbon layer, hence detecting a very small magnesium quantity, likely due to defects in the nanocubes structure. EDX, on the other hand, penetrating much more in the sample, is able to detect the Mg left in the internal part of the cubic structure. Finally, the small quantity of Si, detected by XPS, might be due to the contact of N-CNCs with the glassware.

Sample	C %	O %	N %	Fe %	Mg %	Si %
N-CNCs	80.88	6.97	9.11	-	1.63	1.41

Tab. 5.9: Sample composition: atomic percent from XPS.

The high resolution N1s region has been deconvoluted as shown in **Fig. 5.24**; the two main peaks are attributable to pyridinic nitrogen (~398 eV) and pyrrolic/pyridonic nitrogen (~400.4 eV) [20]. The O1s region, shows two main components at 530.5 eV and 533 eV, due to C=O and C-O, respectively.

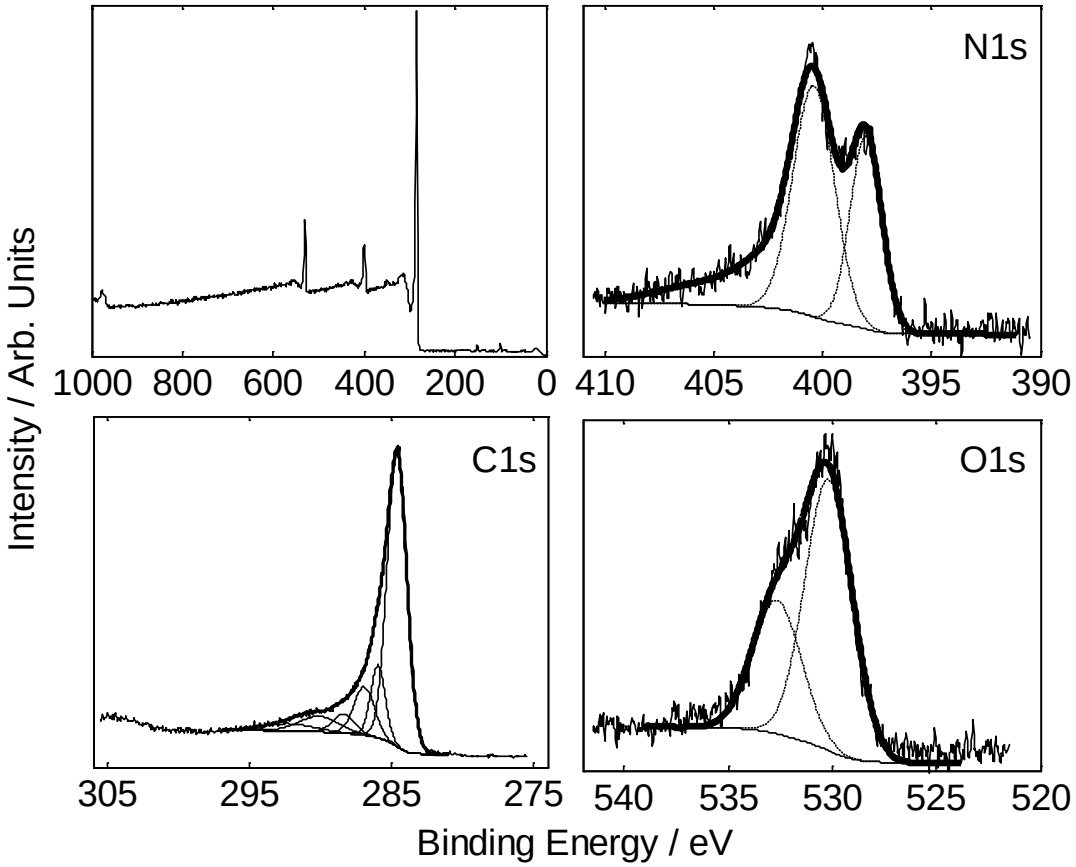

Fig. 5.24: Survey (top left) and High Resolution XP spectra of sample N-CNCs in the C1s, N1s and O1s regions.

In **Fig. 5.25**, a schematic representation of N-doped graphene plane, with all the functionalities typically found when attributing peaks in the O1s and N1s regions, is reported.

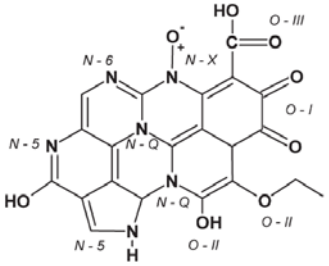

Fig. 5.25: Schematic representation of N and O functionalities in graphene planes [20].

The C1s region is, as expected, the richest in contributions from sp^2 carbon (~284.6 eV), sp^3 carbon (~286 eV) and then other peaks at higher binding energies are attributable to oxygenated species on the surface. By calculating the relative ratio between sp^3 and sp^2 peak areas, equal to 18.4%, a parameter related to the graphitization degree can be achieved [38,20-23].

For comparison with other materials, polarization curves of N-CNCs have been recorded in 0.1 mol dm^{-3} $HClO_4$. Results are not satisfying in terms of ORR activity, as shown in **Fig. 5.26**. The onset potential, laying at about 0.2 V (vs Ag/AgCl), is even lower compared to that one relative to N-CNTs samples.

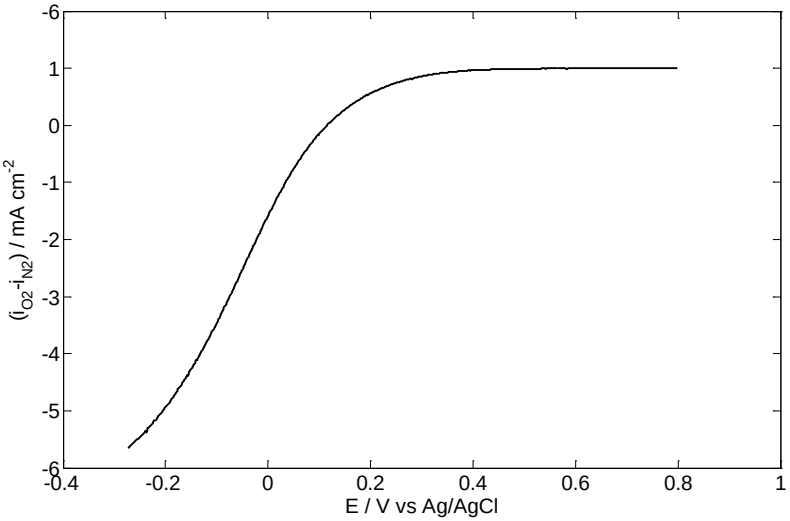

Fig. 5.26: Polarization curves recorded in oxygen-saturated 0.1 mol dm^{-3} $HClO_4$. T= 25 °C; v= 5mV s^{-1}; ω=1600 rpm.

Even if useful N-functionalities, e.g. pyridinic and pyrrolic nitrogen, are present on the nanocubes, as detected by XPS, the absence of iron might be responsible of the poor electroactivity towards ORR.

In conclusion of this section, a very interesting material has been synthesized, with a cubic empty shape. So far there are no other examples in the literature of N-doped carbon nanotubes synthesized by simple methods, like that one used in this work. This opens a very wide range of investigations, aiming at better discovering the formation mechanism, the role of iron in the synthesis, the composition and electronic configuration of the edges and corners of the cubes. On the other side, due to the empty space available in the internal part of each cubes, many applications can be thought for example involving cubes as nano-reactors that can be opened/close in correspondence of temperature changings. As a last aspect, the very interesting property to be kept in mind is the material's changing happening around 37°C, a temperature just a few degrees above the body's temperature; this feature could be taken into considerations for medical applications, after testing and verifying the biocompatibility of N-CNCs.

5.4. N-doped carbon microspheres (N-CMSs)

Developments in the last decades have shown that it is possible to achieve the synthesis of carbon microparticles by a process known as ultrasonic spray pyrolysis (USP) [55-59].

In USP a liquid precursor solution is nebulized into a mist using a high frequency piezoelectric transducer. The mist is then carried via inert or reactive gas flow to a furnace. The solvent evaporates in the furnace and the precursor decomposes. This leaves solid particles behind to be collected. Using this procedure it is possible to obtain a very narrowly dispersed particles size distribution. In general, to achieve this narrowly dispersed particle size distribution two operations have to be performed correctly. Firstly, preparation of uniform sized and fine droplets of mist. Secondly, controlled decomposition of the droplets with respect to time, solvent evaporation and environment is also important. The first condition is achieved by the use of the piezoelectric transducer. The oscillations in the ultrasonic range of the piezoelectric disk cause capillary waves to form in the precursor solution. Using Kelvin's equation, it can be expected that the wavelength of capillary waves is:

$$\lambda = \left(\frac{8\pi T}{\rho F^2} \right)^{\frac{1}{3}} \qquad (1)$$

where ρ is the liquid density, T is the surface tension, F is the exciting frequency and λ is the wavelength of the capillary wave. The droplets generated via capillary waves have a diameter (D) which is proportional to the capillary wavelength:

$$D = 0.34 \left(\frac{8\pi T}{\rho F^2} \right)^{\frac{1}{3}} \qquad (2)$$

The solvent evaporation and precursors decomposition can be controlled by maintaining control over furnace temperature and carrier gas flow rate. Within the furnace each individual droplet acts as a separate reaction vessel containing limited amounts of precursors.
In literature, it has also been shown that the structure of the particles in USP can be changed by varying starting precursors solution. For example, it has been reported that by adding salts to the starting solution causes differences in carbon microsphere porosity and structure [60]. The salts are believed to be responsible for templating the pores. The exact mechanism for the difference is not well understood. Other precursors are also known to give porous carbon structures. This literature gives good indication that it will be indeed possible for the porosity of the carbon microsphere support to be varied and controlled.

Similarly, but without making use of ultrasounds, an aerosol pyrolysis method (APM) was developed. The mist was obtained by mechanically nebulizing the starting solution with a nitrogen flow passing throughout a hole in a specific aerosol device (piston valve aerosol nebulizer). In the recent literature, aerosol route synthesis processes such as spray pyrolysis using soluble iron compounds like nitrates, chlorides, or highly volatile iron pentacarbonyl as starting materials have been demonstrated to produce high-purity, unagglomerated, spherical-shaped submicrometer- to nanometer-sized iron oxide particles by adequately tuning the

process parameters (like precursor flow rate, concentration of the metal ions, decomposition atmosphere and temperature) [61]. In particular, APM method are nowadays often used in the synthesis of carbon nanotubes [62].

In this work, an ultrasonic spray pyrolysis (USP) method and an aerosol pyrolysis (APM) method were developed for the synthesis of N/Fe-doped porous carbon microspheres. USP and APM are both flow methods that are intrinsically scalable without the mass- and heat-transfer problems often encountered in batch processing. Solutions of low cost sugars as precursors for the carbon material were used, to which nitrogen-containing compounds and iron salts for N- and Fe-doping were added, joining the results presented previously for the synthesis of mesoporous carbon [63]. In order to optimize the reaction conditions, a fixed starting solution comprising glucose, histidine and iron (II) acetate was first chosen. By USP, carbon microspheres were synthesized and physico-chemically characterized. This part was carried out at Trinity College Dublin in the laboratory of Prof. Colavita as part of an academic collaboration and an Erasmus exchange. Then, the experiments were shifted in the direction of repeating the previous synthesis by the APM method (in Università degli Studi di Milano), verifying the differences in the obtained products. Finally, the starting solution has been changed, choosing different precursors with the aim of improving the electrocatalytic activity towards ORR.

In order to make order among the large number of materials synthesized in this section , samples are summarized, with their label, synthetic method and specific composition In the following **Tab. 5.10**.

Sample	Synthetic method	C-compound	N-compound	Precursors molar ratio	Fe wt %	Annealing temperature	Other
USP_GH710	USP	Glucose	Histidine	10:1	0.96	710°C	-
USP_GH900	USP	Glucose	Histidine	10:1	0.96	710°C + 900°C	-
USP_FAG710	USP	Fructose	Guanidine acetate	1:1	0.96	710°C	-
USP_FAG900	USP	Fructose	Guanidine acetate	1:1	0.96	710°C + 900°C	-
APM_GH710	APM	Glucose	Histidine	10:1	0.96	710°C	-
APM_GH900	APM	Glucose	Histidine	10:1	0.96	710°C + 900°C	-
APM_FAG710	APM	Fructose	Guanidine acetate	1:1	0.96	710°C	-
APM_FAG900	APM	Fructose	Guanidine acetate	1:1	0.96	710°C + 900°C	-
APM_FAG710noFe	APM	Fructose	Guanidine acetate	1:1	-	710°C	-
APM_FAG900noFe	APM	Fructose	Guanidine acetate	1:1	-	710°C + 900°C	-
APM_GH710Surf	APM	Glucose	Histidine	10:1	0.96	710°C	+ CTACl
APM_GH900Surf	APM	Glucose	Histidine	10:1	0.96	710°C + 900°C	+ CTACl

Tab. 5.10: Summary and details of synthesized samples.

5.4.1. Synthesis of N-CMSs by USP: experimental

All reactants (Glucose, fructose, histidine, guanidine acetate, iron (II) acetate, glacial acetic acid, Nafion® (5 wt. % EtOH solution), 37% hydrochloric acid, concentrated sulfuric acid and ethanol) were purchased from Sigma Aldrich and used as received without further purification. 60% $HClO_4$ solution was from Merck.

The precursor solution consisted of 200 mL of a solution of glucose (GLU, 0.42 M) and histidine (HIS, 0.042 M) in water, yielding a 10:1 GLU:HIS molar ratio, as in a previous work [19]. Glacial acetic acid was added to the above solution in equimolar ratio to HIS in order to dissolve the nitrogen-containing compound; finally, iron (II) acetate was added at 0.96 wt. % Fe concentration (calculated from the total mass of GLU, HIS and iron acetate). Carbon microspheres were synthesized via ultraspray pyrolysis (USP) using a home-built apparatus [64] consisting of a 1.65 MHz piezoelectric crystal (APC) and a 1 m long tube furnace (Carbolite); temperature was held at 710 °C and nitrogen was used as carrier gas at 3 LPM flow.

Solid particles were collected as a suspension in a water-filled flask at the end of the furnace, and later filtered and washed, 3 times with water and 3 times with ethanol, using nylon membranes (0.45 μm, 25 mm, Millipore). Thus prepared particles are hereafter referred to as USP_GH710. Particles were then annealed under nitrogen gas flow (3 LPM) according to the following protocol: 25 min at 25 °C, slow heating (6 °C min^{-1}) up to 900 °C, 3 h held at 900 °C and, finally, rapid cooling to 25 °C under nitrogen flow. The annealed particles are hereafter referred to as USP_GH900.

The previous synthesis was then repeated changing the precursors nature and molar ratio, according to the best results obtained in ORR for mesoporous carbons. Hence, the new solution to be sprayed consisted of 200 mL of a solution of fructose (FRU, 0.42 M) and guanidine acetate (Gua, 0.42 M) in water, yielding a 1:1 FRU:Gua molar ratio; glacial acetic acid (AcAc) was added to the above solution in molar ratio AcAc:Gua=3:1 (because Gua comprises three N-groups). Iron (II) acetate was added at 0.96 wt. % Fe concentration (calculated from the total mass of FRU, Gua and iron acetate). Carbon microspheres were synthesized via the same ultraspray pyrolysis (USP) apparatus, exactly as before. Thus prepared particles are hereafter referred to as USP_FAG710. Particles were then annealed under nitrogen gas flow (3 LPM) according to the following protocol: 25 min at 25 °C, slow heating (6 °C min^{-1}) up to 900 °C, 3 h held at 900 °C and, finally, rapid cooling to 25 °C under nitrogen flow. The annealed particles are hereafter referred to as USP_FAG900.

For a schematic representation of all samples, see **Tab. 5.10**.

5.4.2. N-CMSs by USP: characterization

USP_GH710 and USP_GH900 powders were first characterized by SEM to determine particle size and morphology. **Fig. 5.27** shows SEM images of USP_GH710 and USP_GH900, respectively. USP_GH710 spheres are smooth and spherical in shape; in some of the images it is also possible to discern the presence of darker spots, possibly attributable to relatively large empty cavities below the external solid shell. USP_GH900 annealed particles retain the spherical shape of as-prepared USP_GH710 particles, however, their surface is rougher and

typically displays cracks and wide holes. Furthermore, small bright aggregates that are uniformly distributed throughout the surface of the microspheres can be clearly seen after annealing. SEM images were used to carry out particle-size analysis over 100 particles, yielding size distributions histograms (see **Fig. 5.28**). The average particle size was found to be 0.92 ± 0.11 μm and 0.86 ± 0.12 μm (C.I. 99%) for USP_GH710 and USP_GH900, respectively, suggesting no significant change in the outer diameter of particles due to annealing. The histograms are approximately log-normal in shape, yielding geometric means of 0.81 and 0.74 μm for USP_GH710 and USP_GH900, respectively, and geometric standard deviations of 1.64 in both cases.

The structure of synthesized and annealed particles was analyzed using FIB milling. **Fig. 5.27** shows typical cross sections of USP_GH710 and USP_GH900 particles, respectively, obtained after exposure to a Ga-ion beam. The vast majority of USP_ GH710 particles display a hollow-shell structure, with the largest spheres often containing smaller hollow particles. Similar hollow-sphere structures were obtained by Xu *et al.* using USP methods, albeit with a different precursor solution [65]. FIB cross-sections also confirmed that darker spots visible in the SEM analysis are due to the presence of empty cavities trapped within the carbon shell. FIB cross sections of USP_GH900 indicate that the annealing treatment not only affects the surface of the microspheres but it deeply affects the internal structure (**Fig. 5.27**). USP_GH900 particles were all found to have a solid core containing some internal pores and bright clusters, previously observed also at the surface of USP_GH900 by SEM; these clusters were found to be embedded in the microsphere internal volume resulting in a pudding-like structure. This pudding structure has been previously observed in the literature; Zhan *et al.* [66] synthesized iron/carbon particles via pyrolysis of sucrose solutions for applications in reductive remediation of organochlorides and reported the formation of similar bright clusters after prolonged heating, which they attributed to iron nanoparticle formation and sintering. Formation and sintering of iron oxide nanoparticles within the carbon matrix was also observed via TEM by Atkinson *et al.* [67] after USP pyrolysis of selected sucrose/$Fe(NO_3)_3$ solutions.

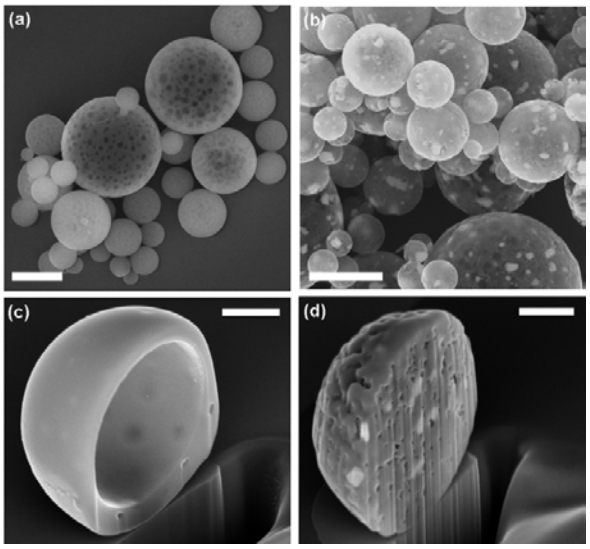

Fig. 5.27: SEM images of (a) USP_GH710 and (b) USP_GH900 microspheres (scalebar = 1 μm). Images of typical cross sections of (c) USP_GH710 and (d) USP_GH900 microspheres obtained using focused Ga-ion milling (FIB)(scalebar = 400 nm) [63].

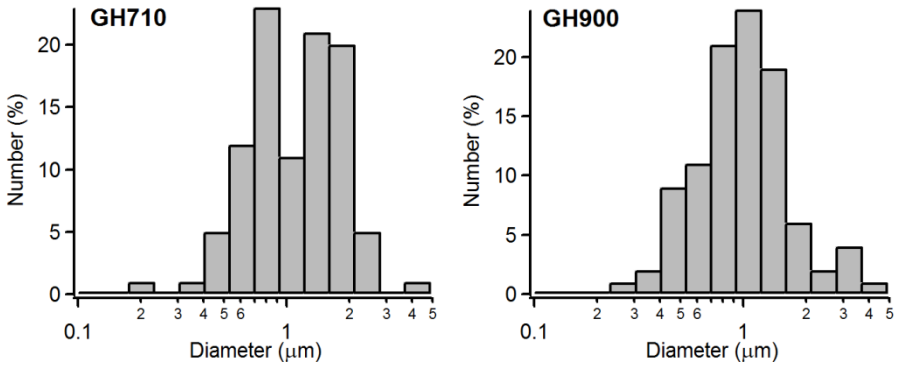

Fig. 5.28: Particle size distributions obtained from SEM images for USP_GH710 and USP_GH900 microspheres [63].

Fig. 5.29 shows Raman spectra of USP_GH710 and USP_GH900. Both spectra show the characteristic D and G peaks of amorphous carbon materials at about 1355 and 1590 cm^{-1}, respectively [68]. This indicates that the GLU:HIS:Fe precursor solution undergoes pyrolysis during its transit in the furnace yielding particles that contain amorphous carbon. The D peak is related to vibrations that are forbidden in perfect graphite and become active in the presence of disorder and defects; the G peak is attributed to in-plane bond-stretching vibrations of trigonally bonded carbon atoms (sp^2 centers) [69,13].

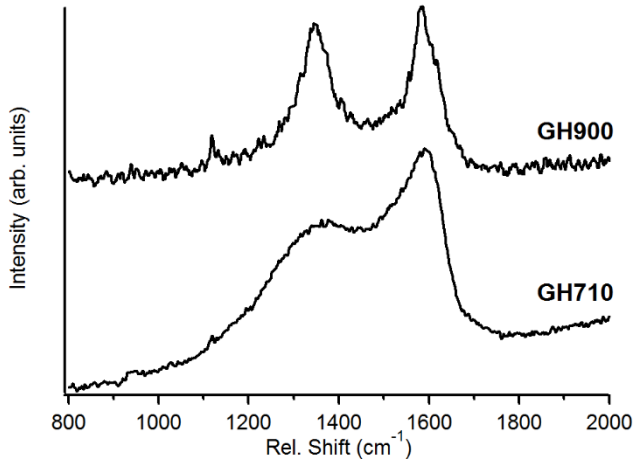

Fig. 5.29: Raman spectra of USP_GH710 and USP_GH900 microspheres (514 nm excitation); spectra were normalized by the G peak height and offset to facilitate comparison [63].

Upon annealing both D and G peaks become narrower and the intensity of the D peak increases relative to that of the G peak: peak fitting yielded an increase in I_D/I_G peak height ratio from 0.66 to 0.90 for USP_GH710 and USP_GH900, respectively. An increase in the number and size of graphitic clusters is known to translate into an increase in I_D/I_G in amorphous carbons, according to the three-stage model of Ferrari *et al.* [68]. Therefore, our results indicate that the annealing step leads to graphitization of the amorphous carbon phase in the particles.

In order to better understand changes in surface morphology observed after annealing, N_2 adsorption/desorption measurements and BET analysis were carried out. N_2 adsorption/desorption isotherms at 77 K of USP_GH710 and USP_GH900 are reported **Fig. 5.30**.

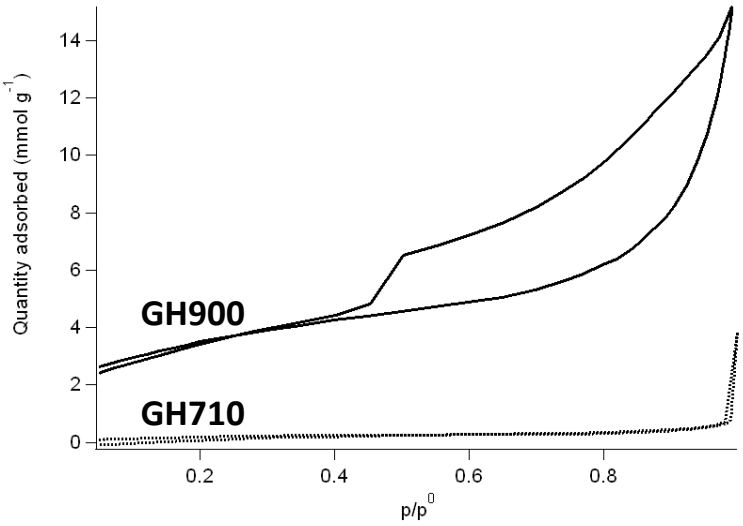

Fig. 5.30: N_2 adsorption/desorption isotherms at 77 K for GH710 and GH900 microspheres [63].

Based on IUPAC classification, USP_GH710 yields II-type adsorption isotherm, typical of non-porous or macroporous solids [32]; the desorption branch does not display any evident hysteresis, thus excluding the presence of a porous structure. The BET surface area of USP_GH710 samples was found indeed to be very low, equal to 16.4 ± 0.9 m^2 g^{-1}, and consistent with the smooth appearance of microspheres observed via SEM (**Fig. 5.27**). Interestingly, the BET surface area value of USP_GH710 is only slightly higher than the theoretical surface area of 10 m^2 g^{-1}, calculated for smooth perfect carbon spheres of 0.8 µm diameter (2.26 g cm^{-3} density [70]) and 0.1 µm wall thickness. The adsorption and desorption branches of GH900 isotherms display a hysteresis loop, often associated with slit-shaped pores on the basis of De Boer's classification (Type B hysteresis) [33]. The BET surface area of GH900 was found to be 279 ± 3 m^2 g^{-1}, a value that is 17 times higher than that of USP_GH710 particles and comparable to that of other carbon materials suitable as electrocatalyst supports [71]. These results indicate that microspheres develop a pore structure upon annealing; this is consistent with the rough surface observed via SEM and with the observation of a solid core via FIB, which could develop without a significant decrease in microsphere diameter only if accompanied by an increase in porosity.

EDX mapping was carried out in order to investigate the elemental distribution of C and Fe. **Fig. 5.31** shows EDX images of USP_GH710 and USP_GH900 obtained by selecting the C and Fe channels. In the case of the C channel, a completely homogeneous distribution is observed both on USP_GH710 and USP_GH900. In the case of the Fe channel, its distribution is homogeneous in USP_GH710 microspheres but it is clearly concentrated in the white aggregates in USP_GH900 microspheres. This result demonstrates that the annealing treatment not only alters the degree of graphitization of the carbon phase of synthesized particles, but it also affects the distribution of Fe, leading to the formation of Fe-rich aggregates.

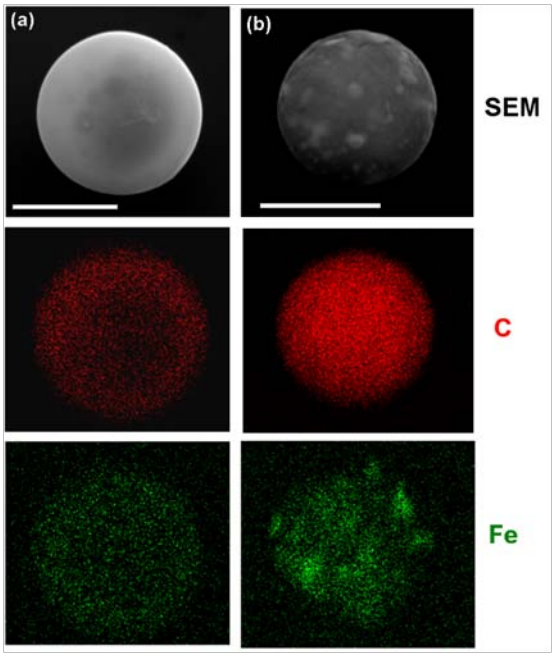

Fig. 5.31: EDX mapping of SEM images of (a) USP_GH710 and (b) USP_GH900 microspheres (scalebar = 1 µm); the panels show the SEM image and its corresponding C (red) and Fe (green) channels showing elemental distribution [63].

The XRD pattern of USP_GH900 microspheres is reported in **Fig. 5.32**.

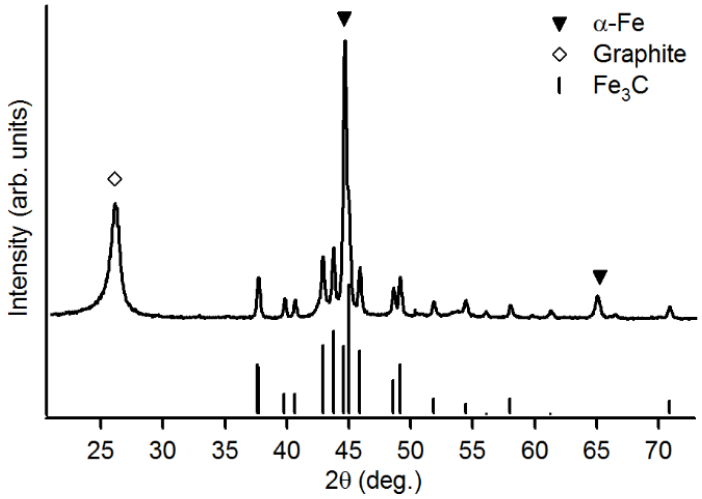

Fig. 5.32: XRD pattern of USP_GH900 microspheres. The reference XRD pattern of Fe_3C is reported at the bottom; reflections due to the presence of α-Fe and graphite are also labeled as indicated in the legend.

The peaks at 2θ = 44.7° and 65.0° are assigned to the (110) and (200) reflections of α-Fe, respectively (PDF#00-006-0696); the peak at 26.4° is assigned to the (002) reflection of graphite (PDF#00-041-1487); the remaining peaks compare well to those of the iron carbide (Fe_3C) pattern (PDF#00-035-0772). The XRD pattern of USP_GH900 is consistent with the majority of the iron being present in metallic or carbide forms. The formation of Fe^0 and Fe_3C is often observed after pyrolysis of organic compounds in the presence of iron salts and are the result of carbothermal reduction and thermal decomposition of iron oxides [66,72,73,63].

The carbon phase undergoes graphitization, as indicated by the appearance of a strong reflection characteristic of graphite. This is in agreement with our Raman results and is consistent with the role played by iron in catalyzing graphitization at relatively low temperatures [74]. USP_GH710 microspheres did not yield diffraction peaks but only a broad background (data not shown), thus indicating that USP_GH710 possesses an amorphous structure.

The surface chemical species were investigated by XPS: C, O, N and Fe were detected and atomic percent results referred to carbon (% O/C, % N/C and % Fe/C), as reported in **Tab. 5.11** and in **Fig. 5.33 a-c**.

Sample	USP_GH710	USP_GH900
O/C %	14	5.1
N/C %	32	3.5
Fe/C %	2.1	1.2

Tab. 5.11: Atomic ratios referred to C 1s line from high resolution XPS spectra for USP_GH710 and USP_GH900 microspheres [63].

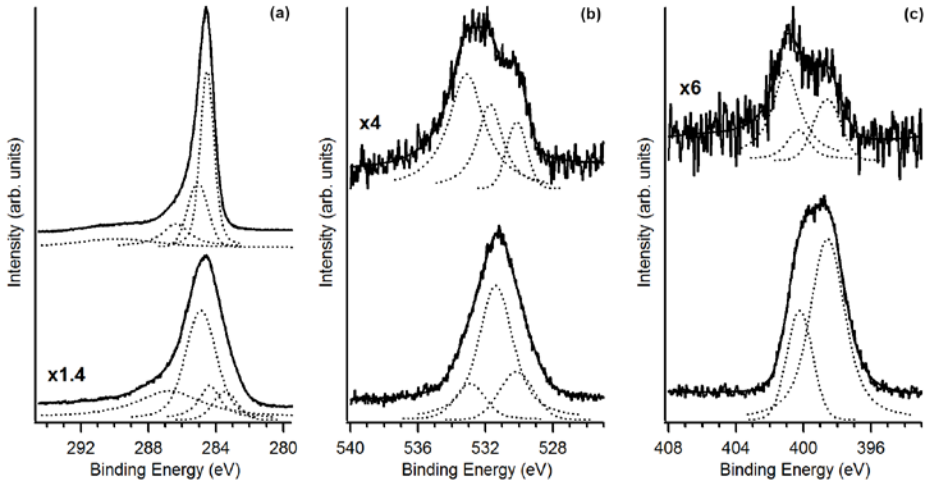

Fig. 5.33 a-c: XPS spectra in the C 1s (a), O 1s (b) and N 1s (c) binding energy regions of USP_GH710 (bottom) and USP_GH900 (top) samples; peak contributions obtained from best fits are shown below each spectrum. Spectra are shown normalized by the C 1s total area and scaled, as indicated in each figure, to facilitate comparison [63].

The C 1s High Resolution spectra, shown in **Fig. 5.33 a** for USP_GH710 (bottom) and USP_GH900 (top), show that the annealing process leads to a remarkable reduction in peak width. The C 1s spectrum of USP_GH710 was deconvoluted into four contributions at 283.4 eV, assigned to carbides [75], at 284.4 eV, assigned to graphitic carbon (sp^2 centres), at 284.9 eV, assigned to aliphatic carbon (sp^3 centres) and, finally, a broad peak at 286.8 eV, assigned to a convolution of nitrogen- and oxygen-bonded C atoms [21,76]; further resolution of this broad peak is difficult due to fit correlations. The C 1s spectrum of USP_GH900 was satisfactorily fitted with 4 peaks at 284.5 eV, 285.1 eV, 286.4 eV and 289.9 eV, that were attributed to sp^2 centres, sp^3 centres, C-O/C-N bonded carbon and the carbon satellite characteristic of sp^2-rich carbons, respectively [21,76]. The peak area ratio $A_{284.5}/A_{285}$ increases from 0.3 for USP_GH710 up

to 2.1 for the annealed USP_GH900 sample, further confirming that the sample undergoes significant graphitization [77].

In **Fig. 5.33 b** a fit of the High Resolution O 1s region of USP_GH710 indicates the presence of three contributions at 530.1 eV, 531.4 eV and 532.9 eV, that can be assigned to O atoms in C=O, iron hydroxides and C—O groups [21,78]. After annealing, the O/C ratio decreases from 14% to 5.1%; three contributions can still be identified albeit with lower intensities, while the peak associated to iron hydroxide species undergoes the most significant reduction, as shown in the fit of the O 1s spectrum of USP_GH900 (**Fig. 5.33 b**) [21]. These results indicate that oxidized groups are lost during the annealing step; this is consistent with the graphitization process of the carbon scaffold, which typically leads to oxygen elimination in the gas phase. The significant reduction of the peak at 531.4 eV also indicates that the surface concentration of metal oxide/hydroxides decreases, in agreement with known thermal decomposition reactions of iron oxides in the presence of carbon [72,79].

The N 1s region of USP_GH710 displays a strong peak that was deconvoluted into two contributions at 398.6 and 400.2 eV, characteristic of pyridinic and pyrrolic nitrogen (see **Fig. 5.33 c**) [14] with the former being more intense than the latter. After annealing, the nitrogen content decreases dramatically and the N 1s line develops two maxima at 298.7 eV, assigned to pyridine-type N-centres, and at 400.9 eV, that typically arises due to a convolution of pyrrolic and quaternary nitrogen at 400 and 401 eV, respectively [15]. The best fit was obtained with three peaks at 398.6 eV, 400.3 eV and 401.0 eV, as shown in **Fig. 5.33 c** (top); however, fit correlations make it difficult to estimate the relative proportion of pyrrolic vs. quaternary nitrogen. Similarly, the possibility of contributions from iron-associated pyridinic nitrogen cannot be excluded, which would yield a peak at 399 eV convoluted under the low binding energy maximum [80]. The A_{398}/A_{TOT} ratio decreases from 74% for USP_GH710, to 27% for USP_GH900, thus suggesting that the proportion of pyridinic nitrogen decreases upon annealing in favor of pyrrolic/quaternary nitrogen, in agreement with previous observations from several groups [19,81]. Finally, iron was also detected in both USP_GH710 and USP_GH900 XPS spectra. The integrated area of the Fe $2p_{3/2}$ peak was used to calculate Fe/C atomic ratios (**Tab. 5.11**) which were found to decrease upon annealing. This decrease is consistent both with the sintering of iron clusters and with the carbon phase having undergone graphitization, a process catalyzed by Fe/Fe_3C that typically leads to iron and its carbide to be encapsulated within a graphite a shell [82,83]. Fe $2p_{3/2}$ HR XPS is shown in **Fig. 5.34**.

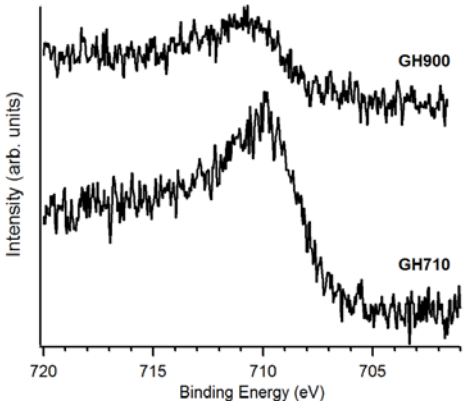

Fig. 5.34: XPS spectra of the Fe $2p_{3/2}$ peak of USP_GH710 and USP_GH900 microspheres [63].

In summary, our results indicate that nebulized GLU:HIS:Fe solutions undergo pyrolysis yielding carbon microspheres. The annealing process results both in graphitization and phase segregation of iron-rich phases as shown by Raman and EDX. XRD results, specifically, show that metallic iron and Fe_3C are formed during the annealing process, whereas XPS suggests that a significant proportion of iron centers disappear into the subsurface. Interestingly, the process of annealing and graphitization also results in the development of pores. It is known from literature that iron plays an important role in carbon particle growth, acting as a Lewis acid catalyst both in the formation of carbon products and in the annealing treatment [67,66,84]. The transition from a hollow spherical structure, left from water evaporation in the furnace, to solid microspheres might be explained by considering that, during the annealing treatment at 900°C, the O- and N-rich carbon network is partially unstable and decomposes. This process is accompanied by the slow aggregation of dispersed iron into nanoparticles, which might serve as seeds for the catalytic "re-growth" of solid carbon spheres [66], in a process similar to the catalytic deposition of carbon nanotubes [11]. Also, the annealing treatment leads to formation of decomposition gases which can template pores thus increasing surface area. Both the catalytic re-growth process and gas evolution within the particles could account for the presence of cracks, holes and eroded areas on USP_GH900 observed from SEM images and the increase in BET surface area. A more detailed understanding of the mechanism of pore development is however challenging, as is often highlighted in the literature on the pyrolysis of organic compounds; mechanistic understanding would require detailed analysis of decomposition products as a function of temperature and reaction conditions as previously reported by other groups [85,86,87,88].

Electrochemical characterization was carried out in order to understand the electrocatalytic properties of USP_GH710 and USP_GH900 in the oxygen reduction reaction. **Fig. 5.35 a** compares cathodic polarization curves for ORR recorded at ω = 1600 rpm in 0.10 M $HClO_4$; current densities were normalized by BET surface areas. The USP_GH710 sample displays poor catalytic behavior for ORR: the limiting current is undetectable and the onset potential (E_{on}), as calculated by the tangent method, is about -0.150 V (vs. Ag/AgCl). This potential is 0.750 V more cathodic than that observed for a commercial Pt catalyst (Eon~0.6 V vs. Ag/AgCl [19]). **Fig. 5.35 a** also shows the polarization curve of GH900 microspheres; the annealing treatment at 900°C shifts the onset potential to E_{on}= 0.400 V, a significant shift of 550 mV. The E_{on} value is more cathodic than commercial Pt catalysts by 0.200 V, and it compares well to other Pt-free carbon based catalysts [19]. Therefore, the annealing process drastically improves the catalytic properties of microspheres in ORR.

Fig. 5.35 b shows the cathodic ORR polarization curves recorded on USP_GH900 samples at different RDE rotation rates. A limiting current dependent on the RDE rotation rate, although not well-defined, is detectable. **Fig. 5.35 c** shows the corresponding Koutecky–Levich plots at different potentials. The average plot slopes display good linearity and yield a number of exchanged electrons n = 3.7 ± 0.2. This result indicates that peroxide formation is not the rate determining step in the reduction process and that the direct formation of H_2O is the preferred ORR mechanism. Thus, the USP_GH900 sample shows a good performance in the reduction of oxygen and can be considered a promising catalyst.

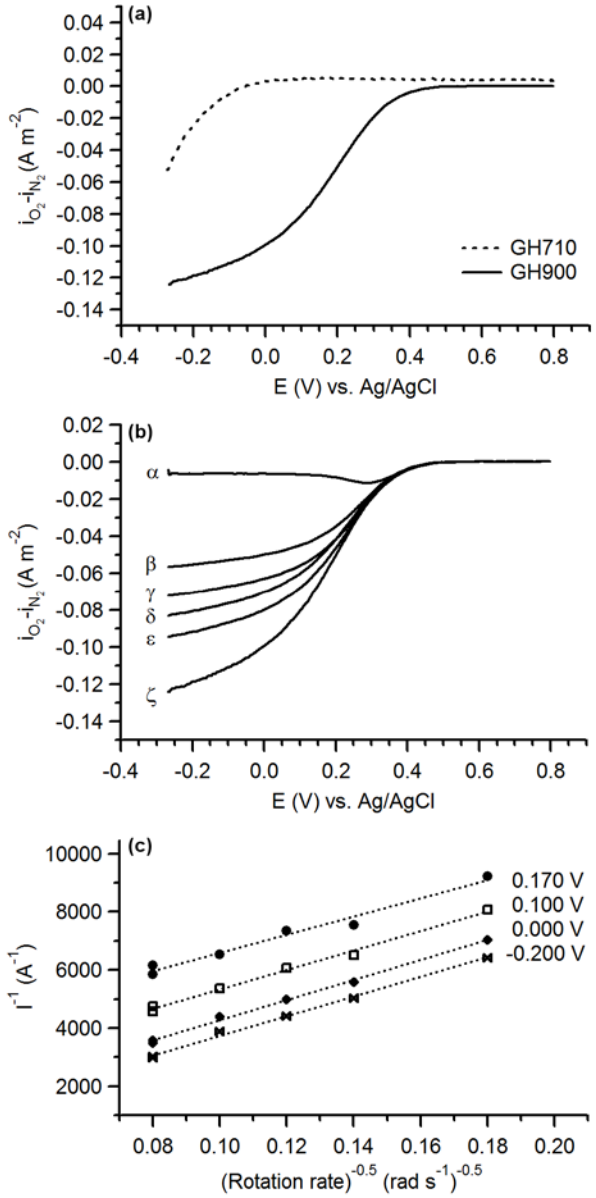

Fig. 5.35 a-c: ORR Polarization Curves recorded in oxygen saturated 0.10 M $HClO_4$. T = 25 °C; (a) RDE voltammetry curves (v= 5 mV s^{-1}; ω= 1600 rpm); (b) RDE voltammetry curves for GH900 (v = 5 mV s^{-1}) at ω= 0 (α), 300 (β), 500 γ), 700 (δ), 900 (ε), 1600 (ζ) rpm. (c) Koutecky–Levich plots for oxygen reduction on USP_GH900 [63].

It is interesting to discuss the results of the electrochemical characterization in the context of the structural and morphological characterization of the microspheres. It has been reported in the literature that the presence of pyridinic [15,63,89-91] and/or quaternary nitrogen [92,93] surface groups enhances the ORR activity of carbon electrodes. Based on XPS and ORR results, however, USP_GH710 displays poor ORR kinetics even though it displays a higher surface density of pyridinic sites than USP_GH900. However, particles synthesized at 710°C are less graphitic with presumably lower conductivity; furthermore, as suggested by previous work, the annealing treatment stabilizes N- and Fe- doped graphitic structures, increases quaternary nitrogen amount, and has been shown to activate catalytic sites for ORR [94]. However, it is difficult to determine the independent roles of N and Fe doping for promoting ORR activity: first, N-doping alone has been shown to promote ORR in carbon materials, [19,95] second, Fe-

doping is known to promote graphitization and improve carbon conductivity [66,72,73] and finally, the presence of N-complexed Fe centres is known to catalyse ORR.
All of the above hypotheses are potential routes for ORR in our materials and further studies are necessary in order to establish a preferred mechanism. It is also important to consider the effect that annealing has on particle morphology, since BET results show that this process leads to pore opening and an increase in accessible surface sites. Therefore, the enhanced performances of USP_GH900 microspheres vs. USP_GH710 is likely to arise from its higher degree of graphitization, the presence of stable and active surface bound catalytic centers, and an increased availability of ORR active sites within their porous structure.

After a wide and deep physico-chemical analysis of samples USP_GH710 and USP_GH900, as previously exposed in the experimental section, the USP synthesis was repeated changing the precursors nature and molar ratio, according to the best results obtained in ORR for mesoporous carbons, yielding now USP_FAG710 and USP_FAG900 particles. The new solution to be sprayed consisted indeed of fructose and guanidine acetate in water (1:1 FRU:GUA molar ratio); glacial acetic acid was added in molar ratio AcAc:GUA=3:1 and iron (II) acetate was added at 0.96 wt. % Fe concentration.

First of all, the morphology of the as-prepared USP_FAG710 and USP_FAG900 materials was analyzed by SEM and compared to USP_GH710 and USP_GH900 particles. Results are shown in **Fig. 5.36**.

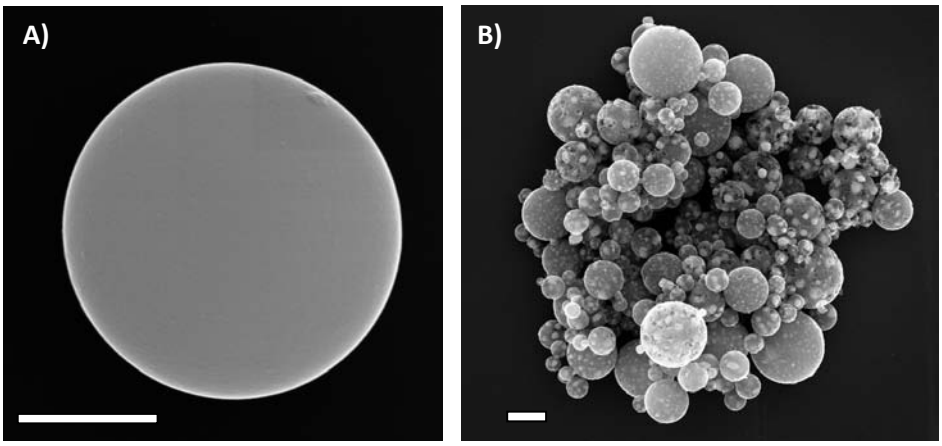

Fig. 5.36 A-B: SEM images of (A) USP_FAG710 and (B) USP_FAG900 microspheres (scalebar = 500 nm).

USP_FAG710 spheres (**Fig. 5.36 A**) are very smooth and spherical in shape, as previously observed in USP_GH710 sample; darker spots, attributed to empty cavities below the external solid shell in USP_GH710 are no more present in USP_FAG710, which shows instead a completely homogeneous morphology. USP_FAG900 annealed particles (**Fig. 5.36 B**) are spherical in shape but, similarly to what observed for GH-samples, their surface is rougher and displays cracks and wide holes. Small bright aggregates, uniformly distributed throughout the surface of the microspheres can be again clearly seen after annealing.
SEM images were used to carry out particle-size analysis over 100 particles. The average particle size was found to be 0.782 ± 0.327 μm and 0.648 ± 0.276 μm (C.I. 99%) for USP_FAG710 and USP_FAG900, respectively, suggesting no significant change in the outer diameter of particles due to annealing and due to precursors change (if compared to

USP_GH710 and USP_GH900 average diameters). EDX mapping was not performed on this samples, considering that brighter spots, observed in SEM images, are surely attributable to iron, as found in EDX analysis on USP_GH900 spheres.

The XRD pattern of USP_FAG900 microspheres is reported in red in **Fig. 5.37** and compared to USP_GH900 one, in black.

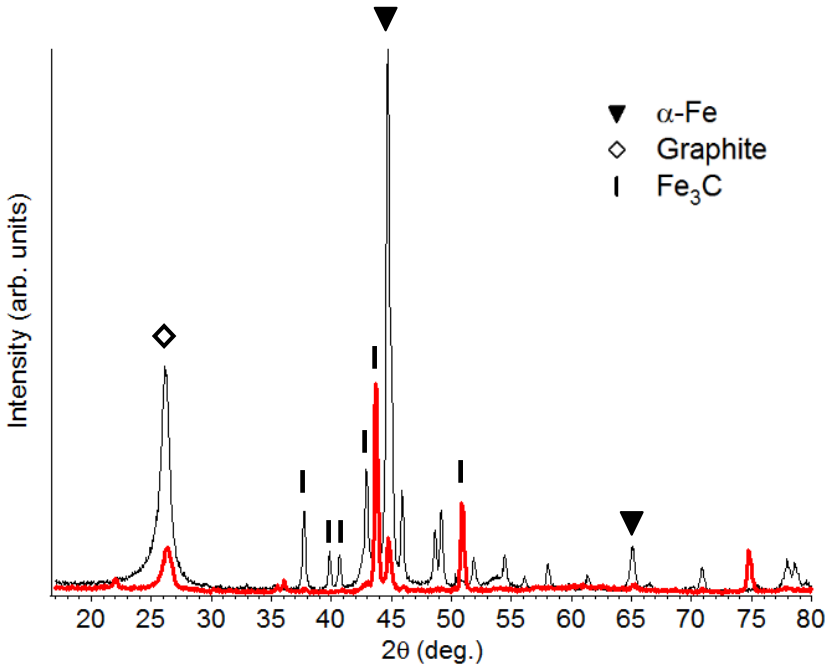

Fig. 5.37: XRD pattern of USP_FAG900 (red line) and USP_GH900 (black line) microspheres. Reflections due to the presence of α-Fe, Fe_3C and graphite are also labeled as indicated in the legend.

The XRD pattern of USP_FAG900 microspheres is reported in red in **Fig. 5.37** and compared to USP_GH900 one, in black. From a first analysis it can be seen that USP_FAG900 XRD pattern shows just a few peaks compared to USP_GH900 pattern, some of them overlapping with USP_GH900 pattern's peaks. The typical peaks of α-Fe at 2θ = 44.7° and 65.0° are weaker in USP_FAG900, and are assigned to the (110) and (200) reflections, respectively (PDF#00-006-0696); the peak at 26.4° is assigned to the (002) reflection of graphite (PDF#00-041-1487), confirming that the carbon phase undergoes graphitization. The remaining peaks, comparing well to those of the iron carbide (Fe_3C) pattern (PDF#00-035-0772) in USP_GH900 sample (**Fig. 5.37**), are not present in USP_FAG900 XRD pattern and, when detectable, they are not intense as they were in USP_GH900 pattern (if compared to other peaks from other phases such as metallic iron and graphite). This confirms that, depending on the precursors solution choice, the overall chemical composition of spheres varies and, because of that, during the 900°C annealing treatment, unstable N- and Fe-containing moieties affect the re-growth mechanism, giving rise to different graphitized samples.

N_2 adsorption/desorption measurements and BET analysis were then carried out (isotherms not reported). Similarly to GH-spheres, the BET surface area of USP_FAG710 samples was found to be very low, equal to 10 ± 2 $m^2\ g^{-1}$, and consistent with the smooth appearance of microspheres observed via SEM. The BET surface area of USP_FAG900 was found to be 299 ± 5 $m^2\ g^{-1}$, a value that is 30 times higher than that of USP_FAG710 particles

and fully comparable to that of USP_GH900. A development of a pore structure upon annealing is again evidenced; this is consistent with the rough surface observed via SEM, which could develop without a significant decrease in microsphere diameter only if accompanied by an increase in porosity.

Electrochemical characterization was carried out in order to compare the electrocatalytic properties of USP_FAG900 and USP_GH900 in the oxygen reduction reaction, expecting an improvement of ORR performances in USP_FAG900 samples, keeping in mind that precursors solution was chosen after gaining good results when testing mesoporous carbon samples prepared from fructose and guanidine-containing molecules (see section "**3.4.1. Fructose as C- and O-source: experimental and results**"). **Fig. 5.38** compares cathodic polarization curves for ORR recorded at ω = 1600 rpm in 0.10 mol dm^{-3} $HClO_4$; current densities were normalized by BET surface areas.

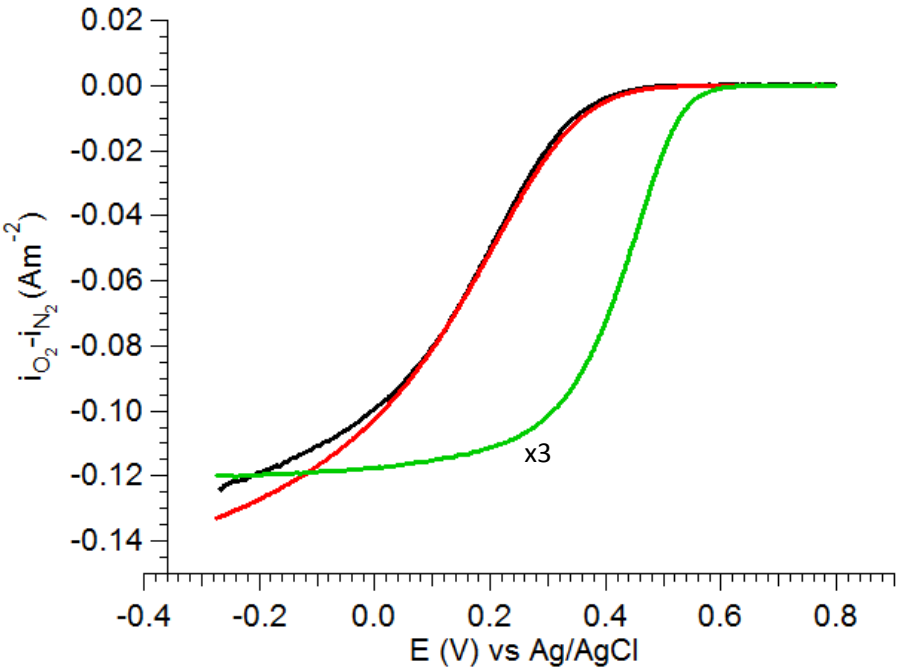

Fig. 5.38: ORR RDE curves recorded in oxygen saturated 0.10 M $HClO_4$. T = 25 °C; v= 5 mV s^{-1}; ω= 1600 rpm. USP_GH900: black, USP_FAG900: red, FAG9: green.

It is surprising that, even changing deeply the precursors solution and relative ratio, the polarization curves for USP_GH900 and USP_FAG900 are almost overlapping. For both samples E_{on} value is more cathodic than commercial Pt catalysts by 0.200 V [19]. The annealing process drastically improves the catalytic properties of microspheres in ORR, as shown previously by a comparison between USP_GH710 and USP_GH900, but the different precursors choice is not able to further improve the catalytic performances in the reduction of oxygen. In the same **Fig. 5.38** is also reported, in green, the cathodic polarization curve recorded in the same conditions for FAG9 mesoporous sample, whose physico-chemical and electrochemical characterization has been shown previously (in the **Fig. 5.38** FAG9 currents have been multiplied by 3 because the surface area of this sample is three times higher, in order to better compare curves). The difference between FAG9 and USP_FAG900 samples are

only relative to the preparation method, the aqueous precursors solution is exactly the same, (4 times more diluted for USP_FAG900 sample, in order to facilitate the nebulization).

By summarizing the above results, in this section a scalable, facile, template-free and rapid synthesis, of Fe- and N-doped C-based microspheres via USP was presented.

- Catalytic materials with relatively narrow size dispersion were prepared using low cost materials and in the absence of a templating agent. The inherent scalability of continuous flow methods such as USP represents a significant advantage compared to alternative synthetic strategies requiring batch processing or surface catalyzed deposition of nanostructured carbon materials (e.g. CVD growth).
- Annealing of thus synthesized materials results in the formation of graphitic microspheres containing Fe/Fe_3C clusters embedded in a porous carbon phase.
- These particles were investigated as non-noble-metal catalytic electrode materials: RDE measurements show that indeed these particles catalyse ORR and could therefore be promising as electrode materials in FCs.
- The surface physico-chemical characterization showed that the enhancement in ORR performances might be related to the higher degree of graphitization, the stabilization of ORR N- and/or Fe-containing active catalytic sites and the increase in surface area obtained from the annealing treatment.

Further optimization of the catalytic performance of these materials could be achieved by investigating the use of alternative and completely different N and Fe dopant compounds in order to control the type of active sites created at the carbon scaffold surface and potentially reduce the overall cost of precursor solutions.

5.4.3. Synthesis of N-CMSs by APM: experimental

All reactants (Glucose, fructose, histidine, guanidine acetate, iron (II) acetate, cetyltrimethylammonium chloride 25 wt.% aqueous solution, glacial acetic acid, Nafion® (5 wt. % EtOH solution), 37% hydrochloric acid, concentrated sulfuric acid and ethanol) were purchased from Sigma Aldrich and used as received without further purification. 60% $HClO_4$ solution was from Merck.

In order to maintain a constant composition of precursors solutions utilized in USP synthetic method, discussed in the previous section, the precursor mixture consisted of two batches of 10 mL of a solution of glucose or fructose (GLU or FRU, 0.42 M) and histidine or guanidine acetate (HIS or GUA, 0.042 M or 0.42 M, respectively) in water, yielding a 10:1 GLU:HIS or 1:1 FRU:GUA molar ratios. Glacial acetic acid was added to the above solution in equimolar ratio to HIS and tri-molar with respect to GUA, in order to dissolve the nitrogen-containing compounds; finally, iron (II) acetate was added at 0.96 wt. % Fe concentration (calculated from the total mass of GLU/FRU, HIS/GUA and iron acetate). Carbon microspheres were synthesized via aerosol pyrolysis (APM) using a home-built apparatus consisting of 90 cm long tube furnace (Carbolite) inside which a quartz tube was positioned. The right side of the tube was connected to a commercial pharmaceutical piston aerosol system (Angelini linea F, droplets dimeter: MMAD=0,7 µm GSD=1,56 µm). 10 mL of the precursors solution were put inside the system, which was sealed and connected to a nitrogen flow (100 LPM), responsible

for the solution nebulization. The fog was carried inside the tube in a 710°C hot furnace by the gas flow and solid particles were collected as a suspension in a water-filled flask at the end of the furnace, and later filtered and washed, 3 times with water and 3 times with ethanol, using nylon membranes (0.45 μm, 25 mm, Millipore). Thus prepared particles are hereafter referred to as APM_GH710 and APM_FAG710, depending if they were prepared starting from GLU and HIS or FRU and GUA, respectively. Particles were then annealed under nitrogen gas flow (3 LPM) according to the following protocol: 25 min at 25 °C, slow heating (6 °C min^{-1}) up to 900 °C, 3 h held at 900 °C and, finally, rapid cooling to 25 °C under nitrogen flow. The annealed particles are hereafter referred to as APM_GH710 and APM_FAG710, depending if they were prepared starting from GLU and HIS or FRU and GUA, respectively.

With the aim of understanding more about the mechanism of formation, during the nebulization/pyrolisis step, some samples have been prepared adding a surfactant, cetyltrimethylammonium chloride (CTACl), to the starting precursors solution. In details, 30 μL of a 25 wt.% solution of CTACl were added to GLU and HIS solution. Obtained samples have been labeled APM_GH710Surf and APM_GH900Surf, depending if they were un-annealed or annealed at 900°C, respectively.

In order to study the re-growth/graphitization phase and the effect of the presence of iron at 900°C, some particles were prepared by eliminating iron from the starting solution. This materials have been labeled APM_FAG710noFe and APM_FAG900noFe, depending if they were un-annealed or annealed, respectively.

For a schematic representation of all samples prepared in this section using USP and APM methods, see **Tab. 5.10**.

5.4.4. N-CMSs by APM: characterization

In the following, a morphologic characterization of particles by SEM and SEM/FIB is reported with the aim of study if there are important differences when using the APM method or the USP one, starting from the same precursors solution. In this specific case the APM method was applied to an aqueous mixture containing glucose, histidine and iron (10:1 molar ratio, 0.96 wt % iron), because the resulting particles, prepared by USP, have been previously fully characterized (see GH710 and GH900 samples above). For the sake of clarity, here below are reported again SEM and SEM/FIB analysis (**Fig. 5.39 a-d**), recorded for samples GH710 and GH900, synthesized by USP. Then analyses were performed on samples prepared by APM, and the relative images are reported in **Fig. 5.39 e-h**. Particles are spherical in shape, but some differences are evidenced.

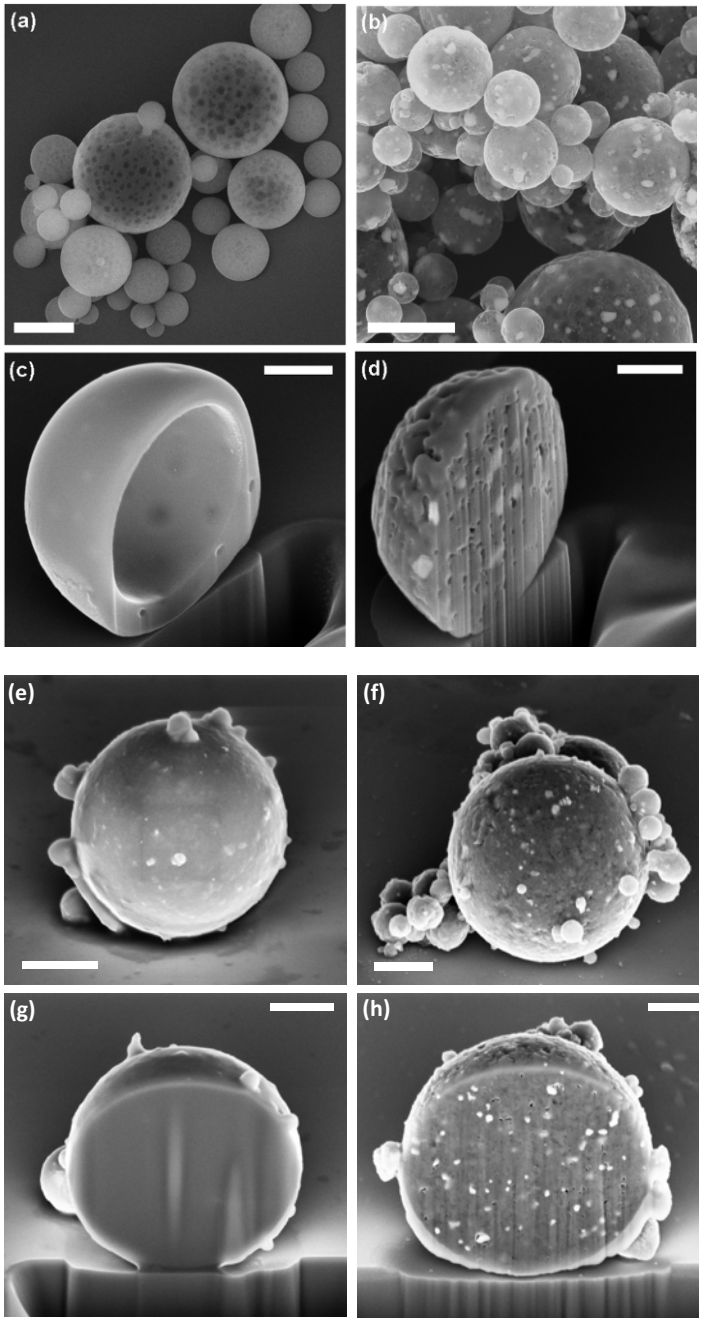

Fig. 5.39 a-h: SEM images and FIB milling of (a,c) USP_GH710, (b,d) USP_GH900, (e,g) APM_GH710, (f,h) APM_GH900 microspheres; (scalebar = 500 nm).

By comparing samples synthesized at 710°C (USP_GH710 and APM_GH710, respectively) in **Fig. 5.39 a** and **Fig. 5.39 e**, it is noticeable that the external appearance of particles is different depending if they have been synthesized by USP (**Fig. 5.39 a**) or APM (**Fig. 5.39 e**): when using the APM method, in fact, spheres are not "clean" and single, but rather surrounded by other smaller particles, with a not well defined spherical shape. One other difference is the narrower size and size dispersion when samples have been synthesized by APM. Moreover, the presence of darker spots in GH710 (**Fig. 5.39 a**), possibly attributable to relatively large empty cavities below the external solid shell, is no more identifiable in APM_GH710 (**Fig. 5.39 e**). The main

differences come out from a comparison between **Fig. 5.39 c** and **Fig. 5.39 g**, after FIB milling: particles prepared by USP are empty and have a hollow-shell structure **Fig. 5.39 c**, while using APM method, the obtained spheres are solid and filled inside, with an homogeneous internal structure (**Fig. 5.39 g**). This reasonably suggests that the nebulization leads to formation of solution's bubbles in USP, and droplets when synthesizing by APM method. Annealed particles (**Fig. 5.39 b,d** and **Fig. 5.39 f,h**) retain the spherical shape of as-prepared ones, however, their surface is rougher and typically displays cracks and wide holes. Furthermore, small bright aggregates that are uniformly distributed throughout the surface of the microspheres can be clearly seen after annealing. This is true for USP_GH900 (**Fig. 5.39 b,d**) and APM_GH900 (**Fig. 5.39 f,h**), with no great differences when applying the two synthetic methods. Some considerations about the collapse of the empty structure in GH900 have already been reported elsewhere (see section "**5.4.2. N-CMSs by USP: characterization**").

In order to verify whether the electrocatalytic properties of samples synthesized by USP and APM, starting from the same precursors mixture, have been somehow changed, in **Fig. 5.40** is shown a comparison between polarization curves recorded in 0.1 mol dm^{-3} $HClO_4$ for the samples USP_GH900 and APM_GH900.

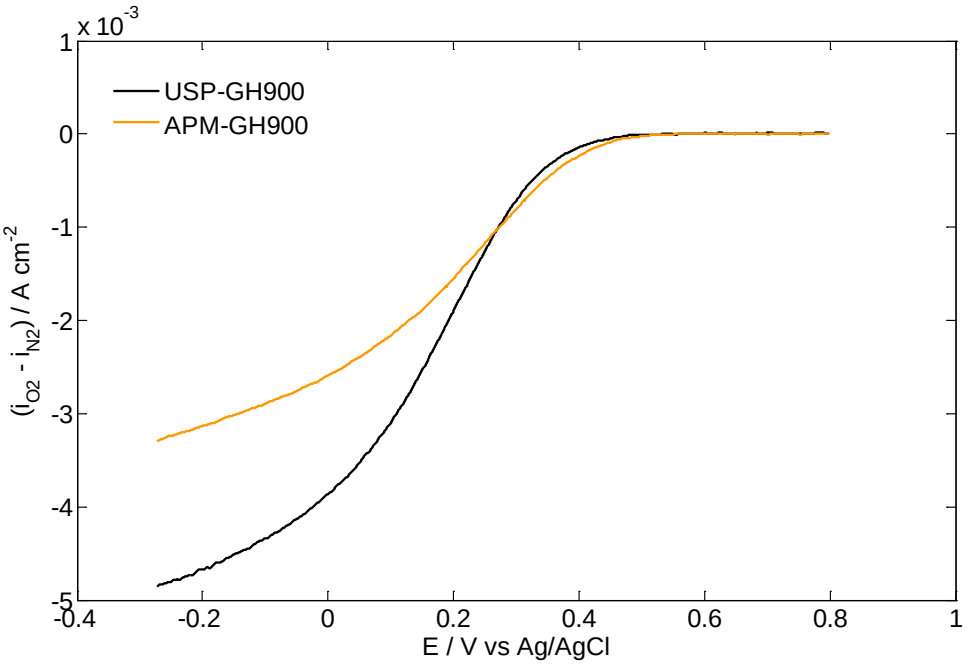

Fig. 5.40: ORR RDE curves recorded in oxygen saturated 0.10 mol dm^{-3} $HClO_4$. T = 25 °C; v= 5 mV s^{-1}; ω= 1600 rpm. USP_GH900: black, APM_ GH900: orange.

The ORR onset potential is almost the same for both samples, currents are however always lower for sample synthesized by APM. This might be attributed to different reactants/products diffusion processes, involving particles different in size and size distribution, and, as a consequence, differently packed onto the electrode.

The following step was the addition of a surfactant in the starting solution in very low quantities, keeping in mind that chlorides are not desirable in catalysts for FCs applications [60], in order to make the bubbles formation easier, even by using an APM method. Since ORR

electrocatalysis involves only the surface of materials, there is no point to desire solid particles, because the inner core of spheres would not been useful for the purpose, wasting material. SEM and FIB milling results from APM_GH710SURF and APM_GH900SURF are reported in **Fig. 5.41 a and Fig. 5.41 b-c**, respectively.

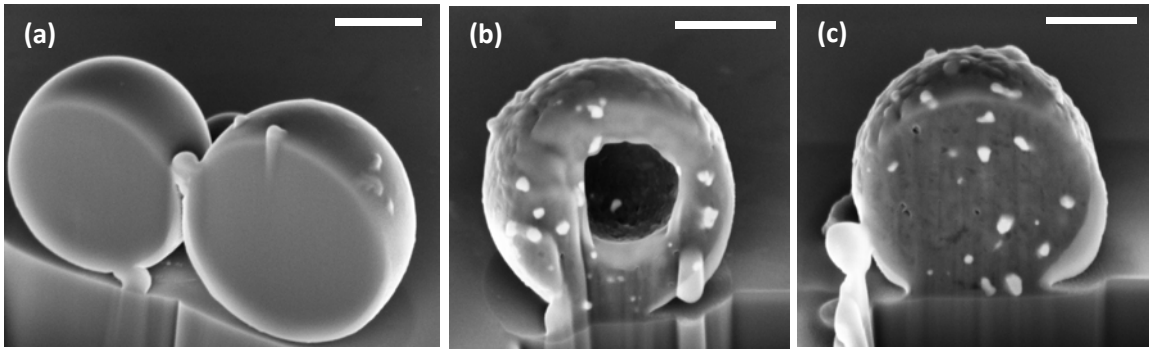

Fig. 5.41 a-c: FIB milling of (a) APM_GH710, (b,c) APM_GH900 microspheres; (scalebar = 500 nm).

It is interesting noting that, through this synthesis, some particles were generated by droplets, retaining a solid structure but some others, likely due to the induced formation of bubbles, resulted empty and, differently from all the previous cases, retained the hollow-shell structure even after the 900°C annealing, as shown in **Fig. 5.41 b**.

In order to compare the electroactivities of the 900°C annealed particles with and without the surfactant, electrochemical measurements were performed in 0.1 mol dm^{-3} KOH, and ORR activity of APM_GH900 and APMGH900SURF was compared, as shown in **Fig. 5.42**.

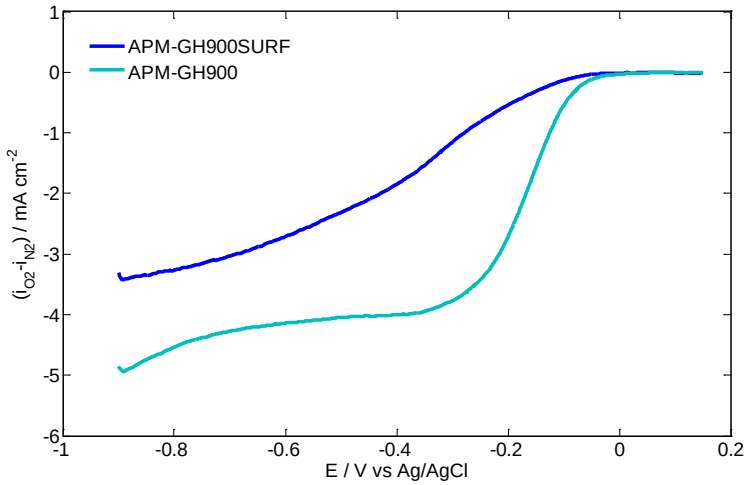

Fig. 5.42: ORR RDE curves recorded in oxygen saturated 0.10 mol dm^{-3} KOH. T = 25 °C; v= 5 mV s^{-1}; ω= 1600 rpm. APM_GH900: light blue, APM_GH900SURF: blue.

It is quite evident that the ORR electroactivity is worsened when the surfactant is present in the sample. In **Fig. 5.42** it is noticeable that in the presence of a surfactant, not only the ORR onset potential, but also and mainly the kinetics of the reaction are getting worse, as detectable by analyzing the shape of the polarization curve. Probably there is more than one only reaction taking place in the analyzed potential range: the reduction of oxygen and the

formation of peroxides. Due to an insufficient quantity of material it was not possible to analyze the APM_GH900SURF by RRDE technique, which would have been fundamental in detecting experimentally the quantity of peroxides forming. However, a clear indication is given by the number of electron calculated applying the Koutecky-Levich equation, found to be equal to 1.9 ± 0.1. This means that the rate determining step is the formation of peroxide species, being the reduction of oxygen catalyzed by an indirect 2-electrons pathway.
This is in agreement with many literature reports showing that, in addition to the kinetic effect of Cl^- adsorbed on the supported metal catalyst particles (e.g. Pt or Fe), chlorides enhance the H_2O_2 production, which is deleterious to the stability of perfluorinated membranes in the catalyst layers (e.g. Nafion® membranes), known to degrade in the presence of peroxide radicals [60].
Hence, at the end of the synthesis APM_GH900SURF particles should be washed to get rid of even small quantities of the halogen. However the yield of this specific synthesis was very low, and the difficulties of manipulating a surfactant-containing solutions (conspicuous and uncontrollable formation of bubbles in the nebulizing system) did not balance the advantage of having, at the end, a few empty particles.

For all the above reasons, the synthesis performed by adding surfactant have been abandoned and not more used in the following.

As last aspect, the presence and, in particular, the role of iron was investigated by synthesizing a blank sample, not containing iron and comparing it with a sample prepared in the same conditions, by APM, adding iron in the precursors solution. Samples containing iron have been labeled APM_FAG710 and APM_FAG900, depending on the annealing temperature, while samples which do not contain iron have been labeled APM_FAG710noFe and APM_FAG900noFe, depending on the annealing temperature, as shown in **Tab. 5.10**.

By comparing SEM pictures on 710°C samples, it can be seen that basically the sample APM_FAG710 containing iron, in **Fig. 5.43 a-d**, is composed by smooth spheres, whose morphology is similar to the same sample FAG710 synthesized by USP method. Some differences can be evidenced when comparing this last sample with its equivalent, without iron, APM_FAG710noFe. In fact, as shown in **Fig. 5.43 b**, together with the presence of spheres similar to APM_FAG710 ones, other unordered and non-structured materials are surrounding spheres.
Focusing on 900°C annealed samples, presented in **Fig. 5.43 c**, APM_FAG900 retains the spherical shape of non-annealed particles, however, as shown above in FAG900 sample synthesized by USP, their surface is rougher and displays cracks and wide holes; small bright aggregates that are uniformly distributed throughout the surface after annealing. From an EDX analysis on GH900 it was demonstrated that they are mainly composed by iron. APM_FAG900noFe, as expected, does not exhibit these small aggregates. Their surface is quite smooth and similar to its correspondent non-annealed APM_FAG710noFe sample. Just a few particles show cracks and wide holes, as shown in the insert in **Fig. 5.43 d**. Overall both APM_FAG710noFe and APM_FAG900noFe are not homogeneous samples: the first one due to the presence of non-ordered materials, the second one due to the presence of different type of spheres, the great part of them smooth, a few of them rougher.

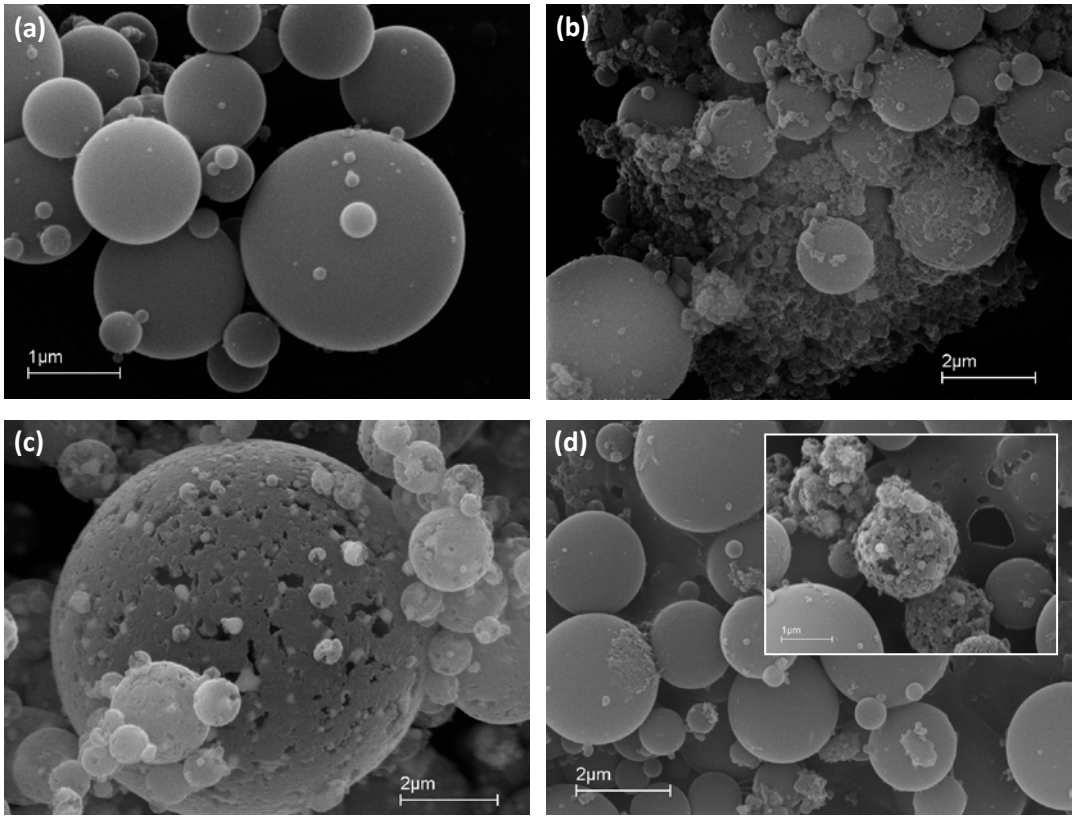

Fig. 5.43 a-d: SEM images of (a) APM_FAG710, (b) APM_FAG710noFe, (c) APM_FAG900, (d) APM_FAG900noFe microspheres.

APM_FAG900noFe was not tested as electrocatalyst for ORR because it is well known in literature that the presence of even small quantities of non-noble metals like Fe are fundamental in order to enhance the ORR performances of N-doped carbons [19].

As discussed above for GH710 and GH900 particles, it is difficult to understand the details of the pyrolysis and then, during 900°C annealing, graphitization mechanisms. However, the almost total absence of cracks and holes in APM_FAG900noFe, observed in all the other annealed samples in the presence of iron, can confirm some hypotheses done before. The annealing process is accompanied by the slow aggregation of dispersed iron into nanoparticles, which might serve as seeds for the catalytic "re-growth" of solid carbon spheres [66], in a process similar to the catalytic deposition of carbon nanotubes [11]. The catalytic re-growth process within the particles could account for the presence of cracks, holes and eroded areas on Fe-containing samples, observed from SEM images and the increase in BET surface area. A more detailed understanding of the mechanism of pore development is however challenging, as it is often highlighted in the literature on the pyrolysis of organic compounds; mechanistic understanding would require detailed analysis of decomposition products as a function of temperature and reaction conditions as previously reported by other groups [85,97,98].

In conclusion of this section, by summarizing the above results, many samples have been prepared by USP and APM methods, starting from a solution containing either glucose or

fructose together with a N-compound, either histidine or guanidine acetate. Small amounts of iron were added.

- In all cases, switching from USP to APM method, or changing the precursors solution, no great differences in external shape and morphology were evidenced. All samples were basically composed of micro-sized spheres. Samples synthesized at 710°C were smooth in shape, with a low surface area; samples annealed at 900°C were, instead, rough with many holes and cracks, which increased noticeably their surface area up to 20 times, when compared to un-annealed samples.
- Size distribution is narrower in the case of particles synthesized by APM.
- The choice between APM and USP does not affect the external structure but influences the internal one: as-prepared 710°C spheres are solid when choosing APM method but they show an empty shell structure if the USP method is used. By the way, the final ORR behavior of 900°C annealed samples is not deeply influenced by the chosen method.
- Some empty spheres have been successfully synthesized by APM adding a surfactant to the starting solution; however this addiction badly affected the ORR electroactivity of the correspondent 900°C annealed samples, hence, this method was left apart.
- Iron segregates upon annealing. This was evidenced by SEM and EDX analyses, which confirmed that iron is concentrated mainly in clearer and small aggregates in 900°C annealed particles.
- When changing the starting solution, synthesizing samples with the same USP method, surprisingly the final ORR behavior was found not to be enhanced. This means that a more accurate choice of the starting solution needs to be studied.
- The presence of cracks and holes in the final annealed sample is mainly due to the presence of iron and its catalytic growth capability on carbon matrix; this was confirmed by the almost total absence of cracked spheres in the blank sample, not containing iron. All these results open interesting questions about the details first on the pyrolysis step, in which iron is supposed to have a fundamental role and, second, of the graphitization and re-growth mechanism happening during annealing.

5.5. References

1. G.A. Ozin, A.C. Arsenault, L. Cademartiri, Nanochemistry. A Chemical Approach to Nanomaterials, RSC Publishing, 2nd Edition, Cambridge, UK, 2009.

2. P.J. Harris, Carbon Nanotubes and Related Structures, Cambridge University Press, Cambridge, UK, 1999.

3. R.H. Baughman, A.A. Zakhidov, W.A. de Heer, Carbon nanotubes-the route toward applications, Science, 297 (2002), 787-792.

4. H.J. Dai, Carbon nanotubes: synthesis, integration, and properties, Accounts of Chemical Research, 35 (2002), 1035-1044.

5. S. Ijima, Helical microtubules of graphitic carbon, Nature, 354 (1991), 56-58.

6. J. Bernholc, D. Brenner, M.B. Nardelli, V. Meunier, C. Roland, Mechanical and electrical properties of nanotubes, Annual Review of Materials Research, 32 (2002), 347-375.

7. R.B. Little, Mechanistic aspects of carbon nanotube nucleation and growth, Journal of Cluster Science, 14 (2003), 135-185.

8. J.P. O'Byrne, Z. Li, S.L.T. Jones, P.G. Fleming, J.A. Larsson, M.A. Morris, J.D. Holmes, Nitrogen-doped carbon nanotubes: growth, mechanism and structure, ChemPhysChem, 12 (2011), 2995-3001.

9. M. Lin, J.P.Y. Tan, C. Boothroyd, K.P. Loh, E. S. Tok, Y.-L. Foo Dynamical Observation of Bamboo-like Carbon Nanotube Growth, Nano Letters, 7 (2007), 2234-2238.

10. W.Y. Wong, W.R.W. Daud, A.B. Mohamad, A.A.H. Kadhum, E.H. Majlan, K.S. Loh, Nitrogen-containing carbon nanotubes as cathodic catalysts for proton exchange membrane fuel cells, Diamond and Related Materials, 22 (2012), 12-22.

11. B.C. Liu, S.C. Lyu, S.I. Jung, H.K. Kang, C.-W. Yang, J.W. Park, C.Y. Park, C.J. Lee, Single-walled carbon nanotubes produced by catalytic chemical vapor deposition of acetylene over Fe–Mo/MgO catalys, Chemical Physics Letters, 383 (2004), 104-108.

12. R. Bresciani, S. Marzorati, A. Lascialfari, B. Sacchi, N. Santo, Nadia, M. Longhi, Effects of catalyst aging on the growth morphology and oxygen reduction activity of nitrogen-doped carbon nanotubes, Electrochemistry Communications 51 (2015), 27-32.

13 . J.H. Lehman, M. Terrones, E. Mansfield, K.E. Hurst, V. Meunier, Evaluating the characteristics of multiwall carbon nanotubes, Carbon, 49 (2011), 2581-2602.

14. S. Maldonado, S. Morin, K.J. Stevenson, Structure, composition, and chemical reactivity of carbon nanotubes by selective nitrogen doping, Carbon, 44 (2006), 1429-1437D.

15. S. Maldonado, K.J. Stevenson, Influence of nitrogen doping on oxygen reduction electrocatalysis at carbon nanofiber electrodes, Journal of Physical Chemistry B, 109 (2005), 4707-4716.

16. C.E. Banks, A. Crossley, C. Salter, S.J. Wilkins, R.G. Compton, Carbon nanotubes contain metal impurities which are responsible for the “electrocatalysis” seen at some nanotube-modified electrodes, Angewandte Chemie, Int. Ed. 45 (2006), 2533-2537.

17. M. Pumera, Voltammetry of carbon nanotubes and graphenes: excitement, disappointment, and reality, Chemical Record, 12 (2012), 201-213.

18. T. Kolodiazhnyi, M. Pumera, Towards an ultrasensitive method for the determination of metal impurities in carbon nanotubes, Small, 4 (2008), 1476-1484.

19. I. Galbiati, C.L. Bianchi, M. Longhi, L. Formaro, A. Carrà, Iron and copper containing oxygen reduction catalysts from templated glucose-histidine, Fuel Cells, 10 (2010), 251-258.

20. D. Hulicova-Jurcakova, M. Seredych, G.Q. Lu, T.J. Bandosz, Combined effect of nitrogenand oxygen-containing functional groups of microporous activated carbon on its electrochemical performance in supercapacitors, Advanced Functional Materials, 19 (2009), 438-447.

21. S. Biniak, G. Szymański, J. Siedlewski, A. Świątowski The characterization of activated carbons with oxygen and nitrogen surface groups, Carbon, 35 (1997), 1799-1810.

22. D. Long, J. Zhang, J. Yang, Z. Hu, G. Cheng, X. Liu, R. Zhang, L. Zhan, W. Qiao, L. Ling, Chemical state of nitrogen in carbon aerogels issued from phenol-melamine-formaldehyde gels, Carbon, 46 (2008), 1259-1262.

23. J.R. Pels, F. Kapteijn, J.A. Moulijn, Q. Zhu, K. M. Thomas, Evolution of nitrogen functionalities in carbonaceous materials during pyrolysis, Carbon, 33 (1995), 1641-1653.

24. Z. Mo, S. Liao, Y. Zheng, Z. Fu, Preparation of nitrogen-doped carbon nanotube arrays and their catalysis towards cathodic oxygen reduction in acidic and alkaline media, Carbon, 50 (2012), 2620-2627.

25. Z. Chen, D. Higgins, Z. Chen, Nitrogen doped carbon nanotubes and their impact on the oxygen reduction reaction in fuel cells, Carbon, 48 (2010), 3057-3065.

26. N. Alexeyeva, E. Shulga, V. Kisand, I. Kink, K. Tammeveski, Electroreduction of oxygen on nitrogen-doped carbon nanotube modified glassy carbon electrodes in acid and alkaline solutions, Journal of Electroanalytical Chemistry, 648 (2010), 169-175.

27. S. Kundu, T.C. Nagaiah, W. Xia, Y. Wang, S. Van Dommele, J.H. Bitter, M. Santa, G. Grundmeier, M. Bron, W. Schuhmann, M. Muhler, Electrocatalytic activity and stability of nitrogen-containing carbon nanotubes in the oxygen reduction reaction, Journal of Physical Chemistry C, 113 (2009), 14302-14310.

28. M. Gara, R.G. Compton, Activity of carbon electrodes towards oxygen reduction in acid: A comparative study, New Journal of Chemistry, 35 (2011), 2647-2652.

29. H. Ghanbarlou, S. Rowshanzamir, B. Kazeminasab, M.J. Parnian, Non-precious metal nanoparticles supported on nitrogen-doped graphene as a promising catalyst for oxygen

reduction reaction: Synthesis, characterization and electrocatalytic performance, Journal of Power Sources, 273 (2015), 981-989.

30. L. Wang, M. Pumera, Residual metallic impurities within carbon nanotubes play a dominant role in supposedly “metal-free” oxygen reduction reactions, Chemical Communication, 50 (2014), 12662-12664.

31. D.H. Lee, W.J. Lee, W.J. Lee, S.O. Kim, Y-H Kim, Theory, synthesis, and oxygen reduction catalysis of Fe-Porphyrin-like carbon nanotube, Physical Review Letters, 106 (2011), 175502.

32. K.S.W. Sing, D.H. Everett, R.A.W. Haul, L. Moscou, R.A. Pierotti, J. Rouquerol, T. Siemieniewska, Reporting physisorption data for gas/solid systems with special reference to the determination of surface area and porosity, Pure Applied Chemistry, 57 (1985), 603-619.

33. S. Lowell and J. E. Shields, in Powder Surface Area and Porosity, Chapman & Hall, London, New York, Tokyo, Melbourne, Madras, Editon edn., 1991, p. 57.

34. T.L. Barr, An ESCA study of the termination of the passivation of elemental metals, The Journal of Physical Chemistry, 82 (1978), 1801-1810.

35. P. Marcus I. Olefjord, A round robin on combined electrochemical and AES/ESCA characterization of the passive films on iron-chromium and iron-chromium molybdenum alloys, Corrosion Science, 28 (1988), 589-602.

36. D. Brion, Photoelectron spectroscopic study of the surface degradation of pyrite (FeS_2), chalcopyrite ($CuFeS_2$), sphalerite (ZnS), and galena (PbS) in air and water, Applications of Surface Science, 5 (1980), 133-152.

37. H.W. Nesbitt,G.M. Bancroft, A.R. Pratt, M.J. Scaini, Sulfur and iron surface states on fractured pyrite surfaces, American Mineralogist, 83 (1998), 1067-1076.

38. A.S. Ingason, A.K. Eriksson, E. Lewin, J. Jensen, S. Olafsson, Growth and structural properties of Mg:C thin films prepared by magnetron sputtering, Thin Solid Films, 518 (2010), 4225-4230.

39. S. Ardizzone, C.L. Bianchi,M. Fadoni, B. Vercelli, Magnesium salts and oxide: an XPS overview, Applied Surface Science, 119 (1997), 253-259.

40. D. Brion, Photoelectron spectroscopic study of the surface degradation of pyrite (FeS_2), chalcopyrite ($CuFeS_2$), sphalerite (ZnS), and galena (PbS) in air and water, Applications of Surface Science, 5 (1980), 133-152.

41. P. Casey, E. O'Connor, R. Long, B. Brennan, S.A. Krasnikov, D. O'Connell, P.K. Hurley, G. Hughes, Growth, ambient stability and electrical characterisation of MgO thin films on silicon surfaces, Microelectronic Engineering 86 (2009), 1711-1714.

42. A. Atrens, S. Jin, ESCA-Studies of the structure and composition of the passive film formed on stainless steels by various immersion temperatures in 0.1 M NaCl solution, Applied Physics A, 42 (1987), 149-165.

43. M. Oncak, R. Wlodarczyk, J. Sauer, Water on the MgO(001) Surface: Surface Reconstruction and Ion Solvation, Journal of Physical Chemistry Letters 6 (2015), 2310-2314.

44. N. Khan, D. Dollimore, K. Alexander, F.W. Wilburn, The origin of the exothermic peak in the thermal decomposition of basic magnesium carbonate, Thermochimica Acta, 367-368 (2001), 321-333.

45. Y. Chen, T. Zhou, , H. Fang, S. Li, Y. Yao, Y. He, A Novel Preparation of Nano-sized Hexagonal $Mg(OH)_2$, Procedia Engineering, 102 (2015), 388-394.

46. D. Cornu, H. Guesmi, G. Laugel, J.-M. Krafft, H. Pernot, On the relationship between the basicity of a surface and its ability to catalyze transesterification in liquid and gas phases: the case of MgO, Physical Chemistry Chemical Physics, 2015, DOI: 10.1039/C5CP00217F.

47. D.A. Torres-Rodríguez, H. Pfeiffer, Thermokinetic analysis of the MgO surface carbonation process in the presence of water vapor, Thermochimica Acta, 516 (2011), 74-78.

48. M.L. Leech, W.G. Ernst, Graphite pseudomorphs after diamond? A carbon isotope and spectroscopic study of graphite cuboids from the Maksyutov Complex, south Ural mountains, Russia, Geochimica et Cosmochimica Acta, 62 (1998), 2143-2154.

49. Y. Saito, T. Matsumoto, Hollow and filled rectangular parallelepiped carbon nanocapsules catalyzed by calcium and stronzium, Journal of Crystal Growth, 187 (1998), 402-409.

50. P. Liu, L. Cao, C.X. Wang, X.Y. Chen, G.W. Yang, Micro- and Nanocubes of Caron with C_8-like anf Blue Luminescence, Nano Letters, 8 (2008), 2570-2575.

51. S.K. Sonkar, M. Saxena, M. Saha, S. Sarkar, Carbon Nanocubes and Nanobricks from pyrolysis of Rice, Journal of Nanoscience and Nanotechnology, 10 (2010), 4064-4067.

52. M. Motiei, J. Calderon-Moreno, A. Gedanken, The Formation of Carbon-Coated MgO Cubes and Carbon Cubes, Advanced Materials, 14 (2002), 1169-1172.

53. Y. Liu, J. Su, Synthesis and Characterization of MgO-filled Rectangular Carbon nanocapsules, Advanced Materials Research, 785-786 (2013), 444-448.

54. R. Bresciani, Master Thesis in Chemical Sciences, Università degli Studi di Milano, 2014.

55. S.E. Skrabalak, K.S. Suslick, Carbon powders prepared by ultrasonic spray pyrolysis of substituted alkali Benzoates, Journal of Physical Chemistry C, 11 (2007), 17807-17811.

56. S.E. Skrabalak, K.S. Suslick, Porous carbon powders prepared by ultrasonic spray pyrolysis, Journal of the American Chemical Society, 128 (2006), 12642-12643.

57. S.E. Skrabalak, K.S. Suslick, Porous MoS_2 synthesized by ultrasonic spray pyrolysis, Journal of the American Chemical Society, 127 (2005), 9990-9991.

58. Y.L. Song, S.C. Tsai, C.Y. Chen, T.K. Tseng, C.S. Tsai, J.W. Chen, Y.D. Yao, Ultrasonic spray pyrolysis for synthesis of spherical zirconia particles, Journal of the American Chemical Society, 87 (2004), 1864-1871.

59. W.H. Suh, K.S. Suslick, Magnetic and porous nanospheres from ultrasonic spray pyrolysis, Journal of the American Chemical Society, 127 (2005), 12007-12010.

60. T.J. Schmidt, U.A. Paulus, H.A. Gasteiger, R.J. Behm, The oxygen reduction reaction on a Pt/carbon fuel cell catalyst in the presence of chloride anions. Journal of Electroanalytical Chemistry, 508 (2001), 41-47.

61. E. Feria-Reyes, C. Torres-Torres, H. Martínez-Gutiérrez, C. Mercado-Zúñiga, R. Torres-Martínez, G. Urriolagoitia-Calderón, Interferometric laser measurement of multi-axial mechanical properties exhibited by carbon nanotubes, Journal of Alloys and Compounds, 643 (2015), S165–S171.

62. V. Pichot, P. Launois, M. Pinault, M. Mayne-L'Hermite, C. Reynaud, Evidence of strong nanotube alignment and for iron preferential growth axis in multiwalled carbon nanotube carpets, Applied Physical Letters, 85 (2004), 473-475.

63. S. Marzorati, J.M. Vasconcelos, J. Ding, M. Longhi, P.E. Colavita, Template-free ultraspray pyrolysis synthesis of N/Fe-doped carbon microspheres for oxygen reduction electrocatalysis, Journal of Materials Chemistry A, 3 (2015), 18920-18927.

64. P. Duffy, L.M. Magno, R.B. Yadav, S.K. Roberts, A.D. Ward, S.W. Botchway, Incandescent porous carbon microspheres to light up cells: solution phenomena and cellular uptake, Journal of Material Chemistry, 22 (2012), 432-439.

65. H. Xu, J. Guo, K.S. Suslick, Porous Carbon Spheres from Energetic Carbon Precursors using Ultrasonic Spray Pyrolysis, Advanced Materials, 24 (2012), 6028-33.

66. J. Zhan J, B. Sunkara, J. Tang, Y. Wang, J. He, G.L. McPherson, *et al.* , Carbothermal Synthesis of Aerosol-Based Adsorptive-Reactive Iron-Carbon Particles for the Remediation of Chlorinated Hydrocarbons, 50 (2011), 13021-13029.

67. J.D. Atkinson, M.E. Fortunato, S.A. Dastgheib, M. Rostam-Abadi, M.J. Rood, K.S. Suslick, Synthesis and characterization of iron-impregnated porous carbon spheres prepared by ultrasonic spray pyrolysis, Carbon, 49 (2011), 587-598.

68. A.C. Ferrari, J. Robertson, Interpretation of Raman spectra of disordered and amorphous carbon, Physical Review B, 61 (2000), 14095-14107.

69. A.C. Ferrari, J. Robertson, Raman spectroscopy of amorphous, nanostructured, diamond-like carbon, and nanodiamond, Philosophical Transactions of the Royal Society A, 362 (2004), 2477-2512.

70. H.O. Pierson, Handbook of Carbon, Graphite, Diamond and Fullerenes - Properties, Processing and Applications, 1st ed. Park Ridge, New Jersey: Noyes Publications; 1993.

71. P. Stonehart, D. Wheeler, Phosphoric Acid Fuel Cells (PAFCs) for Utilities: Electrocatalyst Crystallite Design, Carbon Support, and Matrix Materials Challenges, Conway BE, ed. Modern Aspects of Electrochemistry, Number 38: Springer 2005, p. 407.

72. M. Hermanek, R. Zboril, M. Mashlan, L. Machala, O. Schneeweiss, Thermal behaviour of iron(ii) oxalate dihydrate in the atmosphere of its conversion gases, Journal of Materials Chemistry, 16 (2006), 1273-1280.

73. J.N. Wang, L. Zhang, F. Yu, Z.M. Sheng, Synthesis of Carbon Encapsulated Magnetic Nanoparticles with Giant Coercivity by a Spray Pyrolysis Approach, Journal of Physical Chemistry B, 111 (2007), 2119-2124.

74. A. Ōya, H. Marsh, Phenomena of catalytic graphitization, Journal of Materials Science, 17 (1982), 309-322.

75. E. Papastavros, P.J. Shea, M.A. Langell, Oxygen, Carbon, and Sulfur Segregation in Annealed and Unannealed Zerovalent Iron Substrates, Langmuir, 20 (2004), 11509-11516.

76. S.T. Jackson, R.G. Nuzzo, Determining hybridization differences for amorphous carbon from the XPS C 1s envelope, Applied Surface Science, 90 (1995), 195-203.

77. J. Díaz, G. Paolicelli, S. Ferrer, F. Comin, Separation of the sp^3 and sp^2 components in the C1s photoemission spectra of amorphous carbon films. Physical Review B, 54 (1996), 8064-8069.

78. M.C. Biesinger, B.P. Payne, A.P. Grosvenor, L.W.M. Lau, A.R. Gerson, R.S.C. Smart, Resolving surface chemical states in XPS analysis of first row transition metals, oxides and hydroxides: Cr, Mn, Fe, Co and Ni, Applied Surface Science, 257 (2011), 2717-2730.

79. S.A. Steiner, T.F. Baumann, J. Kong, J.H. Satcher, M.S. Dresselhaus, Iron-Doped Carbon Aerogels: Novel Porous Substrates for Direct Growth of Carbon Nanotubes, Langmuir, 23 (2007), 5161-5166.

80. R. Kothandaraman, V. Nallathambi, K. Artyushkova, S.C. Barton, Non-precious oxygen reduction catalysts prepared by high-pressure pyrolysis for low-temperature fuel cells, Applied Catalysis, B, 92 (2009), 209-216.

81. C. Galeano, J.C. Meier, M. Soorholtz, H. Bongard, C. Baldizzone, K.J.J. Mayrhofer, *et al*., Nitrogen-Doped Hollow Carbon Spheres as a Support for Platinum-Based Electrocatalysts, ACS Catalysis, 4 (2014), 3856-3868.

82. C. Emmenegger, J.M. Bonard, P. Mauron, P. Sudan, A. Lepora, B. Grobety, *et al.*, Synthesis of carbon nanotubes over Fe catalyst on aluminium and suggested growth mechanism, Carbon, 41 (2003), 539-547.

83. J. Geng, D.A. Jefferson, B.F.G. Johnson, Direct conversion of iron stearate into magnetic Fe and Fe_3C nanocrystals encapsulated in polyhedral graphite cages, Chemical Communications, 21 (2004), 2442-2443.

84. Q. Yan, C. Wan, J. Liu, J. Gao, F. Yu, J. Zhang, *et al.*, Iron nanoparticles in situ encapsulated in biochar-based carbon as an effective catalyst for the conversion of biomass-derived syngas to liquid hydrocarbons, Green Chemistry, 15 (2013), 1631-1640.

85. A. Singh, J. Jayaram, M. Madou, S. Akbar, Pyrolysis of negative photoresists to fabricate carbon structures for microelectromechanical systems and electrochemical applications, Journal of the Electrochemical Society, 149 (2002), 78-83.

86. M. Kiyono, P.J. Williams, W.J. Koros, Effect of pyrolysis atmosphere on separation performance of carbon molecular sieve membranes, Journal of Membrane Science, 359 (2010), 2-10.

87. S.M. Saufi, A.F. Ismail, Fabrication of carbon membranes for gas separation - a review, Carbon, 42 (2004), 241-259.

88. V.C. Geiszler, W.J. Koros, Effects of Polyimide Pyrolysis Conditions on Carbon Molecular Sieve Membrane Properties, Industrial and Engineering Chemistry Research, 35 (1996), 2999-3003.

89. L. Lai, J.R. Potts, D. Zhan, L. Wang, C.K. Poh, C. Tang, *et al.*, Exploration of the active center structure of nitrogen-doped graphene-based catalysts for oxygen reduction reaction, Energy & Environmental Science, 5 (2012), 7936-7942.

90. S.M. Unni, S.N. Bhange, R. Illathvalappil, N. Mutneja, K.R. Patil, S. Kurungot, Nitrogen-Induced Surface Area and Conductivity Modulation of Carbon Nanohorn and Its Function as an Efficient Metal-Free Oxygen Reduction Electrocatalyst for Anion-Exchange Membrane Fuel Cells, Small, 11 (2015), 352-360.

91. D. Zhou, L. Yang, L. Yu, J. Kong, X. Yao, W. Liu, *et al.*, Fe/N/C hollow nanospheres by Fe(iii)-dopamine complexation-assisted one-pot doping as nonprecious-metal electrocatalysts for oxygen reduction, Nanoscale, 7 (2015), 1501-1509.

92. R.A. Sidik, A.B. Anderson, N.P. Subramanian, S.P. Kumaraguru, B.N. Popov, O_2 Reduction on Graphite and Nitrogen-Doped Graphite: Experiment and Theory, Journal of Physical Chemistry B, 110 (2006), 1787-1793.

93. N.P. Subramanian, X. Li, V. Nallathambi, S.P. Kumaraguru, H. Colon-Mercado, G. Wu, *et al.*, Nitrogen-modified carbon-based catalysts for oxygen reduction reaction in polymer electrolyte membrane fuel cells, Journal of Power Sources, 188 (2009), 38-44.

94. F. Jaouen, Heat-Treated Transition Metal-N_xC_y Electrocatalysts for the O_2 Reduction Reaction in Acid PEM Fuel Cells, In: Z. Chen, J.-P. Dodelet, J. Zhang, eds. Non-Noble Metal Fuel Cell Catalysts, Weinheim, Germany: Wiley-VCH Verlag GmbH & Co. KGaA 2014, 29-118.

95. S. Chen, J. Bi, Y. Zhao, L. Yang, C. Zhang, Y. Ma, Q. Wu, X. Wang and Z. Hu, Nitrogen-Doped Carbon Nanocages as Efficient Metal-Free Electrocatalysts for Oxygen Reduction Reaction, Advanced Materials, 24 (2012), 5593-5597.

96. N. Ramaswamy, U. Tylus, Q. Jia, S. Mukerjee, Activity Descriptor Identification for Oxygen Reduction on Nonprecious Electrocatalysts: Linking Surface Science to Coordination Chemistry, Journal of the American Chemical Society, 135 (2013), 15443-15449.

97. M. Kiyono, P.J. Williams, W.J. Koros, Effect of pyrolysis atmosphere on separation performance of carbon molecular sieve membranes, Journal of Membrane Science, 359 (2010), 2-10. S.M. Saufi, A.F. Ismail, Fabrication of carbon membranes for gas separation - a review, Carbon, 42 (2004), 241-259.

98. V.C. Geiszler, W.J. Koros, Effects of Polyimide Pyrolysis Conditions on Carbon Molecular Sieve Membrane Properties, Industrial and Engineering Chemistry Research, 35 (1996), 2999-3003.

Chapter 6

Tuning the Electronic Valence Structure of Carbon Films

The understanding of surface behavior of carbon thin films is, at present, attracting great interest due to its multiple applications dealing with nanostructure synthesis, electronics, delivery systems and biomedicine [1,2]. The often-cited advantages of carbon electrodes include low cost, wide potential window, relatively inert electrochemistry, and electrocatalytic activity for a variety of redox reactions [3]. The work presented in this section aims to understand how the electronic properties of carbon influence the interfacial charge transfer behavior in order to provide a rational approach towards accurate control of surface chemical reactions and interfacial processes that underpin many of the applications of carbon materials. A combination of spectroscopic and electrochemical methods was used in order to characterize a number of amorphous carbon materials that differ by their degree of graphitization and investigate their electron transfer reactions.

This section, apparently diverging from the main goals of the present work, was thought to better understand the electronic C-surface behavior in charge transfer reactions. This is actually strongly connected to the oxygen reduction reaction, for which all the catalysts, hereby synthesized, were designed. However, instead of starting from complicated systems involving porous and doped-carbons (as all the above presented samples are), the choice was addressed to the simplest but closest material: annealed and non-annealed amorphous carbon thin films prepared by DC-magnetron sputtering technique.

The work described in this chapter was carried out at Trinity College Dublin in the laboratory of Prof. Colavita as part of an academic collaboration and an Erasmus exchange. In the following the basis of the DC-magnetron sputtering technique is briefly exposed and then, the choice of the redox couples, used to probe the synthesized carbon films, is explained.

6.1 DC-magnetron sputtered C-films

Sputtering is the removal of atoms from a target surface by bombardment of that surface with energetic ions [4]. These atoms then condense on a substrate and form a thin film (**Fig. 6.1**). Sputtering occurs in a vacuum chamber.

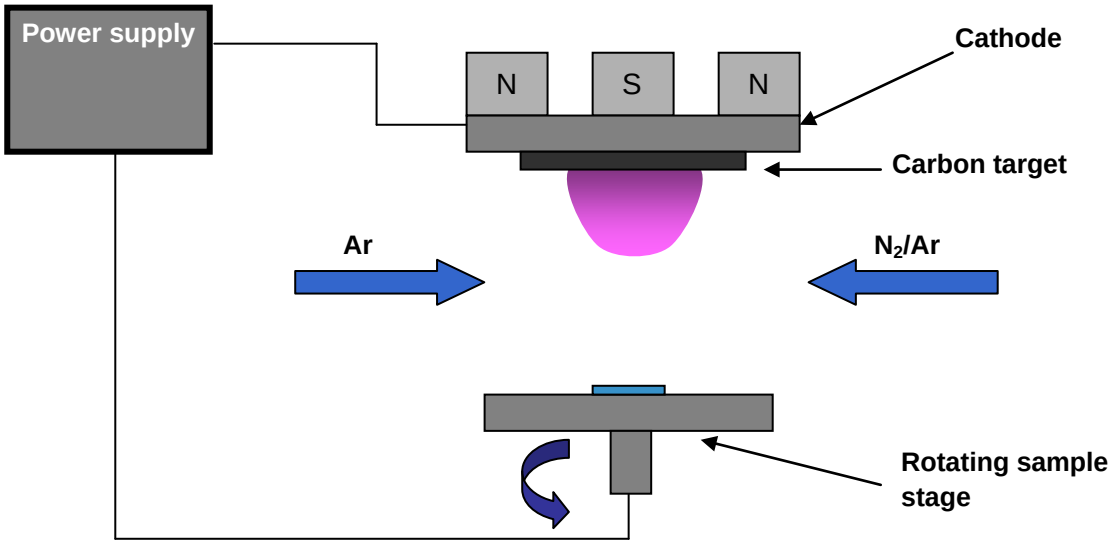

Fig. 6.1: DC-Magnetron sputtering chamber scheme.

The process is limited by low deposition rates and high substrate heating effects, as well as low ionisation efficiencies of the plasma. The sputtering chamber is filled with a low-pressure gas, frequently argon, and high-voltage magnetron cathodes are placed behind the coating material target. They can greatly enhance deposition rates: secondary electrons emitted from the target after ion bombardment are trapped in the vicinity of the target by the magnetron. This results in an increased degree of ionisation of the plasma which in turn leads to higher sputtering and deposition rates. High voltage flows from the magnetrons across the gas and creates high-energy plasma that strikes the coating material target. The force generated by these plasma ion strikes causes atoms to eject from the coating material and bond with the substrate.

The most common forms of magnetron sputtering use direct current (DC) or radio frequency (RF) power supplies coupled with Ar gas to produce the plasma. In this work DC-magnetron sputtering technique was used. Since there is no hydrogen involved in the sputtering process, hydrogen-free films can be deposited. The sp^2 percentages of these films tend to be high due to the low mean ion energies of the depositing species.

6.2 Outer-sphere reversible redox couples

To aid comparison of various carbon electrodes for electron transfer reactivity, it is useful to employ simple outer-sphere redox systems. Electrode reactions are commonly distinguished as inner- and outer-sphere. In an outer-sphere electrode reaction, electron

transfer between the electrode and the oxidant or reductant takes place at the Outer Helmholtz Plane (OHP). Thus, the reactant-electrode interactions should be weak.

On the basis of redox couple classification, shown in **Fig. 6.2**, outer-sphere redox systems are generally considered to lack any electrocatalytic or adsorption step. Examples of commonly used outer-sphere redox systems are $Ru(NH_3)_6^{+3/+2}$ and $IrCl_6^{2-/3-}$. In order to experimentally verify this property, the carbon surface is purposely modified with a physi- or chemisorbed monolayer. In the absence of a significant change in the heterogeneous rate constant *k°*, it can be stated that the redox couple is an outer-sphere one. A second breakpoint in the classification "tree", involves the effect of surface oxides. $Fe(CN)_6^{3-/4-}$, for example, exhibits significantly slower kinetics on a surface modified with a monolayer (e.g. a monolayer of covalently bonded nitrophenyl groups), meaning that this redox couple is "surface-sensitive" but not "oxide-sensitive".

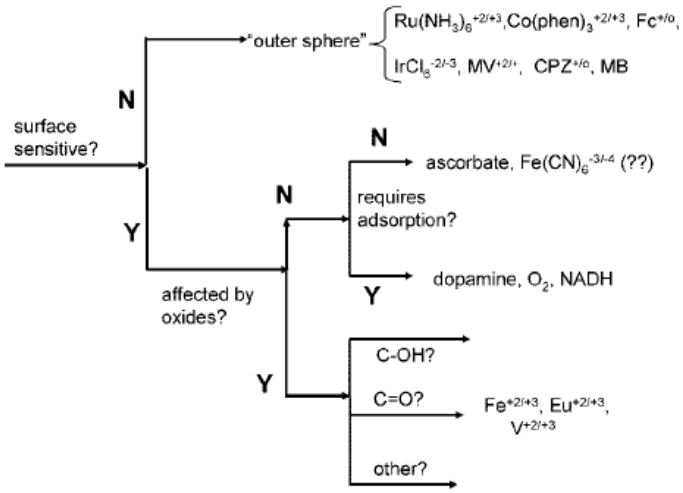

Fig. 6.2: Classification of redox systems according to their kinetic sensitivity to particular surface modifications on carbon electrodes [3].

For all the reasons above, in this work, considering that C-surfaces to be tested differ for their graphitization degree and oxides on the surface, three redox couples have been chosen: $Ru(NH_3)_6^{+3/+2}$ and $IrCl_6^{2-/3-}$, frequently used probes, that are neither "surface-sensitive" nor "oxide-sensitive". Moreover, $Fe(CN)_6^{3-/4-}$ couple was added in experiments, because it is "surface-sensitive" but not "oxide-sensitive".

6.3 Experimental

Potassium chloride (BioXtra, >99%), hexammineruthenium (III) chloride (98%), potassium hexachloroiridate (IV) (99.99%), potassium ferrocyanide (99%), sulfuric acid (95-97%), methanol and hydrogen peroxide (>30% w/v) were obtained from Aldrich and used as received. HOPG substrates (NT-MDT, surface renewed by tape) and Molybdenum foils (Aldrich, 99.9%, 0.1 mm thick) underwent 5 min sonication in methanol before being used. Degassed deionized water was used for all aqueous solutions.

Amorphous carbon films with thicknesses in the range 40-50 nm were prepared via DC-magnetron sputtering (Torr International, Inc.) at a base pressure ≤ 2 × 10^{-6} mbar and a deposition pressure of 7 × 10^{-3} mbar for 40 min. All depositions were performed with the HOPG and Mo substrates at 100 °C. Samples are hereafter referred to as HOPG-aC and Mo-aC, respectively. Annealing was carried out by placing HOPG-aC or Mo-aC samples onto a Mo boat in the centre of a 1 m long quartz tube, positioned inside a horizontal furnace (Carbolite). Samples were annealed at 500°C, 700°C and 900°C for 1h, under a 3 LPM nitrogen flow, and then quenched to room temperature. Thus prepared samples are hereafter referred to as HOPG- or Mo- (depending on the used substrate) 500aC, 700aC and 900aC. Raman, X-ray and ultraviolet spectroscopy were performed onto samples prepared using Mo as a substrate, electrochemical measurements were instead performed onto samples prepared using HOPG as a substrate.

6.4 Results and discussion

6.4.1 Electrochemical characterization

In order to understand how the electronic properties of the prepared materials affect the interfacial charge transfer, electrochemical measurements were carried out in the presence of three reversible redox couples: $Ru(NH_3)_6^{+3/+2}$, $IrCl_6^{2-/3-}$ and $Fe(CN)_6^{3-/4-}$. These couples have been chosen according to McCreery classification of redox systems on the basis of their kinetic sensitivity to particular surface modifications on carbon electrodes [3]. $Ru(NH_3)_6^{+3/+2}$ and $IrCl_6^{2-/3-}$ couples are known to be outer-sphere redox systems lacking any electrocatalytic or adsorption step. $Fe(CN)_6^{3-/4-}$, instead, is "surface sensitive", showing a slower kinetics when the surface is modified with a monolayer, but it does not exhibit a dependence of peak separation on oxide coverage, implying that it is not "oxide-dependent".

First, by cyclic voltammetry (CV), the formal potential (E_0') of each redox couple was determined and found to be equal to E_0' = -0.170 V vs Ag/AgCl for $Ru(NH_3)_6^{+3/+2}$, E_0' = 0.715 V vs Ag/AgCl for $IrCl_6^{2-/3-}$ and E_0' = 0.300 V vs Ag/AgCl for $Fe(CN)_6^{3-/4-}$ (values calculated from an average, fixing the redox couple and varying the substrate from HOPG-aC to HOPG-900aC). A Randles-Sevcik plot (from (1)) was then built for each redox couple on glassy carbon substrates by varying the potential scan rate in the range from 0.005 V s^{-1} to 1 V s^{-1}, in order to calculate the electrode area *A* which was found to be comparable to the geometric electrode area (A_{geom}=0.05 cm^2): *A*=0.06 ± 0.01 cm^2 for $Ru(NH_3)_6^{+3/+2}$, *A*=0.052 ± 0.005 cm^2 for $IrCl_6^{2-/3-}$ and *A*=0.047 ± 0.006 cm^2 for $Fe(CN)_6^{3-/4-}$. Diffusion coefficients for each redox couple were used according to literature [5-7]. Randles-Sevcik plots are displayed in **Fig. 6.4**.

$$I_{peak} = 0.4463 \cdot n \cdot F \cdot A \cdot C\left(\frac{n \cdot F \cdot v \cdot D}{R \cdot T}\right)^{1/2} \qquad (1)$$

where I_{peak} is the current of the oxidation/reduction peak, *n* is the number of exchanged electrons, *A* is the electrode area, *C* is the redox couple concentration, *F* is the Faraday constant, *v* is the potential scan rate, *D* is the diffusion coefficient, *R* is the gas constant and *T* is the temperature.

In **Fig. 6.3** CVs, recorded for each surface varying the redox couple, are displayed. It is qualitatively noticeable how the splitting between reduction and oxidation peaks is decreasing when the annealing temperature is increased. This means that the annealing process reduces the resistance to charge transfer, likely as a result of modifications to both bulk and surface properties of the working electrode.

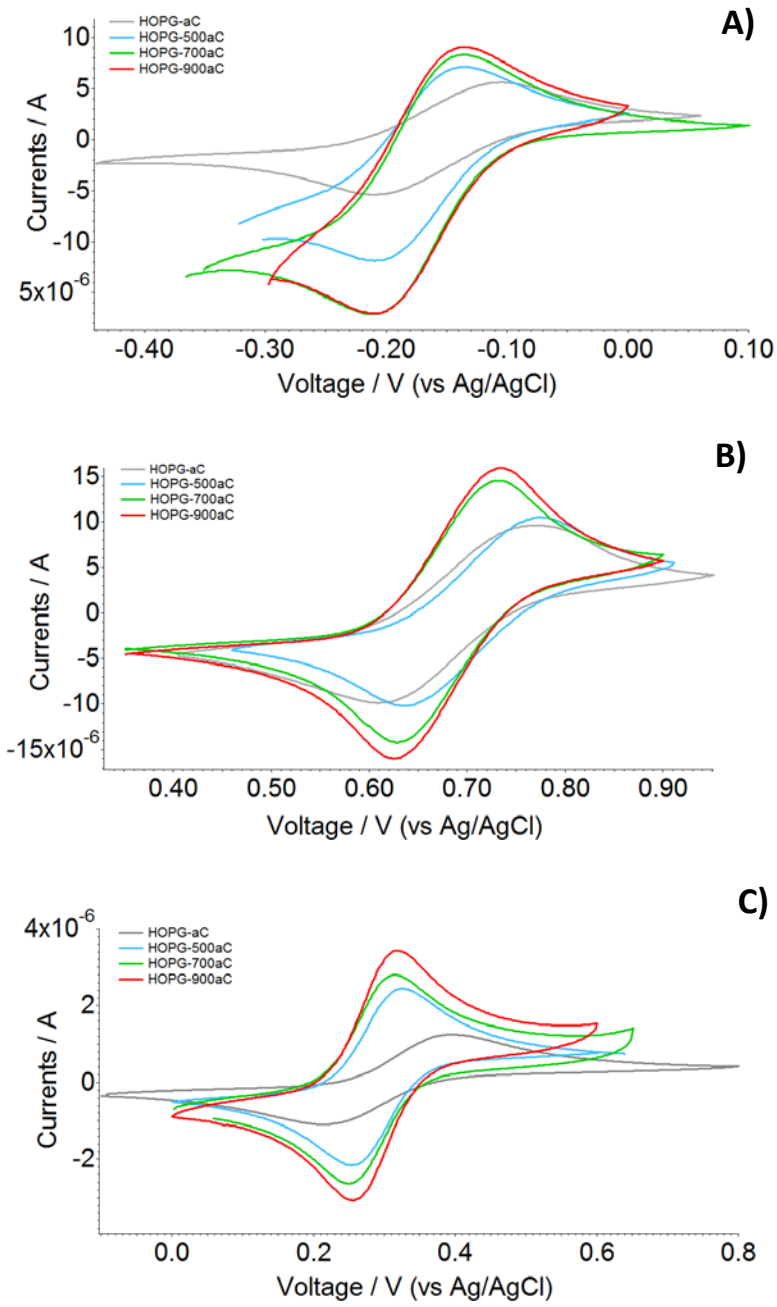

Fig. 6.3: Cyclic voltammetries (0.1 M KCl supporting electrolyte solution) in 1 mM degassed solutions of: A) hexaminеruthenium(III) chloride, B) potassium hexachloroiridate (IV), C) potassium ferrocyanide. T=25°C, v=100 mV s^{-1}.

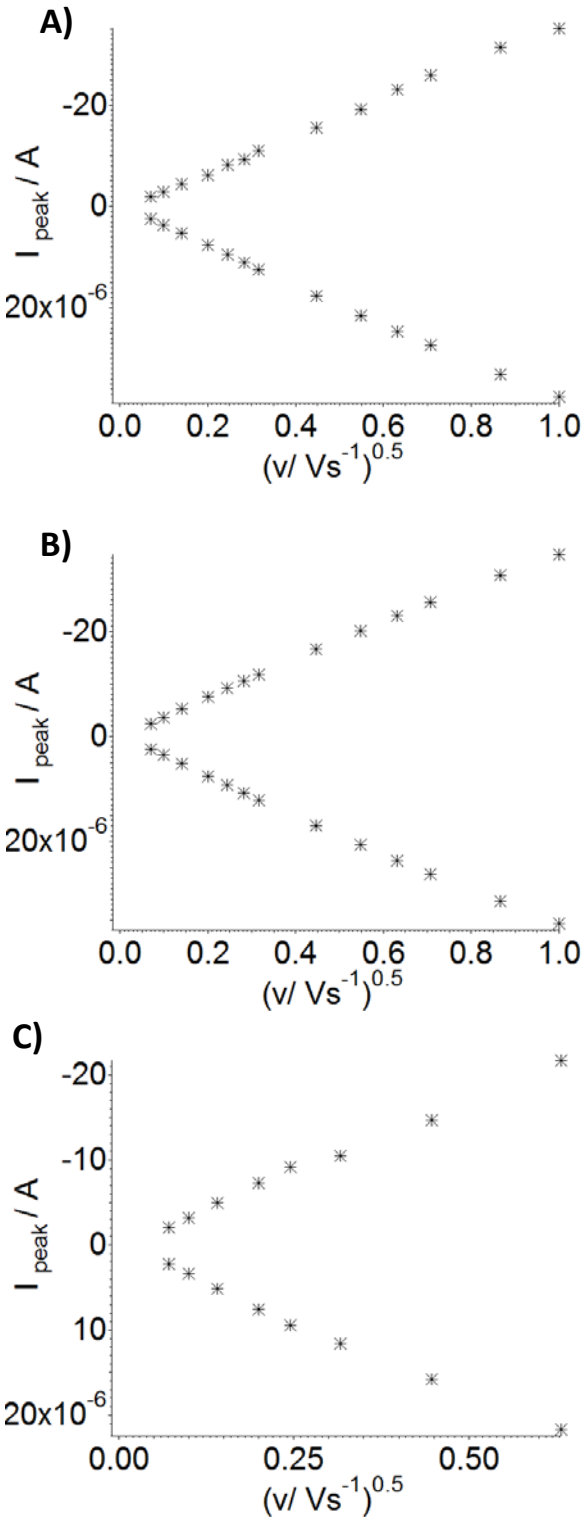

Fig. 6.4: Randles-Sevcik plots, in order to calculate the electrode area: A) $Ru(NH_3)_6^{+3/+2}$, B) $IrCl_6^{2-/3-}$, C) $Fe(CN)_6^{3-/4-}$.

The kinetics of electron transfer was investigated using EIS, running experiments at the formal potential E_0', after 5 min equilibration time. Typical complex plane impedance (Nyquist) plots recorded for each carbon surface are shown in **Fig 6.5**.

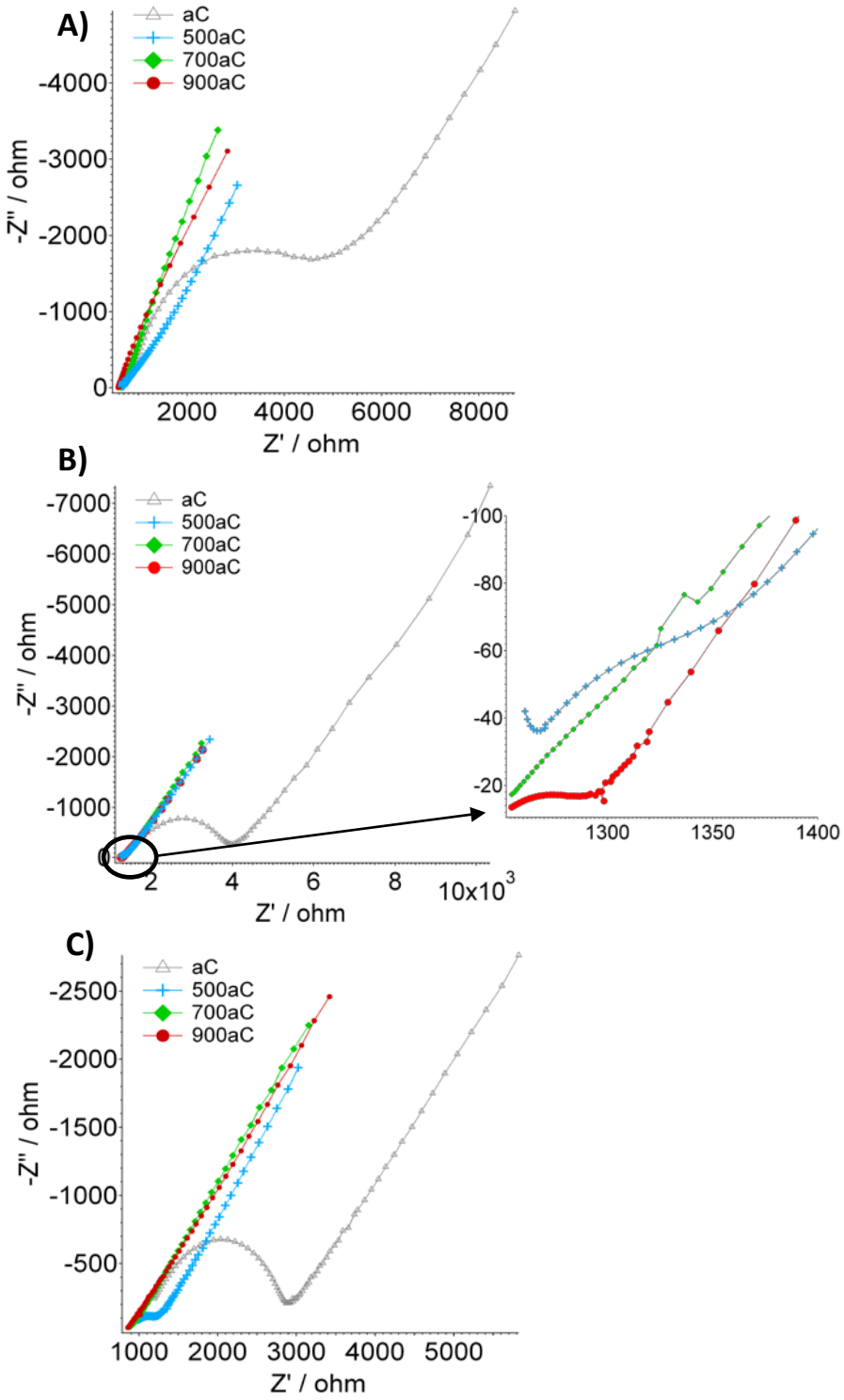

Fig. 6.5: Experimental impedance data represented as Nyquist plots (0.1 M KCl supporting electrolyte solution) in 1 mM degassed solutions of: A) hexamineruthenium(III) chloride, B) potassium hexachloroiridate (IV), C) potassium ferrocyanide. T=25°C, v=100 mV s^{-1}. Inset in B) example of magnification in the high-frequencies region.

A modified Randles circuit, shown in **Fig. 6.6**, was used to fit the recorded data.

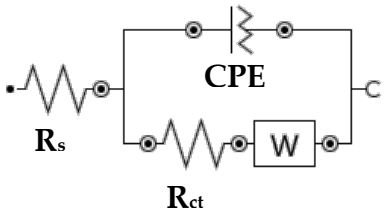

Fig. 6.6: Equivalent circuit used in the fitting.

In this equivalent circuit, the resistance R_s represents the electrolyte resistance; the constant phase element (CPE) represents the double layer capacitance and R_{ct} stands for the charge transfer resistance. The Warburg element (W) models the diffusional impedance. In the **Fig. 6.5**, a large semicircumference is always clearly identifiable in the left-side region at higher frequencies for HOPG-aC electrodes, thus indicating a significant charge transfer resistance. The same feature is considerably smaller for annealed HOPG-500aC electrodes and almost disappearing for HOPG-700aC and HOPG-900aC films, which display an impedance response dominated by the Warburg diffusional impedance, as shown by the linear trend starting in the high frequencies region. For a better understanding, see, as an example, the magnification in the high frequencies region reported in the inset in **Fig. 6.5 B**. By fitting recorded data with the modified Randles circuit model, R_{ct} values were obtained and are shown in **Tab. 6.1**, **Tab. 6.2** and **Tab. 6.3**, together with the corresponding exchange currents (i_0) and, therefore, the standard heterogeneous rate constant (k_0), calculated on the basis of the following equations:

$$i_0 = \frac{R \cdot T}{F \cdot R_{ct}} \qquad (2)$$

where *R* is the gas constant, *T* is the temperature, *F* is the Faraday constant and R_{ct} the resistance for the charge transfer.

$$k_0 = \frac{i_0}{F \cdot c \cdot A} \qquad (3)$$

where *c* is the redox couple concentration and *A* is the electrode's area.

$Ru(NH_3)_6^{+3/+2}$ redox couple (E_0'=-0.170)			
Sample	**R_{ct} / Ω**	**i_0 /A**	**k_0 /cm s^{-1}**
HOPG-aC	4702 ± 542	5.5E-06 ± 6E-07	9E-04 ± 1E-04
HOPG-500aC	1597 ± 203	1.6E-05 ± 2E-06	2.8E-03 ± 4E-04
HOPG-700aC	152 ± 16	1.7E-04 ± 2E-05	2.9E-02 ± 1E-03
HOPG-900aC	39 ± 2	6.5E-04 ± 4E-05	1.13E-01 ± 7E-03

Tab. 6.1: Charge transfer resistance, exchange current and standard heterogeneous rate constant values determined for all samples using $Ru(NH_3)_6^{+3/+2}$ redox couple.

$IrCl_6^{2-/3-}$ redox couple (E_0'=0.715)			
Sample	R_{ct} / Ω	i_0 /A	k_0 /cm s^{-1}
HOPG-aC	2557 ± 130	1.00E-05 ± 5E-07	2.0E-03 ± 1E-04
HOPG-500aC	234 ± 44	1.1E-04 ± 2E-05	2.2E-02 ± 4E-03
HOPG-700aC	177 ± 9	1.45E-04 ± 7E-06	2.9E-02 ± 1E-03
HOPG-900aC	43 ± 21	6E-04 ± 3E-04	1.2E-01 ± 6E-02

Tab. 6.2: Charge transfer resistance, exchange current and standard heterogeneous rate constant values determined for all samples using $IrCl_6^{2-/3-}$ redox couple.

$Fe(CN)_6^{3-/4-}$ redox couple (E_0'=0.300)			
Sample	R_{ct} / Ω	i_0 /A	k_0 /cm s^{-1}
HOPG-aC	1889 ± 206	1.4E-05 ± 1E-06	1.9E-03 ± 2E-04
HOPG-500aC	355 ± 43	7.2E-05 ± 9E-06	9.9E-03 ± 1E-04
HOPG-700aC	217 ± 38	1.2E-04 ± 2E-05	1.6E-02 ± 3E-03
HOPG-900aC	36 ± 1	7.1E-04 ± 3E-05	9.6E-02 ± 4E-03

Tab. 6.3: Charge transfer resistance, exchange current and standard heterogeneous rate constant values determined for all samples using $Fe(CN)_6^{3-/4-}$ redox couple.

The HOPG substrate was not investigated with EIS techniques because it has been already widely studied in the literature, where almost all data confirm that it is not so easy to find a unique and universal value of heterogeneous rate constant for the charge transfer on HOPG. This is due to the high presence of defects, such as step edge defects, whose density depends strongly on the treatment adopted to renew and clean the surface [3].

With regards to prepared samples, for each redox system, as shown in **Tab. 6.1**, **Tab. 6.2 and Tab. 6.3**, the kinetics depend strongly on the electrode treatment. These results indicate that charge transfer becomes faster in the order HOPG-aC < HOPG-aC 500aC < HOPG-aC 700aC < HOPG-aC 900aC . Electron transfer heterogeneous rate constants k_0 reveal significant changes with annealing temperature increasing by orders of magnitude across the temperature series. This is in good agreement to previous determinations of k_0 for pyrolyzed photoresist film electrodes [8,9] and, more simply, for other C-based materials, such as glassy carbon substrates [10,11].

6.4.2. Physico-chemical characterization

With the goal of studying and elucidating the structure/reactivity relationships for the obtained carbon thin films, the bulk and surface properties of the electrode materials were studied with different techniques.

First, Raman spectra of the as deposited film (Mo-aC) and of the film after annealing at 500 °C, 700 °C and 900°C (Mo-500aC, Mo-700aC, Mo-900aC, respectively) were recorded and are presented in **Fig. 6.7**. Peaks were fitted using a Breit-Wigner-Fano line for the G peak and a Lorentzian line for the D peak [12].

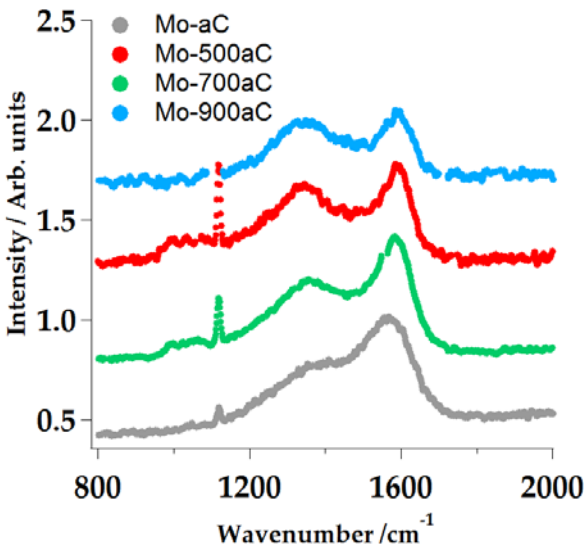

Fig. 6.7: Raman spectra of samples (514 nm excitation); spectra were normalized by the G peak height to facilitate comparison.

Spectra in **Fig. 6.7** show the characteristic D and G peaks of amorphous carbons. Upon annealing, both D and G peaks become narrower, while the G peak also shifts towards higher wavenumbers; this is consistent with increasing sp^2 content and graphitization in the carbon film [12].

Peak fitting of spectra yielded I_D/I_G height ratios and w_{max} (G peak maximum position) that are plotted in **Fig. 6.8** versus the correspondent annealing temperature (for the as deposited sample Mo-aC, the temperature chosen in the plots is 100°C, that is the maximum temperature reached by the sample during the synthetic process in the sputtering chamber).

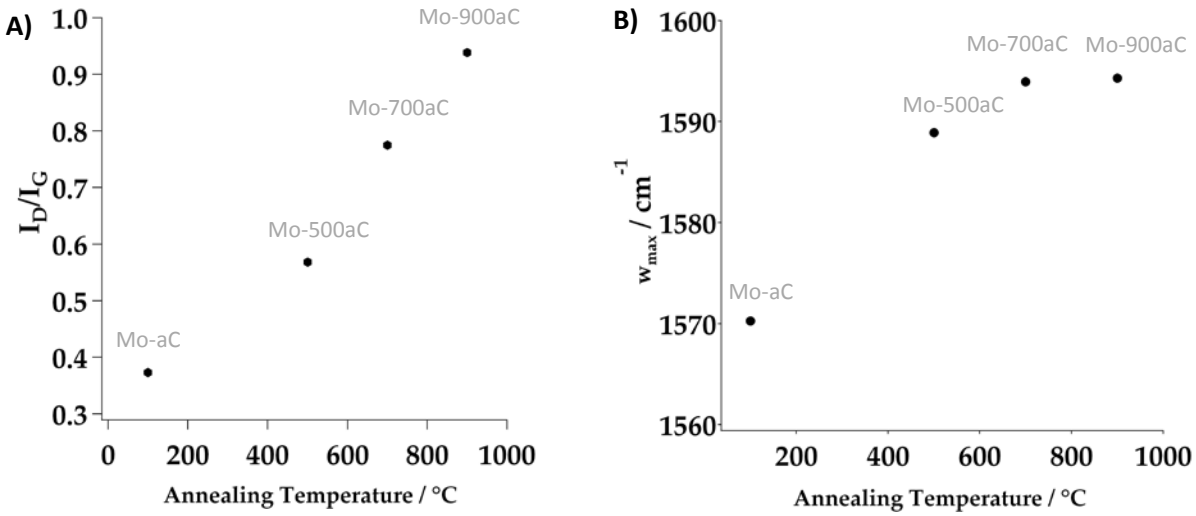

Fig. 6.8: A) Ratio between the two characteristic D and G peaks of samples and B) Raman shift of the G peak, plotted versus the annealing temperature.

Experimental Raman spectra have been interpreted using a three-stage model developed by Ferrari and Robertson [13]. Given a perfect, infinite graphite sheet, a series of defects is introduced, neglecting the possible role of hydrogen, because C-H modes give no detectable contributions to the G and D peaks. The Raman spectrum is considered to depend on clustering of the sp^2 phase, bond disorder, presence of sp^2 rings/chains and the sp^2/sp^3 ratio. The sp^2 content was estimated from the height ratio of the D and G peaks (I_D/I_G). On the basis of this model for amorphous carbons, calculated I_D/I_G values correspond to a change in sp^2 content that increases from ca. 80% to ca. 100% upon annealing, passing from Mo-aC sample to Mo-900aC sample. This evidence confirms the increasing degree of graphitization.

In order to achieve more information about the metallic character and have more details about chemical surface composition, XPS spectra were collected. The High Resolution spectra of C1s and O1s were therefore collected and are shown in **Fig 6.9**. In **Fig. 6.10** is reported, as an example, the survey of Mo-700aC, being representative of all samples. Two main peaks are clearly identifiable and attributable to the presence of carbon and oxygen.

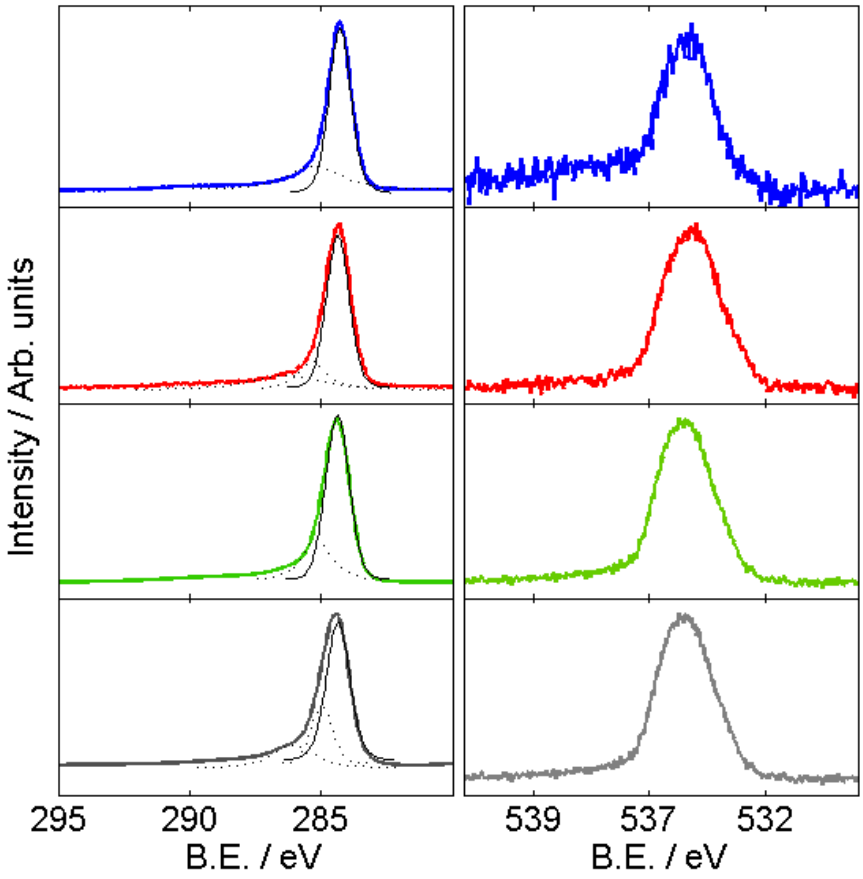

Fig. 6.9: High resolution XPS spectra in the C1s (left column) and O1s (right column) binding energy regions of Mo-aC (grey), Mo-500aC (green), Mo-700aC (red) and Mo-900aC (blue) samples; peak contributions obtained from best fits of C1s are shown below each spectrum. Spectra are shown normalized by the C1s line to facilitate comparison.

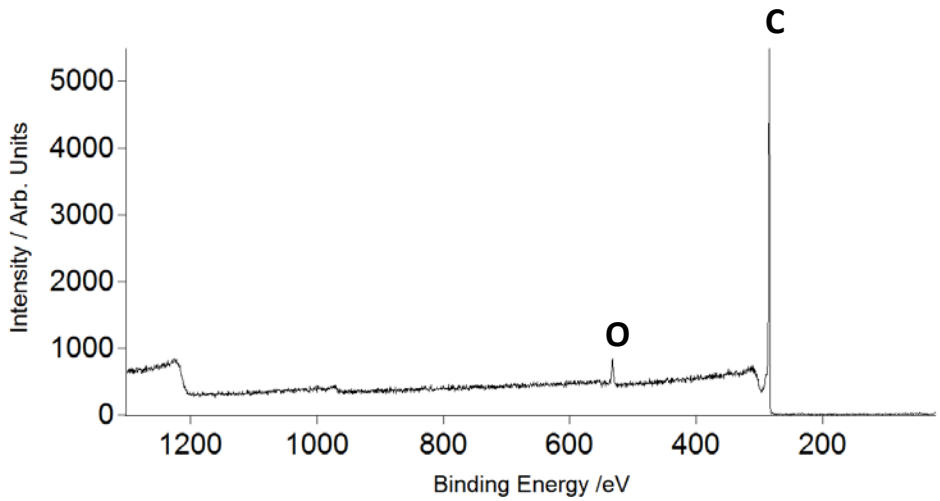

Fig. 6.10: XPS spectra of Mo-700aC: Survey.

In **Fig. 6.11** is presented the oxygen content, calculated as a ratio between O1s and (C1s+O1s) peak areas (values were corrected for the correspondent sensitivity factors derived by Wagner *et al.* [13]: F 1s=1, C 1s=0.25, O 1s=0.66), which was found to decrease upon annealing. As expected, the amount of oxygen decreases when increasing the annealing temperature.

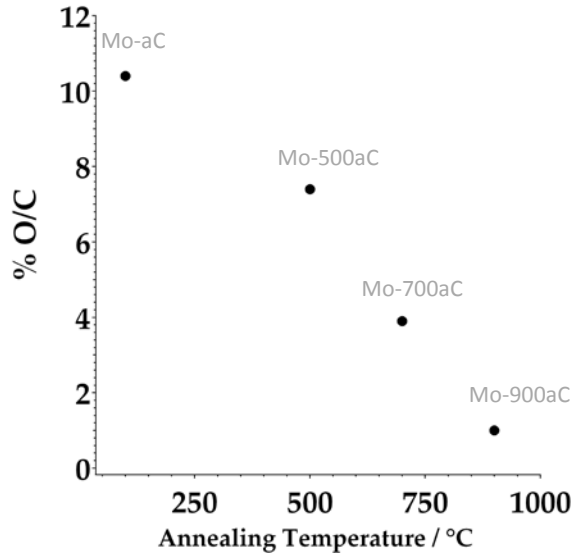

Fig. 6.11: Ratio between oxygen and carbon content plotted versus the annealing temperature.

The C1s spectrum of all samples shows an asymmetric broad line which is characteristic of amorphous carbon [14]. The C1s spectrum was deconvoluted into many contributions. Two main peaks are identified at 284.4 eV, assigned to graphitic carbon (sp^2 centres), and at 285.0 eV, assigned to aliphatic carbon (sp^3 centres). Finally, additional contributions are identifiable at high binding energy, due to oxygen-bonded C atoms and π-π* satellites. **Fig. 6.9** shows that the annealing process leads to a reduction in peak width. After annealing, the C1s peak becomes narrower due to smaller relative contribution of sp^3 centres compared to sp^2 ones [14-16].

The sp^3/sp^2 decrease, observed by annealing in **Fig. 6.12**, is consistent with the electrochemical results, confirming that the degree of graphitization and the metallic character are higher when the annealing temperature is increased. This is in good agreement with results in literature [1,2].

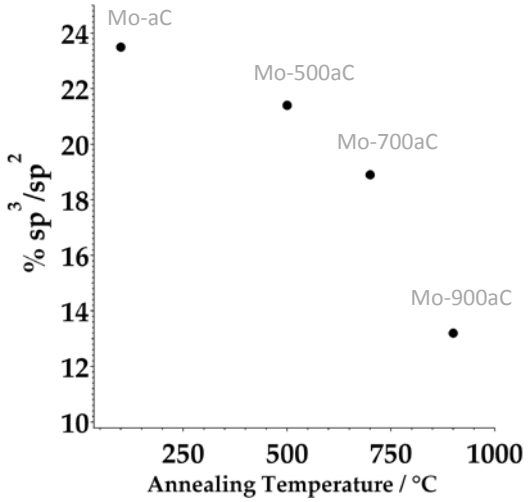

Fig. 6.12: Ratio between the sp^3 and sp^2 contributions of samples plotted versus the annealing temperature.

UPS measurements were collected by applying a negative bias (0, 5, 7, 10 and 12 V) to the sample in order to measure the high binding energy edge of the UPS spectrum. Spectra were corrected for bias and referenced to the Fermi energy (E_F), as measured from the Fermi step of a metallic screw in contact with the sample. An example of the Fermi step and the fitting procedure followed to determine E_F is reported in **Fig. 6.13**.

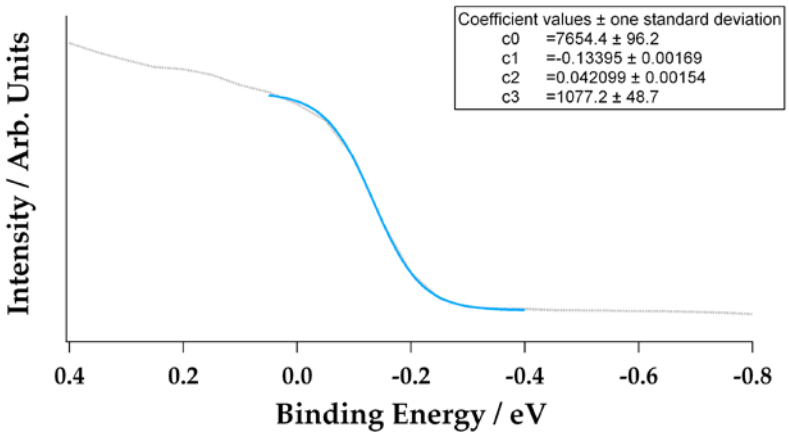

Fig. 6.13: UPS spectrum recorded for the metallic screw. Sample Mo-aC.

Fig. 6.14 shows UPS spectra recorded on sample Mo-aC, as a general example. Spectra were corrected for bias and referenced to the Fermi energy, calculated from the position of the flex in the screw spectrum (c1 parameter in **Fig. 6.13**).

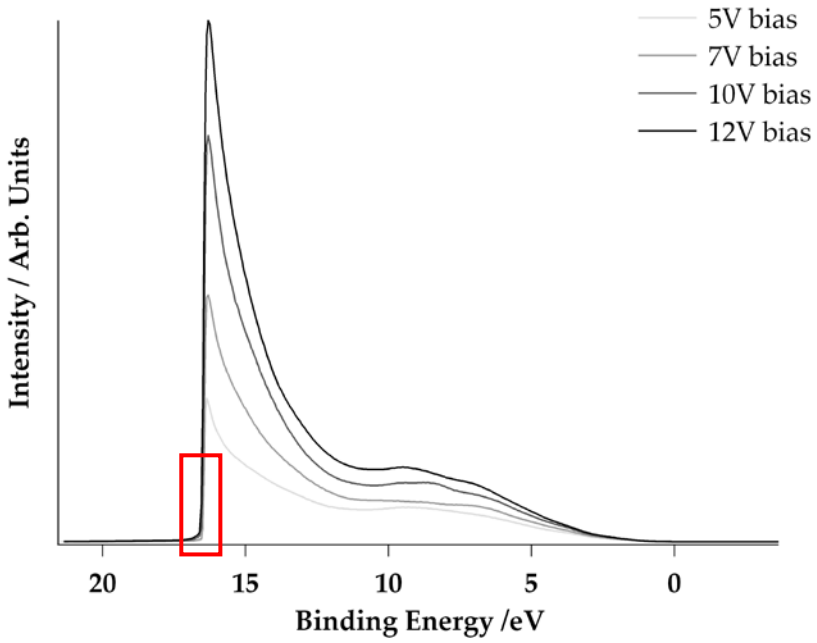

Fig. 6.14: Sample Mo-aC: UPS spectra recorded and corrected for different bias and referenced to Fermi energy. The area in the red rectangle was magnified and each curve in this area was fit to a line to obtain the average energy cutoff value.

The sharp emission threshold at high-binding energy in the UPS spectra was fit to a line and extrapolated to the energy axis in order to find the energy of the high-binding energy cutoff. The work function was calculated from the difference between the incident photon energy (21.2 eV) and the average energy cutoff values previously obtained [17-19]:

$$\Phi = 21.2 - E_{cutoff} \qquad (4)$$

In **Fig. 6.15** the work function values are reported in order to demonstrate that the annealing reduces the work function, confirming that annealed samples behave as better electron donors than as-deposited ones. Moreover, Mo-700aC and Mo-900aC work function values are close to the value reported for glassy carbon in the literature (4.2 eV) [20].

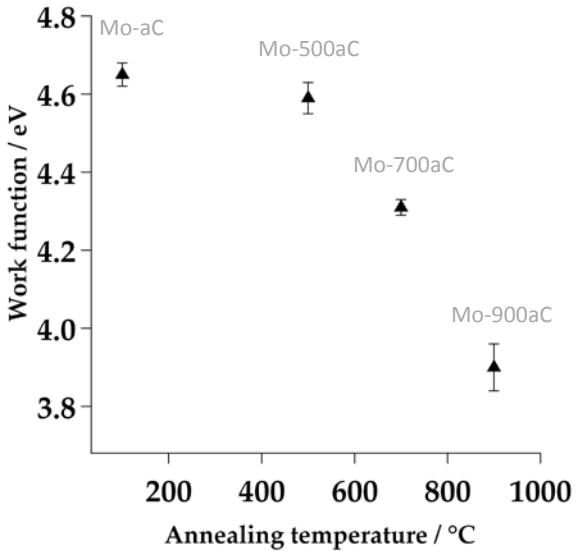

Fig. 6.15: Work function values plotted versus the annealing temperature.

Considering the oxygen content of each sample, as detected by XPS, it suggests that oxidized surfaces have a higher work function, in agreement with previous literature on the effects of surface oxidation of carbon materials [20,21].

6.5 Conclusions

The main goal of this study was to elucidate the structure/reactivity relationships for carbon surfaces, with a specific goal of controlling electron-transfer rates. Achievement of these goals has been done, and it can be concluded that:

- Many samples have been prepared by DC-magnetron sputtering technique and a further annealing process was performed.
- Electrochemical measurements show that the electron transfer increases as the annealing temperature is increased.
- By annealing the graphitization degree is increased, as confirmed by Raman.
- XPS shows that the higher the annealing temperature, the higher the sp^2 content, and the lower the oxygen content.
- UPS shows that work function values decrease with annealing temperature and tend towards reported values for highly graphitic carbons.
- Overall, it can be confirmed that annealed samples behave as better electron donors than as-deposited ones.

Other members of the group are currently continuing this work. In particular, further investigation on the effects that substrate/aC interfaces, electrode contact and cell geometry have on the values of heterogeneous rate constants is currently underway. Latest results obtained by our collaborators show that the relative trends in rate constants are highly reproducible and characteristic of the properties of the carbon materials, however the

absolute values of the constants can be sensitive to the exact preparation of the substrate/aC interface and the contact resistance in the cell. A new cell geometry and a modified electrode deposition configuration have recently been developed to address these issues and determine absolute k_0 values.

In conclusion the work presented in this section successfully correlates the valence structure and the electrochemical charge transfer at differently annealed amorphous carbon films. This deep understanding of the surface behavior is fundamental for rationally optimizing surface preparation in order to better control electrochemical interfacial reactions. Variations in the chemical composition of the surface, for instance by N-doping, are currently under study in order to relate their properties to those of catalysts for the oxygen reduction reaction. In this way the deep understanding of the valence structure properties of the surfaces could be also directly related to the electrocatalytic activity that they might show.

6.6 References

1. D.M. Murphy, R.J. Cullen, D.R. Jayasundara, R.L. Doyle, M. E.G. Lyons, P.E. Colavita, Heterogeneous Charge Transfer at the Amorphous Carbon/Solution Interface: Effect on the Spontaneous Attachment of Aryldiazonium Salts, Journal of Physical Chemistry C, 117 (2013), 22768-22777.

2. R.J. Cullen, D. Jayasundara, L. Soldi, J. Cheng, G. DuFaure, P.E. Colavita, Spontaneous Grafting of Nitrophenyl Groups on Amorphous Carbon Thin Films: A Structure-Reactivity Investigation, Chemistry of Materials, 24 (2012), 1031-1040.

3. R.L McCreery, Advanced Carbon Electrode Materials for Molecular Electrochemistry, Chemical Reviews, 108 (2008), 2646-2687.

4. P.J. Kelly, R.D. Arnell, Magnetron sputtering: a review of recent developments and applications, Vacuum, 56 (2000), 159-172.

5. A.J. Bard, L.R. Faulkner, Electrochemical Methods: Fundamentals and Applications, 2nd ed.; John Wiley & Sons: New York, 2001.

6. I.-W. Sun, E.H. Ward, C.L. Hussey, K.R. Seddon, J.E. Turp, Electrochemistry and Spectroelectrochemistry of the Hexachloroiridate(III) and -(IV) Complexes in the Basic Aluminum Chloride-1-Methyl-3-ethylimidazolium Chloride Room-Temperature Ionic Liquid, Inorganic Chemistry, 26 (1987), 2140-2143.

7. S.J. Konopka, B. McDuffie, Diffusion Coefficients of Ferri- and Ferrocyanide ions in Aqueous Media, Using Twin-Electrode Thin-layer Electrochemistry, Analytical Chemistry, 42 (1970), 1741-1746.

8. C. Fairman, S.C. Yu, G. Liu, A. Downard, D.B. Hibbert, J.J. Gooding, Exploration of Variables in the Fabrication of Pyrolysed Photoresist, Journal of Solid State Electrochemistry, 12 (2008), 1357-1365.

9. S. Ranganathan, R.L. McCreery, Electroanalytical Performance of Carbon Films with near-Atomic Flatness, Analytical Chemistry, 73 (2001), 893-900.

10. S. Tanimoto, A. Ichimura, Discrimination of Inner- and Outer-Sphere Electrode Reactions by Cyclic Voltammetry Experiments, Journal of Chemical Education, 90 (2013), 778-781.

11. Chen, R.L. McCreery, Control of electron transfer kinetics at glassy carbon electrodes by specific surface modification, Analytical Chemistry, 68 (1996), 3858-3965.

12. A.C. Ferrari, J. Robertson, Interpretation of Raman spectra of disordered and amorphous carbon, Physical Reviews B, 61 (2000), 14095-14107.

13. C.D. Wagner, L.E. Davis, M.V. Zeller, J.A. Taylor, R.H. Raymond, L.H. Gale, Empirical atomic sensitivity factors for quantitative analysis by electron spectroscopy for chemical analysis. Surface and Interface Analysis, 3 (1981), 211-25.

14. S.T. Jackson, R.G. Nuzzo, Determining hybridization differences for amorphous carbon from the XPS C 1s envelope, Applied Surface Science, 90 (1995), 195-203.

15. E. Papastavros, P.J. Shea, M.A. Langell, Oxygen, Carbon, and Sulfur Segregation in Annealed and Unannealed Zerovalent Iron Substrates, Langmuir, 20 (2004), 11509-11516.

16. S. Biniak, G. Szymański, J. Siedlewski, A. Świ tkowski, The characterization of activated carbons with oxygen and nitrogen surface groups, Carbon, 35 (1997), 1799-1810.

17. P.E. Colavita, B. Sun, K.Y. Tse, R.J. Hamers, Photochemical Grafting of N-Alkenes onto Carbon Surfaces: The Role of Photo-electron Ejection, Journal of the American Chemical Society, 129 (2007), 13554-13565.

18. G. Ertl, J. Küppers, Low Energy Electrons and Surface Chemistry, Wiley-VCH: Weinheim, 1986.

19. R. Schlaf, P.G. Schroeder, M.W. Nelson, B.A. Parkinson, P.A. Lee, K.W. Nebesny, N.R. Armstrong, Observation of Strong Band Bending in Perylene Tetracarboxylic Dianhydride Thin Films Grown on Sns2, Journal of Applied Physics, 86 (1999), 1499-1509.

20. S.R. Kelemen, H. Freund, C.A. Mims, The interaction of potassium hydroxide with clean and oxidized carbon surfaces, Journal of Catalysis, 97 (1986), 228-239.

21. J.M. Simmons, B.M. Nichols, S.E. Baker, S. Marcus Matthew, O.M. Castellini, C.-S. Lee, R.J. Hamers, M.A. Eriksson, Effect of ozone oxidation on single-walled carbon nanotubes, Journal of Physical Chemistry B, 110 (2006), 7113-7118.

Conclusions

The present PhD thesis was mainly devoted to develop electrocatalysts for the electrochemical oxygen reduction reaction. In this project a number of Pt-free N-doped C-based catalysts have been synthesized on the basis of different synthetic and templating strategies aiming to understand how compositional, morphological and textural aspects of the end material can affect the electrochemical behaviour of ORR. Materials have been characterized using different physico-chemical methods including a study of the kinetics and mechanism of the electrochemical oxygen reduction reaction.

The general achieved conclusions can be briefly summarized as follows.

Mesoporous N-, Fe-doped Carbons

- Two series of sample have been basically synthesized by furnace processes. The former series used fructose as C- and O-source and it was added with iron acetate and a N-compound chosen among either guanidine acetate or 2-Guanidinobenzimidazole or 1,1,3,3-Tetramethylguanidine. Being the sample prepared by fructose and guanidine acetate very active in ORR, in a second series of samples fructose was replaced by other monosaccharides, such as glucose and xylose, keeping guanidine acetate and iron acetate as the N- and Me-sources, respectively.
- All samples are characterized by a very high surface area, above 500 m^2g^{-1}, and a porosity centered in the mesoporosity range (mainly around 5-10 nm).
- All samples show a rewarding activity towards ORR both in acidic and alkaline conditions; moreover they all catalyze the oxygen reduction through a direct 4-electrons pathway.
- The electroactivity of the sample prepared starting from fructose and guanidine acetate is rewarding in acidic conditions and excellent in alkaline media, even better than Pt EC20, a commercial Pt-based catalyst.
- Peroxides production efficiency, monitored in alkaline condition through a RRDE working electrode, was found to be around 5-10% for almost all materials, a quite common value even for very promising Pt-free catalysts. Synthesized catalysts are therefore promising also from the point of view of yielding low quantity of peroxides species.
- A mechanistic study was performed by comparing theoretical value of Tafel slopes, based on a literature ORR proposed mechanism, and experimental ones. Reaction mechanism in acidic and alkaline media is equivalent until the third step of the invoked mechanism, through which $Fe(III)-O-OH$ is formed. Then, the reaction follows different paths because of different stability in acidic and alkaline solutions of involved species.
- An attempt of using polysaccharides has been performed by impregnating a piece of dried sugarcane (collected in Venezuela) with a guanidine acetate and iron containing solution. The ORR electroactivity of the annealed sample, however, was not satisfying if compared to other mesoporous materials prepared in this work. The reasons of the worse behavior might be related to the insufficient presence of mesopores; the surface area, that is actually quite high, is almost entirely comprised into micropores, with consequent issues related to mass transport processes of reactants and products from/to active sites.

Templating Strategies

- Samples of the catalyst were obtained heat-treating a reactant mixture with constant composition and using a variety of templating procedures, i.e. shape-imprinting materials (like high surface area silica and Black Pearls 2000), and some self-templating processes (freeze-drying and in-situ generation of gas bubbles).
- Different catalytic ORR activities resulted depending on templating conditions.

- As shown by comparison of electrochemical CV data and BET determinations mesopores are necessary and of the utmost importance to improve ORR behaviour. This is proposed to be due to the ease by which comparatively large cross section channels favour the diffusion access of reagents/products to the internal surface area. Micropores can also be beneficial provided they have greater width than 0.7 nm, otherwise they may be ineffective, or even harmful, because polymeric electrolytes like Nafion® cannot enter them, thus excluding a main surface area fraction from the reaction. Therefore, some combination of meso and micropores seems useful to ORR.
- Because of their shape, ink-bottle pores are especially detrimental. Besides pore size, pore shape also affects ORR efficiency.
- Improving performance of non-noble ORR electrodes involves the search of some optimized reactant composition, which is still under way, and, as shown by the templating results, a suitable combination of pore size, pore shape and pore size distribution.

Ordered Structures for ORR

N-doped carbon nanotubes

- 1,1,3,3-tetramethylguanidine was selected as precursor because it contains the guanidinium-group; it has been demonstrated that this nitrogen-based functional group enhances the catalytic activity towards ORR. Magnesium oxide, impregnated with an iron (III) solution, was chosen as the catalyst for N-CNTs growth. N-doped carbon nanotubes were synthesized by a CVD process.
- The starting point of this part of work is related to some incomprehensible results obtained repeating the synthesis in different days. In fact, varying the synthesis day, synthesized nanotubes were found to be ORR electrocatalytically and morphologically different.
- By XPS it was detected that sample containing the highest iron and nitrogen amounts is not the most active for ORR. It was assumed that iron and nitrogen can interact in various ways of which only a fraction is useful to the formation of catalytic sites. As a fact, the best ORR results are obtained on the sample that contains the highest amount of pyridinic/pyrrolic nitrogen, that are considered most active for ORR. The same sample is also the material with the best developed morphology.
- By comparing Fe and N surface content, as detected by XPS, the presence and nature of nitrogen surface groups appear more important to improve ORR activity than the presence of metal impurities only.
- The MgO-based catalyst age was found to affect the synthesized nanomaterials with respect to morphology, surface composition and electrocatalytic behavior towards the electrochemical oxygen reduction

N-doped carbon nanocubes

- By a synthetic method similar to the synthesis of carbon nanotubes, a very interesting material has been synthesized, with a nanocubic empty shape. So far there are no

other examples in the literature of N-doped carbon nanotubes synthesized by simple methods.

- Nanocubes were found not electroactive in ORR. However an interesting aspect was evidenced by DSC: surprisingly an endothermic peak was found to start before room temperature, with a maximum at about 37.5°C and end at about 100°C.
- Due to the empty space available in the internal part of each cubes, many applications can be thought, for example involving cubes as nano-reactors that can be opened/close changing the temperature.

N-doped carbon microspheres

- An ultrasonic spray pyrolysis (USP) method and an aerosol pyrolysis (APM) method were developed for the synthesis of N/Fe-doped porous carbon microspheres.
- Catalytic materials with relatively narrow size dispersion were prepared using low cost materials and in the absence of a templating agent. The inherent scalability of continuous flow methods such as USP and APM represents a significant advantage compared to alternative synthetic strategies requiring batch processing or surface catalyzed deposition of nanostructured carbon materials (e.g. CVD growth).
- Annealing of thus synthesized materials results in the formation of graphitic microspheres containing Fe/Fe_3C clusters embedded in a porous carbon phase.
- These particles were investigated as non-noble-metal catalytic electrode materials: RDE measurements show that indeed these particles catalyse ORR and could therefore be promising as electrode materials in FCs.
- The physico-chemical characterization of the surface showed that the enhancement in ORR performances might be related to the higher degree of graphitization, the stabilization of ORR N- and/or Fe-containing active catalytic sites and the increase in surface area that result from the annealing treatment.

Tuning the Electronic Valence Structure of Carbon Films

- The main goal of this study was to elucidate the structure/reactivity relationships for carbon surfaces, with a specific goal of controlling electron-transfer rates.
- This section, apparently diverging from the main goals of the present work, was thought to better understand the electronic C-surface behavior in charge transfer reactions. This is actually strongly connected to the oxygen reduction reaction, for which all the catalysts, hereby synthesized, were designed. However, instead of starting from complicated systems involving porous and doped-carbons (as all the above presented samples are), the choice was addressed to the simplest but closest material: annealed and non-annealed amorphous carbon thin films prepared by DC-magnetron sputtering technique.
- Many samples have been prepared by DC-magnetron sputtering technique and a further annealing process was performed.
- Electrochemical measurements show that the electron transfer increases as the annealing temperature is increased.
- By annealing the graphitization degree is increased, as confirmed by Raman.

- XPS shows that the higher the annealing temperature, the higher the sp^2 content, and the lower the oxygen content.
- UPS shows that work function values decrease with annealing temperature and tend towards reported values for highly graphitic carbons.
- Overall, it can be confirmed that annealed samples behave as better electron donors than as-deposited ones.

Appendix

In the following are given detailed information about the used instrumentation to perform all the analyses presented in the sections above. There are many cases indeed, especially those ones concerning the collaboration with Prof. Colavita from Trinity College Dublin, for which it is not clear if the analysis has been performed in the Department of Chemistry of Università degli Studi di Milano, or in CRANN (Centre for Research on Adaptive Nanostructures and Nanodevices) in Trinity College Dublin.

Then, a list of attended conferences and published and submitted papers is given.

A. Experimental measurements specifications

Chapter 3 Mesoporous N-, Fe-doped Carbons:

- **Tab. 3.1, Fig. 3.6 A-C, Fig. 3.7, Tab. 3.4, Fig. 3.12, Fig. 3.13, Fig. 3.27:** BET performed in Università degli Studi di Milano
- **Fig. 3.8, Fig. 3.14, Fig. 3.26:** RDE performed in Università degli Studi di Milano
- **Fig. 3.9, Fig. 3.10, Fig. 3.15, Fig. 3.16:** RRDE performed in Università degli Studi di Milano
- **Fig. 3.19:** XRPD performed in Università degli Studi di Milano
- **Fig. 3.20, Fig. 3.21:** XPS performed in Università degli Studi di Milano
- **Fig. 3.24:** Optical microscope imaging performed in Università degli Studi di Milano

Chapter 4 Templating Strategies:

- **Fig. 4.4, Fig. 4.5:** RDE performed in Università degli Studi di Milano
- **Fig. 4.7 a-d:** BET performed in Università degli Studi di Milano

Chapter 5 Ordered Structure for ORR:

- **Fig. 5.1 a-d, Fig. 5.16:** TEM imaging performed in Università degli Studi di Milano
- **Fig. 5.2:** Raman spectroscopy performed in Università degli Studi di Milano
- **Tab. 5.1:** Magnetic susceptibility performed in Università degli Studi di Pavia
- **Tab. 5.1:** EDX performed in Università degli Studi di Milano
- **Tab. 5.1, Fig. 5.3 a-j, Fig. 5.10 a-p, Fig. 5.24:** XPS performed in Università degli Studi di Milano
- **Fig. 5.4, Fig. 5.7, Fig. 5.26, Fig. 5.35 a-c, Fig. 5.38, Fig. 5.40:** RDE performed in Università degli Studi di Milano
- **Fig. 5.5:** LSV performed in Università degli Studi di Milano
- **Fig. 5.8, Fig. 5.30:** BET performed in Università degli Studi di Milano
- **Fig. 5.12:** TGA performed in Università degli Studi di Milano
- **Fig. 5.13 A-C:** TPD-MS performed in CNR Milano
- **Fig. 5.14, Fig. 5.37:** XRPD performed in Università degli Studi di Milano

- **Fig. 5.15:** HRXRPD performed by synchrotron facilities in Grenoble and ALBA.
- **Fig. 5.17, Fig. 5.18, Fig. 5.19, Fig. 5.20, Fig. 5.21:** HRTEM imaging performed in CNR Milano
- **Fig. 5.23:** DSC performed in Università degli Studi di Milano
- **Fig. 5.22, Fig. 5.27, Fig. 5.36 A-B, Fig. 5.39 a-d, Fig. 5.41 a-c:** SEM and SEM-FIB imaging performed in Trinity College Dublin
- **Fig. 5.39 e-h, Fig. 5.43 a-d:** SEM performed in Università degli Studi di Milano
- **Fig. 5.29:** Raman spectroscopy performed in Trinity College Dublin
- **Fig. 5.31:** EDX performed in Università degli Studi di Milano
- **Fig. 5.33 a-c, Fig. 5.34:** XPS performed in Università degli Studi di Milano

Chapter 6 Tuning the Electronic Valence Structure of Carbon Films:

- **Fig. 6.3:** CV recorded before EIS in Trinity College Dublin
- **Fig. 6.5:** EIS recorded in Trinity College Dublin
- **Fig. 6.7:** Raman spectroscopy performed in Trinity College Dublin
- **Fig. 6.9, Fig. 6.10:** XPS performed in Trinity College Dublin
- **Fig. 6.13, Fig. 6.14:** XPS performed in Trinity College Dublin

B. List of contributions in conferences

- **Oral communication**: *Template-free ultraspray pyrolysis synthesis of N- and Fe-doped carbon microspheres for oxygen reduction electrocatalysis.*
  Stefania Marzorati, Joana M. Vasconcelos, J. Ding, Mariangela Longhi, Paula E. Colavita
  GEI2015, Bertinoro, Italy, 20th -24th September 2015.

- **Oral communication**: *Effects of catalyst aging on the morphology and oxygen reduction activity of nitrogen-doped carbon nanotubes.*
  Roberto Bresciani, Stefania Marzorati, Alessandro Lascialfari, Benedetta Sacchi, Nadia Santo, Mariangela Longhi.
  GEI2015, Bertinoro, Italy, 20th -24th September 2015.

- **Poster communication**: *Microstructured Pt-free cathodes for oxygen reduction reaction in fuel cells.*
  Stefania Marzorati, Elena Zanzola, Roberto Bresciani, Joana M. Vasconcelos, Paula E. Colavita, Nadia Santo, mariangela Longhi M.
  GEI2015, Bertinoro, Italy, 20th -24th September 2015.

- **Poster communication**: *Template-free ultraspray pyrolysis synthesis of N- and Fe-doped carbon microspheres for oxygen reduction electrocatalysis.*
  Stefania Marzorati, Joana M. Vasconcelos, J. Ding, Mariangela Longhi, Paula E. Colavita
  EFCD2015, La Grande Motte, France, 13th -16th September 2015.

- **Poster communication**: *Effects of catalyst aging on the morphology and oxygen reduction activity of nitrogen-doped carbon nanotubes*.
  Roberto Bresciani, Stefania Marzorati, Alessandro Lascialfari, Benedetta Sacchi, Nadia Santo, Mariangela Longhi.
  EFCD2015, La Grande Motte, France, 13th -16th September 2015.

- **Poster communication**: *Comparison of the photocatalytic activity of TiO2-WO3 materials in oxidation and reduction reactions.*
  Maria Vittoria Dozzi, Stefania Marzorati, Mariangela Longhi, Mauro Coduri, Elena Selli.
  CRC International Symposium: Novel Photocatalysts for Environmental Purification and Energy Generation. Catalysis Research Center, Hokkaido University, Sapporo (Japan), 14th October 2014.

- **Poster communication**: *Effect of WO_3 coupling on the Photocatalytic Activity of TiO_2.*
  Maria Vittoria Dozzi, Francesca Riboni, Stefania Marzorati, Mariangela Longhi, Elena Selli.
  XXV Congresso Nazionale della Società Chimica Italiana, Rende (CS), 7th-12th September 2014.

- **Poster communication**: *Templating-Induced Enhancement Of The Electrocatalytic Activity Of Pt-free Carbons For Oxygen Reduction Reaction*
  Stefania Marzorati, Mariangela Longhi, Leonardo Formaro.
  65th Annual meeting of the International Society of Electrochemistry , Lausanne, 1st -5th September 2014.

- **Poster communication**: *The Electronic Valence Structure Of Amorphous Carbon Thin Films And Its Effects On The Kinetics Of Interfacial Charge Transfer*
  Stefania Marzorati, Ronan J. Cullen, Richard L. Doyle, Mariangela Longhi, Michael E. G. Lyons and Paula E. Colavita.
  65th Annual meeting of the International Society of Electrochemistry , Lausanne, 1st -5th September 2014.

- **Poster communication**: *Modified Carbon Nanostructures As Catalysts For Oxygen Reduction*
  Mariangela Longhi, Leonardo Formaro, Roberto Bresciani, Stefania Marzorati, Theodoros Tsoufis, Fotis Katsaros, Zili Sideratou
  65th Annual meeting of the International Society of Electrochemistry , Lausanne, 1st -5th September 2014.

- **Poster communication**: *Tuning the Electronic Valence Structure of Amorphous Carbon Surfaces: Effects on the Kinetics of Electrochemical Phenomena at the Carbon/Solution Interface*
  Stefania Marzorati, Ronan J. Cullen, Richard L. Doyle, Mariangela Longhi, Michael E. G. Lyons and Paula E. Colavita.
  Faraday Discussion 172: Carbon in Electrochemistry, Sheffield, 28th -30th July 2014.

- **Poster communication**: *Platinum-free electrocatalysts for oxygen reduction reaction*
  Stefania Marzorati, Mariangela Longhi, Leonardo Formaro.
  Faraday Discussion 172: Carbon in Electrochemistry, Sheffield, 28th -30th July 2014.

- ***Poster communication**: Photocatalytic activity of TiO2-WO3 mixed oxides in oxidation and reduction reactions.*
  Maria Vittoria Dozzi, Stefania Marzorati, Mariangela Longhi, Elena Selli.
  European Meeting on Solar Chemistry and Photocatalysis Environmental Applications. Thessaloniki, 25th -28th June 2014.

- **Oral communication**: *Platinum-free carbons for oxygen reduction reaction: relations among electrocatalytic properties and templating procedures.*
  Stefania Marzorati, Mariangela Longhi, Leonardo Formaro.
  GEI 13, Pavia, 22nd - 27th September 2013.

- **Oral communication**: *ORR reaction: Pt-free mesoporous carbon vs Pt*.
  Mariangela Longhi, Stefania Marzorati, Leonardo Formaro.
  GEI 13, Pavia, 22nd - 27th September 2013.

- **Poster communication**: *Templating Effects Onto Electrocatalytic Properties Of Pt-free Carbons For Oxygen Reduction Reaction*.
  Stefania Marzorati, Mariangela Longhi, Leonardo Formaro.
  ICEI 13, Liblice (Praga), 30 th June- 5th July 2013.

- **Oral communication**: *Oxygen Cathode For Fuel Cells. ORR Activity Of Mesoporous N-Modified Carbon Doped With Non-Noble Metals*.
  Mariangela Longhi, Stefania Marzorati, Leonardo Formaro.
  ICEI 13, Liblice (Praga), 30 th June- 5th July 2013.

- **Poster communication**: *Effetti di "templating" su catalizzatori platinum-free per ORR*.
  Mariangela Longhi, Stefania Marzorati, Leonardo Formaro.
  GEIERA2012, Santa Marina Salina (Messina), 17th -22nd June 2012.

C. List of publications

- Roberto Bresciani, Stefania Marzorati, Alessandro Lascialfari, Benedetta Sacchi, Nadia Santo, Mariangela Longhi
  Effects of catalyst aging on the growth morphology and oxygen reduction activity of nitrogen-doped carbon nanotube.
  Electrochemistry Communications, 51 (2015), 27-32.

- Stefania Marzorati, Enzio M. Ragg, Mariangela Longhi , Leonardo Formaro
  Low-temperature intermediates to oxygen reduction reaction catalysts based on amine-modified metal-loaded carbons. An XPS and ss-NMR investigation.
  Materials Chemistry and Physics, 162 (2015), 234-243.

- S. Marzorati, J. M. Vasconcelos, J. Ding, M. Longhia and Paula E. Colavita
  Template-free ultraspray pyrolysis synthesis of N/Fe-doped carbon microspheres for oxygen reduction electrocatalysis.
  Journal of Materials Chemistry A: Materials for Energy and Sustainability, 3 (2015), 18920-18927

- Maria Vittoria Dozzi, Stefania Marzorati, Mariangela Longhi, Mauro Coduri, Luca Artiglia, Elena Selli
  Photocatalytic activity of TiO_2-WO_3 mixed oxides in relation to electron transfer efficiency.
  Submitted to: Applied Catalysis B: Environmental

- Stefania Marzorati, Mariangela Longhi
  Templating Induced Behavior of Pt-free Carbons for Oxygen Reduction Reaction.
  Submitted to: Applied Catalysis B: Environmental

Acknowledgements

When you see the number "200" at the bottom of the page you're writing, something is telling you that you'd better stop typing and rather start thinking and thanking. And if the submission deadline is within the order of hours, you'd also better rush. The very last section is therefore devoted to the big THANKS to that uncountable number of people who, by scientific and/or psychological help, supported my work in the last three years.

No need for tissues. I'm not thanking my family, by boyfriend, grandparents and all the relatives and friends. PhD is a matter of study, work, ideas and luck. I do think that these last four words have nothing to do with "people of my life". I feel grateful to them, but this happens wordlessly almost every single moment of my life, not exclusively in this circumstance. Another world is the university world, and on this scientific side, both in the university of Milano and Trinity College Dublin, so many brains deserve to be mentioned in my THANKS.

I would like first to thank my tutor, Dr. Mariangela Longhi, because she believed in me since I was just a candid master student. She patiently guided and advised me, pressing when necessary. I will be forever grateful to her also for giving me the possibility of spending a period abroad, that opened incredibly my mind and changed my life.

I have been extremely lucky to have Prof. Leonardo Formaro as co-tutor. Even after his retirement, he cared so much about my work and myself, and responded so wisely to all my questions and difficulties. I thank also his terrific frankness…there is no point to dream if there is nothing to dream about.

Thanks to all the guys that spent a period in the lab. My thoughts are addressed especially to Ivano, my dear distant mentor, who taught me the fundamental pine nut therapy, and to Roberto, Luca, Chiara, Anna&Alessandra and Elena. Mirko shared with me a common scientific and academic history, hope for him all the best. Thanks to Mavi and Marco, coffee-break colleagues, mandatory helps in fighting scientific frustration, wish you the dreamt future.

Thanks to Dr. Nadia Santo, with patience and extreme expertise, she shared with us many hours in the dark rooms taking TEM and SEM pictures. Thanks to Benedetta Sacchi, for SEM imaging and SEM support and, together with Prof. Claudia Bianchi and Valeria Oldani, for XPS measurements. Thanks to Dr. Marco Scavini and his PhD student Stefano Checchia; they gave me the possibility of spending a week in Grenoble in ESRF synchrotron facilities and helped me a lot in understanding and elaborating incomprehensible data from HR XRPD. Thanks to Prof. Alessandro Lascialfari for the magnetic susceptibility measurements performed in Università di Pavia. Thanks to Stefano Antenucci, Dr. Vladimiro dal Santo and Prof. Silvia Bruni for TGA, TPD-MS and Raman spectroscopy measurements, respectively. Thanks to SmartMatLab and Dr. Ottavio Lugaresi for DSC measurements and to Prof. Francesco De Marin for XRD measurements and his support in data interpretation. A big thank to Dr. Stefano Trasatti not only for the use of the furnace but rather for thinking outside the box.

In the last year I realized that there is not a specific rule that ensures good luck to people leaving their country and spending a period abroad. This awareness made me understand that Prof. Paula Colavita, who hosted me for 5 months in her labs in Trinity College Dublin, was a fantastic exception. A part from her outstanding intelligence, I feel in debt for having learnt so much in only a few months. This was also thank to “Colavita’s superfriends”, that during these months made me fatter and fatter, poorer and poorer, stronger and stronger. Joana is the boss, end of the story. But let me thank Ronan, Dee and Fede, smiling weird guys. Thanks to Richard, my dear safety impedance-man and Prof. Mike Lyons for supervising the electrochemical activities.
Again Paula was the responsible for finding me a house, even before my arrival in Ireland. Actually I did not find any house. I found a whole family, dog included.

Finally, a sweet thank is straight to Enri, who collected with me pieces of sugarcanes and, much more frequently, pieces of life.

This work was supported by MIUR (Italy) under the Project NAMED-PEM (PRIN 2011).

Research in TCD was conducted with the financial support of Science Foundation Ireland under Grant Number 13/CDA/2213.

Royal Society of Chemistry financed a bursary for participation to Faraday Discussion 172.

Stefania Marzorati thanks the LLP Erasmus Placement for a grant.